Gas and galaxies at $z \sim 3$

Pimpunyawat Tummuangpak

A Thesis presented for the degree of
Doctor of Philosophy

Extragalactic Astronomy and Cosmology
Department of Physics
University of Durham
United Kingdom

December 2013

Dedicated to

My family

Gas and galaxies at $z \sim 3$

Pimpunyawat Tummuangpak

Submitted for the degree of Doctor of Philosophy
December 2013

Abstract

In this thesis we present analyses of $z \approx 3$ star-forming Lyman break galaxy and Lyman-α emitter populations. Additionally, we use QSO sightlines to probe the properties of gas around the LBGs. The observed star-forming galaxy sample is based on spectroscopic redshift data taken from a combination of the VLT LBG Redshift Survey (VLRS) data and Keck LRIS observations in fields centred on bright background QSOs. We compare these data with results from a GIMIC hydrodynamical simulation. We first estimate the auto-correlation function of simulated galaxies and compare these results with the observed Keck + VLRS correlation functions. We find that the observed galaxy real-space autocorrelation function is more consistent with that measured for simulated $M_\star \geq 10^9\ h^{-1}\mathrm{M}_\odot$ galaxies than lower mass galaxies.

We then calculate the cross correlation of galaxies with Lyα absorption in QSO sightlines in both our observed and simulated datasets. We check near star-forming galaxies in both data and simulations for the existence of the transmission spike which previous authors have claimed to be indicative of the effects of star-formation feedback on the IGM. No detection of such a spike is seen in the galaxy-gas correlation function in the combined VLRS+Keck data. The simulated cross-correlation function also shows comparable neutral gas densities around galaxies as seen in the observations. The Lyα auto- and cross-correlation functions in the GIMIC simulations, appear to show infall smaller than implied by the predicted infall parameter of $\beta_{Ly\alpha} \approx 1.3$ (McDonald et al.). There is a possibility that the reduced infall may be due to the galaxy wide outflows implemented in the simulations.

We present the Lyman-α luminosity functions and two-point clustering correlation functions of Lyα emitters (LAEs) at $z = 3.1$. We obtain a photometric sample of $\sim$ 500 LAE candidates from 5 fields based on deep Subaru Suprime-Cam imaging data and a spectroscopic sample of 62 confirmed LAEs in 3 of our 5 fields from VLT VIMOS spectroscopy. We find that our narrowband Lyα luminosity function is in agreement with Ouchi et al. (2008) and is higher than for Gronwall et al. (2007). We estimate the R-band continuum luminosity functions of our sample of LAEs. Our 1700 Å continuum magnitude (auto) LAE luminosity function appears similar to that of Gronwall et al. (2007) with a relatively high number density of LAE being detected at bright magnitudes. We compare LAE and LBG R-band continuum luminosity functions and find that the LAE luminosity function at R < 25.5 amounts to only $\sim$ 30 % of the density of the LBG luminosity function. Nevertheless, most of LAE still lie at the faint end of the LBG luminosity function. Finally, by comparing the 3-D LAE and LBG clustering amplitudes as estimated from the angular correlation function, we find a lower r_0 for LAE than for the LBGs. We measure a correlation length in the range of $r_0 = 1.8$-3.1 h^{-1}Mpc and a bias in the range of $b = 1.4$-2.3 for LAEs. Even the highest LAE r_0 value is significantly lower than that of LBGs. The average LAE dark matter halo mass inferred from clustering is in the range of $10^{9.7\pm0.8}$-$10^{11.2\pm0.2}$ $h^{-1}M_{\odot}$. The lower correlation length leads to the lower halo masses. Our results show that the LAE population is dominated by galaxies fainter than those traditionally selected via the Lyman Break method. It is possible that the LAE population may simply be a faint subset of the LBG selection and our results, in terms of both the luminosity function and clustering, are consistent with this picture.

Declaration

The work described in this thesis was undertaken between 2010 and 2013 while the author was a research student under the supervision of Professor Tom Shanks in the Department of Physics at the University of Durham. This work has not been submitted for any other degree at the University of Durham or any other University.

Portions of this work have appeared in the following papers:

- **"The VLT LBG Redshift Survey - IV. Gas and galaxies at $z \sim 3$ in observations and simulations"** Tummuangpak, P. , Shanks, T., Bielby, R. M., Crighton, N. H. M., Francke, H. ,Infante, L.,Theuns, T.,2013, MNRAS, in press (arXiv:1304.4598)

  Chapter 2 notes -

  The VLRS LBG survey covering, the imaging, data reduction, candidate selection and spectroscopic follow-up of targets are appeared in

- **" The VLT LBG Redshift Survey I: Clustering and Dynamics of $\approx$ 1000 Galaxies at $z \approx 3$"** Bielby R. M., Shanks T., Weilbacher P. M., Infante L., Crighton N. H. M., Bor- nancini C., Bouche N., Heraudeau P., Lambas D. G., Lowenthal J., Minniti D., Padilla N., Petitjean P., Theuns T., 2011, MNRAS, 414, 2

- **"VLT LBG Redshift Survey II: Interactions between galaxies and the IGM at $z \sim 3$."** Crighton, N. H. M., Bielby, R., Shanks, T., Infante, L., Bornancini, C. G., Bouch, N., Lambas, D. G., Lowenthal, J. D., Minniti, D., Morris, S. L., Padilla, N., Proux, C., Petitjean, P., Theuns, T., Tummuangpak, P., Weilbacher, P. M., Wisotzki, L., Worseck, G., 2011, MNRAS, 414, 28

- **"The VLT LBG Redshift Survey - III. The clustering and dynamics of Lyman-break galaxies at z $\sim$ 3"** Bielby, R., Hill, M.D., Shanks, T., Crighton, N.H.M.,Infante, L., Bornancini, C. G., Francke, H. ,Héraudeau, P., Lambas, D. G., Metcalfe, N., Minniti, D., Padilla, N., Theuns, T., Tummuangpak, P. ,Weilbacher, P., 2013, MNRAS, 430,425

Acknowledgements

First of all I would like to thank my supervisor, Prof. Tom Shanks, for his support, time, patience, and guidance. Special thanks to Dr Rich Bielby for his major contribution to the analysis presented in this Thesis. Thank to Dr Neil Crighton and Dr Tom Theuns for their supports on the simulations. I would like to acknowledge others in the department whose advice or assistance I benefited during my time in Durham. I am also grateful for the financial support from Ministry of Science and Technology of The Royal Thai Government during most of my academic career in the UK.

Thank to my friends here in the UK who share the enjoyable/difficult times together, Im, Jung, Som, P'Utane, P'Bird, P'Nim, P'Benz, P'Ke, P'Bom, Bew, Bank, Tom, Ton, Nim, Bas, F, Yetli, Nikos, Alex, Nicolas, Joe, Sergio, Jamie, Yos, and many others. Big thank to Mei-fen Hsin, my housemate & my JJ, who are always there for me. My friends in Thailand; Hem, Jnet, Kit, Ple, Amm, Pun, and others, who always encourage me, thank you very much. Finally, my special gratitude goes to my family who deserves the most thanks of all.

Contents

List of Figures

List of Tables

Chapter 1

Introduction

In this chapter, we outline the cosmological model which we will use in the main investigations of this thesis. Followed by the techniques employed in this study.

1.1 The Cosmology

This section aims to provide a brief overview of the introduction to modern cosmology in order to pursue the main investigations of this thesis. Modern cosmological models are built from "cosmological principle" which assumed two fundamental assumptions. The first assumption is that our Universe is isotropic which means the Universe looks the same in all directions. The second assumption is that Universe looks the same at each point on the large-scale, called homogeneous. From these assumptions, the basic details of the standard cosmology are briefly discussed below.

1.1.1 The Hubble Expansion

From Hubble's law (Hubble, 1929), the relationship of velocity-distance of galaxies is defined as

$$v = H_0 d \tag{1.1.1}$$

where v is the recession velocity of a galaxy at distance d and H_0 is Hubble's constant. The present value of Hubble's constant is $H_0 = 100\ h$ kms^{-1}Mpc^{-1}, where h

is a dimensionless constant to be determined. To estimate the velocity, the redshift parameter, z, is used to parameterise velocity, where $z = \frac{v}{c}$ (at small v). Observations show that our Universe of galaxies is moving away from us. By looking at the spectrum of the emitted light from the distant galaxies, redshift z is defined as

$$1 + z = \frac{\lambda_{obs}}{\lambda_{em}} \tag{1.1.2}$$

Here λ_{obs} is observed wavelength by us at present time. λ_{em} is the emitted wavelength of the radiation in the object's rest-frame.

1.1.2 Gravity, Matter and Geometry

The 'Friedmann-Robertson-Walker' (FRW) metric is established through the modern cosmology assumption that our Universe is isotropic and homogeneous on the large-scale. This is an exact solution of Einstein's field equations and describes a homogeneous, isotropic expanding Universe.

$$ds^2 = c^2dt^2 + a(t)^2\left(\frac{dr^2}{1-kr^2} + r^2(d\theta^2 + sin^2\theta d\phi^2)\right) \tag{1.1.3}$$

Here t is the proper time and r, θ, ϕ are comoving spherical coordinates with the observer at the origin. $a(t)$ represents the expansion factor which can be written in terms of a comoving coordinate r and a physical (proper) coordinate x as

$$r = \frac{a_0}{a(t)}x \tag{1.1.4}$$

$a(t)$ is also related to the redshift z by $a_0/a(t) = 1 + z$ where the subscript 0 refers to the present time and $a(t_0) = a_0 = 1$.

The curvature parameter k describes the spatial geometry of the Universe which can be +1 (closed Universe), 0 (flat Universe), and -1 (open Universe) respectively.

To proceed further in the explanation of the expanding Universe, the Robertson-Walker solution is applied to the Einstein equations which relate the energy-matter content to the space-time geometry of the Universe. The solutions are reduced to the Friedmann equation,

$$H^2 = (\frac{\dot{a}}{a})^2 = \frac{8\pi G}{3}\rho - \frac{kc^2}{a^2} \tag{1.1.5}$$

where G is the gravitational constant, the dot denotes a derivative with respect to proper time t. H is the Hubble constant, $H = \frac{\dot{a}}{a}$. ρ is the overall energy-mass density and p is the isotropic pressure of the fluids of the Universe in its rest frame. ρ and p are related through the Fluid Equation,

$$\dot{\rho} + 3H(\rho + \frac{p}{c^2}) = 0 \tag{1.1.6}$$

The second Friedmann equation which describes the Universe's acceleration is given by combining Eq. 1.1.5 and Eq. 1.1.6. It is sometimes called the 'Acceleration equation'.

$$\frac{\ddot{a}}{a} = -\frac{4\pi G}{3}(\rho + \frac{3p}{c^2}) \tag{1.1.7}$$

The energy-density ρ is then given by the total (energy) density of all the constituents of the Universe,

$$\rho = \sum_i \rho_i = \rho_M + \rho_\gamma + \rho_\Lambda \tag{1.1.8}$$

where ρ_M and ρ_γ are matter and radiation density. The vacuum energy-density ρ_Λ is related to the 'Cosmological Constant' Λ by $\rho_\Lambda \equiv \Lambda c^2/8\pi G$.

Another useful quantity is the density parameter which quantifies the density of the Universe. From Friedmann's equations, the critical value of the energy density in which the Universe is spatially flat (k=0) can be derived as

$$\rho_{crit}(t) = \frac{3H^2}{8\pi G} \tag{1.1.9}$$

The critical density is not the real universal density but it is set to be a scale for the universal density. Furthermore, it is more convenient to express the true density of the Universe ρ to the critical density called **the density parameter** Ω.

$$\Omega(t) = \frac{\rho}{\rho_{crit}} \tag{1.1.10}$$

The Friedmann equation Eq. 1.1.5 is now expressed in term of density parameter :

$$H^2 = \frac{8\pi G}{3}\rho_{crit}\Omega - \frac{k}{a^2} = H^2\Omega - \frac{k}{a^2} \tag{1.1.11}$$

Thus

$$\Omega - 1 = \frac{k}{a^2H^2} \tag{1.1.12}$$

In the case of a critical-density Universe when $k = 0$, thus $\Omega = 1$ and it is often called a critical-density Universe. This is true independent of the type of matter that we have in the Universe (Liddle, 2003). However, when $\Omega \neq 1$, Friedmann's equation is very useful for analysing the evolution of the density. There are many different types of matter which can be expressed by the different notation of the density component, for instance, the matter density Ω_M and the radiation density Ω_γ.

The density parameter can also be expressed in term of the curvature, k, by

$$\Omega_k = -\frac{k}{a^2H^2} \tag{1.1.13}$$

and

$$\Omega + \Omega_k = 1 \tag{1.1.14}$$

The cosmological constant

Λ, a free parameter, is set to be a cosmological constant. This parameter is proposed by Einstein to balance the curvature in order to have a static Universe. Its unit is $[time]^{-2}$. With this modification, the Friedmann equation becomes

$$H^2 = (\frac{\dot{a}}{a})^2 = \frac{8\pi G}{3}\rho + \frac{\Lambda}{3} - \frac{k}{a^2} \tag{1.1.15}$$

and

$$\frac{\ddot{a}}{a} = -\frac{4\pi G}{3}(\rho + 3p) + \frac{\Lambda}{3} \tag{1.1.16}$$

Parameters ρ, p, and Λ are set to be nonnegative, in order to find a static ($\dot{a} = 0$) solution in the case of the Einstein static Universe. When Λ is positive, $\ddot{a}$ will be positive which implies a repulsive force.

Cosmological model with Λ

$$\Omega_\Lambda = \frac{\Lambda}{3H^2} \tag{1.1.17}$$

Λ is a constant but Ω_Λ is a time-dependent due to its dependence on H. Rearranging the Friedmann equation, we then have

$$\Omega + \Omega_\Lambda - 1 = \frac{k}{a^2 H^2} \tag{1.1.18}$$

In a flat Universe (k=0) gives

$$\Omega + \Omega_\Lambda = 1 \tag{1.1.19}$$

Different values of k and Ω result different curvatures and fates of the Universe. When k = -1 (open Universe) : $0 < \Omega + \Omega_\Lambda < 1$, this scenario made the underdense Universe. If k =1 (closed Universe) : $\Omega + \Omega_\Lambda > 1$, in this case Universe is overdense. In the ΛCDM model, the Ω value is dominated by the cold dark matter and dark energy. This model has zero spatial curvature, $k = 0$ with $\Omega_m = 0.26 \pm 0.03$, $\Omega_\Lambda = 0.74 \pm 0.03$.

1.1.3 The cosmic microwave background

According to the Big Bang model, the Universe has been cooling and expanding. It was very hot and very dense in the very beginning state of the Universe. After 400,000 years of the start of the Universe, the temperature of the Universe cooled to around 3000 Kelvin. The matter does not have enough energy to remain ionized in this state. When photons and electrons bind together, it reduces the cross-section of Compton scattering. The radiation then expands and cools to a black body temperature (2.7 Kelvin). At this temperature, it shows a peak signal at microwave frequencies ($\approx$ 1-1000 GHz) called the Cosmic Microwave Background (CMB). The

first confirmation of the CMB detection was made by Penzias & Wilson 1965. Dicke et al. 1965 made the theoretical interpretations from Penzias & Wilson 1965's data. When we observe the sky we see no difference as it looks the same from all directions. This raised the question of what caused the growth of the large-scale structure if the Universe is so smooth. It was suggested that there might be an effect of the density fluctuations in the early state of the Universe. In early 1970s, there were predictions of the spectrum of initial fluctuations which grew into the large scale structure in the Universe we see today. The predictions made by Harrison 1970; Peebles & Yu 1970; Zel'dovich 1970. With CMB observations, the study of the initial density perturbations from the large-scale Universe leads to the investigations of the components of the structure as well as the nature of the Universe.

1.1.4 The growth of large scale structure

The CMB observations helped us understand more about the initial conditions of the density perturbations which we can learn more about the information of the large scale structure in the Universe. The distribution of mass in the Universe can be quantified by the density perturbations as a function of mass density (ρ):

$$\delta(x) = \frac{\rho(x) - <\rho>}{<\rho>} \tag{1.1.20}$$

At early times, the perturbation scale depends on the expansion factor $a(t)$.

$$\delta(x) \propto a(t) \propto \frac{1}{1+z} \tag{1.1.21}$$

The amplitude of the perturbation is affected by gravity. For instance, the formation of stars, galaxies and clusters are caused by the collapse of density perturbations. The autocorrelation function of the density field can be used to measure the clustering properties of the visible component of the density field and is defined as :

$$\xi(r) = \langle \delta(x)\delta(x+r) \rangle \tag{1.1.22}$$

The separation between two local densities is given by r. The clustering of the

luminous components measured by the correlation function can link to the evolution of the galaxy. The peaks of the luminous component may approximately trace how the dark matter is distributed. The linear bias parameter, b, gives information on how the amplitude of dark matter clustering is related to galaxy clustering (Kaiser, 1987). For linear bias

$$\xi_{gg} = b^2 \xi_{mm} \tag{1.1.23}$$

where ξ_{gg} and ξ_{mm} are the galaxy and mass auto-correlation function.

1.2 High-redshift Universe

Observing the young Universe allows us to understand the evolution of stars and galaxies. Searches for galaxies and QSOs at high redshifts have progressed quickly over the past 10-15 years. The impressive achievements of these observations lead to a better understanding of our Universe. There are several methods of finding high redshift galaxies. In this introduction, we discuss methods of finding high redshift galaxies based on their Lyα emission line which we use in this thesis.

The Lyman series (Lyα, Lyβ, Lyγ...) is the series of transitions and resulting emission lines of the hydrogen atom when an electron falls from any higher energy level of the electron, n, to the ground state $n = 1$. The energy levels are given by $E_n = -13.6eV/n^2$. The transitions are named sequentially by Greek letters: from $n = 2$ to $n = 1$ is called Lyman-alpha, $n = 3$ to $n = 1$ is Lyman-beta, $n = 4$ to $n = 1$ is Lyman-gamma, etc.

1.2.1 Lyman-Break galaxies

The Lyman Break technique was successfully used from early 1990s (eg. Steidel & Hamilton 1992). It was used to collect and identify high-redshift galaxies by imaging in multiple broad photometric bands. By comparing the galaxy in several imaging filters, it will appear differently due to the position of the Lyman-forest limit. The Lyman limit is a continuum discontinuity at 912 Å in the UV spectrum

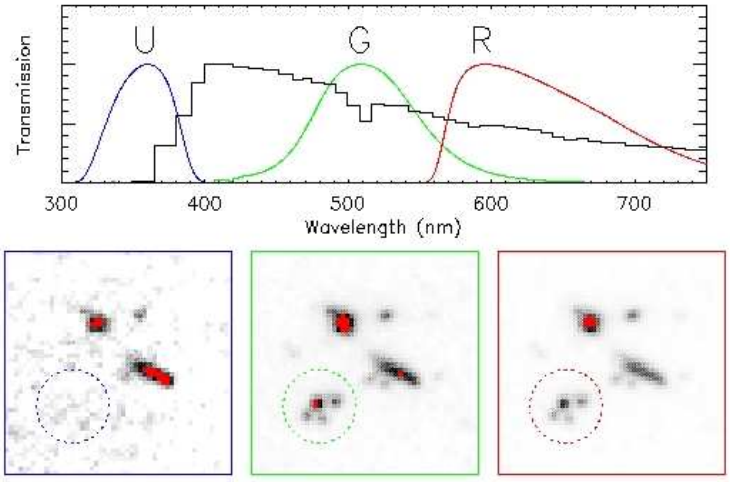

Figure 1.1: Illustration of Lyman Break technique (Image credit: Johan Fynbo). The top panel shows the typical shape of a $z \sim 3$ galaxy spectrum. Candidate galaxies at redshift $z \sim 3$ can be selected by looking for galaxies which appear in optical images (which are sensitive to wavelengths greater than 3600 Å), but do not appear in ultraviolet images (which are sensitive to light at wavelengths shorter than 3600 Å). A Lyman-Break Galaxy as observed through the three broad-band filters U, G and R is shown in the dashed circle (in the bottom plot). The galaxy is appeared in the G and R filters, but not in the U-filter. The galaxy will not be observed in the filter blueward of the break, but is clearly seen in the red filters.

of star-forming galaxies. A neutral hydrogen atom in the ground state, $n = 1$, has an ionisation potential of E = 13.6 eV, and can therefore be ionised by a photon with $\lambda = h/(13.6eV) = 912\mathring{A}$. Light at wavelengths shorter than 912 Å will be heavily absorbed by neutral gas around star-forming regions of galaxies and it is very difficult to escape from a galaxy, thus we will see no light travel to us from a galaxy at wavelengths shorter than that. This makes a "break" in the galaxy spectrum which used to identify the position of the Lyman limit. This cut-off is also enhanced by intergalactic absorption in the Lyman-α forest. At $\lambda < 1216$ Å, the high-redshift source will emit photons in its continuum and these photons will be absorbed by neutral intergalactic gas. In conclusion, a break feature in high-redshift galaxy spectra can be detected at $\lambda < 1216$ Å which deepens at $\lambda < 912$ Å. Moreover, the interstellar medium absorption from galaxies themselves suppress the fraction of ionizing photons in the same wavelength range. This is the reason why such a small fraction of this ionizing radiation is detected (Schneider, 2006).

To use this technique, three broad-band filters are commonly applied to non-

overlapping wavelengths, $\lambda_1 \pm \Delta\lambda_1 \leq \lambda_2 \pm \Delta\lambda_2 \leq \lambda_3 \pm \Delta\lambda_3$ and the presence of the 912 Å Lyman break at optical wavelengths is then identified. If central wavelengths $\lambda_1 \leq (1+z)912\mathring{A} \leq \lambda_2$, we should see a galaxy containing young stars in the redder filters λ_2 and λ_3 (see Fig. 1.1) and disappears in bluer λ_1 filter because of the absorption (Schneider, 2006). It is sometimes called "drop-out" technique as it is dropped out in the bluest filter. A Lyman break galaxy at redshift $z \sim 3$ can be selected by looking for galaxies which appears in optical images (which are sensitive to wavelengths greater than 4000 Å), but do not appear in ultraviolet images (which are sensitive to light at wavelengths shorter than 4000 Å). As mentioned above, galaxies selected like this are termed "Lyman Break Galaxies" (LBG). At the KECK and VLT spectra have been measured for LBGs at $z \sim 3$ selected via UV dropout. This technique measures spectra in magnitude up to an R band magnitude of $R \sim 25.5$ for U-band drop-outs. However, the confirmation rate of UV dropout candidates decreases at higher redshift (see Giavalisco 2002 for a summary of LBGs). The Lyman break technique could exclude some significant fraction of the high-redshift galaxy population due to associated uncertainties and assumptions from the selection criterion. Those undetected galaxies from the colour-selection technique might have been very dusty. Therefore the question of how many galaxies at similar distances that have escaped searches at optical wavelengths still remains. Steidel et al. (1999) claimed that the undetected fraction from the z < 3 LBG selection at magnitude $I_{AB} = 24$ is about 40 %.

1.2.2 Lyman alpha emitters

The Lyman break technique selects galaxies based on a drop in their continuum near their rest-frame Lyman limit. On the other hand, Lyman Alpha Emitters (LAE) are selected by their strong Lyα emission line using the narrow-band imaging method. Only a very small range of wavelengths can pass through a narrow-band filter, therefore a narrow range of redshifts for Lyα is observed. This narrow-band observing can cover a large area in relatively little observing time. The follow-up spectroscopy is needed to confirm the line and its identification, however, the survey is very time consuming as only very small volumes can be observed at a time (Nilsson

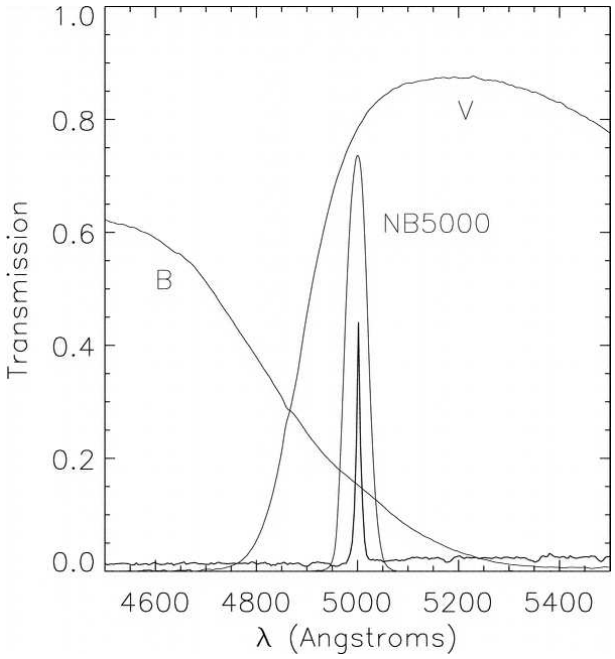

Figure 1.2: Narrowband filters used in $z \sim 3.1$ LAEs selection (from Gronwall et al. 2007). An LAE is selected as being a bright object in the narrow-band filter but fainter or not detected in the broad-band filter. Thus LAEs are selected based on comparing their magnitudes in narrow-band and broad-band filters. The narrowband filter falls between the broad-band filters (B is the blueward and V is the redward) as shown.

& Meisenheimer, 2009).

There are many observations that been made to uncover galaxies with strong Lyα emission at various redshifts (e.g., Hu & McMahon 1996; Steidel et al. 1996; Hu et al. 1998; Cowie & Hu 1998; Ouchi et al. 2003, 2008, 2010; Hayashino et al. 2004; Gawiser et al. 2007; Gronwall et al. 2007). At redshift $z \sim 3$, there are several hundreds of spectroscopically confirmed LAE by several groups (e.g., Steidel et al. 2000; Fynbo et al. 2003; Hayashino et al. 2004; Matsuda et al. 2005; Venemans et al. 2007; Nilsson et al. 2007; Gawiser et al. 2007; Gronwall et al. 2007; Ouchi et al. 2008).

LAEs are selected based on their excess flux ratio of narrowband vs. broadband measurement. An LAE is a bright object in the narrow-band filter but fainter or not detected in the broad-band filter. The narrow-band filter falls between the broad-band filters (B is the blueward and R/V is the redward) as shown in Fig. 1.2. As a result, objects with redder colours will tend to have colour (V - NB) < 0 and colour

(B - NB) > 0, while bluer sources will have positive (V - NB) and negative (B - NB). After a comparison of broad and narrow band magnitudes, a spectroscopic follow-up observation is needed to confirm LAE selection.

LAE have been found to be much fainter than LBGs since they normally are extremely faint in the continuum and also younger, less massive, and less dusty than LBGs (Gawiser et al., 2007; Pirzkal et al., 2007; Finkelstein et al., 2009; Guaita et al., 2011).

1.2.3 Intergalactic Medium

Knowledge about the intergalactic medium (IGM) mostly comes from studying at the absorption spectra of high redshift QSOs. When light travels from distant objects passing through the intervening gas clouds, it will be absorbed by hydrogen gas and leaving the absorption features in objects' spectra (as shown in Fig. 1.3). The neutral hydrogen clouds along the line of sight (LOS) to the QSO produce a number of absorption lines of the QSO continuum by the redshifted Lyα (1215.67 Å). The broad emission feature at the right of the spectrum of Fig. 1.3 is the Lyman alpha intrinsic to the quasar which we use to get a redshift of the quasar. While the dense series of absorption lines to the left of the spectrum plot are from the intervening neutral hydrogen at lower redshifts (shorter wavelengths). The dense series of absorption lines in the absorption spectra is called "Lyman alpha forest". Other metal lines (ie, C, O, Mg, Si, Fe, and Al) can also be seen in the quasar spectrum redward the Lyα forest (Rauch, 1998). A comprehensive review of the Lyα forest can be found at Rauch (1998).

The QSO absorption lines from these intervening clouds provides us lots of useful information about IGM which we can study in various aspects such as measuring the large scale structure of the universe (Liske et al., 2000), measuring the fine structure constant (Murphy et al., 2003) and the magnitude of the cosmic microwave background radiation (Silva & Viegas, 2002) in the distant past. Not only the IGM is a gas reservoir for galaxies, but also gives the information about galactic feedback (e.g. Adelberger et al., 2003, 2005; Rakic et al., 2012; Busca et al., 2013) which we will discuss in the next section.

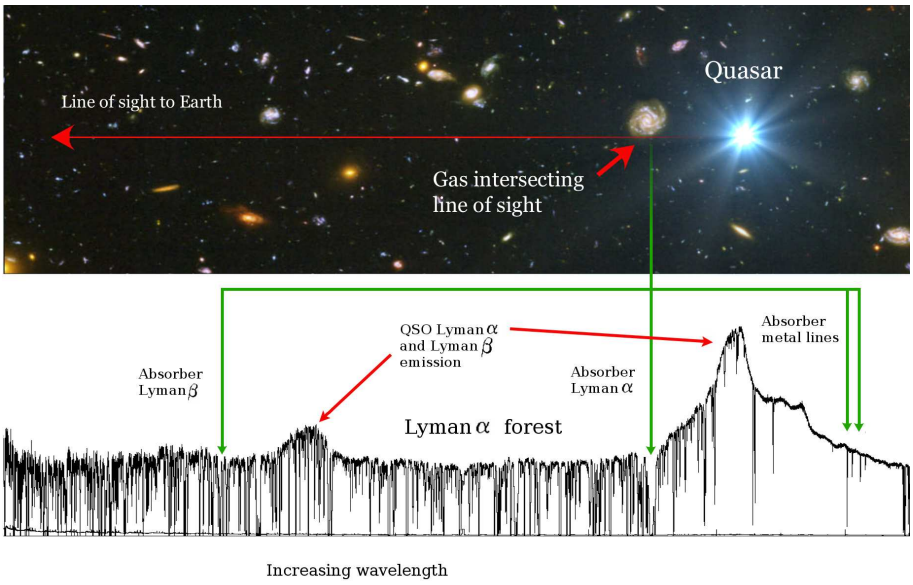

Figure 1.3: A picture of an absorption line from a distant quasar. As the light moves from the distant quasar towards Earth through the intervening gas clouds, it is absorbed by neutral hydrogen gas (HI) and is causing a forest of hundreds of sharp absorption lines in the QSO spectra (black line). Some of the important metal spectral features are masked by green arrows. (Image from Neil Crighton : a typical echelle resolution quasar spectrum taken on the 10m diameter Keck telescope (HS 0105+1919, from O'Meara et al. 2001))

1.2.4 Feedback of Star-Forming Galaxies

Feedback is now suspected to be a very important aspect of galaxy formation. The reason is that in the standard cosmological model, gas cooling considerations imply the formation of too many small galaxies at early times. Feedback processes therefore have to be invoked to regulate star-formation. The effect of feedback via supernovae and AGN driven winds is thought to be a key factor in the process of galaxy formation and evolution. Semi-analytical cosmological models require some injection of feedback to regulate the star formation activity in order to limit both the number of low-mass and high mass galaxies (White & Rees, 1978; White & Frenk, 1991). In addition, cosmological smoothed particle hydrodynamics (SPH) simulations from Springel & Hernquist (2003) have shown that galactic outflows from supernova feedback is fundamental to recreating the cosmic star-formation history. It is also evident that simulations lacking some sort of feedback struggle to reproduce realistic disk galaxies (Scannapieco et al., 2012; Schaye et al., 2010; Weil

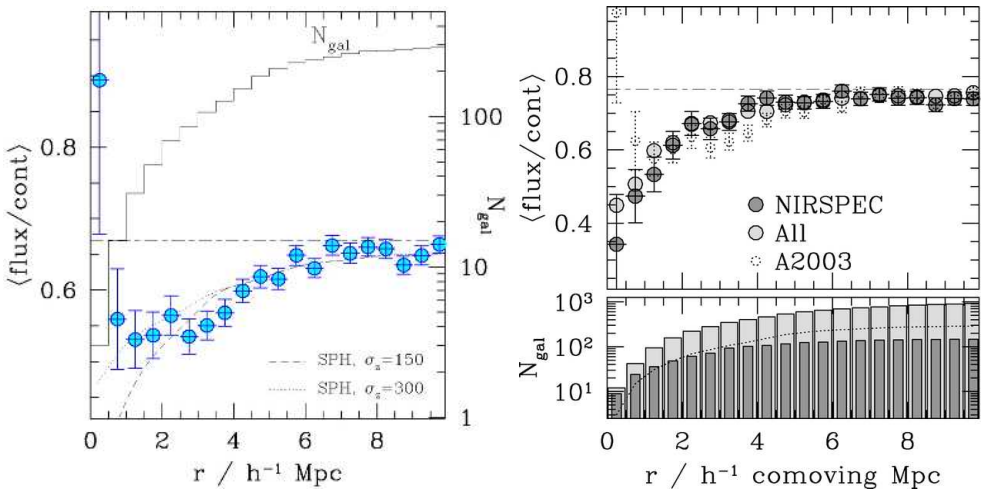

Figure 1.4: (left) shows the mean Lyα transmissivity as a function of distance from LBGs, as originally measured by Adelberger et al. 2003. There appeared to be excess Lyα absorption clouds within $\sim$8h^{-1}Mpc of a Lyman-break galaxy except within 1h^{-1}Mpc where the Lyα absorption again drops. The claim was that the LBGs form in peaks of the Lyα cloud density field and that on smaller scales, 'feedback' winds from the heavily star-forming LBGs are evaporating the Lyα clouds. However, as shown (right), Adelberger et al. 2005 did not confirm the effect either from the Lyα/ISM (All) or nebular (NIRSPEC) redshifts. LBG and Lyα cloud peculiar velocities may also confuse the clustering signal throughout this range of scales.

et al., 1998) and that powerful galactic winds are required in order to produce the observed metal enrichment of the IGM (Cen & Ostriker, 1999; Theuns et al., 2002; Aguirre et al., 2005; Oppenheimer & Davé, 2006).

In terms of observing the effects of feedback at high redshift, Adelberger et al. (2003)[A03 hereafter] presented the cross-correlation between $z \sim 3$ galaxies and the IGM (as traced by QSO sightlines) and claimed an observed lack of absorbing gas within $\sim 0.5\ h^{-1}$Mpc. They interpreted this as evidence of strong galactic winds removing HI gas from the vicinity of these star-forming galaxies. The work was based on the Keck HiRES ($R \sim 40,000$) spectra of 8 background QSOs at $z \approx 3$ combined with 431 Lyman Break Galaxies (LBGs) from the survey of Steidel et al. (2003). But these pioneering observations suffer from two serious weaknesses. First, at small scales, the LBG-Lyα statistics are very poor, based on just 3 LBGs within $0.5\,h^{-1}$ Mpc of their QSO sightlines. Second, the small angular extent of the fields of Adelberger et al severely limited any attempt to disentangle real and redshift space effects. Only by probing a larger range of scales is it possible to isolate the effects of

feedback on the gaseous, proto-galaxy environment from other physically interesting effects such as the gravitational infall of gas and the unknown form of the underlying real-space correlation between IGM clouds and star-forming galaxies. Adelberger et al (2003) suggested that the LBGs form in peaks of the Lyα density field and that on smaller scales, 'feedback' winds from star-forming LBGs evaporate the Lyα clouds. The LBG-CIV and LBG-Lyα $\xi(r_\theta, r_z)$ appear more isotropic than that for LBG-LBG and Adelberger et al. suggested that, with better statistics, such comparisons could place limits on both dynamical infall and gas outflows. Following the results of Adelberger et al. (2003), Adelberger et al. (2005)[A05 hereafter] updated the result with greater numbers of galaxies, this time centred at $z \sim 2$. Based on this new sample, A05 found increase in Lyα absorption down to scales of r $\sim 0.5\ h^{-1}$ comoving Mpc of LBG positions, with no evidence for HI gas having been removed from the vicinity of these galaxies. Indeed, Crighton et al. (2011) surmised that the cross-correlation at such small scales would likely be affected by uncertainties in the galaxy redshifts in the A03 data. It is therefore still unclear to what extent galactic winds have an effect on the galaxy surroundings.

In addition to the above evidence for gas outflows, gas inflows or infall down to galaxy scales is also expected in simple models of galaxy formation. Gas inflow is expected to be coherent down to the virial radius of a massive galaxy ($\approx$ 50 kpc), below which scale the situation is more complicated due to shocks and the gas pressure becoming more important. Gas flow infall into galaxies along filaments is also expected in secular models of galaxy formation where the gas accretion rate may not be simply dictated by merging rates in a hierarchical model Dekel et al. (2009). Rakic et al. (2012) presented a study of the galaxy-IGM cross-correlation at $z \approx 2.4$ using 15 fields of the Keck Baryonic Survey. They saw fingers-of-god on sub-100 kpc scales and evidence for infall on larger scales.

In order to constrain simulations of galaxy formation, it is imperative to provide extensive observations of the IGM via hydrogen and metal absorption lines and thus identify and probe the infall and outflow processes. As such, we undertook a large galaxy survey centred on distant bright QSOs in the form of the VLT LBG Redshift Survey (VLRS). Bielby et al. (2011) presented the first stage of the galaxy

survey, comprising $\approx$ 1,000 $z \sim 3$ galaxies within $\sim 30'$ of $z > 3$ QSOs. Using this sample, Crighton et al. (2011) performed a cross correlation analysis between the galaxy positions and the Lyman-α forest of the available QSO spectra in the fields, finding increased absorption within $\sim$ 5 h^{-1}Mpc of galaxy positions. This result was consistent with the results of A03 and A05, but lacked the galaxy numbers to probe the $\sim$ 0.5 h^{-1}Mpc scales at which A03 claimed to see the effects of galaxy winds. Since then, the VLRS has been extended to incorporate $\sim$ 2000 LBGs within 9 separate fields containing bright $z > 3$ QSOs Bielby et al. (2013), comparable in number to the the only other equivalent surveys at this redshift (e.g. Rakic et al. (2012); Rudie et al. (2012)).

Over the past 2 years, our group has used VLT VIMOS to test these important conclusions of Adelberger et al., by extending these investigations of the interaction between forming galaxies and the surrounding IGM at $z \sim 3$, both in terms of their precision and in terms of the range of galaxy-cloud separations studied. In this thesis, we update the work of Crighton et al. (2011), adding the galaxy redshifts of Bielby et al. (2011) and also Steidel et al. (2003) in conjunction with the available high-resolution QSO spectra in these survey fields. This work thus combines the higher galaxy sampling rate of the Steidel et al. (2003) survey with the wide fields of the VLRS and provide a galaxy sample that can probe the full range of scales from a few 100s of kpc to 10s of Mpc. This large range of scales is imperative for distinguishing between models of gas inflow and outflow in 2-D galaxy-gas cross-correlation analysis.

1.3 The two-point correlation function

1.3.1 Estimators

The two-point correlation function (ξ) is used to quantify and describe the clustering and the distribution of objects. We calculate the real and redshift-space functions, $\xi(r)$ and $\xi(s)$, of the galaxy samples using the Davis & Peebles (1983) estimator:

$$\xi(r) = \frac{N_R}{N_G}\frac{\langle DD(r)\rangle}{\langle DR(r)\rangle} - 1 \tag{1.3.24}$$

where $\langle DD(r)\rangle$ is the average number of galaxy-galaxy pairs, $\langle DR(r)\rangle$ is the number of pairs of galaxy-randoms at the separation, r, where we use r to represent the separation in real space and s the separation in redshift-space. The factor $\frac{N_R}{N_G}$ is the ratio of the number of random to data points.

We also estimate the two-point correlation function using the Landy-Szalay estimator (Landy & Szalay, 1993).

$$\xi(r) = \frac{\mathrm{DD}(r) - 2\mathrm{DR}(r) + \mathrm{RR}(r)}{\mathrm{RR}(r)} \tag{1.3.25}$$

where $\mathrm{DD}(r)$, $\mathrm{DR}(r)$, and $\mathrm{RR}(r)$ is the number of galaxy-galaxy pairs, galaxy-random pairs and random-random pairs as a function of r.

1.3.2 Uncertainty estimation for correlation function

We have considered several ways to estimate statistical uncertainty in our measurements.

1. We used Poisson uncertainty which is given by

$$\sigma_{\mathrm{Poi}} = \frac{(1+\xi)}{\sqrt{\langle DD\rangle/2}} \tag{1.3.26}$$

2. The field-to-field uncertainty is also used. This is simply a standard error on the mean of the measurement in each field from the best estimate and is calculated using

$$\sigma_{\mathrm{FtF}} = \sqrt{\frac{1}{N}\frac{1}{N-1}\sum_{i=1}^{N}[\xi_i - \overline{\xi}]^2} \tag{1.3.27}$$

where N is the number of subsamples. ξ_i is a measurement from the ith field and $\overline{\xi}$ is the mean value.

3. We also used the jackknife technique which is used in a number of correlation studies (see e.g. Scranton et al., 2002; Zehavi et al., 2005; Ross et al., 2007). We

estimate errors on the correlation results using jack-knife estimates based on splitting the simulation into equal volume octants and excluding each octant in turn to create 8 jack-knife realisations of the data. The error is then given by the standard deviation of these around the value from the full sample, times (8 - 1) = 7.

The jackknife error is then

$$\sigma_{\rm JK} = \sqrt{\frac{N-1}{N}\sum_{j=1}^{N}[\xi_{j'} - \xi]^2} \tag{1.3.28}$$

where ξ is a correlation function measured using the whole sample but $\xi_{j'}$ is a correlation function estimated using the whole sample except the jth subsample. N is the number of subsamples and $(N-1)/N = 7/8$.

4. We take this opportunity to mention an error method that will be particularly used in the cross-correlation function, $\xi(s)$ Lyα-LBG. At each separation, all the Lyα transmissivity pixels $< DT >$ and the number LBGs (N) are summed up. The average value of transmissivity in each bin is calculated from $\bar{x} =< DT/N >$. We then used the standard deviation from LBG-LBG variation which depends on the different numbers of overall LBGs in a bin to calculate the error bar.

$$\sigma = \sqrt{\frac{1}{N}\frac{1}{N-1}\sum_{i=1}^{N}[x_i - \bar{x}]^2} \tag{1.3.29}$$

where $x_i = DT(i)/N(i)$ for each bin.

1.3.3 Integral constraint

In the calculation of the correlation function, we make a correction for the integral constraint which is required to compensate for the effect of the limited field sizes. Following Bielby et al. (2013), we use the random-random pair distributions, which have been constructed to match the survey geometry, to determine the magnitude of the integral constraint. This method has been well described by a number of authors (e.g. Groth & Peebles, 1977; Peebles, 1980; Roche et al., 1993; Baugh et al., 1996; Phleps et al., 2006), with Phleps et al. 2006 in particular providing a detailed discussion in relation to the projected correlation function. A brief description of

the calculation is provided here.

The measured correlation function is given by the true correlation function minus the integral constrant $\mathcal{I}$:

$$w_{measure}(\sigma) = w_{true}(\sigma) - \mathcal{I} \tag{1.3.30}$$

Assuming a power-law form for the the real-space clustering, the true projected clustering is fit by:

$$w_{measure}(\sigma) = C r_0^{\gamma} \sigma^{1-\gamma} \tag{1.3.31}$$

where γ and r_0 are the slope and the clustering length of the real-space clustering function, $\xi(r)$, respectively. The clustering function $\xi(r)$ is characterised by a power-law of the form:

$$\xi(r) = \left(\frac{r}{r_0}\right)^{-\gamma} \tag{1.3.32}$$

The factor C is

$$C = \left(\frac{\Gamma\left(\frac{1}{2}\right)\Gamma\left(\frac{\gamma-1}{2}\right)}{\Gamma\left(\frac{\gamma}{2}\right)}\right) \tag{1.3.33}$$

where Γ is the Gamma function. Given this framework, the integral constraint can be estimated from the mean of the random-random pair counts, $\langle RR \rangle$, and the slope of the correlation function, such that:

$$\frac{\mathcal{I}}{C r_0^{\gamma}} = \frac{\Sigma \langle RR(\sigma) \rangle \, \sigma^{1-\gamma}}{\Sigma \langle RR(\sigma) \rangle} \tag{1.3.34}$$

1.4 Redshift-space distortions

When measuring the clustering of distant objects, the third dimension is redshift not radial distance. The measured redshift is not only affected by the expansion of the Universe, but also includes the effect of the peculiar velocities and also by geometric distortions. The geometric distortions caused by assuming the wrong cosmology

when converting the observed redshifts into physical distances (da Ângela et al., 2005). While real-space (r) refers to the true positions of the measured object, redshift-space (z) refers to a map where radial distance estimates are based on redshifts which include the effect of peculiar velocity.

The redshift distance, s, between 2 objects is given by $s \approx \sqrt{\sigma^2 + \pi^2}$. The separation along the line of sight, π, is given by the difference of the comoving distance in the redshifts of two objects.

$$\pi = |s_2 - s_1| \tag{1.4.35}$$

While the transverse separation, σ, is given by the separation on the sky.

$$\sigma = (s_1 + s_2)\theta/2 \tag{1.4.36}$$

θ is the angular separation between 2 objects. The measurement of $\xi(\sigma, \pi)$ will be calculated in the same way as $\xi(s)$, except that now the number of pairs is binned in two variables, rather than one.

1.4.1 Galaxy clustering and redshift-space distortions

The difference between real-space and redshift space two-point correlation function is the effect of the peculiar velocity from the objects, v_{pec}, in redshift space. Firstly, the peculiar velocity from the random motions within the objects will extend the clustering signal on small scales along the line-of-sight with respect to the observer. This feature is called the "finger-of-God" effect. While at the large scale, the peculiar motion due to gravitational infall make a significant effect on the clustering. This infall will make the objects on the far side of an overdensity appear closer and those on the near side appear further away. Thus the clustering appears flattened at large scale in the redshift direction. These two contributing effects are called redshift-space distortion.

Fig. 1.5 shows an example of the redshift-space distortion effect on the correlation function as a function of separation σ across and π along the line-of-sight from 2dF

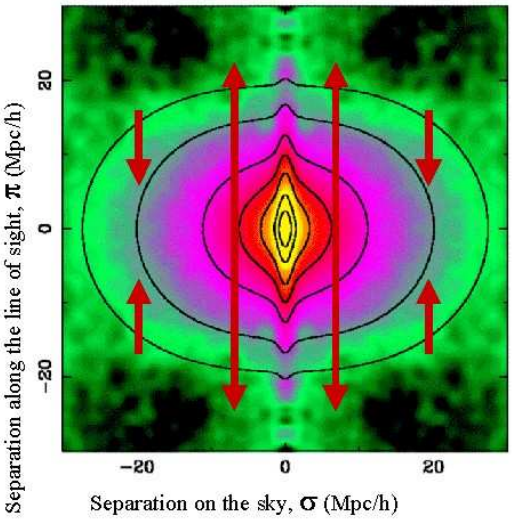

Figure 1.5: The correlation function computed in redshift-space from 2dF data as a function of σ and π (Peacock et al. 2001). On small scales, the peculiar velocity from galaxies causes a characteristic stretching of the redshift space distribution along the line of sight. This is called the Finger-of-God effect which points directly at the origin in a redshift σ-π diagram. An opposite effect, the Kaiser flattening, is seen most clearly at larger scales. The objects on the far side of an overdensity appear closer thus the clustering appears flattened at large scale in the redshift direction.

galaxy z survey data (Peacock et al., 2001). The Finger-of-God effect is stretching out a cluster in redshift space (clearly elongated in the π direction) at small angular scales ($\sigma < 2h^{-1}$ Mpc). The Kaiser Effect causes a "flattening" of the correlation function at larger scales. The contours are flattened along the line of sight, π, as seen at the scales across the line of sight ($\sigma > 10h^{-1}$ Mpc).

These two effects can be quantified. The effect of the large-scale motions can be calculated via linear theory. According to Kaiser 1987, the power spectrum $P(k)$ distorted by the peculiar velocity field is defined as

$$P_{gal}(k_s) = P_{gal}(k_r)(1 + \beta\mu^2)^2 \tag{1.4.37}$$

where the real-space coordinate is defined by the subscript r while the redshift-space coordinate is defined by the subscript s. The cosine between the line-of-sight vector and velocity vector is defined as μ. β measures the observed infall in clustering from large-scales caused by redshift space distortions.

$P_{gal}(k_s)$ in the complete form can be written (Cole et al., 1994) as

$$\begin{aligned} P_{gal}(k_s) &= P_{gal}(k_r)(1+\beta\mu^2)^2 \\ &= [(1+\frac{2}{3}\beta+\frac{1}{5}\beta^2)P_0(\mu) \\ &\quad +(\frac{4}{3}\beta+\frac{4}{7}\beta^2)P_2(\mu) \\ &\quad +\frac{8}{35}\beta^2 P_4(\mu)]P_{gal}(k_r) \end{aligned} \tag{1.4.38}$$

The Legendre polymonials $P_l(\mu)$ at each order are $P_0 = 1$, $P_2 = (3\mu^2 - 1)/2$, and $P_4 = (35\mu^4 - 30\mu^2 - 3)/8$.

The linear redshift-space distortion derived by Kaiser (1987) can also be written in the correlation function form as:

$$\xi_{gal}(s) = \xi_{gal}(r)(1+\frac{2}{3}\beta+\frac{1}{5}\beta^2) \tag{1.4.39}$$

The relationship of β to cosmology and the matter distribution can be defined by

$$\beta = \frac{f(\Omega_m(z), \Omega_\Lambda(z), z)}{b} \tag{1.4.40}$$

The term bias, b, is related to the luminous matter clustering to the dark matter ($b^2 = \xi_{gal}/\xi_{mass}$) (da Ângela et al., 2005). In the case of flat Universe, the growth structure can be defined as :

$$f(\Omega_m(z), \Omega_\Lambda(z), z) = \frac{d\ln\delta}{d\ln a} \tag{1.4.41}$$

This can then be approximated to (Lahav et al., 1991),

$$f \approx \Omega_m(z)^{0.6} + \frac{1}{70}(1 - \frac{1}{2}\Omega_m(z)(1+\Omega_m(z))) \tag{1.4.42}$$

or approximately

$$f \approx \Omega_m(z)^{0.6} \tag{1.4.43}$$

For more understanding about the effect of z-space distortions, the infall parameter β has been taken into account. To derive the infall velocities, we start by following Kaiser 1987. The acceleration vector from this velocity is given by

$$\mathbf{a_r} \equiv \int_{V_r} d^3r \Delta(\mathbf{r}) \frac{\mathbf{r}}{r^3} \tag{1.4.44}$$

where V_r is the survey volume and $\Delta(\mathbf{r})$ $(= \frac{\delta\rho_m}{\rho_m})$ is the density contrast. Then from linear theory, the peculiar velocity of the particle at the origin is

$$\mathbf{v} = -\frac{2}{3}\frac{G\rho_{crit}\mathbf{a}}{H_0} f(\Omega) \tag{1.4.45}$$

Assuming a sphere of radius r for V_r, and $\frac{\delta\rho_m}{\rho_m}$ is constant in V_r. Solving Eq. 1.4.44 and Eq. 1.4.45 to find $\mathbf{v}$, the expression for the infall velocity of the biased particles is

$$\mathbf{v} = -\frac{1}{3} H_0 \mathbf{r} \Omega^{0.6} \frac{1}{b} \frac{\delta\rho_g}{\bar{\rho}_g} \hat{r} \tag{1.4.46}$$

Here we have also used $\rho_{crit} = \frac{3H_0^2}{8\pi G}$ and $\frac{\delta\rho_m}{\rho_m} = \frac{1}{b}\frac{\delta\rho_g}{\bar{\rho}_g}$. Since $\mathbf{v}_{Hubble} = H_0\mathbf{r}$, this gives

$$\frac{\mathbf{v}_{infall}}{\mathbf{v}_{Hubble}} = -\frac{1}{3}\frac{\delta\rho_g}{\bar{\rho}_g}\beta\hat{\mathbf{r}} \tag{1.4.47}$$

for the infall velocity of a galaxy at a distance r from a centre of a spherical overdensity.

There are several methods for determining the value of β (Landy & Szalay, 2002) but in this thesis we usually choose the simple way using the ratio of the correlation function in redshift $\xi(s)$ and real space $\xi(r)$. But also fit β by modelling $\xi(\sigma, \pi)$ as we describe in section 1.4.3.

1.4.2 Infall parameter for Lyα forest

We measure the Lyα forest flux correlations along the lines of sight. According to Slosar et al. 2011, the transmitted flux is related to the optical depth, τ, and the

gas overdensity by

$$F = e^{-\tau} \;=\; exp[-A(1+\delta)^{(2-0.7(\gamma-1))}] \tag{1.4.48}$$

This transmitted flux is related to the dark matter overdensity δ where $\delta \equiv \delta/\bar{\delta} - 1$. A is a constant depending on the redshift. The slope of the temperature-density relation, $\gamma - 1$, depends on the IGM reionization history. According to Croft et al. 1999; McDonald et al. 2000; Croft & Gaztanaga 1998, it is difficult to predict the amplitude of the flux correlation function but the three-dimensional power spectrum of the field $\delta_F \equiv F/\bar{F} - 1$ should have the similar shape to the power spectrum of $\delta \equiv \delta/\bar{\delta} - 1$ on large scales. A turnover in the 1-D flux power spectrum at high k is caused by the thermal motions of atoms. However, Slosar et al. 2011 mentioned that this turnover is mostly affected by the peculiar velocities at larger scales rather than thermal motions. The peculiar velocity will shift the apparent locations of the absorbing neutral hydrogen in the radial direction. On large scales, the power spectrum should follow the linear theory model (Kaiser, 1987) of redshift-space distortions,

$$P_F(k, \mu_k) = b^2 P_L(k)(1 + \beta\mu_k^2)^2 \tag{1.4.49}$$

where μ_k is the cosine of the angle between the wavevector k and the line of sight. $P_L(k)$ is the real-space linear power spectrum. b is the bias factor for the Lyα. Note that b is the bias factor of the contrast of the flux fluctuations but not the bias factor of the neutral hydrogen.

In the previous subsection, we discussed the way of finding b and β from galaxy clustering where $\beta \approx \Omega_m(z)^{0.6}/b$. However, β for Lyα is an independent parameter from bias b and $\Omega_m(z)$, there is no simple relation between b and β in this case. For Lyα flux, the linear theory of gravitational collapse (Kaiser, 1987) (Eq. 1.4.49) is invalid on small scales due to nonlinear effects (McDonald, 2003).The amplitude of the large-scale (i.e., linear) power is set by the β and b but values of β and b actually come from small-scale structure of the field.

As mentioned earlier, the non-linear relation at small scales makes the amplitude

of the correlation function difficult to predict. Thus the simulation is needed. From a number of studies, (e.g. Blanton et al., 2000; Benson et al., 2000; Cen & Ostriker, 2000; Somerville et al., 2001), we can use simulation to predict the amplitude of the correlation function by simulated the small-scale structure in most of the volume of the IGM and computed model predictions for any observable statistic of the Lyα forest transmitted flux, including the large-scale bias.

McDonald (2003) extracted the power spectrum from the simulations directly. In their simulation, they used redshift-space pixels which identical in size to the real-space cells. They made redshift-space cells by calculating the average velocity of the cells at the edge of separations of real-space cells and translating that to each cell-edge into redshift-space. The optical depth contributed by each real-space cell is distributed to multiple redshift-space pixels based on its fractional overlap with each. The different contributions to a redshift-space pixel are thermally broadened separately, based on the temperature of the originating real-space cells. The observable quantity is then given by $F(x) = exp[-\tau(x)]$. McDonald (2003) found results for $\beta_{Ly\alpha}$ = 1-1.6 depending on the resolution of the simulations and remarked that low resolution simulations produce lower β.

1.4.3 Constraints on β from redshift-space distortions

Description of $\xi(\sigma, \pi)$ models

In subsection 1.4.1 we described the simple way to obtain infall parameter from the galaxy-galaxy correlation in redshift and real space by using a simpler form of $\xi_{gal}(s)/\xi_{gal}(r) = (1 + \frac{2}{3}\beta + \frac{1}{5}\beta^2)$. In a more complicated case where we need to calculate β from Lyα-LBG correlation function to see the effect of LBG infall and feedback from Lyα outflow velocity, it requires a combination of β_{gal} and β_{gas}.

As described in Mountrichas et al. (2009), the infall parameter β is constrained by modelling the measured 2-D redshift-space distributions. We firstly define the linear bias parameter b by

$$\xi_{mm} = \frac{\xi_{12}}{b_1 b_2} \tag{1.4.50}$$

where b_1 and b_2 are the bias of two samples. Bias parameter is defined by

$$b_1 = \Omega_m^{0.6}/\beta_1, \qquad b_2 = \Omega_m^{0.6}/\beta_2 \tag{1.4.51}$$

In a flat Universe, $\Omega_m(z)$ is given as

$$\Omega_m = \frac{\Omega_m^0(1+z)^3}{\Omega_m^0(1+z)^3 + \Omega_\lambda} \tag{1.4.52}$$

We then applied Model I of da Ângela et al. (2008) to our auto- and cross-correlation function in this study.

Recall the linear theory (Kaiser, 1987), the relationship of the power spectrum in real and redshift space is given by,

$$P_s(k) = (1 + \beta(z)\mu_k^2)^2 P_r(k) \tag{1.4.53}$$

where $P_s(k)$ and $P_r(k)$ are the power-spectrum in redshift and real space, respectively. μ_k is the cosine angle between the line-of-sight and the wavevector k.

Similarly to the relationship between $\xi(s)$ and $\xi(r)$, we would expect to see the 'Kaiser boost' given by (Hamilton, 1992),

$$\xi(s) = (1 + \frac{2}{3}\beta + \frac{1}{5}\beta^2)\xi(r) \tag{1.4.54}$$

Eq. 1.4.53 can also be transformed to,

$$\begin{aligned} \xi(\sigma,\pi) &= (1 + \frac{2}{3}\beta(z) + \frac{1}{5}\beta^2(z))\xi_0(r)P_0(\mu) \\ &\quad +(-\frac{4}{3}\beta(z) + \frac{4}{7}\beta^2(z))\xi_2(r)P_2(\mu) \\ &\quad +\frac{8}{35}\beta^2(z)\xi_4(r)P_4(\mu) \end{aligned} \tag{1.4.55}$$

where $P_l(\mu)$ is the Legendre polymonials $P_l(\mu)$ at each order where $P_0 = 1$, $P_2 = (3\mu^2 - 1)/2$, and $P_4 = (35\mu^4 - 30\mu^2 - 3)/8$.

In our analysis where we want to find two infall parameters, β_1 and β_2. Therefore,

Eq. 1.4.54, 1.4.53, 1.4.55 should be modified as follows (Mountrichas et al., 2009):

$$\xi(s) = (1 + \frac{1}{3}[\beta_1(z) + \beta_2(z)] + \frac{1}{5}\beta_1(z)\beta_2(z))\xi(r) \tag{1.4.56}$$

Which is similar to relationship of the power spectrum in real and redshift space,

$$P_s(k) = (1 + \beta_1(z)\mu_k^2)(1 + \beta_2(z)\mu_k^2)P_r(k) \tag{1.4.57}$$

Eq. 1.4.55 can now be written into the form,

$$\begin{aligned} \xi(\sigma,\pi) &= (1 + \frac{1}{3}[\beta_1(z) + \beta_2(z)] + \frac{1}{5}\beta_1(z)\beta_2(z))\xi_0(r)P_0(\mu) \\ &+(-\frac{2}{3}[\beta_1(z) + \beta_2(z)] + \frac{4}{7}\beta_1(z)\beta_2(z))\xi_2(r)P_2(\mu) \\ &+\frac{8}{35}\beta_1(z)\beta_2(z)\xi_4(r)P_4(\mu) \end{aligned} \tag{1.4.58}$$

The problem with this formalism is that the model only constrains the sum of the infall parameters, i.e. $\beta_1 + \beta_2$, and not each of them individually. So, in what follows we keep β_1 or β_2 constant. In particular, when we want to find $\beta_{Ly\alpha}$ from LBG-QSO correlation function, we will fix the value of β_{gal} from the LBG-LBG correlation measurement.

In case of $\xi(\sigma,\pi)$, the magnitude of the elongation along the π-direction which caused by the peculiar velocity of the object is denoted by $< w_z^2 >^{\frac{1}{2}}$. This peculiar velocity can be expressed by a Gaussian (Ratcliffe et al., 1996), as

$$f(w_z) = \frac{1}{\sqrt{2\pi} < w_z^2 >^{\frac{1}{2}}} exp(-\frac{1}{2}\frac{|w_z|^2}{< w_z^2 >^{\frac{1}{2}}}) \tag{1.4.59}$$

To include the small scale redshift-space effects due to the random motions of galaxies, we convolve the $\xi(\sigma,\pi)$ model with the peculiar velocity distribution, given by Eq. 1.4.59. Thus, $\xi(\sigma,\pi)$ is given by

$$\xi(\sigma,\pi) = \int_{-\infty}^{+\infty} \xi^{'}(\sigma, \pi - w_z(1+z)/H(z))f(w_z)dw_z \tag{1.4.60}$$

where $\xi^{'}(\sigma, \pi - w_z(1+z)/H(z))$ is defined by Eq. 1.4.55.

To check our $\xi(\sigma, \pi)$ model, we will use the γ values from our fits to $\xi(s)$, let r_0 and the velocity dispersion vary as free parameters and compute the χ^2 values for each $\Omega_m^0 - \beta(z)$ pair.

1.5 Thesis outline

The aim of the thesis is to study the relationship between galaxies and gas at redshift $z \sim 3$ by measuring their correlation function. This thesis is organised as follows. We have already described backgrounds of modern cosmology, the backgrounds of high redshift Universe, the correlation function, and redshift-space distortions in this Chapter.

Chapter 2 presents the observational data from a large VLT LBG Redshift Survey (VLRS) which we aim to extend the study of the interaction between gas and galaxies at z $\sim$ 3. We want to combine the power of the VLRS at large spatial scales with the statistical power of the Keck sample (Steidel et al., 2003). The X-shooter survey is also presented.

Chapter 3 describes the Galaxies-Intergalactic Medium Interaction Calculation (GIMIC) simulation which helps us to interpret the correlation function from obser-vatonal data. The simulations are used to create synthetic Lyα spectra and galaxies. We study both galaxy clustering and the relationship between gas and galaxies via the (cross-) correlation functions $\xi(s)$ and $\xi(\sigma, \pi)$.

Chapter 4 show the LBG + Lyα clustering results and their interpretation. We use the combination data from VLRS and KECK to perform LBG-LBG correlation function. We aim to roughly estimate β from $\frac{\xi(s)}{\xi(r)}$. we then use Lyα-LBG correlation function to study the interaction between galaxies and gas at z $\sim$ 3. We attempt to investigate the effect of feedback on the LBG-Lyα cross correlation. We employ mock Lyα spectra and Galaxies from GIMIC simulations to calculate LBG-LBG $\xi(s)$ to see if we can detect the effects of peculiar velocities and possibly feedback by comparing real and redshift space correlation function, (b) LBG-Lyα $\xi(s)$ to understand more about outflow and feedback and (c) Lyα-Lyα auto-correlation.

Chapter 5 provides LAEs observation photometric observation from narrowband

images and the spectroscopic follow-up observation for our LAE candidates. We use our observational data to perform the Lyman Alpha luminosity functions and two-point correlation functions of LAE at $z = 3.1$.

Chapter 6 presents the conclusions and summarise our findings as well as the future research.

Throughout this work, we adopt a cosmology consistent with the GIMIC (and hence the Millennium) simulation. This corresponds to $\{\Omega_m, \Omega_\Lambda, \Omega_b, n_\mathrm{s}, \sigma_8, H_0, h\} = \{0.25, 0.75, 0.045, 1, 0.9, 100, 0.73\}$. We primarily use comoving coordinates in this paper and where proper coordinates are used, we denote these as pkpc, pMpc etc. Unless stated otherwise all distances are comoving in units of h^{-1}Mpc, and magnitudes use the AB system.

Chapter 2

Observational data

In this work, we use a combination of spectroscopically identified $z \sim 3$ star-forming galaxies and high-resolution spectral observations of the Lyα forest of $z \gtrsim 3$ QSOs. The galaxy data are a combination of the VLRS data presented by Bielby et al. (2011) and Bielby et al. (2013) and the publicly available Keck LBG data presented by Steidel et al. (2003). These two datasets are based on different observing strategies, whereby the VLRS offers coverage across large fields of view, whilst the Keck sample covers relatively small separations ($\lesssim 8 - 10$ h^{-1}Mpc) with higher sampling rates of the galaxy population. The QSO spectra with which we trace the distribution of HI within the fields have all been obtained from archival VLT UVES and Keck HiRES observations. We will also use new moderate resolution quasar spectra from the VLT X-Shooter (Bielby et al. in prep). In this chapter, we give details of all the data used and the reduction processes.

2.1 VLRS + Keck LBG Observations

Our group undertook a large galaxy survey centred on distant bright QSOs in the form of the VLT LBG Redshift Survey (VLRS). We have used deep optical imaging to select galaxies via the Lyman break technique. Spectroscopy of the LBGs was then made using the VLT VIMOS instrument. Bielby et al. (2011) presented the first stage of the galaxy survey, comprising $\approx$ 1,000 $z \sim 3$ galaxies within $\sim 30'$ of $z > 3$ QSOs. Since then, the VLRS has been extended to incorporate $\sim$ 2000 LBGs

within 9 separate fields containing bright $z > 3$ QSOs (Bielby et al., 2013). Full details of the VLRS LBG survey covering, the imaging, data reduction, candidate selection and spectroscopic follow-up of targets are appeared in Bielby et al. (2011, 2013).

2.1.1 VLRS Imaging

The selection of $z \approx 3$ LBG candidates was performed using photometry from optical broadband imaging. The imaging data of our fields were obtained from various instruments such as the Mosaic wide-field imager on the 4m Mayall telescope at Kitt Peak National Observatory (KPNO), the MOSAIC-II Imager on the Blanco 4-m at Cerro Tololo Inter-American Observatory (CTIO), the Wide Field Camera on the 2.5m Isaac Newton Telescope (INT) on La Palma, the MegaCam imager on the 3.6m Canada France Hawaii Telescope (CFHT), and VLT VIMOS in imaging mode. Q0042-2627, HE0940-1050 and PKS2126-158 were observed at CTIO between January 2004 and April 2005. J0124+0044 and J1201+0044 were observed at KPNO in September 2001 and April 2006 respectively. Q2359 and Q0301 were also observed at KPNO in September 2005. Q2231 was observed at INT in August 2005. All of these observations were carried out in the U, B and R bands. The HE0940 and Q2348 data were obtained from CFHT in April 2004 and in August-December 2004 as part of the observing run 2004BF03 (PI: P. Petitjean). These data are in the u^*, g', r' rather than the U, B and R bands. Table 2.1 gives details of all the imaging data (quoted from Bielby et al. 2011, 2013).

Table 2.1: Details of the imaging data acquired in each of nine VLRS target fields.

Field	RA(J2000)	Dec	Facility	Band	Exp time(ks)	Seeing(arcsec)	completeness (50%)
Q0042-2627	00:46:45	-25:42:35	MOSAIC2 (CTIO)	U	12.6	1.8	24.09
				B	3.3	1.8	25.15
			VIMOS (VLT)	R	0.23	1.1	24.72
J0124+0044	01:24:03	+00:44:32	MOSAIC (KPNO)	U	13.4	1.5	...
				B	2.8	1.5	...
				V	3.1	1.4	...
HE0940-1050	09:42:53	-11:04:25	MOSAIC2 (CTIO)	U	29	1.3	25.69
				B	4.8	1.3	25.62
				R	2.25	1.0	25.44
			MegaCam (CFHT)	u^*	6.8	0.99	25.39
				g'	3.1	0.86	25.54
				r'	3.7	0.85	25.08
J1201+0116	12:01:43	+01:16:05	MOSAIC (KPNO)	U	9.9	1.6	24.50
				B	6	2.4	24.43
			VIMOS (VLT)	R	0.23	0.7	25.47
PKS2126-158	21:29:12	-15:38:42	MOSAIC2 (CTIO)	U	26.4	1.3	25.08
				B	7,800	1.6	24.94
				R	6,400	1.5	24.6
Q2359	00:01:44.85	+07:11:56.0	MOSAIC (KPNO)	U	19.2	1.46	24.76
				B	7.2	1.45	25.28
				R	6.0	1.15	24.74
Q0301	03:03:45.27	-00:21:34.2	MOSAIC (KPNO)	U	19.2	1.34	24.93
				B	6.4	1.28	25.51
				R	4.8	1.19	24.59
Q2231	22:34:28.00	+00:00:02.0	WFCam (INT)	U	54.0	1.23	25.08
				B	13.2	1.01	25.88
				R	19.2	1.01	24.75
Q2348	23:50:57.90	-00:52:09.9	MegaCam (CFHT)	u^*	9.9	0.78	25.97
				g'	5.5	0.79	25.71
				r'	4.4	0.75	25.22

2.1.2 VLRS Spectroscopy

The LBG candidates were targeted in spectroscopic follow-up observations with the VLT UT3 (Melipal) between September 2005 and March 2007 (for the first 5 fields presented in Bielby et al. 2011) and with the VLT VIMOS spectrograph between September 2008 and December 2009 (for other fields presented in Bielby et al. 2013).

The reduction was done by using the VIMOS ESOREX reduction pipeline. Full details of the reduction is provided by Bielby et al. (2011, 2013), however, we briefly outline the procedure here. The pipeline generates bias-subtracted, flat-fielded, wavelength-calibrated science frames consisting of a series of 2D spectra. The `imcombine` in IRAF was used to combine the reduced frames from each observing run, generating a master science frame for each quadrant of each field. The `crreject` mode was applied to get rid of the cosmic rays. We extracted 1D spectra from the reduced, combined 2D spectra using the IDL routine `specplot`. One-dimensional object and sky spectra are found by averaging across the respective apertures, and the sky spectrum is then subtracted from the object spectrum to give a final spectrum for the object.

The LBG redshifts were identified using Lyα emission lines and interstellar medium (ISM) absorption lines where visible. For both the Lyα and ISM features it is necessary to correct the ascertained redshift for intrinsic velocity effects, due to these features being affected by outflowing gas (e.g. A03, Steidel et al., 2010). As such the VLRS galaxy redshifts have been corrected according to the prescription given by Steidel et al. (2010). The total numbers of $R \leq 25$ sources identified in each of the 9 fields presented here are given in Table 2.2.

Fig. 2.1-2.2-2.3 show the sky distribution of LBGs and QSOs in the VLRS fields. Black dots show LBGs with spectroscopically-confirmed redshifts. Quasars are shown by red circles and the bright central quasars, which have been observed at high resolution, are shown by red filled stars. Green circles show the archival high-resolution spectra available. Blue triangles show the quasars observed at moderate spectroscopic resolution using VLT X-Shooter.

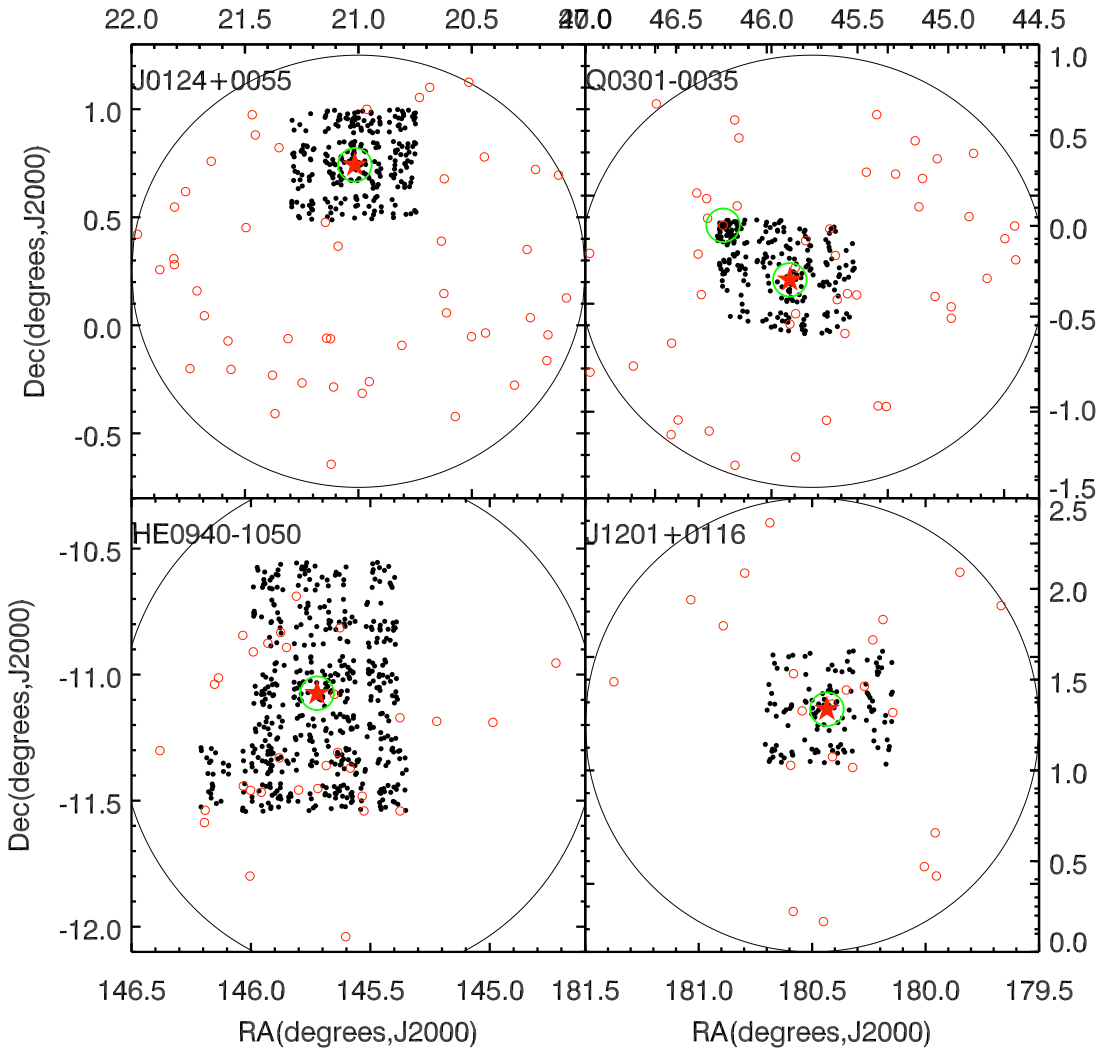

Figure 2.1: Quasar and LBG positions in the J0124+0044, Q0301-0035, HE0940-1050 and J1201+0116 fields. Black dots show LBGs with spectroscopically-confirmed redshifts. Quasars are shown by red circles and the bright central quasar is shown by red filled star. Green circles show the archival high-resolution spectra available.

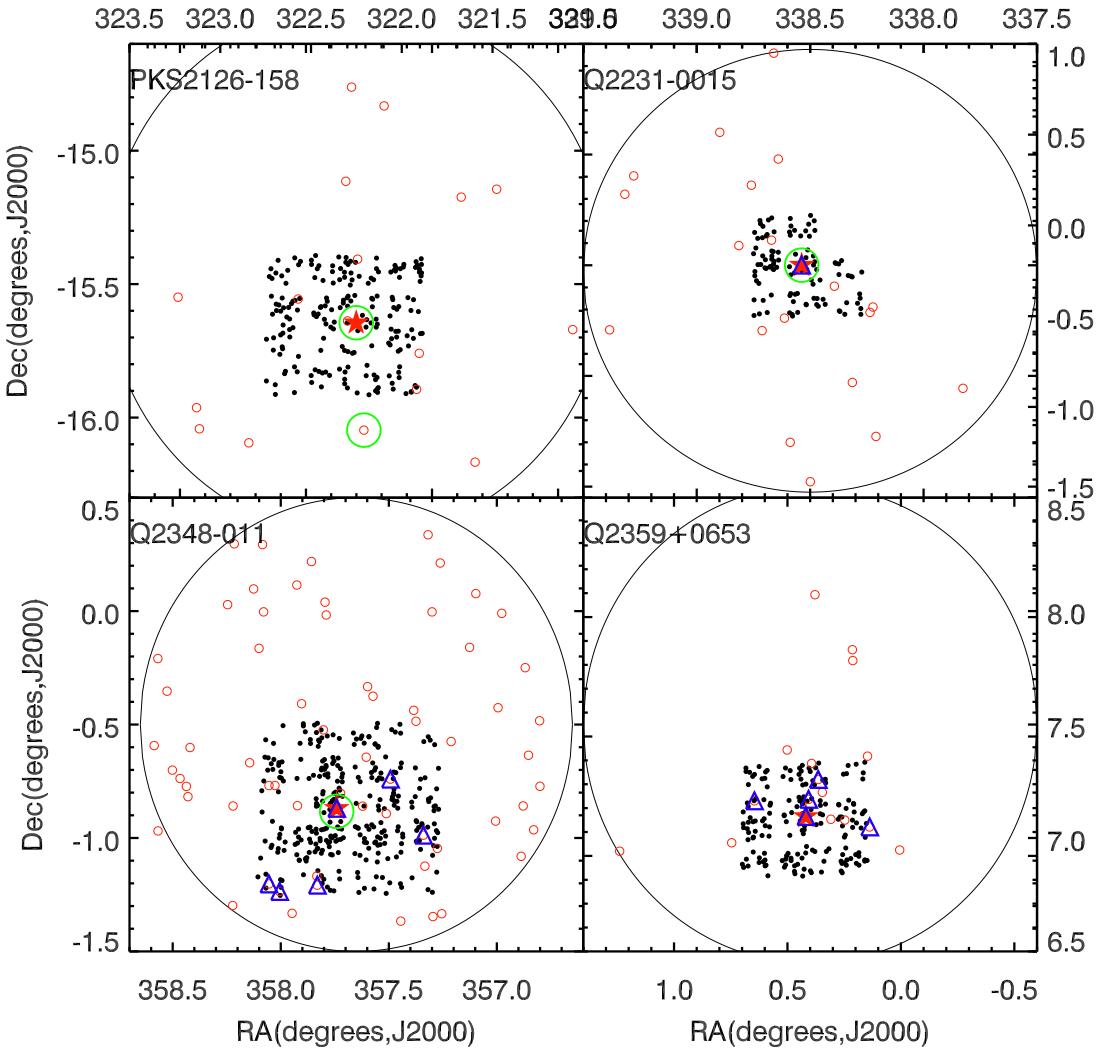

Figure 2.2: Quasar and LBG positions in the PKS2126-158, Q2231-0015, Q2348-011 and Q2359+0653 fields. Symbols are the same as in Fig. 2.1. Blue triangles show the quasars observed at moderate spectroscopic resolution using VLT X-Shooter.

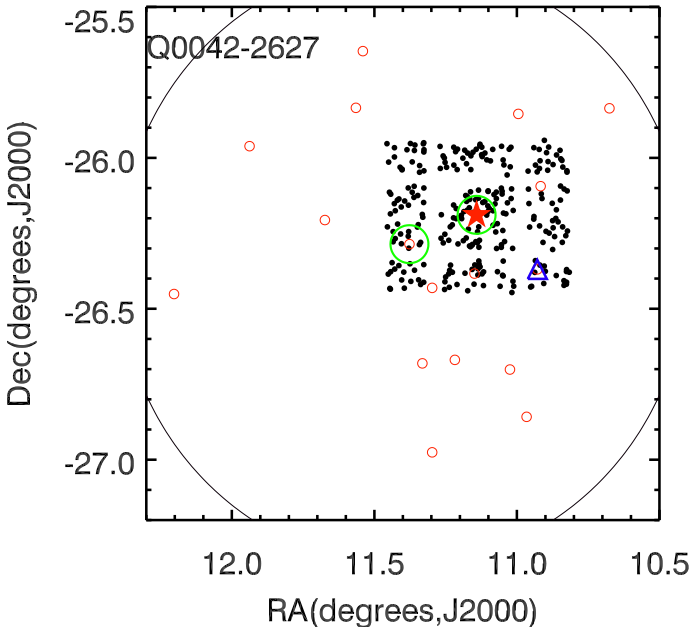

Figure 2.3: Quasar and LBG positions in the Q0042-2627 fields. Symbols are the same as in Fig. 2.1. Blue triangles show the quasars observed at moderate spectroscopic resolution using VLT X-Shooter.

Table 2.2: Numbers of objects in each target field spectroscopically identified at $R \leq 25$ as high-z LBGs.

Field	$z \approx 3$ LBGs	Presented in
Q0042-2627	264 (0.29 arcmin^{-2})	Bielby et al. (2011)
J0124+0044	264 (0.29 arcmin^{-2})	Bielby et al. (2011)
HE0940-1050	169 (0.25 arcmin^{-2})	Bielby et al. (2011)
J1201+0116	120 (0.13 arcmin^{-2})	Bielby et al. (2011)
PKS2126-158	203 (0.23 arcmin^{-2})	Bielby et al. (2011)
Q2359+0653	143 (0.18 arcmin^{-2})	Bielby et al. (2013)
Q0301-0035	164 (0.21 arcmin^{-2})	Bielby et al. (2013)
Q2231-0015	108 (0.18 arcmin^{-2})	Bielby et al. (2013)
HE0940-1050	358 (0.30 arcmin^{-2})	Bielby et al. (2013)
Q2348-011	303 (0.17 arcmin^{-2})	Bielby et al. (2013)
Total	2,096 (0.21 arcmin^{-2})	

Table 2.3: LBG survey of Steidel et al. 2003. Only six out of their 17 fields are used in this work.

Field	Dimensions (arcmin^2)	Number of LBGs
Q0201+1120	8.69 ×8.72	21
Q0256-000	8.54×8.46	42
Q0302-003	6.50 ×6.90	40
Q0933+2854	8.93×9.28	58
Q2233+1341	9.25×9.25	38
Q1422+2309	7.28×15.5	109
	Total	308

2.1.3 Keck LBG sample

We also included the LBGs sample of Steidel et al. (2003). The Keck survey comprises 17 fields, covering an area of 0.38 deg^2, and provides a sample of $\sim$ 940 LBGs observed using the Keck LRIS instrument (Oke et al., 1995). The QSOs from six (Q0201+1120, Q0256-0000, Q0302-0019, B0933+2854, Q2233+1341 and Q1422+2309) out of the 17 Keck fields are available to us through the public archive and taking only those galaxies in fields around these 6 Keck QSOs, the numbers of LBGs are reduced to 308 as shown in Table 2.3. The Keck LBGs are limited to $\mathcal{R} = 25.5$. The sky distribution of LBGs and QSOs from KECK (Steidel et al., 2003) are shown in Fig. 2.4 - 2.5. The re-reduced KECK quasar is shown by red filled star. Black dots show LBGs with spectroscopically-confirmed redshifts.

2.2 QSO data

We have analysed publicly available archival spectroscopy for 17 QSOs in the redshift range $2.9 < z < 3.8$, with 13 additional QSO spectra provided by our own X-Shooter observations to make a total of 30 QSO sightlines. The publicly available data are all high resolution ($R \gtrsim 30,000$), high signal-to-noise ($S/N \gtrsim 20$) spectra observed using either the UVES instrument on the VLT (Dekker et al., 2000) or the HiRES instrument on the Keck telescope (Vogt et al., 1994).

Full details of the reduction of UVES and HiRES QSO spectra for 11 of the QSOs used here are provided by Crighton et al. (2011). The 6 KECK spectra were

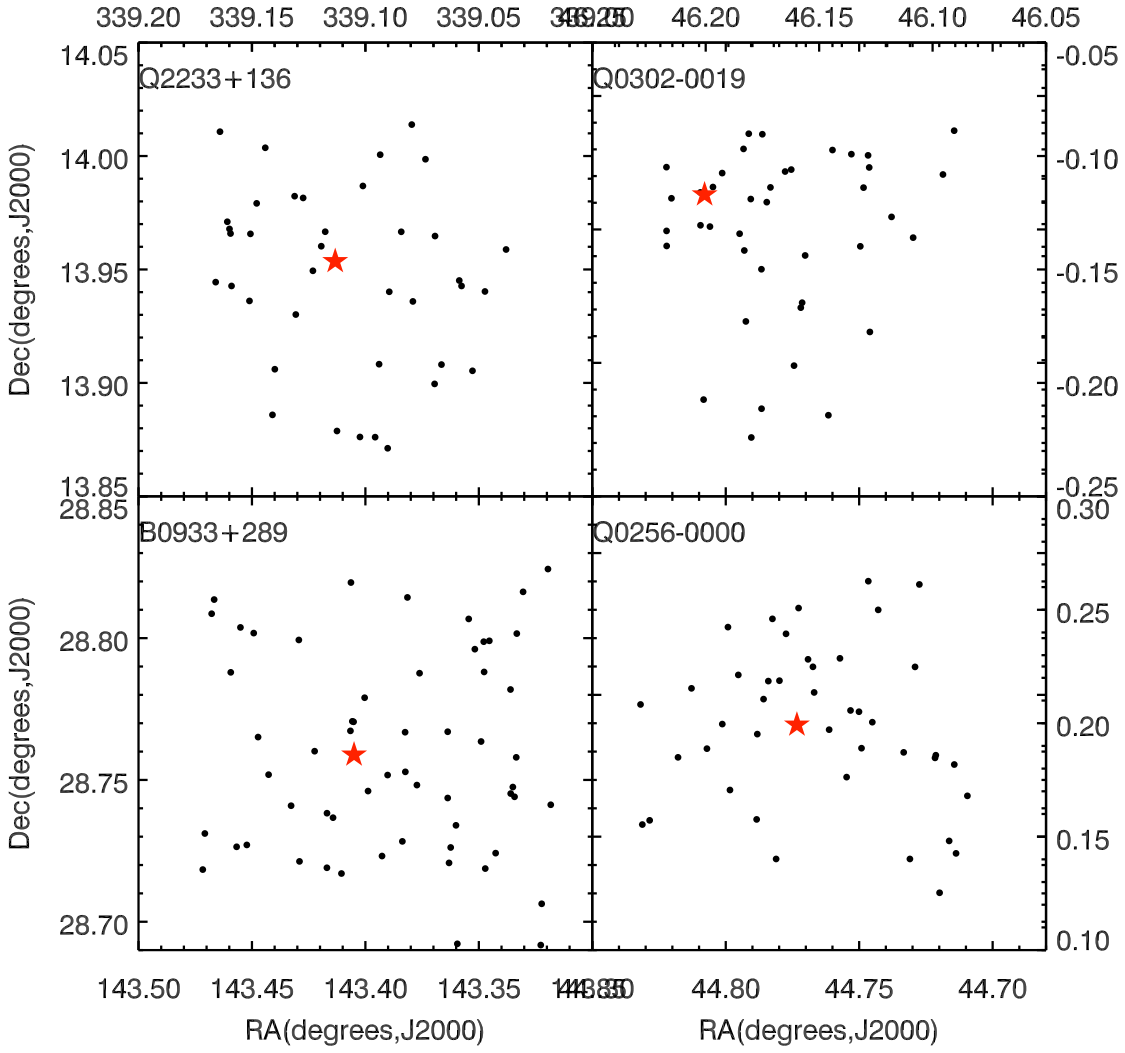

Figure 2.4: Quasar and LBG positions in the Q2233+136, Q0302−0019, B0933+289 and Q0256−0000 fields. Black dots show LBGs with spectroscopically-confirmed redshifts from Steidel et al. 2003. The re-reduced KECK quasar is shown by red filled star.

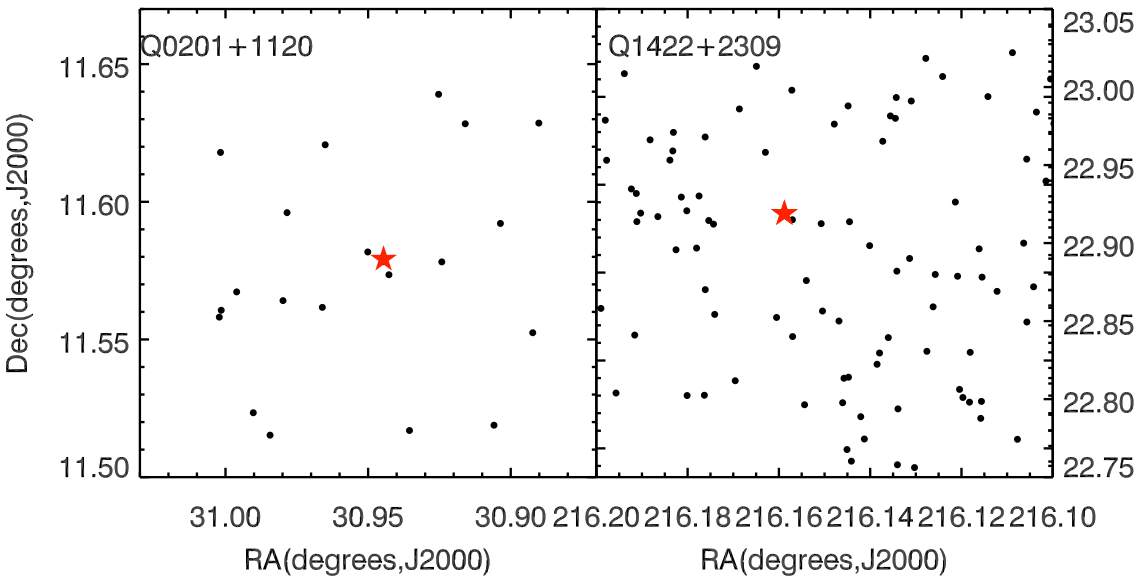

Figure 2.5: Quasar and LBG positions in the Q0201+1120 and Q1422+2309 fields. Symbols are the same as in Fig. 2.4.

all observed with the Keck HiRES instrument.

In addition to the publicly available QSO spectra, we also include new moderate resolution X-Shooter data for 13 $z \sim 3$ quasars in a subset of the VLRS fields from our own observations using the X-Shooter instrument on the VLT (Vernet et al., 2011). The full list of QSOs used in this study is provided in Tables 2.4, 2.5, 2.6.

2.2.1 KECK re-reduced high resolution QSO spectra

We downloaded the high resolution quasar from the Keck archive as used by Adelberger et al. (2005). These will increase our current data set to study the relationship between galaxies and the IGM at $z \approx 3$. We will have more QSO sightlines to cross-correlate LBGs with Lyα transmissivity. The details of KECK QSOs are in Table 2.4. The high resolution ($R \sim 40,000$) quasar spectra of Q0256-0000, Q0302-0019, Q0933+2845, Q1422+2309, and Q2233+1341 were obtained with the HIRES echelle spectrograph (Vogt et al., 1994) on Keck I between 1996 and 2000 (see Adelberger et al. 2005 for full details).

The spectra were reduced by using MAKEE (MAuna Kea Echelle Extraction)

Table 2.4: Details of high resolution spectroscopic observations of the QSOs from Keck Archive.

Name	R.A.	Dec	z	Mag
Q2233+136	22:36:27.2	+13:57:13	3.209	18.7
Q0302-0019	03:04:49.9	-00:08:13	3.281	17.8
QSO B0933+289	09:33:37.2	+28:45:32	3.428	17.8
Q0256-0000	02:59:05.6	+00:11:22	3.364	18.2
Q0201+1120	02:03:46.7	+11:34:45	3.610	20.1
Q1422+2309	14:24:38.1	+01:22:56	3.620	16.5

package 5.2.4[1] written by Tom Barlow (2002). Briefly, the main procedure of the package are determining the position of echelle order from all raw HIRES FITS input files, calculating the object and background extraction boundaries, extracting a spectrum for each order, and finally performing the wavelength calibrations.

Following the manual, as we wanted to reduce all HIRES data for each QSO at once therefore we created a list of all input image as *image.list*. The list with details of the observation was read by makeepipe. In the next step, the pipeline calculated the electrons per digital number (eperdn) and readout noise (ronoise) by using bias frames and flat fields. We put these values manaully in makeepipe command lines We summed up all bias frames and flat fields. We made *makee.script* which is a list of command lines for each reduction. In each line of *makee.script* includes object file, trace file, flat file, arclamp file for each reduction. After executed the script, output files were given. The output were Object Spectrum (2-D spectrum of object and each row is an echelle order), Error Spectrum (one sigma error spectrum), Sky Spectrum (nightsky or background spectrum), Flat Field Spectrum (non-normalized spectrum of the flat field), Signal-to-Noise Spectrum (signal-to-noise per pixel corresponding to the object spectrum), and Digital Number Spectrum (object spectrum in digital number units). We will use the "spectral images" (Flux-***.fits : 2-D object spectrum). The wavelength was calibrated with a 6th order polynomial fit to each echelle order.

After getting the reduced frames from MAKEE, we applied SPIM2 to splice the echelle orders and combine individual observations. This involved producing

[1]http://www2.keck.hawaii.edu/inst/hires/makeewww/

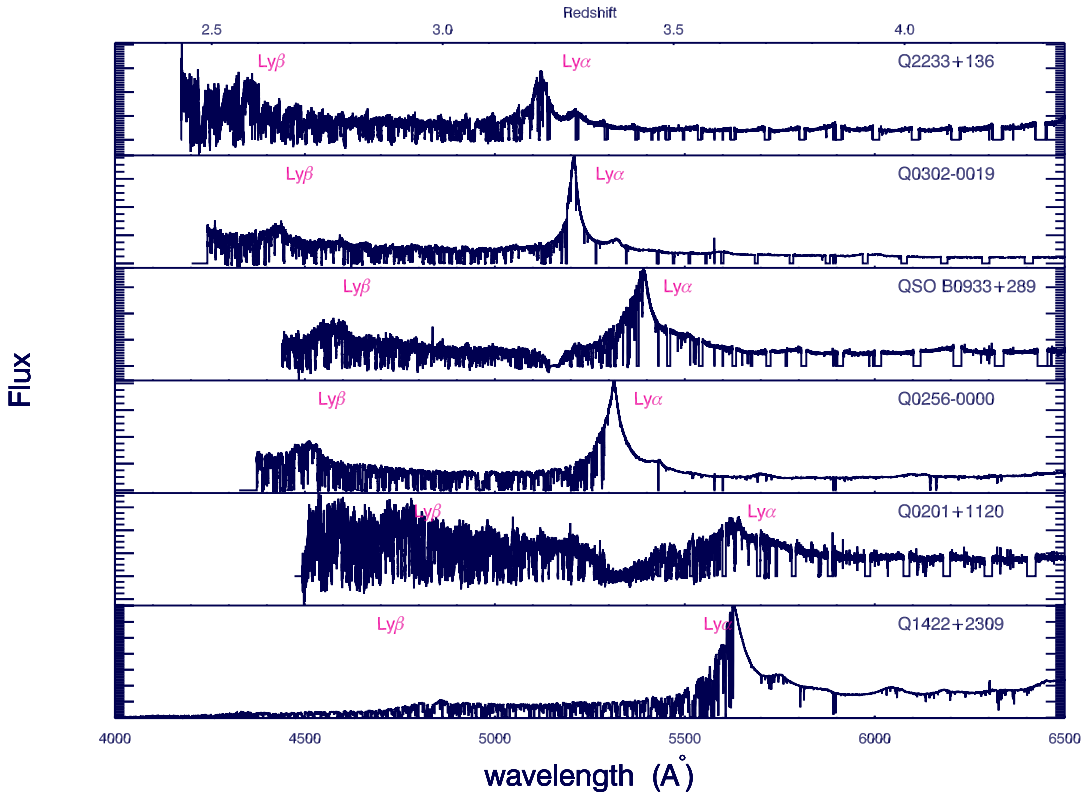

Figure 2.6: High resolution spectra from KECK. The wavelength range between Lyβ and Lyα which will be used in analysis are labelled with the quasar name.

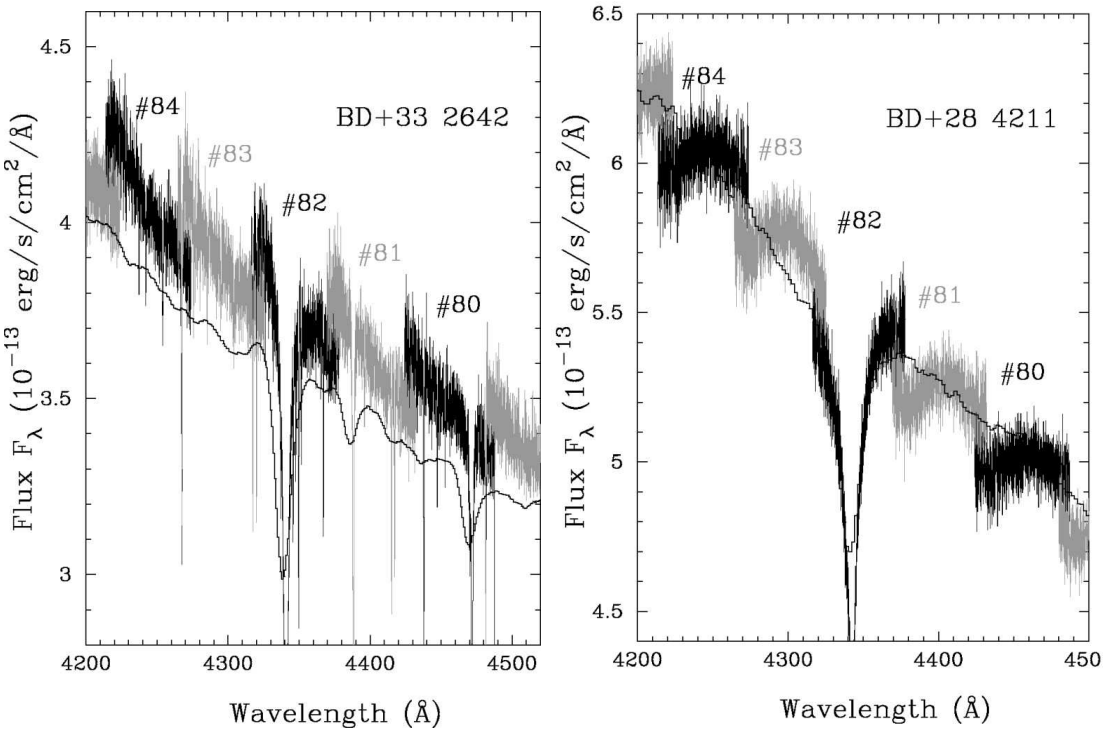

Figure 2.7: HIRES spectra of stars that have been flux-calibrated in the usual manner (Suzuki et al. 2003). In both cases, we see overlap wavelengths where echelle orders join. (Left) HIRES integration of star BD+33° 2642. (Right) HIRES integration of BD +28° 4211

template spectra constructed by combining the individual observations, masking bad regions of the CCDs and rescaling. A template was applied to rescale the original observations. We divided out the continuum for each individual observation, then multiplied this normalised flux by a continuum fit to the template. After scaling each order of each observation individually, we combined them to get the final spectrum. Fig. 2.6 shows the reduced spectra which will be used to calculate the correlation functions. The overlap region between echelle orders were treated differently bluewards and redwards of the Lyα emission wavelength. Redwards, the missing wavelengths at the red end of the spectra in Fig. 2.6 are caused by cutting out the overlap regions. The spectra redwards of Lyα are not used in any of our analysis. Bluewards, we used a weighted mean to combine the orders in these regions, producing a single flux calibrated spectrum. Therefore, there are no gaps in the Lyα forest region of the spectrum. As discussed in Suzuki et al. (2003), flux errors are most severe near the ends of each spectral order, where there can be discontinuous jumps. In Fig. 2.7 we show order overlap where echelle orders join for spectra of stars. The source of these errors is uncertain, but may include changes in the vignetting connected to the optical alignment. It is difficult to combine the spectra from the many spectral orders of an echelle to produce a single continuous spectrum.

2.2.2 QSO spectra in VLRS fields

We have used publicly available archival spectra of the bright quasars centrally positioned in the VLRS fields (the exception to this is the Q2359-0653 field). In addition, two further quasars ([WHO91] 0043-265 and Q212904.90-160249.0) lie in the VLRS fields and have archival high-resolution spectra available. In total, this gives us 11 QSOs with high resolution spectroscopy of the Lyα forest, as presented by green circles in Fig. 2.1-2.2-2.3.

Our quasar sample consists of $R < 21$ quasars with emission redshifts $2 < z < 4$ in and around our nine LBG fields. Each field was selected to have one bright (mag=16-18) $z \sim 3 - 4$ QSO at the centre. These spectra have resolution full widths at half maximum (FWHM) of 6-8 kms^{-1}. An overview of these quasars is

Table 2.5: List of high resolution QSO spectra in the VLRS fields.

QSO	R.A.	Dec.	z	Mag	Instrument
	J2000				
Q0042-2627	00:44:33.9	-26:11:19	3.29	$B = 18.5$	HIRES
$[WHO91]$0043-265	00:45:30.5	-26:17:09	3.44	18.34	HIRES
J0124+0044	01:24:03.8	+00:44:32	3.83	$g = 19.2$	UVES
HE0940-1050	09:42:53.5	-11:04:25	3.06	$B = 17.2$	UVES
J1201+0116	12:01:44.4	+01:16:11	3.23	$g = 17.7$	HIRES
Q212904.90-160249.0	21:29:04.9	-16:02:49	2.90	19.2	HIRES
PKS2126-158	21:29:12.2	-15:38:40	3.27	$V = 17.3$	UVES
LBQS 0301-0035	03:03:41.0	-00:23:22	3.23	17.6	HIRES
Q2231+0015	22:34:08.9	+00:00:01	3.02	$r = 17.3$	UVES
Q2348-011	23:50:57.9	-00:52:10	3.02	$r = 18.7$	UVES
LBQS Q0302-0019	03:03:41.1	-00:23:22	3.23	17.6	HIRES

given in in Table 2.5. In addition to the central bright quasars, we also searched for any other known quasars with the appropriate redshift and magnitude in either the NASA Extragalactic Database[2] or the survey by Worseck et al. (2008). Most of these QSOs have high resolution spectra in the ESO or Keck archives.

The remaining low resolution spectra (shown by red circles in Fig. 2.1- 2.2- 2.3) were obtained from AAOmega. Since, the QSOs are low resolution (1300) and generally have S/N < 3 per resolution element in the Lyα forest, which introduces systematic errors in the background subtraction over the Lyα forest region and thus systematic errors in the inferred transmissivity, we therefore decided not to include them in our analysis.

The reduction for UVES quasars were done by using Ultraviolet-Visible Echelle Spectrograph (UVES) pipeline which generates the calibration products and science products. UVES POPLER software[3] was used to combine all frames. The HIRES spectra from KECK were reduced in the same way described in subsection 2.2.1. More details of observations and data reduction can be found in Crighton et al. (2011).

Fig. 2.8 shows high resolution QSO spectra in the VLRS fields. The wavelength range between Lyβ and Lyα which will be used in analysis are labelled. Note that

[2]http://nedwww.ipac.caltech.edu/

[3]http://astronomy.swin.edu.au/m̃murphy/UVES_popler

these spectra have not been flux calibrated. In our analysis, we excluded some region such as Lyman Limit Systems (LLS), Damped Lyα (DLA) systems, and bad/gap regions in our spectra. In short, we masked out a gap at 4460Å $< \lambda <$ 4520Å in LBQS Q0301-0035, 2 gaps at wavelength range of 4420Å $< \lambda <$ 4540Å and 4790Å $< \lambda <$ 4850Å) in J1201+0116, a gap at 4510Å $< \lambda <$ 4630Å. The DLAs masked out are at $\sim 4160\mathring{A}$ and $\sim 4400\mathring{A}$ in Q2348-011, $\lambda \sim 4640\mathring{A}$ of WH091 0043-265, $\lambda \sim 4950\mathring{A}$ of J0124+0044, and $\lambda \sim 4650\mathring{A}$ of Q212904.90-160249.0.

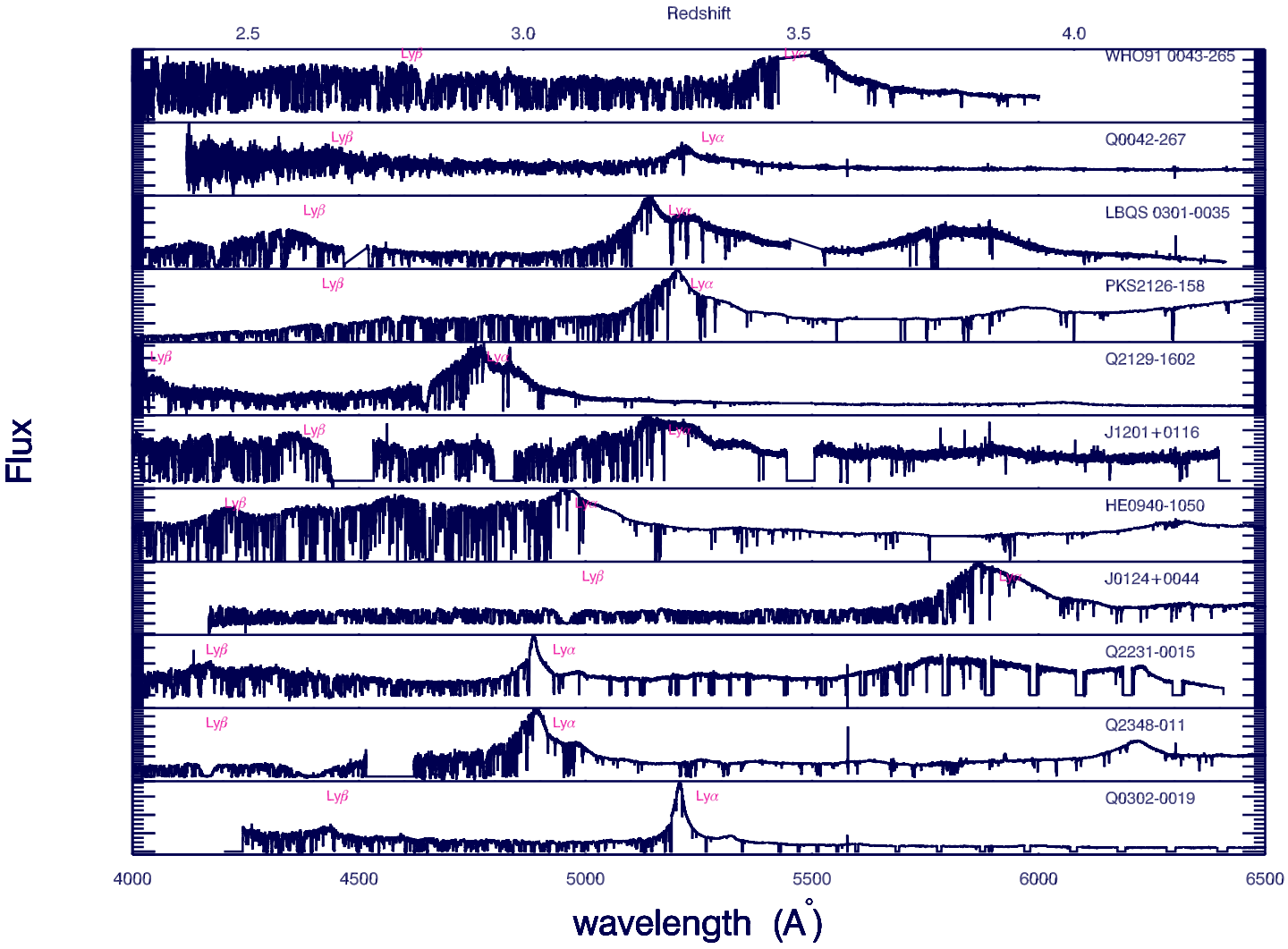

Figure 2.8: High resolution QSO spectra in the VLRS fields.

2.2.3 VLT X-Shooter spectra

Here we have obtained X-shooter spectra of confirmed QSOs in the VIMOS LBG fields in order to significantly increase the number of close LBG-QSO-sightline pairs (full details are in Bielby et al.(in prep)). As part of ESO observations 085.A-0327 and 087.A-0906, we observed 19 quasars using the X-Shooter instrument. All of these QSOs have $2.6 < z < 4.0$ and $18 < R < 22$. We will use 13 of 19 observed quasars because other QSOs have too low-signal-to-noise to be useful in the analysis of the Lyα forest and are therefore not included in any of the analysis presented here. The sky distribution of X-shooter QSOs are shown by blue triangles in Fig. 2.1- 2.2- 2.3. The remaining high quality spectra are shown in Fig. 2.9. Table 2.6 presents the list of quasars from X-shooter.

The observations were performed in NOD mode with individual exposure times of 694s, 695s and 246s with the UV-blue (UVB), visual (VIS) and near-infrared (NIR) arms respectively. For quasars with magnitudes of $R \leq 20$, 2 exposures were made in the UVB arm, 2 with the VIS arm and 6 with the NIR arm. Quasars fainter than $R = 20$ were observed with double the number of exposures as for the brighter quasars. Slit widths of $1.0''$, $1.2''$ and $1.2''$ were used for the UVB, VIS and NIR arms respectively, giving resolutions of $R = 4,350$, $R = 6,700$ and $R = 3,890$ in each arm. Standard flux observations were made using the spectrophotometric standard stars GD71, LTT7987 and EG 131. The X-Shooter spectra were reduced using the ESO X-Shooter pipeline package version number 1.4.6 and the ESOREX command line reduction tool. We followed the standard reduction procedure as outlined in the X-Shooter Pipeline User Manual. All of the X-Shooter spectra were flux calibrated using the observed spectrophotometric stars.

Table 2.6: Quasars observed at moderate spectroscopic resolution using VLT X-Shooter.

Name	RA	Dec	R	z
	(J2000)		(Vega)	
Q000234.97+071349.3	00:02:34.97	+07:13:49.3	20.6	2.59
Q000137.67+071412.2	00:01:37.67	+07:14:12.2	20.8	2.99
Q000127.48+071911.8	00:01:27.48	+07:19:11.8	20.7	2.87
Q000033.06+070716.1	00:00:33.06	+07:07:16.1	19.6	2.86
Q2359+0653	00:01:40.60	+07:09:54.0	18.4	3.23
Q2231+0015	22:34:09.00	+00:00:01.7	17.3	3.02
Q234958.23-004426.4	23:49:58.23	-00:44:26.4	21.0	2.58
SDSS J234921.56-005915.1	23:49:21.56	-00:59:15.2	19.9	3.09
Q2348-011	23:50:57.88	-00:52:09.9	18.7	3.01
Q235119.47-011229.2	23:51:19.47	-01:12:29.2	20.1	2.94
Q235201.36-011408.2	23:52:01.36	-01:14:08.2	20.4	3.12
Q235213.16-011209.7	23:52:13.16	-01:12:09.7	20.9	3.26
LBQS 0041-2638	00:43:42.79	-26:22:10.2	18.3	3.05

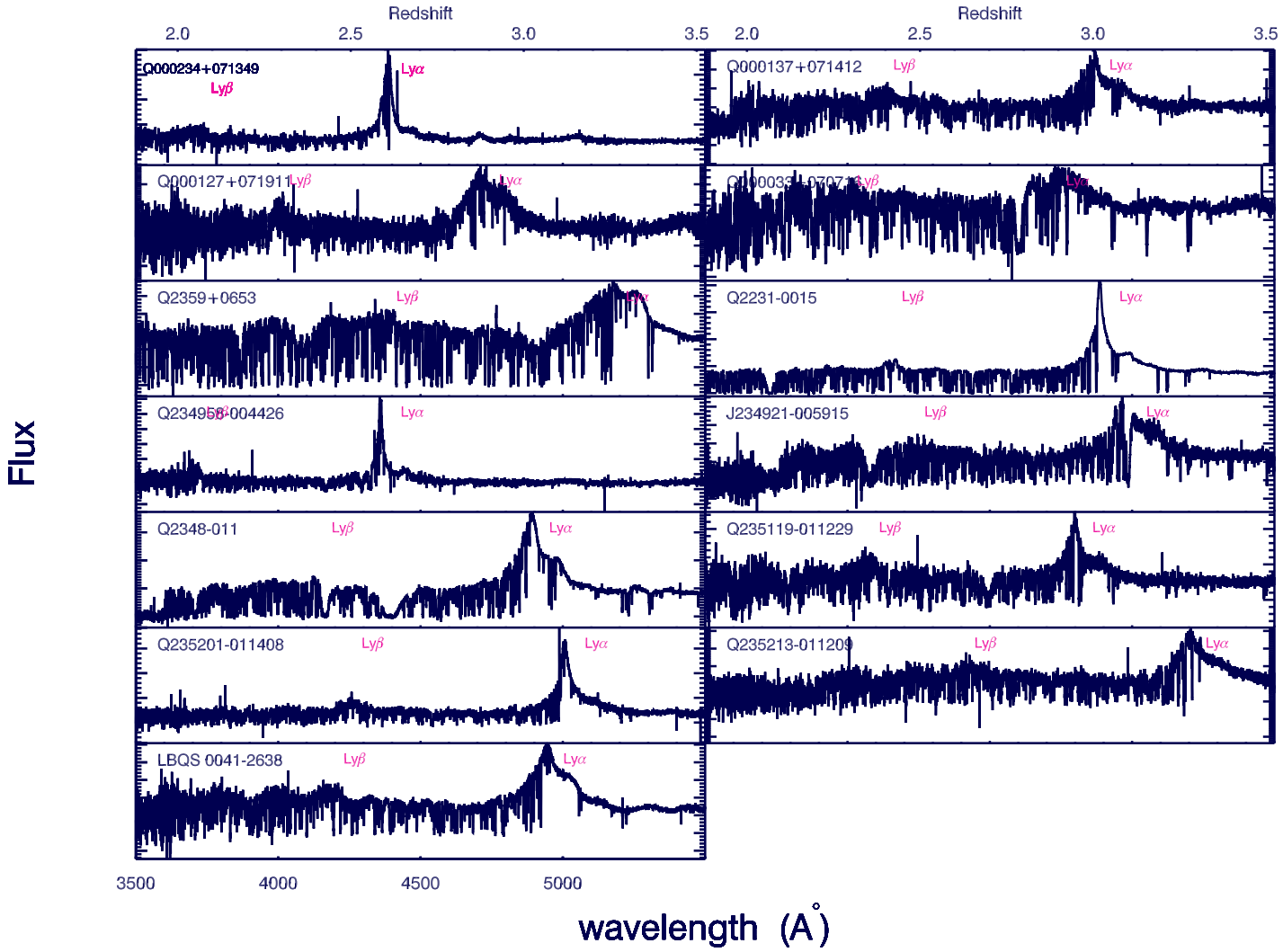

Figure 2.9: Spectra from VLT X-Shooter.

Chapter 3

Simulations

3.1 GIMIC simulations

3.1.1 Overview

We simulate both Lyα spectra and galaxies to compare with the observational data using a hydrodynamical cosmological simulation. Our main aims are to study the real and redshift-space auto and cross-correlation functions to see if we can detect the effects of peculiar velocities to understand more about gas outflow and infall into galaxies, for (a) LBG-LBG pairs (b) Lyα-Lyα pairs and (c) the LBG-Lyα forest. The results will then be used to interpret the observable 1-D and 2-D correlation functions $\xi(r)$ and $\xi(\sigma, \pi)$ in terms of both simulation and observational results. Here σ is the distance transverse to the line of sight, π is the line of sight distance and r is the vector combination of the two coordinates, thus $r = \sqrt{\sigma^2 + \pi^2}$. In addition, we differentiate between the separation in real and redshift-space by using r for the real-space separation and s for the redshift-space separation.

For this purpose we use the GIMIC simulation, which is a cosmological hydrodynamical re-simulation of selected volumes of the Millennium simulation (Springel, 2005). GIMIC is designed to overcome the issues in simulating large cosmological volumes ($L \gtrsim 100h^{-1}$ Mpc) at high resolution ($m_{gas} \lesssim 10^7 h^{-1}$ $M_\odot$) to $z = 0$ by taking a number of smaller regions with 'zoomed' initial conditions (Frenk et al., 1996; Power et al., 2003; Navarro et al., 2004). These individual regions each have

approximate radii of $18h^{-1}$Mpc outside of which the remainder of the Millennium simulation volume is modelled with collisionless particles at much lower resolution.

GIMIC was run using the TreePM SPH code GADGET3, which is an update of the GADGET2 code (Springel, 2005). The cosmological parameters adopted were: $\Omega_m = 0.25$, $\Omega_\lambda = 0.75$, $\Omega_b = 0.045$, $h_0 = 100\ h$ kms^{-1}Mpc^{-1}, $h = 0.73$, $\sigma_8 = 0.9$ and $n_s = 1$ (where n_s is the spectral index of the primordial power spectrum).

The GIMIC simulations are particularly well suited to the study of $\sim L^\star$ galaxies. As shown in Crain et al. (2009), the implementation of efficient (but energetically feasible) feedback from SNe largely prevents overcooling on the mass scale of $L^\star$ galaxies, and is key to the reproduction of the observed X-ray scaling relation presented in that study. Indeed, GIMIC accurately reproduces the rotation speeds and star formation efficiencies of $z = 0$ disc galaxies for $10^9 \lesssim M < 10^{10.5}M_\odot$, although galaxies with $M_\star \gtrsim 10^{11}$M$_\odot$ do still suffer from some overcooling (McCarthy et al., 2012). Moreover, Font et al. (2011) demonstrated that $L^\star$ galaxies in GIMIC exhibit satellite luminosity functions and stellar spheroid surface brightness distributions that are comparable to those of the Milky Way and M31, whilst McCarthy et al. (2012) further demonstrated that this correspondence extends also to their global structure and kinematics.

In terms of reproducing the Lyα forest, Theuns et al. (1998) conducted simulations across a range of resolutions (i.e. gas particle masses) in order to evaluate the effect of resolution on such studies. They found convergence of the mean effective optical depth (at $z = 3$) in their SPH simulations at gas particle masses of $\lesssim 1.4 \times 10^8\ h^{-1}M_\odot$, whilst column density distributions were found to be consistent given gas particle masses of $\lesssim 1.8 \times 10^7\ h^{-1}M_\odot$. Both of these limits are significantly higher than the GIMIC gas particle mass of $1.45 \times 10^6\ h^{-1}$M$_\odot$ (Crain et al., 2009), indicating that resolution effects are not an issue for our work in terms of the Lyα forest. In terms of the selected dark matter (DM) halos, the dark matter particle masses in GIMIC are $6.6 \times 10^6\ h^{-1}$M$_\odot$, which is $\gtrsim 2$ orders of magnitude lower than any halo mass we will be considering in this study.

In this work, we focus on the Lyα forest, i.e. $N_{\rm HI} \lesssim 10^{17}$ cm^{-2}. In this regime, the gas is optically thin, such that radiative transfer implementations such as that

of Altay et al. (2011) are not necessary.

An area of interest for this study is the effect of supernovae (SNe) feedback on the local environment of galaxies. GIMIC contains an implementation of SN feedback based on the generation of winds as follows. Firstly, after a delay corresponding to the maximum lifetime of stars that undergo core collapse SNe, newly formed star particles impart a randomly directed 600 kms^{-1} kick to, on average, $\eta = 4$ of its neighbours. Here η is the mass loading (defined as $\eta \equiv \dot{m}_{\rm wind}/\dot{m}_{\star}$) and it's value for GIMIC was chosen to match the global star formation rate density (SFRD) to observational data. The 600 kms^{-1} initial kick is not equivalent to measured outflow velocities given that it is a 'launch' velocity and is not necessarily what observations measure. However, we note that it is consistent with the Lyα wind velocities reported by Pettini et al. (2001), although it is at the higher end of the distribution of the larger sample measured by Shapley et al. (2003).

In the work presented here, we use the '0σ' GIMIC region, which is identified as having a mean density at $z = 1.5$ equal to the mean density of the Universe at that epoch. In addition, we use only one snapshot of this region, chosen to be at a redshift of $z = 3.1$ in order to provide a suitable comparison to our $z \sim 3$ observed population of star-forming galaxies. All the analysis is limited to a sphere of radius 16 h^{-1}Mpc in order to negate the effects of particles being 'moved' out of the analysis region when moved to redshift-space. Given a limiting radius of 16 h^{-1}Mpc, the same number of $M_{\star} \geq 10^8$ h^{-1}M$_{\odot}$ galaxies are present in the region regardless of whether redshift-space distortions (RSD) are applied or not.

3.1.2 Simulated galaxy population

Identifying the galaxy population

The galaxy population is identified in the simulation based on first identifying the dark matter halos using a Friends of Friends (FoF, Davis et al., 1985) algorithm. A group finding algorithm then locates the nearest dark matter halo for each baryonic (gas or star) particle and identifies the particle with this halo. The SUBFIND algorithm (Springel et al., 2001; Dolag et al., 2009) is then used to identify self-bound

sub-structures within the halos, to which star particles are associated and defined as galaxies.

We use cuts in stellar mass to define our simulated galaxy samples. In the first instance we take galaxies with stellar masses of $M_\star \geq 10^8\ h^{-1}\mathrm{M}_\odot$. This is intended as a large sample, which is not representative of the $z \sim 3$ population sampled by present observations, but as a comparison data-set for the second more representative sample. Taking our limiting radius within the GIMIC volume of 16 h^{-1} Mpc radius, this low-mass cut gives a sample of 4,070 galaxies from the snapshot at $z = 3.06$ in the 0σ density region. The distribution of galaxy stellar mass (blue histogram) and host halo mass (black histogram) for this sample is shown for reference in the top panel of Fig. 3.1. The mean galaxy stellar mass is $M_\star = 10^{8.9}\ h^{-1}\mathrm{M}_\odot$ (blue vertical dashed line), whilst the mean host halo mass is $M_{\mathrm{halo}} = 10^{10.5}\ h^{-1}\mathrm{M}_\odot$ (black vertical dashed line).

With our second simulated galaxy sample, we aim to more closely mimic the observed LBG samples and specifically to reproduce the observed clustering. To do so, we again select simulated galaxies using a minimum stellar mass constraint. We find that a stellar mass cut of $M_\star \geq 10^9\ h^{-1}\mathrm{M}_\odot$ provides a simulated galaxy sample with a clustering signal well matched to the observed clustering of LBGs. This is presented in detail in section 4.1, whilst here we show a comparison of the stellar and halo mass properties of the sample compared to observations. These are shown in the lower panel of Fig. 3.1 with the galaxy stellar mass distribution shown by the blue histogram and the host halo mass distribution shown by the black histogram. The mean of the galaxy stellar masses is $M_\star = 9.9\ h^{-1}\mathrm{M}_\odot$ (blue vertical dotted line) and the mean host halo mass is $M_{\mathrm{halo}} = 11.4\ h^{-1}\mathrm{M}_\odot$. This $M_\star \geq 10^9\ h^{-1}\mathrm{M}_\odot$ cut gives a sample of 287 simulated galaxies within $r \leq 16\ h^{-1}$ Mpc, equating to a space density of $\rho_g \sim 5 \times 10^{-3}\ h^3\mathrm{Mpc}^{-3}$ (for comparison Adelberger et al. 2005b measure a space density of $\rho_g = (4 \pm 2) \times 10^{-3}\ h^3\mathrm{Mpc}^{-3}$ for the Keck LBG sample).

The cyan shaded region in the lower panel of Fig. 3.1 shows the standard deviation range around the mean galaxy stellar mass derived from the observations of Shapley et al. (2005) (i.e. $M_\star = 10^{10.32}\ h^{-1}\mathrm{M}_\odot$, with a standard deviation of $\sigma_{\log(M\star)} = 0.51$). The galaxy stellar mass of the GIMIC selection overlaps the

range of the observed galaxies, but extends further to lower stellar masses (i.e. $M_\star < 10^{9.5}\ h^{-1}\mathrm{M}_\odot$). We note that the Shapley et al. (2005) result is based on K_s observations and that 23% of their UV selected sample is not included in the stellar mass distribution due to not being detected in the K_s observations. It is reasonable to assume that the excluded 23% will occupy the low-mass region of their sample.

Bielby et al. (2013) present measurements of the halo masses of the VLRS spectroscopic $z \sim 3$ galaxy sample, finding masses of $10^{11.57\pm0.15}\ h^{-1}\mathrm{M}_\odot$. Similarly, Adelberger et al. (2005) measure halo masses of $10^{11.5\pm0.3}\ h^{-1}\mathrm{M}_\odot$ for a comparable sample of $z \sim 3$ LBGs. We thus vary the stellar-mass constraints on the galaxy selection to match the mean halo mass to the observations (where the total masses for the GIMIC galaxies are available from the SUBFIND algorithm). The result is plotted in Fig. 3.1 where we show the stellar mass and total mass distributions for both our $M_\star \geq 10^8\ h^{-1}\mathrm{M}_\odot$ (top panel) and our 'LBG' samples (lower panel). For the $M_\star \geq 10^8\ h^{-1}\mathrm{M}_\odot$ stellar mass cut, we find a mean halo mass for the galaxy population of $M_{\mathrm{halo}} = 10^{10.5}\ h^{-1}\mathrm{M}_\odot$, i.e. significantly lower than observed galaxy populations. However, raising the stellar mass cut to $M_\star \geq 10^9\ h^{-1}\mathrm{M}_\odot$ gives a mean halo mass for the simulated galaxies of $M_{\mathrm{halo}} = 10^{11.4}\ h^{-1}\mathrm{M}_\odot$, well matched to the observed samples to the $\sim 1\sigma$ level. The mean halo masses (and the mean stellar masses) are plotted as black (blue) vertical dotted lines in Fig. 3.1. Both the mean halo mass and mean stellar mass for the $M_\star \geq 10^9\ h^{-1}\mathrm{M}_\odot$ sample lie at approximately the -1σ error of the observations, where the shaded blue and grey regions show the 1σ range of the observational constraints. We note that the simulation was performed with a relatively high value for σ_8 (a value of $\sigma_8 = 0.9$ which originated from a combined analysis of 2dFGRS and WMAP3, Springel et al. 2005) when compared to the present observed constraints ($\sigma_8 = 0.83 \pm 0.01$, Planck Collaboration et al. 2013) and so for a given mean halo mass, we would expect a higher clustering amplitude for a given halo mass from the simulation when compared to the observations. Our focus here is to recreate the observed clustering signal and so by taking a marginally low mean halo mass compared to observations, we may better achieve this as we show in section 4.1.

All combined, the GIMIC $M_\star \geq 10^9\ h^{-1}\mathrm{M}_\odot$ simulated galaxies provide a popu-

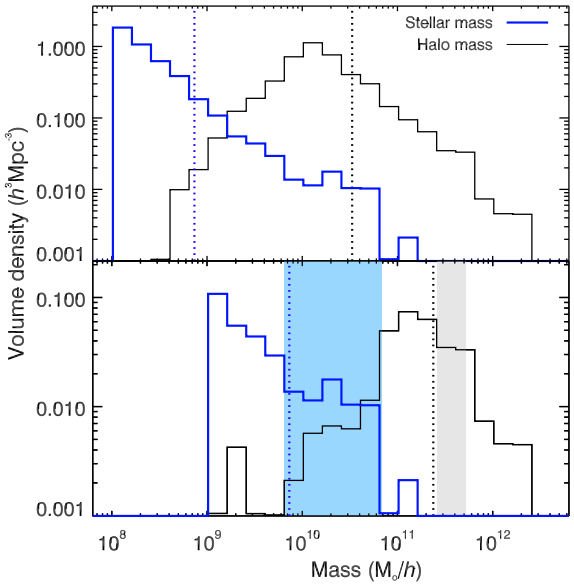

Figure 3.1: Distribution of total halo and galaxy stellar masses for the two GIMIC galaxy selections, $M_\star \geq 10^8\ h^{-1}\mathrm{M}_\odot$ (top) and $M_\star \geq 10^9\ h^{-1}\mathrm{M}_\odot$ (bottom). The blue histograms in each panel show the numbers of galaxies as a function of stellar mass, whilst the black histograms show the numbers of galaxies as a function of total halo mass. The dotted vertical lines show the mean halo mass, $M_{halo} = 10^{10.5}\ h^{-1}\mathrm{M}_\odot$ and $M_{halo} = 10^{11.4}\ h^{-1}\mathrm{M}_\odot$ for the low and high mass cuts respectively.

lation that is consistent with the observed LBG population.

Velocity field of the simulated galaxies

The distribution of $M_\star \geq 10^9\ h^{-1}\mathrm{M}_\odot$ galaxies in real- (asterisks) and redshift-space (diamonds) is shown in Fig. 3.2. Throughout this work, we use the x and y coordinates as the transverse to the line of sight coordinates and z as the line of sight coordinate, either in real or redshift-space. Fig. 3.2 illustrates the measured positional shifts in the z-axis given by the peculiar velocities of the galaxies within the simulation. It is evident from this plot that there is an overall large scale 'bulk' motion directed in the positive redshift direction due to the motion of the zoomed region with respect to the full 500 h^{-1}Mpc Millennium volume. Measuring the distribution of the galaxy velocities, we find an average velocity $\langle v_z \rangle = 93$ kms^{-1} with a standard deviation of 128 kms^{-1} for the $M_\star \geq 10^9\ h^{-1}\mathrm{M}_\odot$ galaxy sample and $\langle v_z \rangle = +94$ kms^{-1} with a standard deviation of 125 kms^{-1} for the $M_\star \geq 10^8\ h^{-1}\mathrm{M}_\odot$ galaxy sample.

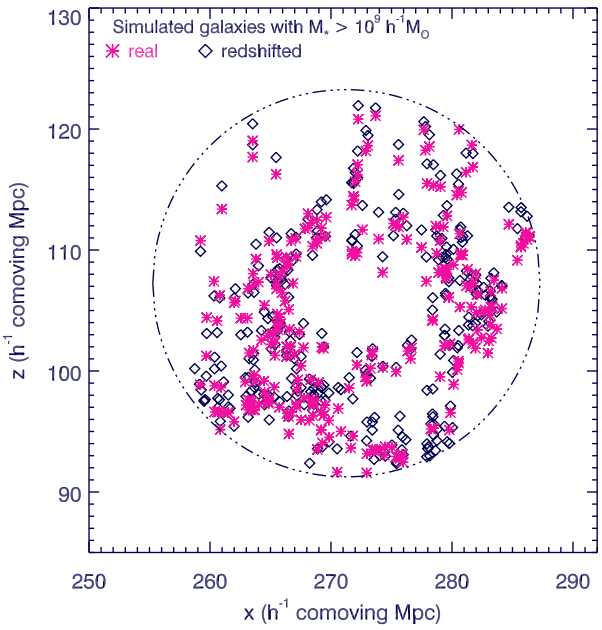

Figure 3.2: The distribution of $M_\star \geq 10^9\ h^{-1}\mathrm{M}_\odot$simulated galaxies in real-space (pink asterisks) and redshift-space(diamonds).

We show the pairwise velocity ($\sqrt{\langle w_z^2 \rangle}$) distributions (black histograms) of galaxies in Fig. 3.3. For the $M_\star \geq 10^9\ h^{-1}\mathrm{M}_\odot$ and $M_\star \geq 10^8\ h^{-1}\mathrm{M}_\odot$ galaxy samples we find $\sqrt{\langle w_z^2 \rangle} = 176$ kms^{-1} and $\sqrt{\langle w_z^2 \rangle} = 172$ kms^{-1} respectively. The red dashed histograms show the distribution for only those pairs within $r = 1\ h^{-1}$Mpc of each other, thus isolating the intra-halo velocity dispersion and excluding the effect of the halo-halo velocity dispersion. This is important when considering the effect of the velocity dispersion on the galaxy-galaxy clustering measurement. The standard deviations of the pairwise velocities for pairs within $r \leq 1\ h^{-1}$Mpc are 142 kms^{-1} and 104 kms^{-1} for $M_\star \geq 10^9\ h^{-1}\mathrm{M}_\odot$ and $M_\star \geq 10^8\ h^{-1}\mathrm{M}_\odot$ galaxies respectively. None of these standard deviations include redshift uncertainties due to measurement errors that affect the observed galaxy redshifts.

3.1.3 Simulating Lyα forest spectra

We next generated spectra along the z-direction through the GIMIC volume to compare with the observations. The sightlines were extracted using SPECWIZARD[1].

[1]Developed by J. Schaye, C. Booth and T. Theuns, refer to Theuns et al. (1998) for details

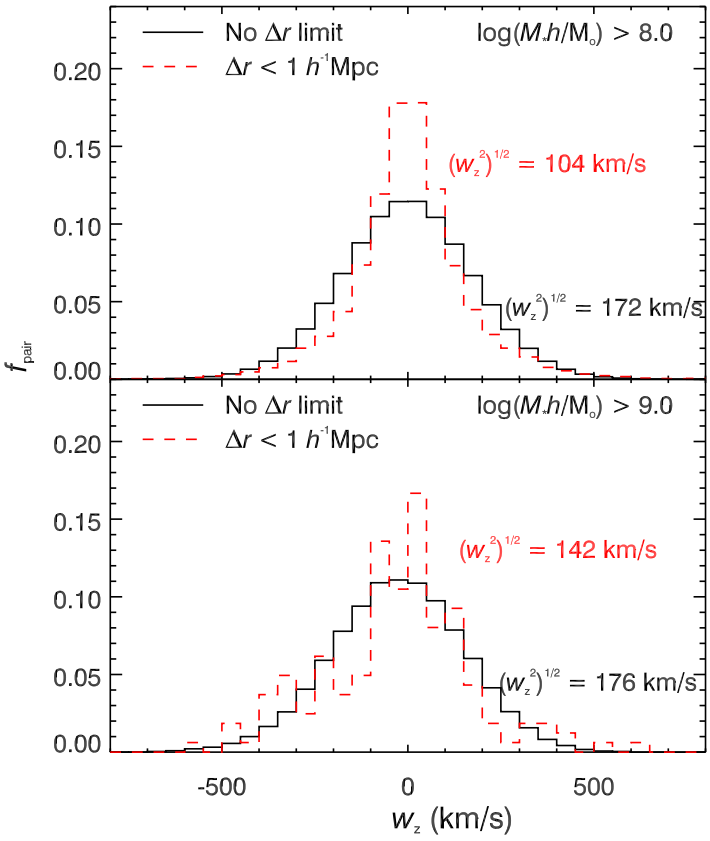

Figure 3.3: The distribution of pairwise velocities (w_z, solid histograms) for the GIMIC galaxy samples. The top panel shows the distribution for the $M_\star \geq 10^8\ h^{-1}\mathrm{M}_\odot$ galaxy cut and the lower panel that for the $M_\star \geq 10^9\ h^{-1}\mathrm{M}_\odot$ cut. Given the effect of pairwise velocities will be dominant at small scales (i.e. $\lesssim 1\ \ h^{-1}$Mpc), we also show the distributions in each case for only those pairs separated by $\Delta r < 1\ \ h^{-1}$Mpc (dashed red histograms in both panels). The resulting RMS pairwise velocities are indicated in each case and the separation limit gives smaller values of the RMS pairwise velocity in both cases.

The transmission is given by, $T = e^{-\tau}$, where τ is the optical depth along the line-of-sight. We use a spectral resolution FWHM of 7.0 kms^{-1} to convolve each spectrum, a signal-to-noise of 50 per pixel, and pixels of width 2.8 kms^{-1} which are typical values of our UVES and HIRES QSO spectra.

The sightlines were generated with random X, Y positions, then parallel to the $Z-$axis. We constructed 200 sightlines, with this number providing an approximate optimum between maximising the statistics available and minimising the oversampling of any region of the volume. Each sightline was constrained to not extend beyond 16 h^{-1} Mpc from the centre of the GIMIC volume in order to avoid any edge effects in terms of the gas extent. The average transmission, $\bar{T}_r$ for real space is 0.69 while the $\bar{T}_z$ for redshift-space is 0.72. An explanation for this difference is that infall of saturated absorption lines towards each other in redshift space may result in an overall increase in the measured flux. This will cause the average transmissivity over the full spectrum to increase in redshift space as seen. Some hint of this effect can be seen in Fig. 3.5 in which we show a number of examples of the flux from each sightline compared in real and redshift space. These values for the mean transmission at $z \sim 3$ are comparable to the observed values, for example McDonald et al. (2000) measure a value of $\bar{T}(z = 3) = 0.684 \pm 0.023$, whilst measurements of the effective optical depth by Faucher-Giguère et al. (2008) give $\bar{T}(z = 3) = 0.680 \pm 0.020$.

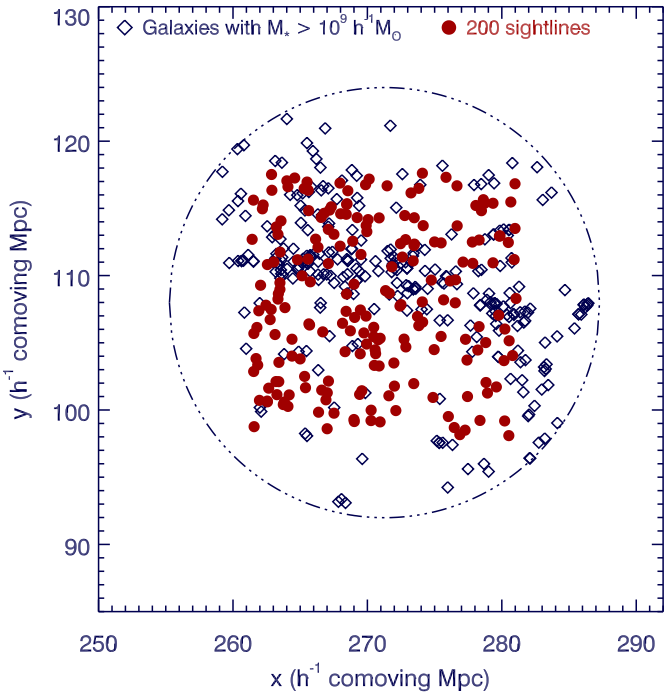

Figure 3.4: The projected position of $M_\star \geq 10^9\ h^{-1}\mathrm{M}_\odot$ galaxies (diamonds) and 200 Lyα sightlines (circles) on the XY plane.

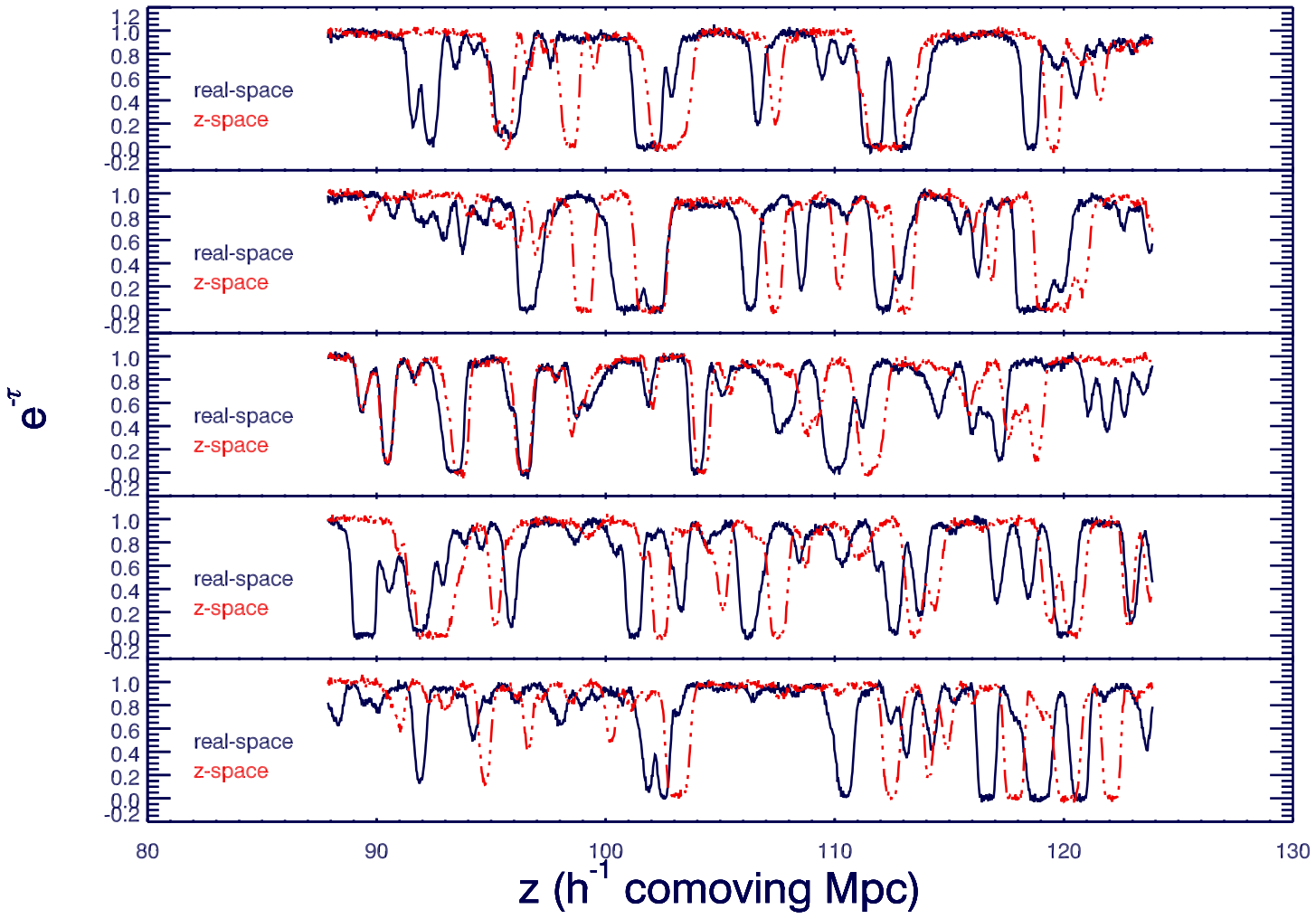

Figure 3.5: Examples of absorption spectra from simulated QSO sightlines. The blue solid line shows $e^{-\tau}$ in real space the red dashed line shows $e^{-\tau}$ in redshift-space.The scale is measured in h^{-1} comoving Mpc.

Using SPECWIZARD, we calculate the mass weighted line-of-sight (LOS) peculiar velocities for each pixel in our 200 spectra. The distribution of the peculiar velocities is given in Fig. 3.6. As with the galaxy population, the gas traced by the simulated spectra shows the bulk motion in the positive z-direction, with a mean peculiar velocity of $\langle v_z \rangle = 110$ kms^{-1} and an R.M.S of 120 kms^{-1}. This peculiar velocity if lower than that measured for the galaxy samples, reflecting that these gas particles trace lower mass systems.

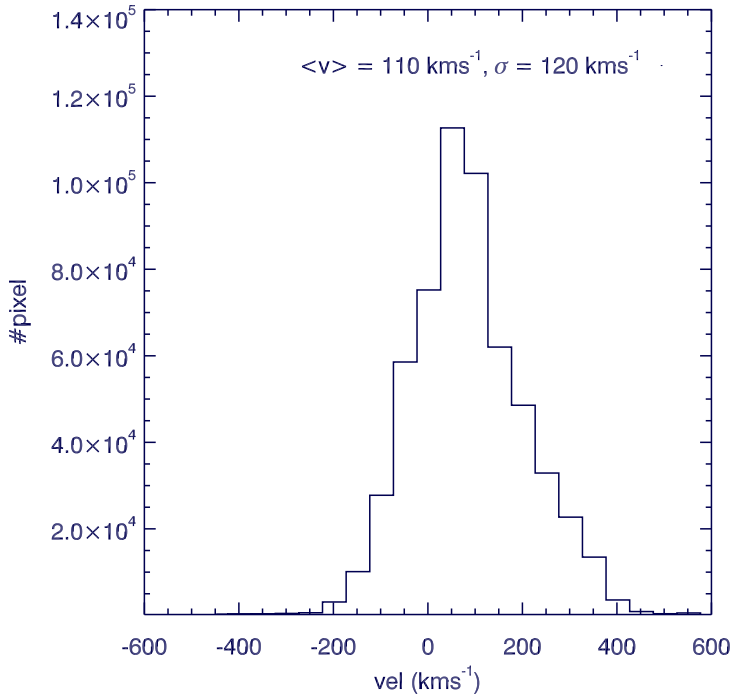

Figure 3.6: The distribution of LOS optical depth weighted peculiar velocities measured within each pixel in each of the GIMIC simulated spectra. This illustrates the underlying dynamics present in the spectra. The LOS peculiar velocity distribution shows a mean peculiar velocity of $\langle v_z \rangle = 110$ kms^{-1} with a standard deviation of 120 km s^{-1}.

Chapter 4

Interactions Between Galaxies and the IGM at z $\sim$ 3

In this chapter , we present the analysis of the interaction between IGM and galaxies at $z \sim 3$ with the data from VLRS and KECK. We also include interpretations from the GIMIC simulations. We aim to study (a) the LBG-LBG $\xi(s)$, to see if we can detect the effects of peculiar velocities and possibly feedback by comparing real and redshift space correlation function, (b) the LBG-Lyα $\xi(s)$ to understand more about outflow and feedback, and (c) Lyα-Lyα auto-correlation. We roughly estimate β from $\xi(s)/\xi(r)$ for galaxies and gas and hence estimate the bias factor, b, in the standard cosmology at z = 3.

4.1 Galaxy Clustering

4.1.1 1-D correlation function

Estimator

Bielby et al. (2013) presented a clustering analysis of the LBG data used in this study (combining the VLRS and Keck data). In this section, we compare the observed galaxy clustering presented by Bielby et al. (2013) to results obtained using the galaxy population within the GIMIC simulation. In so doing, we may validate how representative the GIMIC galaxy population is of the observed $z \approx 3$ LBG

population in terms of intrinsic clustering properties and the effects of the galaxy velocity field on the galaxy clustering.

We calculate the real and redshift-space functions, $\xi(r)$ and $\xi(s)$, of the GIMIC $z = 3.06$ galaxy samples using the Davis & Peebles (1983) estimator:

$$\xi(r) = \frac{N_R}{N_G} \frac{\langle DD(r) \rangle}{\langle DR(r) \rangle} - 1 \tag{4.1.1}$$

where $\langle DD(r) \rangle$ is the average number of galaxy-galaxy pairs, $\langle DR(r) \rangle$ is the number of pairs of galaxy-randoms at the separation, r, where we use r to represent the separation in real space and s the separation in redshift-space. The factor $\frac{N_R}{N_G}$ is the ratio of the number of random to data points.

We estimate errors on the auto-correlation results using jack-knife estimates based on splitting the simulation into equal volume octants and excluding each octant in turn to create 8 jack-knife realisations of the data. The correlation functions are then fit using a power-law of the form of:

$$\xi(r) = \left(\frac{r}{r_0} \right)^{-\gamma} \tag{4.1.2}$$

where γ is the slope of real-space clustering, $\xi(r)$, and r_0 is the real-space clustering length.

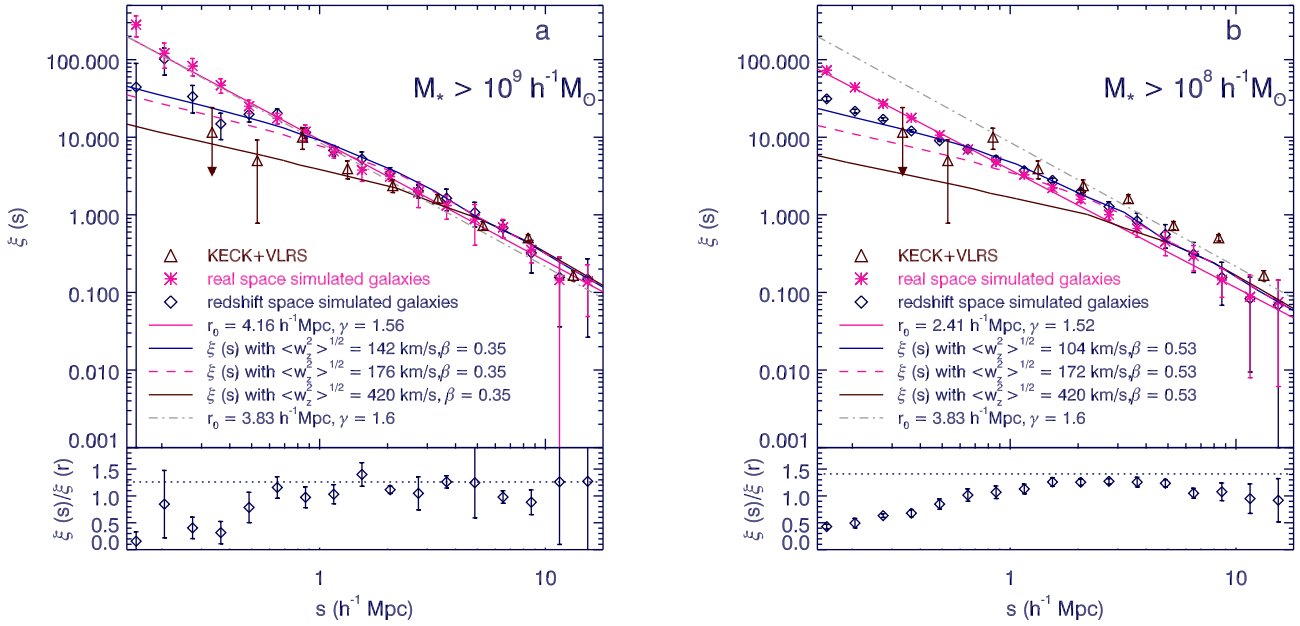

Figure 4.1: (a) Galaxy correlation functions for 287 simulated $M_\star \geq 10^9\ h^{-1}\mathrm{M}_\odot$ galaxies compared to the observed LBGs. real-space - pink asterisks, redshift-space - blue diamonds, LBG data - brown triangles. Also shown are fits to simulated real-space (pink line) with $\gamma = 1.56$ and $r_0 = 4.16\ h^{-1}$Mpc. The real-space fit to the Keck+VLRS data is shown by the grey dot-dashed line. The pink dashed line is the predicted $\xi(s)$ assuming the real-space fit with the full pairwise velocity dispersion of $\sqrt{\langle w_z^2 \rangle} = 176$ kms^{-1}. The blue solid line is the same except with the $s < 1\ h^{-1}$ Mpc pairwise dispersion of $\sqrt{\langle w_z^2 \rangle} = 142$ kms^{-1}. The brown line is the same model now with $\sqrt{\langle w_z^2 \rangle} = 420$ kms^{-1}, with velocity errors added to allow comparison with the Keck+VLRS LBG $\xi(s)$. (b) The same for 4,070 simulated $M_\star \geq 10^8\ h^{-1}\mathrm{M}_\odot$ galaxies with real-space fit $\gamma = 1.52$, $r_0 = 2.41\ h^{-1}$Mpc. The $\xi(s)$ predictions now assume the appropriate pairwise velocity dispersion of $\sqrt{\langle w_z^2 \rangle} = 172$ kms^{-1} (pink dashed line) and $\sqrt{\langle w_z^2 \rangle} = 104$ kms^{-1} (blue solid line). Bottom panels present $\xi(s)/\xi(r)$ with jack-knife error bars. The dotted line represents the predicted Kaiser boost (Kaiser et al. 1987) with (a) $\beta = 0.35$ giving $\xi(s)/\xi(r) = 1.26$ for $M_\star \geq 10^9\ h^{-1}\mathrm{M}_\odot$ galaxies and the Kaiser boost with (b) $\beta = 0.53$ giving $\xi(s)/\xi(r) = 1.41$ for $M_\star \geq 10^8\ h^{-1}\mathrm{M}_\odot$ galaxies.

Simulated real-space galaxy correlations

Fig. 4.1 shows the results for the simulated galaxy-galaxy correlation function with (a) $M_\star \geq 10^9\ h^{-1}\mathrm{M}_\odot$ and (b) $M_\star \geq 10^8\ h^{-1}\mathrm{M}_\odot$ simulated galaxies. The blue diamonds show results from galaxies in redshift-space while the pink asterisks show results from galaxies in real space. The integral constraint, $\mathcal{I}$, is included in the data in order to compensate for the effect of the limited field sizes (as described in Sec 1.3.3). The estimated integral constraints are $\mathcal{I} = 0.21$ and $\mathcal{I} = 0.11$ for $M_\star \geq 10^9\ h^{-1}\mathrm{M}_\odot$ galaxies and the full sample respectively. The pink lines represent power-law fits to the real-space correlation function based on Eqn. 4.1.2 with $\gamma = 1.56 \pm 0.26$ and $r_0 = 4.16 \pm 1.16\ h^{-1}$Mpc in the $M_\star \geq 10^9\ h^{-1}\mathrm{M}_\odot$ galaxies' plot while $\gamma = 1.52 \pm 0.10$, $r_0 = 2.41 \pm 0.24\ h^{-1}$Mpc in $M_\star \geq 10^8\ h^{-1}\mathrm{M}_\odot$ galaxies' plot. These power-law results give good fits to the real-space clustering results and we note that there is little sign of a double power-law or two-halo break in the clustering for either of the samples. However, we note that in $z \sim 3$ galaxies, the break between the 1-halo and 2-halo terms is measured to be at $\sim 0.1'$, which corresponds to $\approx 0.14\ \ h^{-1}$Mpc at $z = 3$. Any break is therefore expected to be at scales smaller than those that we consider in Fig. 4.1, scales at which we have little sensitivity with which to probe for any possible break.

Simulated $\xi(s)/\xi(r)$ and infall

In the lower panels we show the ratio between the real and redshift-space clustering results in order to highlight the signatures of redshift-space distortions in the redshift-space correlation function. Here the errors are again constructed from the jack-knife realisations. At scales above $s \sim 1.5 - 2\ h^{-1}$Mpc, we see the effects of dynamical infall, which acts to boost the clustering signal in the redshift-space measurement. From linear theory (Kaiser 1987; Hamilton 1992) we expect to see the 'Kaiser boost', which is given given by:

$$\xi(s) = (1 + \frac{2}{3}\beta + \frac{1}{5}\beta^2)\xi(r) \tag{4.1.3}$$

where β is the dynamical infall parameter (Kaiser, 1987), given for galaxies by

$\beta \approx \Omega^{0.6}/b$, where b is the linear galaxy bias and is given by $b = \sqrt{\xi_{\rm gal}/\xi_{\rm DM}}$ (here $\xi_{\rm gal}$ is the galaxy clustering and $\xi_{\rm DM}$ is the dark matter clustering). At $z \approx 3$, we proceed via the volume averaged clustering amplitude, $\bar{\xi}(8)$ from

$$\bar{\xi}(x) = \frac{3}{x^3}\int_0^x r^2 \xi(r) {\rm d}r \tag{4.1.4}$$

For the $M_\star \geq 10^9\ h^{-1}{\rm M}_\odot$ simulated galaxy case, the above power-law parameters fitted to $\xi(r)$ give $\bar{\xi_g}(8) = 0.75 \pm 0.05$ which with $\bar{\xi}_{DM}(8) = 0.088$ gives bias $b = 2.80 \pm 0.18$. Taking $\Omega_m(z = 3.0) = 0.98$ gives $\beta = 0.35 \pm 0.02$. So the predicted value of the Kaiser boost, based on Eq. 4.1.3, is 1.26 ± 0.12 compared to the measured amplitude ratio at $1 < s < 8\ h^{-1}$Mpc of 1.17 ± 0.06.

Assuming the power-law fitted to $\xi(r)$ for the set of $M_\star \geq 10^8\ h^{-1}{\rm M}_\odot$ galaxies, we find $\bar{\xi_g}(8) = 0.33 \pm 0.02$, giving $b = 1.85 \pm 0.12$ and $\beta = 0.53 \pm 0.03$. The predicted Kaiser boost is therefore $\xi(s)/\xi(r) = 1.41 \pm 0.14$. At separations of $1 < s < 8\ h^{-1}$Mpc, we find a mean amplitude ratio of 1.26 ± 0.03, consistent at the $\sim 1\sigma$ level with a Kaiser boost, although marginally lower than predicted by linear theory. We conclude that for the simulation, the ratio, $\xi(s)/\xi(r)$, is in reasonable agreement with linear theory infall predictions for both high and low mass galaxies.

Simulated galaxy correlations and velocity dispersion

At smaller separations ($r < 1\ h^{-1}$ Mpc) for both high- and low-mass simulated galaxies, the galaxy-galaxy $\xi(s)$ in redshift space has lower clustering than $\xi(r)$. This turn-over of the real space correlation function is the result of z-space smoothing due to the peculiar velocity dispersion, $\sqrt{\langle w_z^2 \rangle}$. This peculiar velocity refers to the motion of a pair of galaxies which are close together on the sky, relative to one another in the same potential well. We model the effects of the velocity dispersion on the clustering results using a gaussian distribution to the velocity dispersion, following previous work (e.g. Hawkins et al., 2003; da Ângela et al., 2005). The model accounts for two key effects on the clustering statistics caused by galaxy motions. The first is the finger-of-god effect, which is constrained by the velocity dispersion $\sqrt{\langle w_z^2 \rangle}$ and the second is the Kaiser effect (i.e. the coherent motion of

galaxies on large scales), which is characterised by β. Using the pairwise velocity dispersions derived from Fig. 3.3 for the two samples (i.e. $\sqrt{\langle w_z^2 \rangle} = 176$ kms^{-1} and $\sqrt{\langle w_z^2 \rangle} = 172$ kms^{-1} for the $M_\star \geq 10^9\ h^{-1}\mathrm{M}_\odot$ and $M_\star \geq 10^8\ h^{-1}\mathrm{M}_\odot$ samples respectively - pink dashed lines in both panels), we find that the reduction of the real-space clustering at small scales is over-predicted compared to the measurements of $\xi(s)$. As illustrated in Fig. 3.3 however, we note that the measured pairwise velocity dispersion is separation dependent. The observed discrepancy is therefore likely the result of the effect of small scale peculiar motions on the clustering function being dominated by galaxies within $\sim 1\ h^{-1}$Mpc of each other, whereas the initial pairwise velocity histogram presented in Fig. 3.3 includes pairwise velocities between galaxies across all separation scales within the simulation. If we thus limit the histogram of pairwise velocities to only those pairs within $1\ h^{-1}$Mpc of each other (dashed histograms in Fig. 3.3), we retrieve pairwise velocity dispersions of $\sqrt{\langle w_z^2 \rangle} = 142$ kms^{-1} and $\sqrt{\langle w_z^2 \rangle} = 104$ kms^{-1} for the $M_\star \geq 10^9\ h^{-1}\mathrm{M}_\odot$ and $M_\star \geq 10^8\ h^{-1}\mathrm{M}_\odot$ samples respectively. Using these values in the redshift-space distortion model, we find improved agreement between the model (solid blue line in Fig. 4.1) and the galaxy auto-correlation function measured from the GIMIC simulations. Ultimately, the appropriate velocity dispersion for modelling the redshift-space distortion effects on the galaxy clustering, is the velocity dispersion present within groups, whilst the peculiar velocity measured from the simple histogram case included the imprint of the velocity dispersion of galaxy groups as well as the dispersion within groups. Taking the histogram of only pairs of galaxies within $\sim 1\ h^{-1}$Mpc of each other effectively measures the intra-group peculiar velocities. We conclude that $\xi(s)$ is better explained on sub-Mpc scales with the intra-group velocity dispersion appropriate for these scales.

4.1.2 Simulated and observed correlation functions compared

Bielby et al. (2013) report the best fit scale-length and slope for the observed Keck + VLRS LBG-LBG semi-projected $w_p(\sigma)$ for the data is $r_0 = 3.83 \pm 0.24\ h^{-1}$ Mpc with a slope of $\gamma = 1.60 \pm 0.09$. Within the reported errors, the clustering of our $M_\star \geq$

$10^9\ h^{-1}\mathrm{M}_\odot$ sample reproduces the observed survey clustering very well in terms of both clustering length and slope. As would be expected, the $M_\star \geq 10^8\ h^{-1}\mathrm{M}_\odot$ sample gives a somewhat lower clustering length than the observational data, but does at least have a consistent slope within the quoted errors.

We now apply the measured $\sqrt{\langle w_z^2 \rangle}$ from the observations of Bielby et al. (2013) to our correlation functions measure from GIMIC. Bielby et al. (2013) measured pairwise $\sqrt{\langle w_z^2 \rangle} = 420$ kms^{-1}, which includes both the intrinsic velocity dispersion and the velocity errors on measuring the galaxy redshifts. Combining these two elements in quadrature, we can calculate a pairwise velocity dispersion by using

$$\sqrt{\langle w_z^2 \rangle} \approx \sqrt{2} \times \sqrt{(intrinsic\ velocity\ dispersion)^2 + (velocity\ \ errors)^2} \quad (4.1.5)$$

The measured $\xi(s)$ from Bielby et al. (2013) is shown in Fig. 4.1 (brown triangles) and a model based on the GIMIC $\xi(r)$ combined with the observational $\sqrt{\langle w_z^2 \rangle} = 420$ kms^{-1} is given by the brown solid line. By introducing the observationally measured pairwise velocity errors to the GIMIC $M_\star \geq 10^9\ h^{-1}\mathrm{M}_\odot$ result, we find that the GIMIC clustering measurement reproduces the measured LBG clustering well. Unfortunately, the $\sqrt{\langle w_z^2 \rangle} = 420$ kms^{-1} is dominated by the velocity error thus it is difficult to constrain the intrinsic effect of peculiar velocities in the observational data.

4.1.3 2-D correlation function

We now turn to the 2-D galaxy auto-correlation functions in order to further investigate the impact of galaxy velocities on clustering measurements within the simulation. In the 2-D correlation function, $\xi(\sigma, \pi)$, we parameterise the line of sight separation between two galaxies by π and the transverse separation by σ. We calculate $\xi(\sigma, \pi)$ using the same methods as used for the 1-D correlation functions and with the same samples.

Simulations

Figs. 4.2 and 4.3 show the 2-D galaxy auto-correlation function, $\xi(\sigma, \pi)$, for $M_\star \geq 10^8\ h^{-1}\mathrm{M}_\odot$ and $M_\star \geq 10^9\ h^{-1}\mathrm{M}_\odot$ simulated galaxies respectively (both with the integral constraint added). In both cases the top-left panel shows the real-space measurement and the top-right panel shows the redshift-space measurement. The bottom panels show the respective error contours for the $\xi(\sigma, \pi)$ measurements.

Taking the $M_\star \geq 10^8\ h^{-1}\mathrm{M}_\odot$ results first, the effects of the redshift-space distortions (RSD) are clearly visible in the top panels of Fig. 4.2, where the redshift-space $\xi(\sigma, \pi)$ contours are more extended at scales of $\lesssim 4\ \ h^{-1}\mathrm{Mpc}$, whilst being flattened at scales of $\gtrsim 4\ \ h^{-1}\mathrm{Mpc}$ in comparison to the real-space result. In terms of the latter, the shift in position of the $\xi = 0.5$ and $\xi = 0.2$ contours from the left to right panels is clear evidence of the Kaiser boost. This is affirmed when fitting the RSD model as shown by the lower panels of Fig. 4.4. The fitting is performed by applying the redshift-space distortion model to the power-law fit given in Fig. 4.1b (i.e. $r_0 = 2.41\ \ h^{-1}\mathrm{Mpc}$ and $\gamma = 1.52$). We fit the model firstly to the real-space $\xi(\sigma, \pi)$ in order to constrain any geometric effects on the 2D clustering that may mimic RSD. The model fitting applied in real-space gives best fit parameters of $\sqrt{\langle w_z^2 \rangle} = 0^{+30}_{-0}\mathrm{kms}^{-1}$ and $\beta = 0.00^{+0.06}_{-0.00}$, consistent with this measurement having been made in real-space. Performing the same fitting to the redshift-space result returns best fit values of $\sqrt{\langle w_z^2 \rangle} = 160^{+45}_{-35}\mathrm{kms}^{-1}$ and $\beta = 0.47 \pm 0.22$. From the measured bias for the galaxy sample of $b = 1.85$, we predicted an infall parameter value for this galaxy sample of $\beta = 0.53 \pm 0.03$. Additionally, from the ratio of $\xi(s)/\xi(r)$, we find $\beta = 0.35$, which again is within the 1σ errors of the 2D fitting result. As for the velocity dispersion, we find that the result is $> 1\sigma$ higher than the result for the 1D clustering measurement ($\sqrt{\langle w_z^2 \rangle} = 104\ \mathrm{kms}^{-1}$), but is consistent with the intrinsic velocity dispersion measured from the galaxy sample directly ($\sqrt{\langle w_z^2 \rangle} = 172\ \mathrm{kms}^{-1}$).

Turning to the $M_\star \geq 10^9\ h^{-1}\mathrm{M}_\odot$ galaxy sample, the top panels of Fig. 4.3 show $\xi(\sigma, \pi)$ in real (left-panel) and redshift (right-panel) space (with the lower panels showing the error contours). The χ^2 contours for the fits to the real and redshift-space measurements are shown in the top panels of Fig. 4.4. The fitting

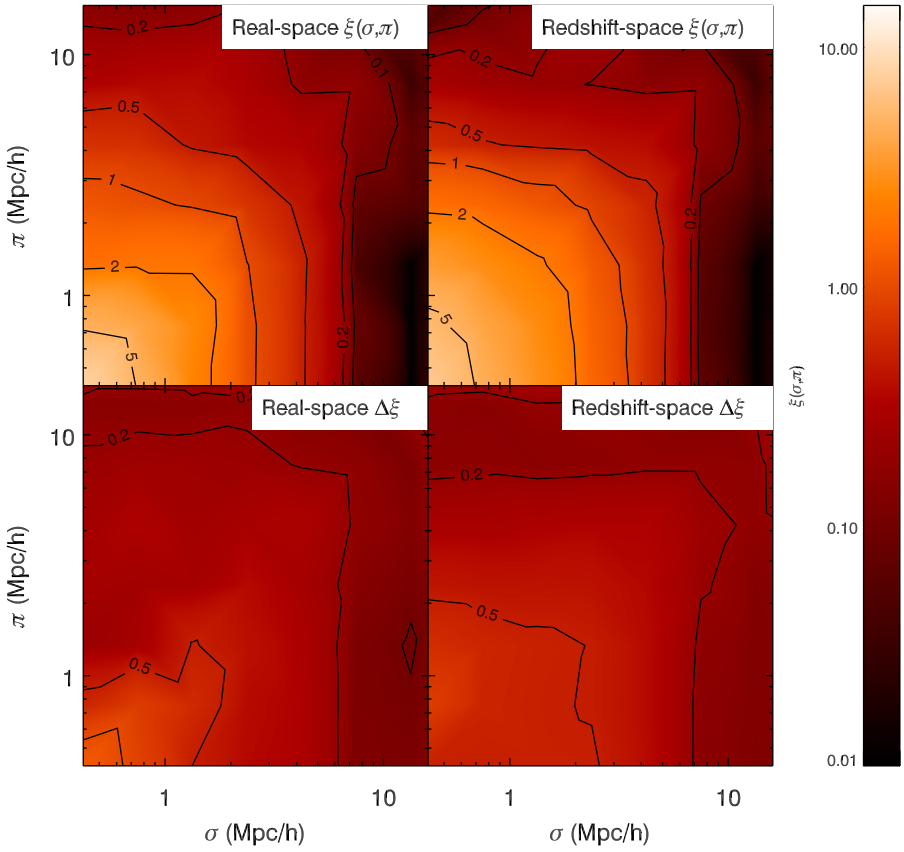

Figure 4.2: The 2D auto-correlation function $\xi(\sigma, \pi)$ results based on the simulated $M_\star \geq 10^8\ h^{-1}\mathrm{M}_\odot$ galaxies. The top panels show $\xi(\sigma, \pi)$ measured in real (left-panel) and redshift-space (right-panel), with a clear shift in the contours in the line-of-sight (π) direction at small scales showing the effect of peculiar velocities. Large scale bulk motions are also in evidence via the flattening of the the $\xi = 0.2$ contour at $\pi \sim 10\ h^{-1}$Mpc. The lower panels show the error contours over the same scales.

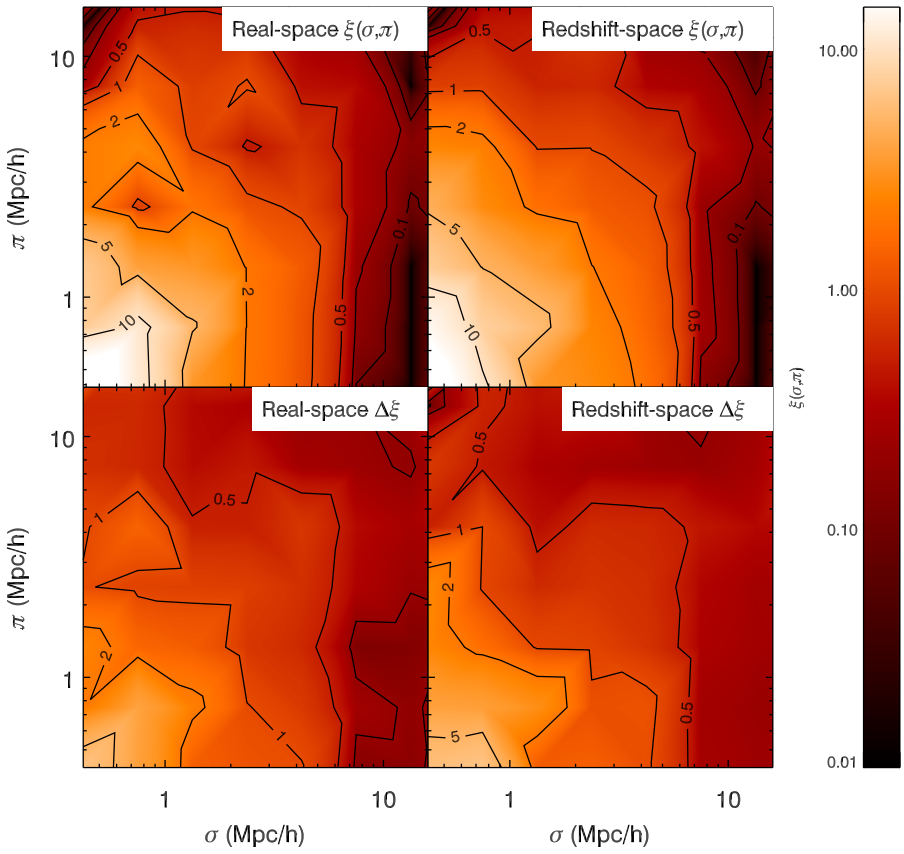

Figure 4.3: As in Fig. 4.2 but for the GIMIC $M_\star \geq 10^9\ h^{-1}\mathrm{M}_\odot$ galaxy sample. The top left and right panels show $\xi(\sigma,\pi)$ measured in real and redshift-space respectively, whilst the lower left and right panels show the error estimates on ξ.

was again made based on the real-space $\xi(r)$ power-law fit (i.e. $r_0 = 4.16\ h^{-1}$Mpc and $\gamma = 1.56$). The best fit for real-space is $\beta = 0.00^{+0.04}_{-0.00}$ and velocity dispersion $\sqrt{\langle w_z^2 \rangle} = 0^{+60}_{-0}\mathrm{kms}^{-1}$ with reduced $\chi^2 = 0.7$. In redshift-space, we found $\beta = 0.00^{+0.24}_{-0.00}$ and $\sqrt{\langle w_z^2 \rangle} = 210^{+90}_{-70}\mathrm{kms}^{-1}$ with reduced $\chi^2 = 0.7$.

As discussed above, the measured bias of $b = 2.80$ would suggest a value of $\beta \approx \Omega_m^{0.6}/b = 0.35 \pm 0.02$, which is $> 1\sigma$ different from the best fitting parameter given by the $\xi(\sigma,\pi)$ fitting. The fitted value of $\beta = 0.00^{+0.24}_{-0.00}$ is however consistent at the $\approx 1\sigma$ level with the $\beta = 0.24$ implied by the ratio of $\xi(s)/\xi(r)$. In terms of the velocity dispersion fitting parameters, the 1D and 2D fitted $\sqrt{\langle w_z^2 \rangle}$ values ($\sqrt{\langle w_z^2 \rangle} = 142$ kms^{-1} and $\sqrt{\langle w_z^2 \rangle} = 210^{+90}_{-70}\mathrm{kms}^{-1}$ respectively) are consistent at $\sim 1\sigma$, although the 2D result is again higher than the 1σ result.

In summary, the analysis of $\xi(\sigma,\pi)$ from the simulation has shown that we may determine RSD effects using the 2D clustering consistently (at the $\sim 1\sigma$ level) with

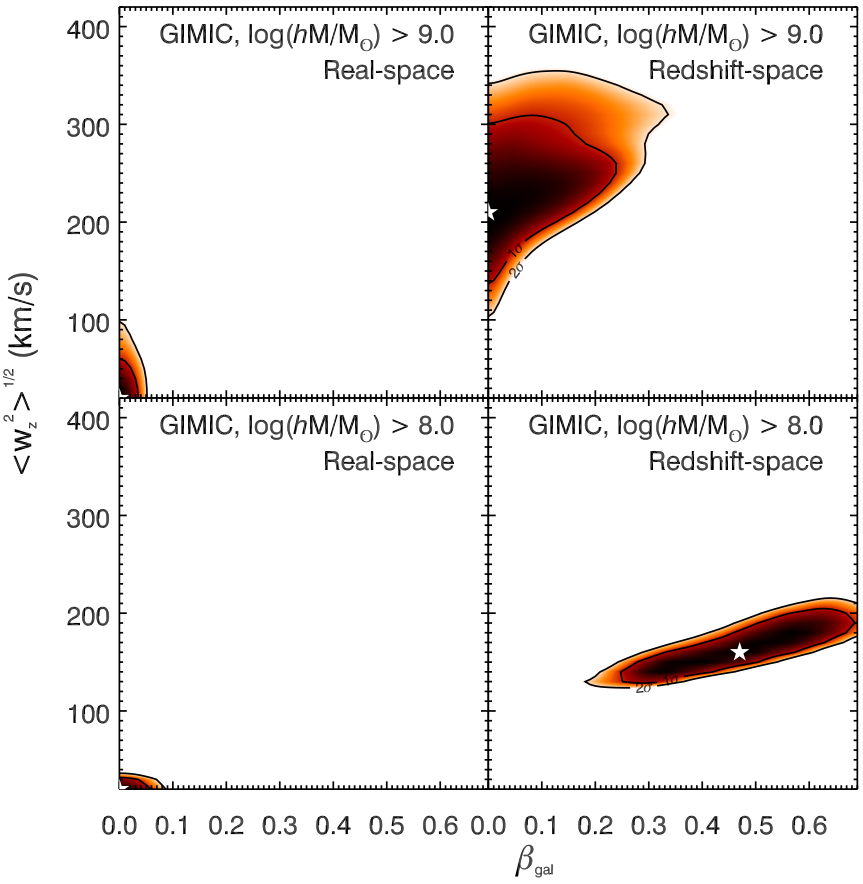

Figure 4.4: The top panels show the RSD fitting results in real (left) and redshift-space (right) for the GIMIC $M > 10^9\ h^{-1}\mathrm{M}_\odot$ galaxy sample. The real-space fitting is consistent with the lack of velocity effects in the data, giving best fitting parameters of $\sqrt{\langle w_z^2 \rangle} = 0^{+60}_{-0}\mathrm{kms}^{-1}$ and $\beta = 0.00^{+0.04}_{-0.00}$. In the redshift-space measurement, we find a velocity dispersion of $\sqrt{\langle w_z^2 \rangle} = 210^{+90}_{-70}\mathrm{kms}^{-1}$. The large scale motions is constrained as $\beta = 0.00^{+0.24}_{-0.00}$. The lower panels show the best fitting parameters to the real and redshift-space results using the RSD model described in the text for the GIMIC $M > 10^8\ h^{-1}\mathrm{M}_\odot$ galaxy sample. Fitting to the real-space result gives parameters consistent with the null velocity field, with $\sqrt{\langle w_z^2 \rangle} = 0^{+30}_{-0}\mathrm{kms}^{-1}$ and $\beta = 0.00^{+0.06}_{-0.00}$ (left-panel). Applying the same model to the redshift-space $\xi(\sigma, \pi)$ we retrieve best fitting parameters of $\sqrt{\langle w_z^2 \rangle} = 160^{+45}_{-35}\mathrm{kms}^{-1}$ and $\beta = 0.47 \pm 0.22$ (right-panel), consistent with the simulated velocity field.

the analysis of the 1D clustering. There is some tension for the $M_\star \geq 10^9\ h^{-1}\mathrm{M}_\odot$ sample where the best fitting β is zero, however this is still consistent with the 1D clustering analysis at the 1σ level. In all cases, the model successfully constrains the real-space clustering to be consistent with there being no RSD effects. In addition, the infall-parameter results are consistent with the linear theory analysis at the 1σ level in the case of the $M_\star \geq 10^8\ h^{-1}\mathrm{M}_\odot$ sample and the 2σ level for the $M_\star \geq 10^9\ h^{-1}\mathrm{M}_\odot$ sample.

Further to this, we have shown that the GIMIC galaxy population has consistent properties with observations of LBGs at $z \sim 3$. For example, Bielby et al. (2013) presented the results for $\xi(\sigma, \pi)$ for $z \sim 3$ LBGs, finding $\beta(z = 3) = 0.38 \pm 0.19$, with $r_0 = 3.83 \pm 0.24\ h^{-1}$ Mpc and $\gamma = 1.60 \pm 0.09$. The $M_\star \geq 10^9\ h^{-1}\mathrm{M}_\odot$ galaxy clustering gives consistent values for all three of these parameters at the 1σ level. Unfortunately, the small scale velocity field for the observations is dominated by redshift errors, rather than the intrinsic galaxy peculiar velocities, so we have no suitable $z \sim 3$ data to compare our small-scale results with. However, the results obtained from the simulation for $\sqrt{\langle w_z^2 \rangle}$ are instructive for observational analyses.

4.2 Galaxies and the IGM

As discussed earlier, the relationship between the galaxy population and the IGM is key to understanding galaxy growth and evolution. Galaxies require large halos of gas in order to grow to the large masses we observe at the present day, whilst the supply and regulation of the flow of gas into galaxies dictates the distribution of galaxy masses we observe.

From observations of galaxy winds with speeds of $\gtrsim 300$ kms^{-1} for the LBG population (e.g. via the offsets nebulae and inter-stellar medium spectral features), it is evident that outflowing material exists in these star-forming galaxies (e.g. Pettini et al., 2001; Shapley et al., 2003; Bielby et al., 2011). A number of authors have thus attempted to distinguish the effects of such outflows on the distribution of gas around the $z \sim 2 - 3$ star-forming galaxy population via the Lyα forest observed in the spectra of background sightlines (e.g. A03, A05, Crighton et al. 2011; Rudie

et al. 2012; Rakic et al. 2012).

In this section, we perform an analysis of the cross correlation between galaxies and the Lyα forest using both the VLRS observational data and the GIMIC simulation. We apply the same dynamical models as in the previous sections to the cross-correlation analysis. However, in the case of the galaxy-gas cross-correlation the relation between redshift and real-space correlations will become (Mountrichas & Shanks, 2007):

$$\xi(s)/\xi(r) = (1 + \frac{1}{3}(\beta_{gal} + \beta_{Ly_\alpha}) + \frac{1}{5}\beta_{gal}\beta_{Ly_\alpha}), \tag{4.2.6}$$

The linear bias of the gas obtained from $b^2 = \xi_{Ly\alpha - Ly\alpha}/\xi_{mm}$ is $b \approx 0.3$ (see Section 4.3) but this is not the bias required to assess the effect of gas infall via β_{Ly_α}. This is because of the non-linear relation $F = \exp(-\tau)$ between Lyα transmission and optical depth, τ, where most of the physics in the Lyα forest is contained in τ. According to McDonald et al (2000, 2003) the infall parameter $\beta_{Ly_\alpha} = \Omega_m^{0.6} \times b_\eta/b_\delta$ and b_η and b_δ have to be determined from simulations. McDonald (2003) found results for $\beta_{Ly_\alpha} = 1 - 1.6$ depending on the resolution of the simulations. We therefore took $\beta_{Ly_\alpha} = 1.3$ as our estimate of the gas dynamical infall parameter. McDonald (2003) did not use the redshift-space distortion techniques used here so this and the fact that we are using higher resolution SPH simulations makes it interesting to check whether linear theory with their $\beta_{Ly\alpha}$ fits our simulated data. McDonald et al. (2000) argue that the form of the flux correlation function is proportional to the mass correlation function in the linear regime. Following McDonald (2003), we shall assume that we can take account of 'finger-of-God' velocity dispersions in the usual way by convolving the transmission correlation function with a Gaussian of the appropriate dispersion.

We perform the LBG-Lyα cross correlation using the normalised pixel flux values along the QSO sightlines, where the normalised flux or transmissivity is given by:

$$T(\lambda) = \frac{f(\lambda)}{f_{con}(\lambda)}, \tag{4.2.7}$$

where f is the observed flux at a given wavelength and f_{con} is the flux continuum at

that wavelength. Following A03, for the observational data we normalised the QSO transmissivities for QSOs at $z \sim 3$ by dividing the measured flux transmissivities, T, by

$$\bar{T}(z) = 0.676 - 0.220(z - 3), \tag{4.2.8}$$

where z is the redshift of a given pixel. This normalisation is used to correct for the evolution of flux transmissivity with redshift since the transmissivity is higher at low redshift. To avoid the effect of contamination of Lyα absorption lines, we cut out the spectrum below the Lyβ emission. Thus the spectrum between the Lyβ and Lyα is only used in this calculation. We also excluded the wavelength within 20 $\mathring{A}$ of the intrinsic Lyα emission to prevent the proximity effects from the QSOs.

We then use the transmissivity of the Lyα forest as calculated above to perform the Lyα-LBG cross correlation function. The Lyα-LBG cross correlation function is calculated from

$$\langle T(s) \rangle = \frac{\langle DT(s) \rangle}{N(s)}, \tag{4.2.9}$$

where $\langle DT(s) \rangle$ is the number of galaxy-Lyα pairs weighted by the normalised transmissivity, $T/\bar{T}(z)$, for each separation. $N(s)$ is the number of LBGs that contribute to the cross-correlation function at each separation.

4.2.1 Observed LBG-Lyα cross-correlation

1D cross correlation, $\langle T(s) \rangle$

In Fig. 4.5, we present the latest result for the LBG-Lyα cross-correlation from the VLRS (asterisks) and the x-shooter (green diamonds). This covers a broad range of scales, measuring out to a separation of $s = 20 \ \ h^{-1}$Mpc. We see an overall continuous decrease in Lyα transmission down to the minimum scale probed of $s = 0.25\ h^{-1}$Mpc (although this smallest bin contains only a single galaxy).

We also show the LBG-Lyα transmissivity correlation function for the publicly available Keck data (pink diamonds); the results from A03 (triangles), A05 (squares) and for the combined VLRS+Keck+X-Shooter result (filled circles). At distances

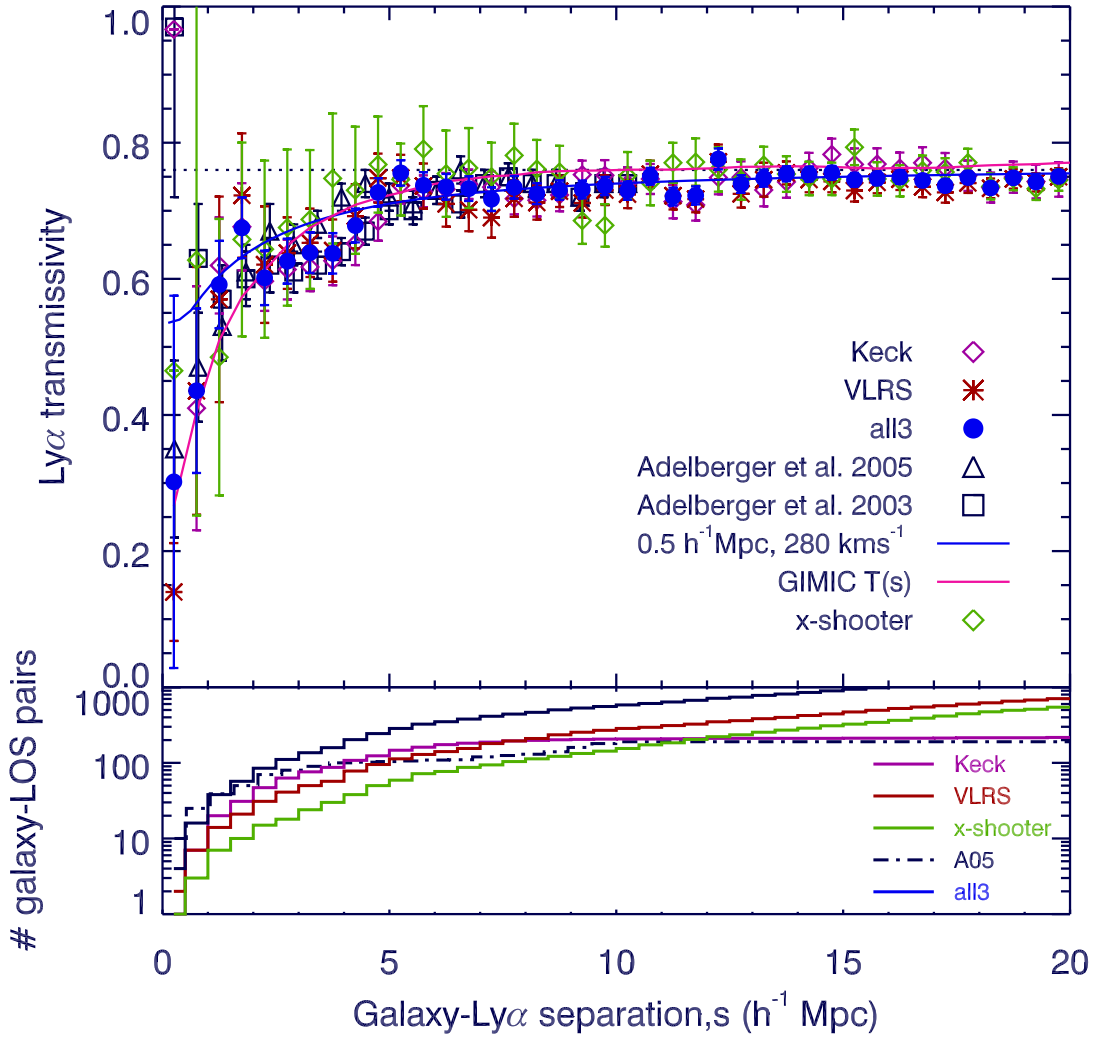

Figure 4.5: The mean Lyα-Galaxy transmissivity as a function of distance from an average $z \approx 3$ galaxy. Blue filled circles show VLRS+Keck+X-Shooter result. Brown asterisks, pink diamonds and green diamonds show results from VLRS, Keck and X-Shooter respectively. A03 and A05 are also represented by squares and triangles. The pink solid line shows the GIMIC redshift-space result. In addition, a power law fit to the data is shown, which is given by $s_0 = 0.3\ h^{-1}$Mpc and $\gamma = 1.0$, convolved with velocity errors of 280 kms^{-1}(solid blue line). The bottom panel shows the number of LBGs contributing to each bin in each sample.

greater than 3 h^{-1}Mpc, we find good agreement with both A03 and A05. We note in passing that our own reductions of the Keck sample HIRES data gives results consistent with A03 Lyα-LBG results. At separations below 3 h^{-1} Mpc, the combined sample seems to have the same trend as A05, with no evidence for a turn-up at $s < 1$ h^{-1}Mpc, a feature that was thought to be evidence for feedback. With the larger sample of LBGs close to QSO sightlines compared to Crighton et al. (2011), we have now strengthened the evidence against feedback strongly decreasing Lyα absorption on $s \lesssim 1$ h^{-1}Mpc scales around galaxies.

2-D cross correlation, $\xi(\sigma, \pi)$

We now use the latest VLRS data sample of $\approx 2,000$ LBGs alongside the Keck-based LBG-Lyα dataset to measure the 2-D LBG-Lyα cross-correlation, $\xi(\sigma, \pi)$. By combining these two surveys, we can compare the correlation functions in a wider range of separations than would otherwise be possible (the VLRS giving $2-3\times$ the coverage in the σ scale than the Keck data). The LBG-Lyα $\xi(\sigma, \pi)$ from Keck+VLRS sample is presented in Fig. 4.6.

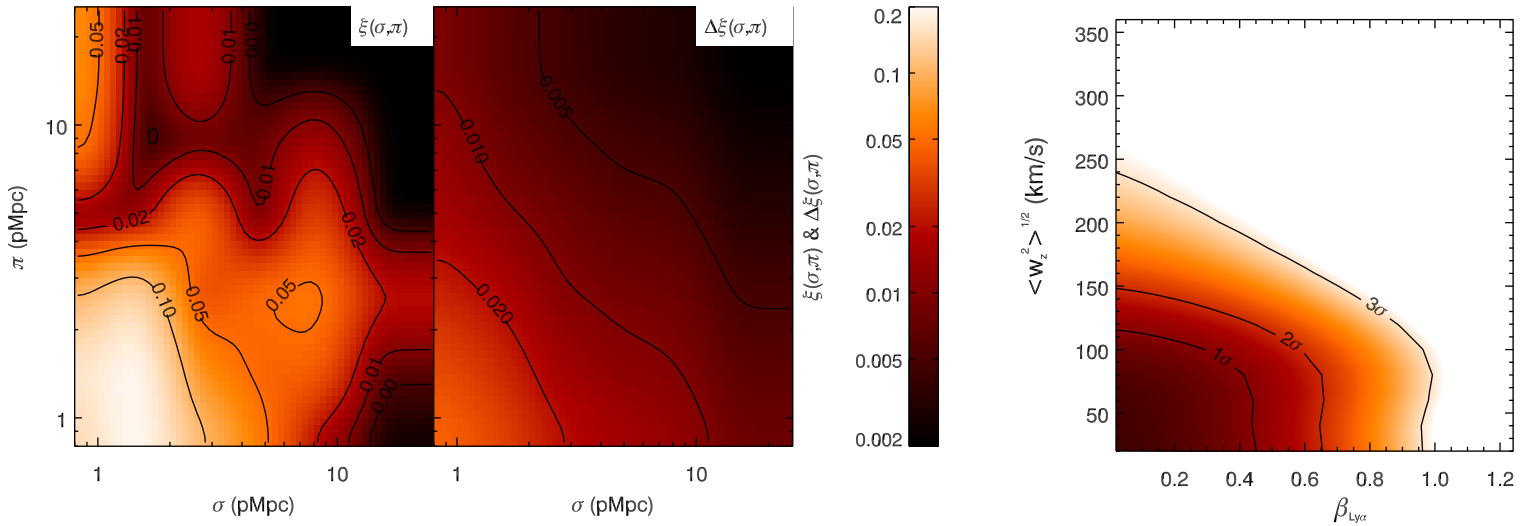

Figure 4.6: The left hand panels show the Lyα-LBG $\xi(\sigma, \pi)$ and jack-knife errors on $\xi(\sigma, \pi)$ for the combined Keck+VLRS data. The right hand panel shows the result of fitting the $\xi(\sigma, \pi)$ model to the data, with best fit parameters given by $\beta_{Ly\alpha} = 0.00^{+0.45}_{-0.00}$ and $\sqrt{\langle w_z^2 \rangle} = 0^{+115}_{-0}$ kms^{-1}. This result is based on a real-space power-law relation given by $r_0 = 0.3\ h^{-1}$Mpc and $\gamma = 1$, with $\beta_{gal} = 0.38$.

There is little sign of any 'finger-of-god' effect at small σ scales ($\sigma \lesssim 2-3\ h^{-1}$Mpc), i.e. in the form of the clustering power being extended in the π direction. We fit the $\xi(\sigma,\pi)$ measurement using the $\sqrt{\langle w_z^2\rangle} - \beta$ model described above and show the resulting $\Delta\chi^2$ contours in the right hand panel of Fig. 4.6. The fit uses a power-law form for the cross-correlation function, with a clustering length of $s_0 = 0.3\ \ h^{-1}$Mpc and a slope of $\gamma = 1$. Additionally, a value for β_{gal} is required, which we take from Bielby et al. (2013) to be $\beta_{gal} = 0.38$. The γ and s_0 from fitting LBG-Lyα $\xi(s)$ using $\xi(s) = (s/s_0)^{-\gamma}$. As shown in Fig. 4.5, this model reproduces the observed LBG-Lyα $\xi(s)$ results well. We shall therefore take our starting model for the cross-correlation $\xi(r)$ by scaling the above $\xi(s)$ downwards by the predicted Kaiser boost of 1.5. We checked that this factor gave the best reduced χ^2 since we are aiming to fit the shape rather than the amplitude of $\xi(\sigma,\pi)$ here. The best fit to $\xi(\sigma,\pi)$ is $\beta_{Ly\alpha} = 0.00^{+0.45}_{-0.00}$, $\sqrt{\langle w_z^2\rangle} = 0^{+115}_{-0}$ kms^{-1}, and reduced $\chi^2 = 0.65$.

We shall return to these Keck+VLRS results to compare with the results from the GIMIC simulations described below. For the moment, we note that the theoretically predicted value of the infall parameter is $\beta_{Ly\alpha} = 1.3$ and the predicted velocity dispersion, including the effects of LBG velocity error and intrinsic dispersions for gas and galaxies, is $\sqrt{\langle w_z^2\rangle} = \sqrt{297^2 + 120^2} = 320$ kms^{-1}. The observed value of $\beta_{Ly\alpha} = 0.0$ is more than 3σ lower than the predicted value (see right hand panel of Fig. 4.6).

4.2.2 Lyα-Galaxy $\xi(s)$ from simulations

As with the data, we compute the galaxy-Lyα cross correlation using the methods described above. We note however that the renormalisation to $z = 3$ is here redundant given that the simulated gas and galaxies are all at the same epoch already.

Coherent motion of gas and galaxies

In Fig. 4.7 (a) we show the Lyα-galaxy $\xi(s)$ for the Lyα in z-space and $M_\star \geq 10^9\ h^{-1}M_\odot$ galaxies in z-space and real-space. Fig. 4.7 (b) shows the same plot but now for the sample of $M_\star \geq 10^8\ h^{-1}M_\odot$ galaxies. Since the high mass sample has poorer statistics here we mainly focus on the $M_\star \geq 10^8\ h^{-1}M_\odot$ sample in Fig. 4.7

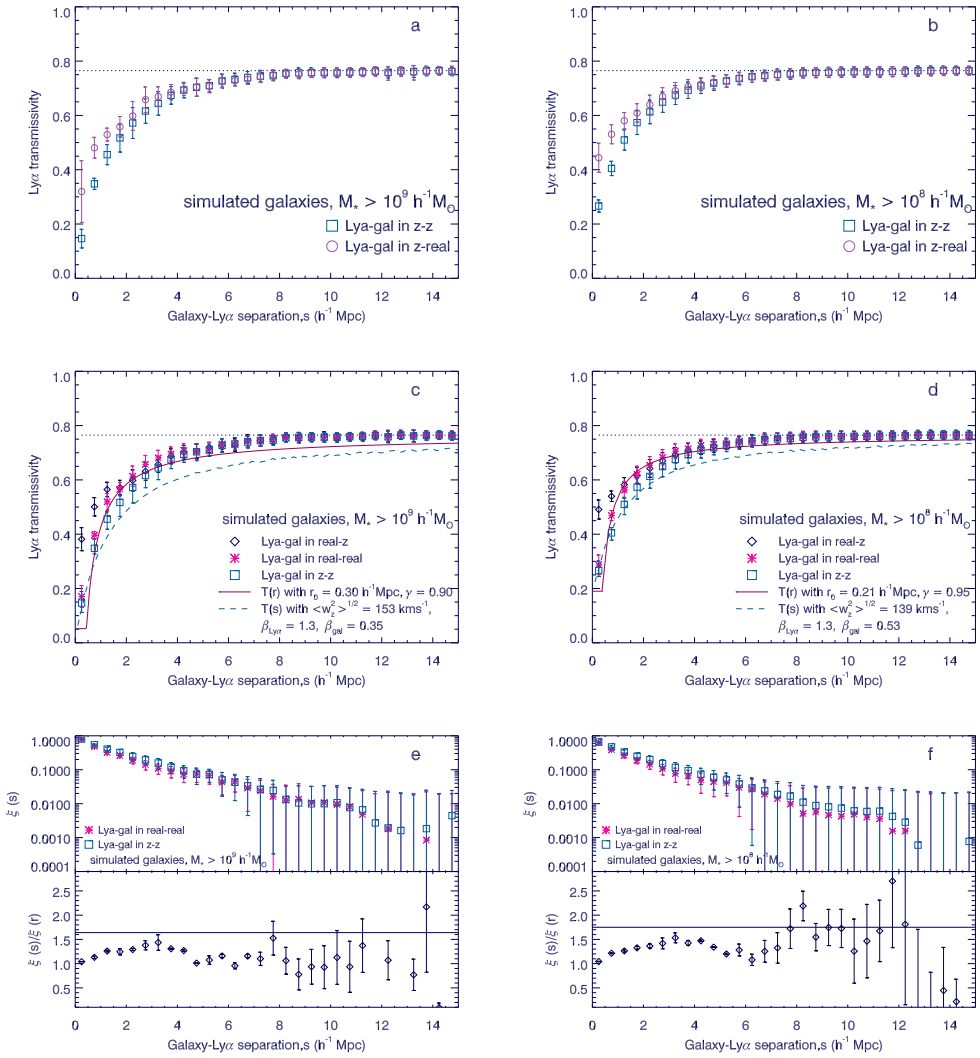

Figure 4.7: Lyα-galaxy transmissivity, $\langle T(s) \rangle$ from GIMIC $M_\star \geq 10^9\ h^{-1}\mathrm{M}_\odot$ and $M_\star \geq 10^8\ h^{-1}\mathrm{M}_\odot$ galaxy samples. The error bars are calculated by using jack-knife method. (a) $M_\star \geq 10^9\ h^{-1}\mathrm{M}_\odot$ galaxy sample with $z-$space galaxies + $z-$space gas (light blue squares) and real-space galaxies + $z-$space gas (purple circles). (b) Same as (a) for $M_\star \geq 10^8\ h^{-1}\mathrm{M}_\odot$ galaxies. (c) Lyα-galaxy transmissivity for $M_\star \geq 10^9\ h^{-1}\mathrm{M}_\odot$ sample with Lyα-galaxies in real-z (blue diamonds), real-real (pink asterisks) and in redshift-space (light blue squares). A fit to the real-real $\xi(r)$ with $r_0 = 0.30\ \ h^{-1}$Mpc, $\gamma = 0.90$ is shown (red line). The expected Lyα-galaxy $\xi(s)$ in redshift-space space with $\beta_{Ly\alpha} = 1.3$, $\beta_{gal} = 0.35$ and $\sqrt{\langle w_z^2 \rangle} = \sqrt{95^2 + 120^2}$ kms^{-1} is also shown (light blue dashed line). Note that these velocities are calculated from pairs within $s < 1\ h^{-1}$Mpc. (d) Same as (c) for the $M_\star \geq 10^8\ h^{-1}\mathrm{M}_\odot$ galaxy sample. Here the $\xi(r)$ fit assumes $r_0 = 0.21\ \ h^{-1}$Mpc, $\gamma = 0.95$ and the $\xi(s)$ model assumes $\beta_{Ly\alpha} = 1.3$, $\beta_{gal} = 0.53$ and $\sqrt{\langle w_z^2 \rangle} = \sqrt{71^2 + 120^2}$ kms^{-1}. (e) $\xi(s)$ and $\xi(s)/\xi(r)$ for the high mass galaxy sample. The blue line in the lower panel represents the linear theory prediction with $\beta_{gal} = 0.35$, $\beta_{Ly\alpha} = 1.3$ giving $\xi(s)/\xi(r) = 1.64$. (f) Same as (e) for the $M_\star \geq 10^8\ h^{-1}\mathrm{M}_\odot$ galaxy sample with $\beta_{gal} = 0.53$, $\beta_{Ly\alpha} = 1.3$ giving $\xi(s)/\xi(r) = 1.75$.

(b) but we believe that the same interpretations apply to both samples. The first thing to note is that the anti-correlation is increased as we go from $r-z$ to redshift-space. This is surprising if we assume that random Gaussian motions dominate galaxy peculiar motions. In this model we expect more smoothing in z-space than in real-space and that is not observed.

Fig. 4.7 (c and d) shows the Galaxy-Lyα transmissivity correlation function from the Lyα in real- and redshift-space with (c) $M_\star \geq 10^9\ h^{-1}\mathrm{M}_\odot$ and (d) $M_\star \geq 10^8\ h^{-1}\mathrm{M}_\odot$ galaxies. Focussing on the low mass sample of $M_\star \geq 10^8\ h^{-1}\mathrm{M}_\odot$ galaxies, the open diamonds show the results from galaxies in redshift-space and the Lyα in real-space while the pink asterisks illustrate the results from galaxies and the Lyα both in real-space. At separations $s < 5\ h^{-1}$ Mpc, we see that Galaxy-Lyα transmissivity correlation functions in redshift-space (light blue squares) and real-space pink asterisks both lie lower than the Lyα-galaxy $r-z$ version (open diamonds). This behaviour is again different from the expected result for random Gaussian motions when the $r-z$ result might be expected to lie between real-space and redshift-space. This and the previous anomaly can be explained by coherent motion when the galaxies and the gas move together and make the correlation from the same space (redshift-space or real-space space) stronger than the correlation from $r-z$ space combinations. Although the positions of the clouds and the galaxies move, they move coherently so that their relative positions in real-space and redshift-space remain the same, similar to the effect seen in Fig. 3.2. This would leave the cross-correlation function the same when redshift or real-space was used consistently but undergo smoothing when gas was used in redshift-space and galaxies in redshift-space or vice versa. The $M_\star \geq 10^9\ h^{-1}\mathrm{M}_\odot$ results are shown in the left-hand panels and show a consistent picture in which coherent motion forms the dominant velocity field.

Ignoring the real-redshift-space combinations, we see that both the real-real and redshift-space results show the same trends. At a distance $s > 5\ h^{-1}$Mpc, the measured $\langle f/f_{con}\rangle$ increases to reach the mean value. As separations decrease below $5\ h^{-1}$Mpc, the transmissivity decreases and hence the HI density increases as we approach the galaxy.

Dynamical Infall in $\xi(s)$

As discussed earlier, we note that the mean transmissivities for the simulated real and redshift-space Lyα forests are somewhat different, with the redshift-space forest having a mean of $\bar{T} = 0.72$ and the real-space forest a mean of $\bar{T} = 0.69$. This is surmised to be the result of Lyα absorption lines overlapping increasingly once RSD are applied and potentially indicative of infall effects. We shall now discuss dynamical infall of the gas further, by looking for the effect of gas infall on the cross-correlation function.

To better visualise any distortions in the cross-correlation, we calculate the function $\xi = 1 - T/\bar{T}$, using a value of $\bar{T} = 0.69$ in the real-space case and $\bar{T} = 0.72$ in the redshift-space case. The results for $\xi(s)$ are shown in panels (e) and (f) of Fig. 4.7.

We fit the real-space cross-correlation function $\xi(r)$ by using $\xi(r) = \left(\frac{r}{r_0}\right)^{-\gamma}$ with $r_0 = 0.30\ h^{-1}$ Mpc, $\gamma = 0.90$ for $M_\star \geq 10^9\ h^{-1}\mathrm{M}_\odot$ galaxies and $r_0 = 0.21\ h^{-1}$ Mpc, $\gamma = 0.95$ for $M_\star \geq 10^8\ h^{-1}\mathrm{M}_\odot$ galaxies. Taking into account a Kaiser boost of $\xi(s)/\xi(r) \approx 1.5$, this r_0 for the high mass sample is reasonably consistent with the s_0 =0.3 h^{-1} Mpc fitted to the GIMIC cross-correlation $\xi(s)$ in Fig. 4.7 (see also Crighton et al. 2011). Thus the pink lines in Fig. 4.7 (c and d) represent $T(r) = \bar{T} - (\frac{r}{r_0})^{-\gamma}$. $\bar{T}$ is the mean Lyα transmissivity at $z \approx 3$ (A05).

We then apply the linear theory redshift-space distortion model of Kaiser (1987), in the form for cross-correlation Eq. 4.2.6 discussed by Mountrichas & Shanks (2007). As indicated earlier we shall assume the value $\beta_{Ly\alpha} = 1.3$ to represent the $1.0 < \beta < 1.6$ range suggested from the simulations of McDonald 2003. The redshift-space distortion analysis is then implemented following da Ângela et al. (2008). Focussing again on the $M_\star \geq 10^8\ h^{-1}\mathrm{M}_\odot$ galaxies sample, we assume the appropriate values above of r_0 and γ, with dynamical infall values $\beta_{gal} = 0.53$ and $\beta_{Ly\alpha} = 1.3$, predicting $\xi(s) = 1.75 \times \xi(r)$, plus velocity dispersion $\sqrt{(172/\sqrt{2})^2 + 120^2} = 171$ kms^{-1}. This provides a poor fit even when we reduce the galaxy velocity dispersion from 122 kms^{-1} to 71 kms^{-1}, previously suggested to be the 'within-clump' value (see Fig. 4.7 (d, f)). It is the $\beta_{Ly\alpha} = 1.3$ value that is proving too high here, resulting in this model tending to over-predict the Lyα-galaxy cross-correlation function. The $M_\star \geq$

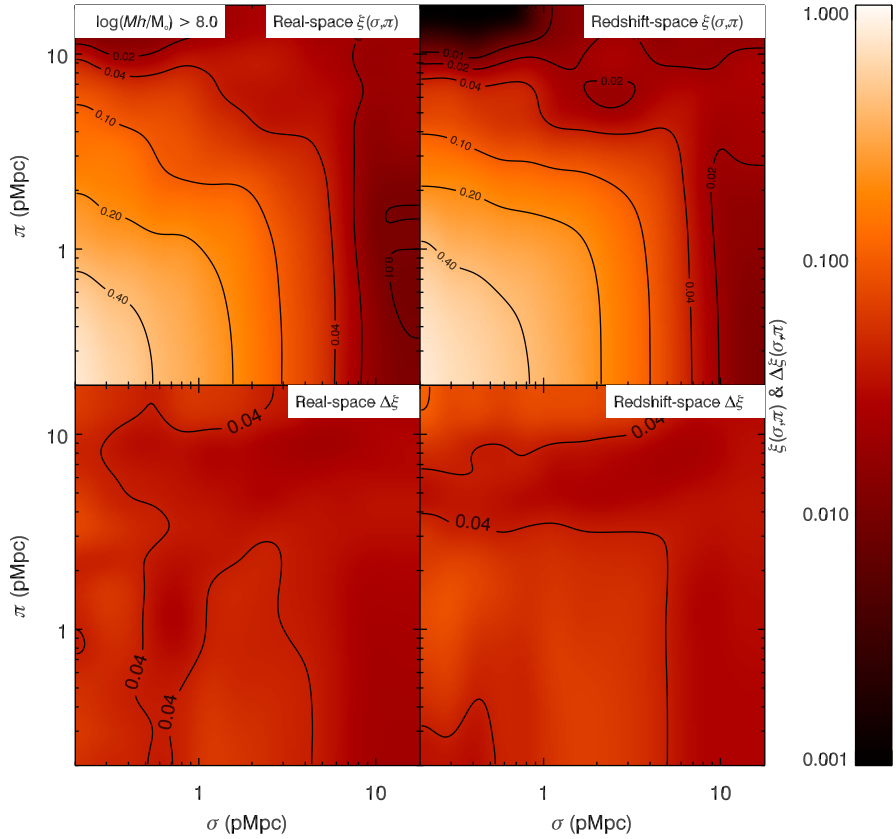

Figure 4.8: The top two panels shows the GIMIC Lyα-galaxy $\xi(\sigma, \pi)$ based on the $M_\star \geq 10^8\ h^{-1}\mathrm{M}_\odot$ galaxy sample in real-space (top-left panel) and in redshift-space (top-right panel). The errors were calculated by using the jack-knife method and are shown in the lower panels.

$10^8\ h^{-1}\mathrm{M}_\odot$ galaxy sample rather indicates in (f) that $\xi(s) \approx 1.4 \times \xi(r)$ implying $\beta_{Ly\alpha} \approx 0.7$. Similar results are found for the high mass sample of $M_\star \geq 10^9\ h^{-1}\mathrm{M}_\odot$ galaxies (see Fig. 4.7 (c,e)) where fits in (e) indicate $\beta_{Ly\alpha} \approx 0.15$.

Dynamical Infall in $\xi(\sigma, \pi)$

The GIMIC Lyα-LBG $\xi(\sigma, \pi)$ results are presented in Fig. 4.8 for the $M_\star \geq 10^8\ h^{-1}\mathrm{M}_\odot$ galaxy sample and Fig. 4.9 for the $M_\star \geq 10^9\ h^{-1}\mathrm{M}_\odot$ sample. In each case the top left panel shows $\xi(\sigma, \pi)$ in real-space and the top right panel in redshift-space, with the lower panels showing the associated error profiles on the same scale. Visually, the changes between real and redshift-space are more ambiguous than for the galaxy auto-correlation results. We again fit the RSD model to the results using the real-space results as a baseline by which to judge the redshift-space results.

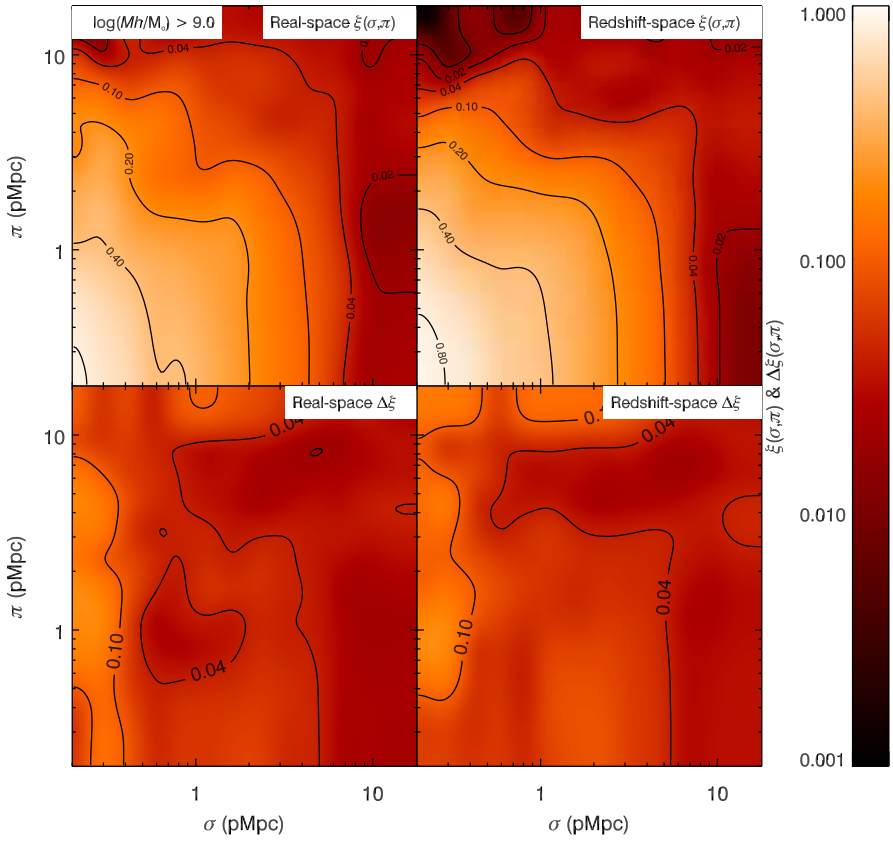

Figure 4.9: The top two panels shows the GIMIC Lyα-galaxy $\xi(\sigma, \pi)$ based on the $M_\star \geq 10^9\ h^{-1}\mathrm{M}_\odot$ galaxy sample in real-space (top-left panel) and in redshift-space (top-right panel). The errors were calculated using the jack-knife method and are shown in the lower panels.

The χ^2 contours for the model fits are shown in Fig. 4.10, where the top panels show the results for the $M_\star \geq 10^9\ h^{-1}\mathrm{M}_\odot$ galaxy sample and the lower panels show the results for the $M_\star \geq 10^8\ h^{-1}\mathrm{M}_\odot$ sample. In both cases the left hand panels show the result in real-space and the right hand panel the result in redshift-space. For the models we have assumed the same values of r_0, γ and (in the redshift-space case) β_{gal} as given above. As in the 1D clustering results, we see little change in the shape of $\xi(\sigma,\pi)$ between the real-space and redshift-space results, suggesting that the effect of the peculiar motions, apart from coherent bulk motion, is again small. Restricting the fitting range to $\sigma,\pi < 12\ \ h^{-1}$Mpc we find a fit to the real-space $\xi(\sigma,\pi)$ giving $\beta_{Ly\alpha} = 0.0^{+0.1}_{-0.0}$ and $\sqrt{\langle w_z^2\rangle} = 0^{+55}_{-0}$ kms^{-1}, with reduced $\chi^2 = 1.2$. Fitting to the redshift-space correlation function gives $\beta_{Ly\alpha} = 0.15 \pm 0.15$ and $\sqrt{\langle w_z^2\rangle} = 40^{+25}_{-40}$ kms^{-1}, with reduced $\chi^2 = 1.8$.

Cross-correlating the Lyα profiles with the $M_\star \geq 10^8\ h^{-1}\mathrm{M}_\odot$ galaxy sample, the best fit for real-space gives $\beta_{Ly\alpha} = 0.55 \pm 0.25$, $\sqrt{\langle w_z^2\rangle} = 50 \pm 35$ kms^{-1}, and reduced $\chi^2 = 0.6$, assuming $r_0 = 0.21\ h^{-1}$Mpc and $\gamma = 0.95$. The best fit for redshift-space gives $\beta_{Ly\alpha} = 0.70^{+0.25}_{-0.30}$, $\sqrt{\langle w_z^2\rangle} = 60^{+25}_{-30}$ kms^{-1}, and reduced $\chi^2 = 0.8$.

For the $M_\star \geq 10^8\ h^{-1}\mathrm{M}_\odot$ galaxies, the values that we would expect are $\beta = \sqrt{\langle w_z^2\rangle} = 0$ for the real-space case and $\beta_{Ly\alpha} = 1.3$ and $\sqrt{\langle w_z^2\rangle} \approx \sqrt{120^2 + 71^2} = 139$ kms^{-1} for the redshift-space case. From the $\Delta\chi^2$ contours in Fig. 4.10 we see that in the redshift-space cases such values are quite clearly rejected by the simulated data, the more so when it is realised that the best fit parameters for both mass ranges are the same in redshift-space and in real-space. We conclude again that the main result is the lack of difference between the real and redshift-space fits for both high and low mass galaxies. The effect of peculiar motions on the simulated redshift-space 2-D correlation function is smaller than expected both for the gas infall parameter and for the gas-galaxy velocity dispersion. The explanation may be due to the gas motion being coherent with the galaxies and so $\sqrt{\langle w_z^2\rangle} \approx 120$ kms^{-1} may need reducing to $\sqrt{\langle w_z^2\rangle} \approx 71$ kms^{-1} as for the galaxies implying $\sqrt{\langle w_z^2\rangle} \approx 100$ kms^{-1} which is less easy to reject at least in the case of the low mass galaxy results in Fig. 4.10.

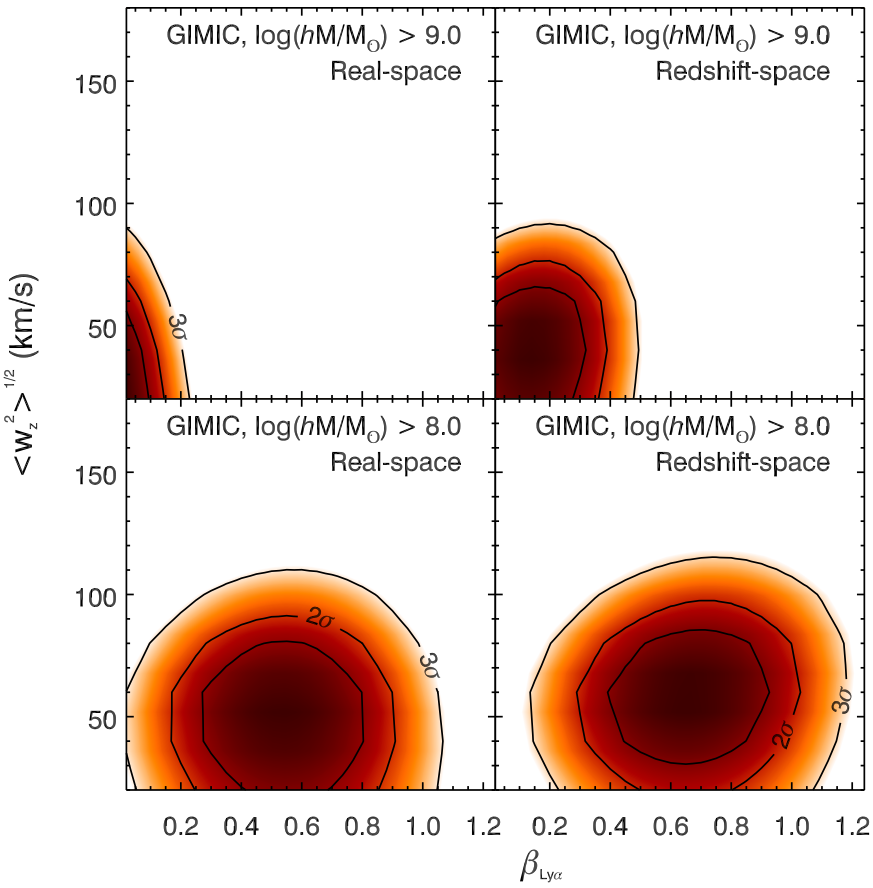

Figure 4.10: The $\Delta\chi^2$ contours for the RSD model fitting to the 2D galaxy-Lyα cross-correlation are shown. The top panels show the fitting results for the $M_\star \geq 10^9\ h^{-1}\mathrm{M}_\odot$ galaxy sample in real-space (left) and redshift-space (right). In real-space, we find best fitting parameters of $\beta_{Ly\alpha} = 0.0^{+0.1}_{-0.0}$ and $\sqrt{\langle w_z^2\rangle} = 0^{+55}_{-0}$ kms^{-1}. For the redshift-space $\xi(\sigma,\pi)$ the best fitting parameters are $\beta_{Ly\alpha} = 0.15 \pm 0.15$ and $\sqrt{\langle w_z^2\rangle} = 40^{+25}_{-40}$ kms^{-1}. Both fits are based on an underlying power-law relation for $\xi(\sigma,\pi)$ given by $r_0 = 0.3\ \ h^{-1}$Mpc and $\gamma = 0.9$. The lower panels show the results for the $M_\star \geq 10^8\ h^{-1}\mathrm{M}_\odot$ GIMIC sample. The best fit for the real-space sample (left panel) is $\beta_{Ly\alpha} = 0.55 \pm 0.25$, $\sqrt{\langle w_z^2\rangle} = 50 \pm 35$ kms^{-1}. For the redshift-space $\xi(\sigma,\pi)$ we find $\beta_{Ly\alpha} = 0.70^{+0.25}_{-0.30}$, $\sqrt{\langle w_z^2\rangle} = 60^{+25}_{-30}$ kms^{-1}. Both of the $M_\star \geq 10^8\ h^{-1}\mathrm{M}_\odot$ fits are based on a power-law $\xi(\sigma,\pi)$ given by $r_0 = 0.21\ h^{-1}$Mpc and $\gamma = 0.95$.

Simulation and observation compared

We next compare the simulated results for Lyα-galaxy $\xi(s)$ with the Keck+VLRS data as shown in Fig. 4.5. The Keck + VLRS result shown is the including A03, A05 and VLRS rather than VLRS plus the 6 re-reduced Keck QSOs because the larger number of QSOs means that the errors are smaller at $s < 1$ h^{-1}Mpc. The pink line shows the GIMIC redshift-space space result. We have assumed the same model as Crighton et al to fit the GIMIC result ie $\langle T(s) \rangle = \bar{T} - (s/s_0)^{-1}$ with $s_0 = 0.3$ h^{-1}Mpc with a small-scale cutoff with $T = 0.29$ for $s < 0.5$ h^{-1} Mpc. Using the GIMIC simulations we have analysed the mean velocity dispersion of LBG-like galaxies and find a value of ≈ 100kms^{-1}. The blue solid line is the expected Lyα-Galaxy $\xi(s)$ when convolving the empirically determined velocity error of $\sqrt{(420^2 - 2 \times 100^2)/2} = 280$ kms^{-1} (Eq. 4.1.5) into this. We only applied the velocity error to the model because the velocity dispersion was already included to the result in $z-space$ from GIMIC. Our bin size is 0.5 h^{-1}Mpc. The GIMIC model convolved with the empirical velocity dispersion lies above the LBG-Lyα data but only at the $1-2\sigma$ level and we regard it as being in excellent agreement with the combined LBG-Lyα data.

We finally compare the simulated results for Lyα-galaxy $\xi(\sigma, \pi)$ now with the 6 Keck QSOs + VLRS data as shown in Fig. 4.6. We have seen that the observed best fit parameters for the Keck + VLRS data are $\beta_{Ly\alpha} = 0.0$, $\sqrt{\langle w_z^2 \rangle} = 0$ kms^{-1} and we noted that the measured infall parameter of $\beta_{Ly\alpha} = 0.0$ was $\approx 3\sigma$ lower than the predicted value of $\beta_{Ly\alpha} = 1.3$. The best fit parameters for the simulated $M_\star \geq 10^8$ h^{-1}M$_\odot$ galaxy sample are $\beta_{Ly\alpha} = 0.70$, $\sqrt{\langle w_z^2 \rangle} = 60$ kms^{-1}. This simulated $\beta_{Ly\alpha}$ value therefore lies between the expected value of $\beta_{Ly\alpha} = 1.3$ and the observed Keck+VLRS value of $\beta_{Ly\alpha} = 0.0$, an intermediate result where the $\Delta\chi^2$ contours shown in panel b of Fig. 4.6 allow consistency with both these values. We conclude the Keck+VLRS data also prefers low values of $\beta_{Ly\alpha}$ like the simulation. We also note that neither the minimum value of $\sqrt{\langle w_z^2 \rangle} = 297$ kms^{-1} from LBG velocity error nor the $\sqrt{\langle w_z^2 \rangle} = 320$ kms^{-1} value from including the full simulated $\sqrt{\langle w_z^2 \rangle} = 120$ kms^{-1} is consistent with the data at the few sigma level. We conclude that while the Keck+VLRS $\beta_{Ly\alpha}$ and $\sqrt{\langle w_z^2 \rangle}$ estimates are low compared to initial expectation

from theory, they may still be consistent with the similarly low values of these parameters estimated from $\xi(s)$ and $\xi(\sigma, \pi)$ in the simulations.

4.3 Lyα auto-correlation

We measure the Lyα auto-correlation along and across QSO lines-of-sight. By doing this, we can measure the velocity dispersion of HI gas to see if this has a significant effect on the Lyα-LBG cross-correlation function. Following Crighton et al. (2011), for each pixel in a QSO line-of-sight, we calculate

$$\delta = \frac{T}{\bar{T}} - 1, \tag{4.3.10}$$

where T and $\bar{T}$ are the measured and the mean normalised flux. We used this to calculate the auto-correlation

$$\xi(\Delta r) = \langle \delta(r)\delta(r + \Delta r) \rangle, \tag{4.3.11}$$

We sum all pixels with the separations Δr, both parallel and perpendicular to the line of sight using all the QSO data listed in Tables 2.4, 2.5, 2.6 and again for the simulations. For the observations, there are only 3 pairs of QSOs that can provide transverse separation measurements. Two of the pairs are separated by $\sim 30\ h^{-1}$Mpc and the third pair are separated by $\sim 20\ h^{-1}$Mpc. Therefore, the observational results presented here will only incorporate pixels along the line of sight of a given QSO spectrum for separations of $\lesssim 20\ h^{-1}$Mpc.

Fig. 4.11 (a) shows the auto-correlation of Lyα pixels along the line-of-sight from the observational data. Keck, VLRS and combined samples are presented by pink diamonds, light blue asterisks and blue circles respectively. Error bars were estimated by using jack-knife method. We first compare these to the result from Crighton et al. 2011 (triangles) who measured the auto-correlation using 7 high resolution QSOs (resolution FWHM ~ 7 kms^{-1}). The agreement appears to be excellent.They all show similar results at small scales. We also compared our results with the recent BOSS result of Slosar et al. 2011 (squares) but it is mostly seen at

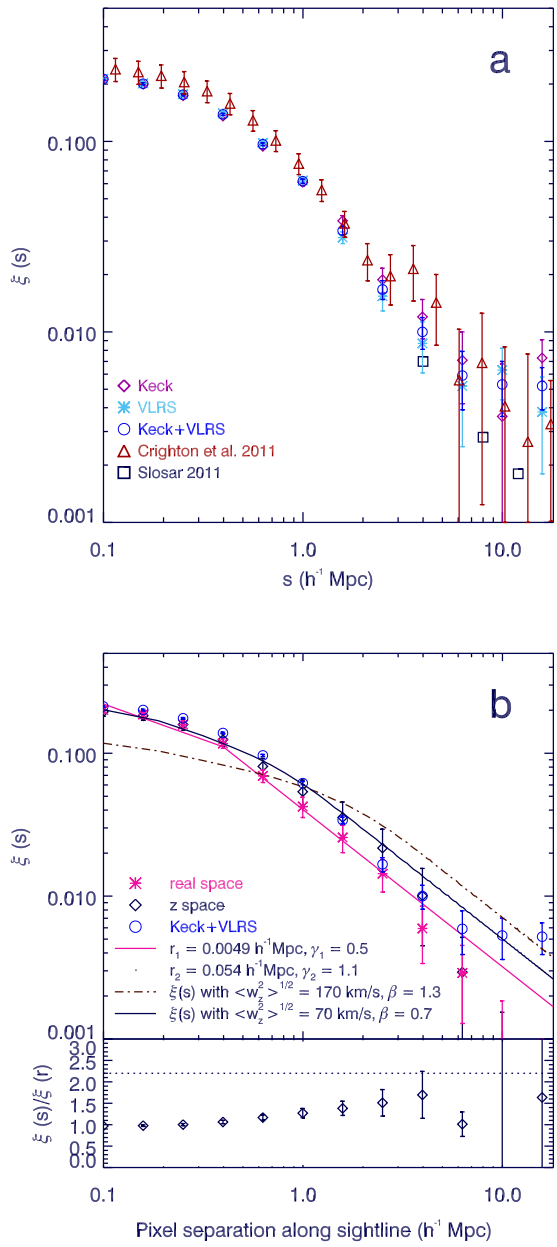

Figure 4.11: (a) The auto-correlation of Lyα pixels along the line-of-sight. Keck, VLRS and combined samples are shown by pink diamonds, light blue asterisks and blue circles respectively. The measurement of Crighton et al. (2011) is also shown (triangles). The recent BOSS result of Slosar et al. (2011) is also shown (squares). (b)-top panel : The auto-correlation functions of GIMIC Lyα pixels at $z = 3.06$ in the 0σ simulation. Real-space (pink asterisks) and redshift-space (blue diamonds) results are shown. Errors are calculated via the jack-knife method. A double power-law fit to the real-space $\xi(r)$ with $r_{01} = 0.0049$, $\gamma_1 = 0.5$, $r_{02} = 0.054$, $\gamma_2 = 1.1$ is also shown (pink line). The brown dot-dashed line is the expected result for the Lyα $\xi(s)$ in redshift-space if we convolve in the velocity dispersion $\sqrt{\langle w_z^2 \rangle} = 170$ kms^{-1} and $\beta_{Ly\alpha} = 1.3$ to the redshift-space distortion model. The blue solid line is a predicted $\xi(s)$ with $\sqrt{\langle w_z^2 \rangle} = 70$ kms^{-1}, $\beta_{Ly\alpha} = 0.7$ which appears to fit the simulated data. Bottom panel : GIMIC $\xi(s)/\xi(r)$ with jack-knife error bars. The dashed line corresponds to $\xi(s)/\xi(r) = 2.2$ as predicted from linear theory with $\beta_{Ly\alpha} = 1.3$.

large scales as they are more interested in large-scale correlations.

The auto-correlation of simulated Lyα pixels are presented in Fig. 4.11 (b). The real and redshift-space Lyα auto-correlations are shown as the asterisks and diamonds, respectively. The real-space gas simulations are derived from the redshift-space simulations by switching off the effect of peculiar velocities in the output data. We then compare these to the result from Keck+VLRS. They show a good agreement.

Focussing on the simulation, we see again that the redshift and real-space correlation functions are quite similar in amplitude and form. At small scales, convolving the real-space correlation function with a Gaussian of width $120 \times \sqrt{2} = 170$ kms^{-1} representing the simulation gas peculiar velocity (see Fig. 3.3) is seen to overestimate the small-scale turnover in the redshift-space correlation function. This is better fitted by a velocity dispersion of width 30 kms^{-1} but this assumes $\beta_{Ly\alpha} = 0$ which is unphysical. Now at larger scales we see that the observed ratio of $\xi_s/\xi_r \approx 1.5$ is smaller than that expected from the linear theory in Eq. 4.1.3. For the gas the value of the bias is $b \approx 0.3$ which arises from comparing the mass linear correlation function to the simulated real-space correlation function in Fig. 4.11 in the range $1 < r < 6$ h^{-1}Mpc. This bias corresponds to $\beta_{Ly\alpha} \approx 3.3$ which implies $\xi(s)/\xi(r) \approx 5.4$. But again as noted by McDonald (2003), $\beta_{Ly\alpha}$ has no simple relation to density bias as for galaxies. $\beta_{Ly\alpha}$ has to be estimated from simulations and the simulations of McDonald et al implied a range $\beta_{Ly\alpha} = 1 - 1.6$. If we therefore take $\beta_{Ly\alpha} = 1.3$, then this predicts $\xi(s)/\xi(r) = 2.2$ from Eq. 4.1.3 whereas the simulated value in Fig. 4.11 is more like $\xi(s)/\xi(r) = 1.5$ which corresponds to $\beta \approx 0.7$. The reason for this discrepancy is unclear. With $\beta_{Ly\alpha} = 0.7$, the best fit velocity dispersion is $\sqrt{\langle w_z^2 \rangle} = 70$ kms^{-1}. Models where we fixed $\beta_{Ly\alpha} = 1.3$ and took $\sqrt{\langle w_z^2 \rangle} = 170$ kms^{-1} as expected from Fig. 3.6 were also strongly rejected. With $\beta_{Ly\alpha} = 1.3$, again a best fit value of $\sqrt{\langle w_z^2 \rangle} = 70$ kms^{-1} was found although the model was still rejected in a chi-square test.

Whatever value of $\beta_{Ly\alpha}$ is chosen it appears that the fitted value of the velocity dispersion is much lower than measured in the simulation. However, as shown by Crighton et al. (2011), the intrinsic width of the Lyα lines convolved with the

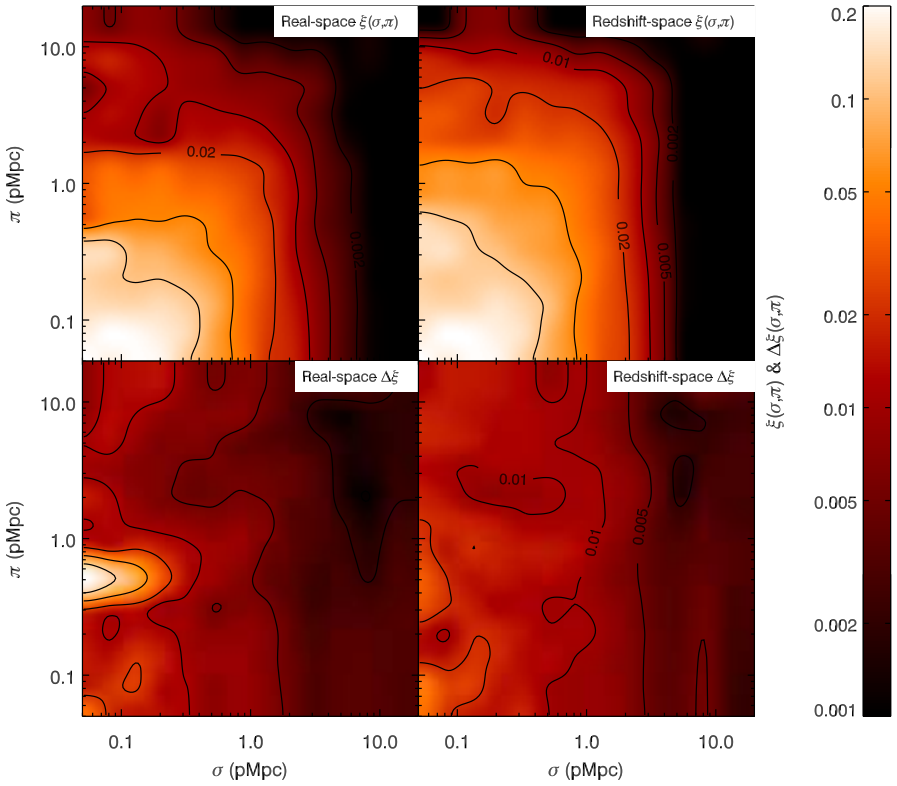

Figure 4.12: The GIMIC Lyα $\xi(\sigma, \pi)$ auto-correlation at $z = 3.06$ in real (top-left panel) and redshift-space (top-right panel). The lower panels show the corresponding jackknife error estimates on the $\xi(\sigma, \pi)$ results.

instrumental response of the spectrograph can induce artificial autocorrelations at scales 0.7 h^{-1}Mpc, so this effect may contribute to the poor fit of the peculiar velocity z-distortion model on small scales.

We note that the z-distortion model for the Ly-α auto- and cross-correlation assumes spherical symmetry as we move from real-space to redshift-space and the Lyα auto-correlation function involves summing along and across QSO lines of sight which may not be exactly spherically symmetric. However, we shall see that this explanation cannot apply to the Lyα $\xi(\sigma, \pi)$ which we calculate next and which gives consistent results.

For each pixel in the Lyα line-of-sight, we next calculate the Lyα $\xi(\sigma, \pi)$ by using,

$$\xi(\sigma, \pi) = \frac{\langle DT(\sigma, \pi) \rangle}{N(\sigma, \pi)}, \tag{4.3.12}$$

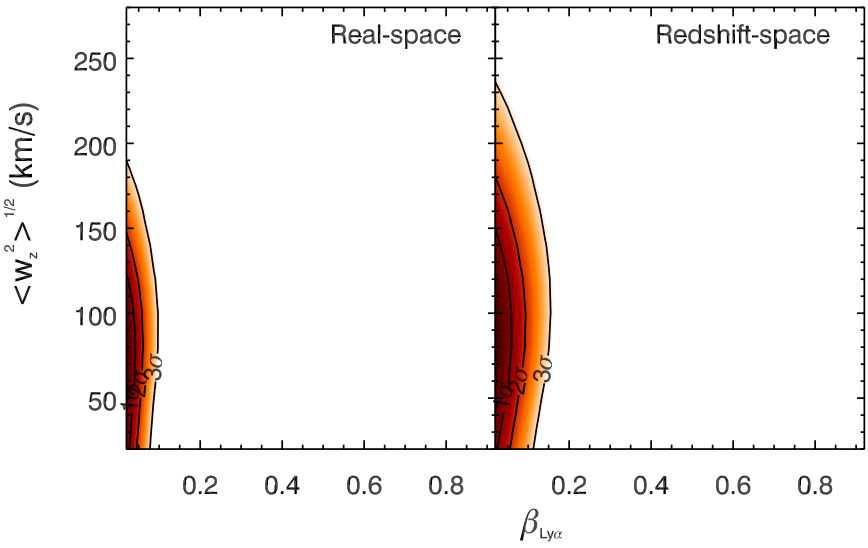

Figure 4.13: Restults for the model fits to the GIMIC 2D Lyα auto-correlation functions shown in Fig. 4.12. The left panel shows the $\Delta\chi^2$ contours for fit to the real-space $\xi(\sigma,\pi)$ with best fitting parameters of $\beta = 0.00^{+0.04}_{-0.00}$ and $\sqrt{\langle w_z^2\rangle} = 80^{+40}_{-60}$ kms^{-1} (with a reduced χ^2 of 1.1). The right panel shows the same for the redshift-space auto-correlation function. Here the best fit is $\beta = 0.00^{+0.06}_{-0.00}$, $\sqrt{\langle w_z^2\rangle} = 80^{+70}_{-60}$ kms^{-1} with reduced $\chi^2 = 2.4$. The fits are based on an underlying double power-law function given by $r_{01} = 0.0049\ \ h^{-1}$Mpc, $r_{02} = 0.054\ \ h^{-1}$Mpc, $\gamma_1 = 0.5$, $\gamma_2 = 1.1$ with a break point at 0.40 h^{-1}Mpc.

where $< DT(\sigma,\pi) >$ is the number of Lyα pairs weighted by the normalised transmissivity: T_z, for each separations. N(σ,π) is the number of Lyα pixels that contributed to each pair.

The Lyα $\xi(\sigma,\pi)$ results at $z = 3.06$ for the 0σ simulation are shown in Fig. 4.12, the top-left panel showing the result in real-space and the top-right panel showing the result in redshift-space, with the associated errors again shown in the lower panels. We see similar results for real-space and redshift-space. There does seem to be some evidence of smoothing due to Gaussian convolution, but we see no sign of flattening due to infall in Lyα auto-correlation.

Again we fit the RSD model to the GIMIC results and find $\sqrt{\langle w_z^2\rangle} = 80^{+40}_{-60}$ kms^{-1} and $\beta = 0.00^{+0.04}_{-0.00}$ for the real-space result. For redshift-space the best fitting parameters are the same with $\beta = 0.00^{+0.06}_{-0.00}$ and $\sqrt{\langle w_z^2\rangle} = 80^{+70}_{-60}$ kms^{-1}. The predicted value of $\beta_{Ly\alpha} = 1.3$ is as strongly rejected for redshift-space as for real-space with $\chi^2_{red} = 11$). We again conclude that the effects of infall in the gas in the GIMIC

simulation are much less than predicted from the previous work of McDonald (2003) with an upper limit of $\beta_{Ly\alpha} = 0.7$ from $\xi(s)$ and $\beta_{Ly\alpha} \approx 0$ from Lyα $\xi(\sigma, \pi)$. Given $\beta = 0.7$, a gas velocity dispersion of $\sqrt{\langle w_z^2 \rangle} = 70$ kms^{-1} fits the simulated Lyα $\xi(s)$ and this is close to the sub-1h^{-1}Mpc value of the velocity dispersion estimated for simulated galaxies, due to correlated motions. Good agreement is observed between the GIMIC simulation and the Keck+VLRS gas $\xi(s)$.

We do not calculated the Lyα 2-D autocorrelation from the observations as the QSO sample does not have a high enough sky density to properly probe the on-sky projected profile.

4.4 Conclusions

We have analysed the interaction between IGM and galaxies at $z \sim 3$ using VLRS data and KECK LBGs, also the spectroscopy for 17 QSOs in the redshift range $2.5 < z < 4.0$ obtained from the publicly available QSO spectra and 13 spectra from our own observations using the X-Shooter instrument on the VLT. Apart from the observational data, we employ the SPH GIMIC simulations to analyse the clustering of gas and galaxies.

1. The observed galaxy real-space autocorrelation function is more consistent with that measured for simulated $M_\star \geq 10^9\ h^{-1}\mathrm{M}_\odot$ galaxies than low mass galaxies. When an empirically determined velocity dispersion dominated by velocity errors is convolved with the simulated real-space correlation functions, a similar preference is found for the lower amplitude clustering of the $M_\star \geq 10^9\ h^{-1}\mathrm{M}_\odot$ galaxies. In the simulated data the difference between the real and redshift-space correlation functions is too small to be self-consistently explained by the measured peculiar velocity distribution. We suggest that this is the consequence of a scale dependence in the measurement of the peculiar motions and that the peculiar motions taken within $\lesssim 1\ h^{-1}$Mpc give a more consistent result.

2. We have checked for the existence of the transmission spike near star-forming galaxies in the data and GIMIC simulations which would be indicative of the effects of star-formation feedback on the IGM. For the data, we combined the full VLRS

and Keck LBG-Lyα datasets to study both $\xi(s)$ and $\xi(\sigma, \pi)$ and the LBG-Lyα correlation functions. No detection of feedback is seen in the galaxy-gas correlation function in the combined VLRS+Keck data. We find that the gas transmissivity monotonically drops towards the galaxy, consistent with the density of neutral gas rising towards the galaxy position. Although the simulation transmission rises when LBG velocity errors are taken into account, the simulated and observational results remain in good statistical agreement.

3. The redshift-space gas-galaxy cross-correlation function in the simulation is close to the real-space correlation function and to some extent this is predicted from linear theory applied to the Lyα forest flux which has a non-linear relation with optical depth and thus implies lower rates of dynamical infall of gas into galaxies than would otherwise apply. We have also considered whether galaxy-wide outflows may be cancelling out the infall effect.

4. The observed Lyα autocorrelation function is also consistent with the simulation. At small scales the difference between real and redshift-space correlation functions in the simulation is again less than predicted given the peculiar velocity distribution but may be consistent with previous simulations of the Lyα forest. At larger scales the effects of dynamical infall are in line with linear theory, if the non-linear relation between flux and optical depth is taken into account. There may also be some residual effect from gas outflows cancelling out the effects of dynamical infall.

5. In the simulations, both gas and galaxies show evidence of a strong bulk motion. This bulk motion is undetectable by observable correlation functions but may have a connection with the local coherence needed to explain why distribution of peculiar velocities overestimates the finger-of-God effect.

Chapter 5

Lyman Alpha Emitters

Selecting high redshift galaxies through their strong emission in the Lyα feature using the narrow-band imaging method has come to be a very effective technique to isolate high redshift galaxies. Objects selected in this way are called Lyman Alpha Emitters (LAE). There are many observations that have been made to uncover galaxies with strong Lyα emission at various redshifts (e.g., Hu & McMahon 1996; Hu et al. 1998; Cowie & Hu 1998; Steidel et al. 1996; Ouchi et al. 2003, 2008, 2010; Hayashino et al. 2004; Gawiser et al. 2007; Gronwall et al. 2007). At redshift $z \sim 3$, there are several hundreds of spectroscopically confirmed LAE by several groups (e.g., Steidel et al. 2000; Fynbo et al. 2003; Hayashino et al. 2004; Matsuda et al. 2005; Venemans et al. 2007; Nilsson et al. 2007; Gawiser et al. 2007; Gronwall et al. 2007; Ouchi et al. 2008).

In this chapter we discuss LAE observational data both from photometric observation and spectroscopic follow-up observation. We then use our LAEs at $z = 3.1$ to measure LAE number densities and the clustering correlation function.

5.1 Observational data

We used the observational data from the Subaru Suprime-Cam to measure the distribution of the Ly-alpha emitters at z $\sim$ 3 in five 0.5 x 0.5 degree^2 fields where we have both spectroscopically-confirmed Lyman break galaxy redshifts and spectra of bright quasars at z $>$ 3. LAE fields were selected from our LBG VIMOS survey for

Field	RA (J2000)	DEC (J2000)	total exposure time (s)	Seeing (arcsec)
Q2359	00:01:40.6	+07:09:54.0	6000	0.61
Q0302	03:03:41.0	-00:23:22	7200	0.60
J0124	01:24:03.77	+00:44:32.7	4800	0.55
PKS2126	21:29:24.	-15:38:41.0	6000	0.96
Q2231	22:34:01.79	+00:00:01.7	6000	0.87

Table 5.1: Details of narrowband imaging (NB497) from the Subaru/Suprime-Cam.

Field	RA (J2000)	Dec (J2000)	Band	Exposure (ks)	Seeing (arcsec)	Instrument
Q2359	00:01:44.85	+07:11:56.0	B	7.2	1.45	KPNO/MOSAIC
			R	6.0	1.15	
Q0302	03:03:45.27	-00:21:34.2	B	6.4	1.28	KPNO/MOSAIC
			R	4.8	1.19	
J0124	01:24:03	+00:44:32	B	2.8	1.5	KPNO/MOSAIC
			V	3.1	1.4	
PKS2126	21:29:12	-15:38:42	B	7.8	1.6	CTIO/MOSAIC2
			R	6.4	1.5	
Q2231	22:34:28.00	+00:00:02.0	B	13.2	1.01	WFCam (INT)
			R	19.2	1.01	

Table 5.2: Details of broadband imaging observations from Bielby et al. (2011,2013).

LBGs at $2.5 < z < 3.5$.

We obtained narrowband imaging from the Subaru/Suprime-Cam on 24 September 2009. Suprime-Cam is a mosaic CCD camera with ten 2048x4096 pixels CCDs which covers a $34'$ x $27'$ field of view with a pixel scale of 0.20 arcsec. The observed fields were Q2359, Q0302, J0124, PKS2126, and Q2231 (details are in Table 5.1). The fields were observed by using the narrow band [OIII] NB497 filter (4977 nm, FWHM 77 Å (Hayashino et al., 2003)) with the aim of identifying Lyα emission at $z \approx 3.1$. The exposure times were 1200 seconds for each frame and the seeing was generally sub-arcsecond. A standard star (LTT 9491 23:19:34.98, -17:05:29.8 J2000) was also observed during the same observation night. The other broadband (B,V,R) images with the reduction already done are obtained from the KPNO MOSAIC or CFHT MegaCAM imaging archives (see Bielby et al. (2011,2013)). Details of broadband observations are summarised in Table 5.2.

5.1.1 Data Reduction

To reduce the Suprime-Cam raw narrowband data, we used the pipeline software, SDFRED (the Suprime-Cam Deep field REDuction package[1]) which comprises IRAF, SExtractor (Bertin & Arnouts, 1996), and the mosaic-CCD data reduction software (Yagi et al., 2002). This pipeline software, SDFRED, was originally written and developed by Dr. M. Ouchi and M. Yagi (Ouchi et al., 2004a). We applied this package to our observational data and made stacked images. The package includes bias subtraction, flat fielding, distortion+atmospheric dispersion corrections, matching the PSF size, sky subtraction, masking vignetting caused by the auto-guider, masking bad pixels, image alignments and scaling, and mosaicing. The reduction procedure is briefly described below.

We firstly applied a bias correction to our raw data by subtracting the median value of the overscan region and trimming that region off. At each column of the pixel array, the script computed the median count of the overscan region and treated it as a typical bias level at that line. This median value was then subtracted from the counts in all the pixels in that line. The overscan regions were subtracted by starting from the right- or left-edges of the CCDs and then completed with the top- or bottom edges of the CCDs. The overscan regions were trimmed off after the bias subtraction.

The flat fielding process started by creating a flat frame from a number of normalised object frames. Our flat frame was made from 25 dithered frames. The large number of frames used here is to make sure that we produced a sensible flat which has less noise and residual effects of objects in the frame. The flat file was used to correct the difference in sensitivities between pixels in a frame. Areas which were affected by bright objects and vignetted by the auto-guider (AG) probe were masked out, normalised, and a median value of each pixel was taken. The object frames were then divided by the flat frame. After the flat fielding process, the pixel-to-pixel variation in sensitivity was corrected and the background level over the entire image should be flat. We note that the flat-field might be better done

[1] http://www.naoj.org/Observing/DataReduction/

with a two pass process rather than a simple median. Using a simple median might lead to problems since it is possible to include objects and also to lose statistical precision if the normalisations are not exact. The two pass process would get rid of these problems because it only takes the area with no objects (star or galaxy) and calculates a mean to maintain accuracy. This would give a value appropriate for a flat uniform illumination.

The astrometric distortion correction was performed after the flat-fielding process. This process corrected for two distortions, the telescope optics and the differential atmospheric dispersion. A 5-th order polynomial transformation (Miyazaki et al., 2002) was applied to flat-fielded images.

Matching the point spread function (PSF) was required before making the final mosaiced images. The script used all frames in the list, measured the FWHM of the PSF, and determined an appropriate target PSF. The target PSF was then compared to individual images. If image has smaller PSF than the target within an acceptable range, it will be smoothed with a corresponding Gaussian. The PSF matching was applied to all frames so that the final mosaiced images will have a common PSF FWHM value.

In the sky subtraction process, the script computed the sky background by using a mesh pattern, interpolated the pattern, and subtracted the sky background from each image. Normally, the image was divided into the "sky-mesh size squares" (a grid) of 64 x 64 pixels, corresponding to $12''.9$ x $12''.9$. The script assigned the centre of the mesh, calculated counts of each mesh, and used bilinear interpolation to determine the global sky background value from the surrounding meshes. After sky subtraction, an image would have the background level close to zero and the photometric accuracies of compact objects such as galactic stars and faint galaxies should not be affected.

Before producing a final image, estimating alignment and scaling was applied. In this process, the script corrected the positional shifts, rotations, and flux scales of different frames. The stellar objects in each frame were used to identify the differences from the reference image (the first image in the list). The final mosaiced image was produced by combining all relevant frames and merging into a single large

image. The script calculated and adjusted the relative positions from all frames at different CCDs and at different exposures by using commonly detected stars in the frames. The final mosaiced image was then merged into a single image and this narrow-band output from Suprime-cam was ready to use.

The geometry differences between narrow-band and other broadband images were corrected with several IRAF tasks (ie. GEOMAP, GEOTRAN). We applied those to our narrow-band and broadband images to have a geometrical transformation and alignment of final stacked images. Final versions used SCAMP and SWARP when matching narrowband and broadband astrometry.

5.1.2 Object Detection and Photometry

SExtractor (Bertin & Arnouts, 1996) was used to get the photometric catalogues. Although bad pixels in images were flagged out from the reduction processes, there were still some obvious areas that need to be masked out. We masked out bad areas of the stacked images (ie.at very low-S/N regions near the edges of the images) before performing the object detection and photometry. We also re-applied the cosmic ray rejection using the rejected-mean algorithm, *crreject*, from IRAF. Each individual image was the same size. The object positions extracted from the NB497 image were used as a position registration to the broadband images via the dual-image mode. The accuracy in making a position registration was within 0.2 pixels (0.04 arcsec).

The photometric zero-points were calculated from the photometry of standard star LTT 9491 (23:19:34.98, -17:05:29.8 J2000) observed during the same observation night. The same reduction with object frames applied to the standard star frames. To calculate zero-points, we know that the magnitude difference of two objects with known observed flux is given by

$$m_1 - m_2 = -2.5 log_{10} \left(\frac{f_1}{f_2} \right) \tag{5.1.1}$$

where m_1 and m_2 are the apparent magnitudes, and f_1 and f_2 are the observed flux.

Similar to Eq. 5.1.1, the zeropoint of an instrument can be defined as

$$m = -2.5log_{10}\left(\frac{DN}{EXPTIME}\right) + ZEROPOINT \tag{5.1.2}$$

In this case, f is the count rate calculated by data number (DN) counts per an observation of length of exposure time (EXPTIME). m is the magnitude of the standard object in the AB system. ZEROPOINT is the magnitude at 1 count/s.

The magnitude value of our observed standard star (LTT 9491) in V band is provided by Oke 1990, V_{AB} (λ5460) of LTT 9491 is 14.06. Because NB497 is not far off from V band and there is no much spectral change in (λ5460), we assumed that NB has the same magnitude as V. We then used V_{AB} (λ5460) = 14.06 to calculate the ZEROPOINT.

We observed LTT 9491 in NB band with 60 s, thus the zeropoint for the star ZP_{NB} for that NB frame can be arranged as

$$ZP_{NB} = -2.5log_{10}(\frac{DN_{LTT9491}}{60}) + 14.06 \tag{5.1.3}$$

ZP_{NB} in Eq. 5.1.3 is NB magnitude for star that gives 1 count in second. As other NB object frames were observed in 1200 s, we need to calculate m'_{NB} for any star in 1200 s frame.

$$m'_{NB} = ZP_{NB} - 2.5log_{10}(\frac{DN_{NB}}{1200}) \tag{5.1.4}$$

The zero points of all fields and all bands are summarised in Table 5.3. We checked the zero points of all images (both in narrow-band and broadband) by comparing the colours of stellar objects in our field. We derived NB497 magnitudes of stars by interpolating their B, V, and R magnitudes. Our broadband zero points are based on the standard stars obtained from the observations. We checked the air mass of the observation and found that the changes in air mass equate to a few hundredth of a magnitude difference in the zero-points. These zero-points are accurate to within Δmag $\approx$ 0.03.

Since we applied the geometric transformation to all images, the object positions in each broad-band image were matched with objects in the NB band. The distortion correction in the reduction process corrected the geometric distortion and

Table 5.3: Zero points of all fields.

Field	NB band	NB-ZP*	Band1	B1-ZP	Band2	B2-ZP
Q2359	NB497	31.17	B	32.28	R	31.92
Q0302	NB497	31.17	B	32.28	R	31.96
J0124	NB497	31.17	B	31.56	V	31.81
PKS2126	NB497	31.17	B	31.72	R	31.97
Q2231	NB497	31.17	B	30.00	R	30.00

*Magnitude that gives 1 count/1200 s in NB

we obtained good astrometry to $\pm$ 0.2″ rms over the image. Astrometry was made based on USNO at ESO catalogue and $\sim$ 1000 stars identified in the stacked images. The position of USNO objects were approximately uniformly distributed over the entire stacked images. The absolute coordinates of our objects were obtained from these USNO objects.

We employed SExtractor's "double image mode" to get object photometry from the astrometry calibrated images, so that their magnitudes and other parameters can be measured at exactly the same positions as in narrow band. We extracted sources from broadband images by using the same aperture sizes used for narrow band images and matched to the NB catalogue with a search within 1.″0 radius. We measured MAG−AUTO and adopted that as total magnitudes while the measured 2.0 arcsec diameter aperture magnitudes were used to measure colours of objects. After removing objects that were in the masked regions, the final number of objects obtained in each field were 90261 (Q2359), 112985 (Q0302), 48235 (J0124), 59729 (PKS2126), and 50323 (Q2231). The SExtractor flag parameter, "Flags", are included in the catalogue to indicate possible or known bad data (e.g., "flag =1" indicates a source has neighbours, bright and close enough to significantly bias the photometry, or bad pixels, "flag =2" is for the object that was originally blended with another one, "flag =4" for a source that has at least one saturated pixel, etc). Objects with "flag=0" values indicate no known problems. We therefore exclude anything with nonzero flag values.

We calculated the 1σ magnitude depths using the errors calculated on 2.0 arcsec diameter apertures in SExtractor. The 1σ flux error at the faint limit is effectively given by:

$$f_{1\sigma} = \sqrt{A\sigma^2} \tag{5.1.5}$$

Table 5.4: Image depths.

Field	Band	Image depth (1σ) [AB mag]
Q2359	NB	28.36
	B	28.32
	R	27.55
Q0302	NB	28.55
	B	28.39
	R	27.45
J0124	NB	27.45
	B	28.08
	V	27.72
PKS2126	NB	27.88
	B	28.53
	R	28.06
Q2231	NB	27.75
	B	27.37
	R	26.77

where A is the area in pixels and σ is the standard deviation of the noise measured from the background. The 1σ magnitude limit is then simply $m_{1\sigma} = -2.5log_{10}(f_{1\sigma})+ m_{ZP}$.

5.1.3 Sample selection

We show colour magnitude diagrams for our fields in Fig. 5.1 - 5.2. Based on the colour-magnitude properties, we make the following cuts for Set A LAE samples.

$$SetA:$$

$$R - NB497 > 1.0 \qquad (20 < NB497 < 25)$$

$$B - NB497 > 1.6 \ : \ Q2359\ ,\ Q0302\ ,\ PKS2126\ ,\ Q2231$$

$$V - NB497 > 1.0 \qquad (20 < NB497 < 25)$$

$$B - NB497 > 1.6 \ : \ J0124$$

An LAE is selected as being a bright object in the narrow-band filter but fainter or not detected in the broad-band filter. Thus LAEs are selected based on comparing their magnitudes in narrow-band and broad-band filters. The NB497 narrow-band filter falls between the broad-band filters (B is the blueward and R/V is the redward) as shown in Fig. 5.3. As a result, objects with redder colours will tend to have colour (R - NB) < 0 and colour (B - NB) > 0, while bluer sources will have positive (R - NB) and negative (B - NB). The first criterion is used to reject objects whose spectra are on the redder side of NB497 while the second criterion is applied to reject the bluer objects.

To select Set A LAEs, we started with cutting out objects that lie in the image edges where the S/N drops and only used objects that have flag = 0. We selected objects with NB497 total magnitudes (MAG−AUTO) between 20 and 25. The colour cut is then made by using aperture magnitudes difference (R - NB497) $>$ 1.0. With those selected objects, we applied another colour cut and selected if aperture magnitudes (B - NB497) > 1.6. Note that we selected the NB497 excess objects for J0124 by using mag(V - NB497) instead of mag(R - NB497). Our Set A selection criteria correspond to a rest-frame equivalent width (EW_{rest}) of ≈ 20.5 Å (approximately 84 Å in the observers frame) as shown by the black horizontal line in the left panels of Fig. 5.1 - 5.2. The diagonal line in the Figures represents objects undetected in B band which are attributed the 1σ limiting magnitude of the source image. Red curves indicate the distributions of 3σ errors in measuring B-NB497 or BR-NB497 colour. There are more undetected objects in fields Q2231, PKS2126 because the broad-band data in these fields is poorer in term of seeing and therefore the value of their magnitude limit is lower than other fields as given in previous section.

We also made another selection (Set B) based on NB497 excess from aperture magnitudes (B+R)/2 which the selection criteria are defined as :

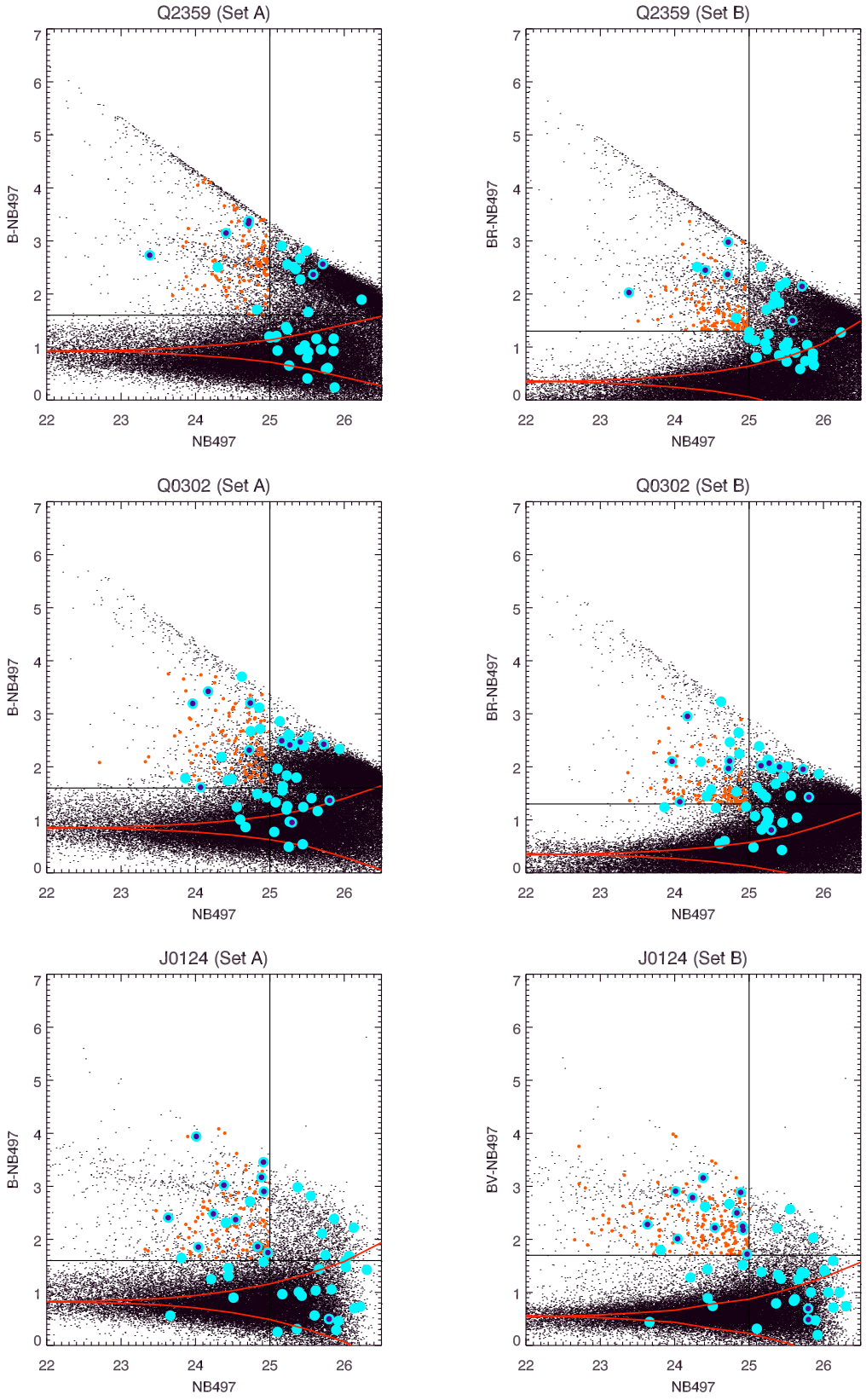

Figure 5.1: Colour magnitude diagrams of NB497 for Q2359, Q0302, and J0124. The black dots are all the detected objects. Orange dots present the photometrically selected LAEs. The observed VIMOS LAEs and the spectroscopically confirmed LAEs are represented by light blue circles and purple filled circles. Objects (light blue circles) below the selection line were observed by VIMOS and selected only using NB-R(VIMOS preimage). Red curves indicate the distributions of 3σ errors in measuring B-NB497 or BR - NB497 colour. LHS is Set A selection while RHS is Set B selection.

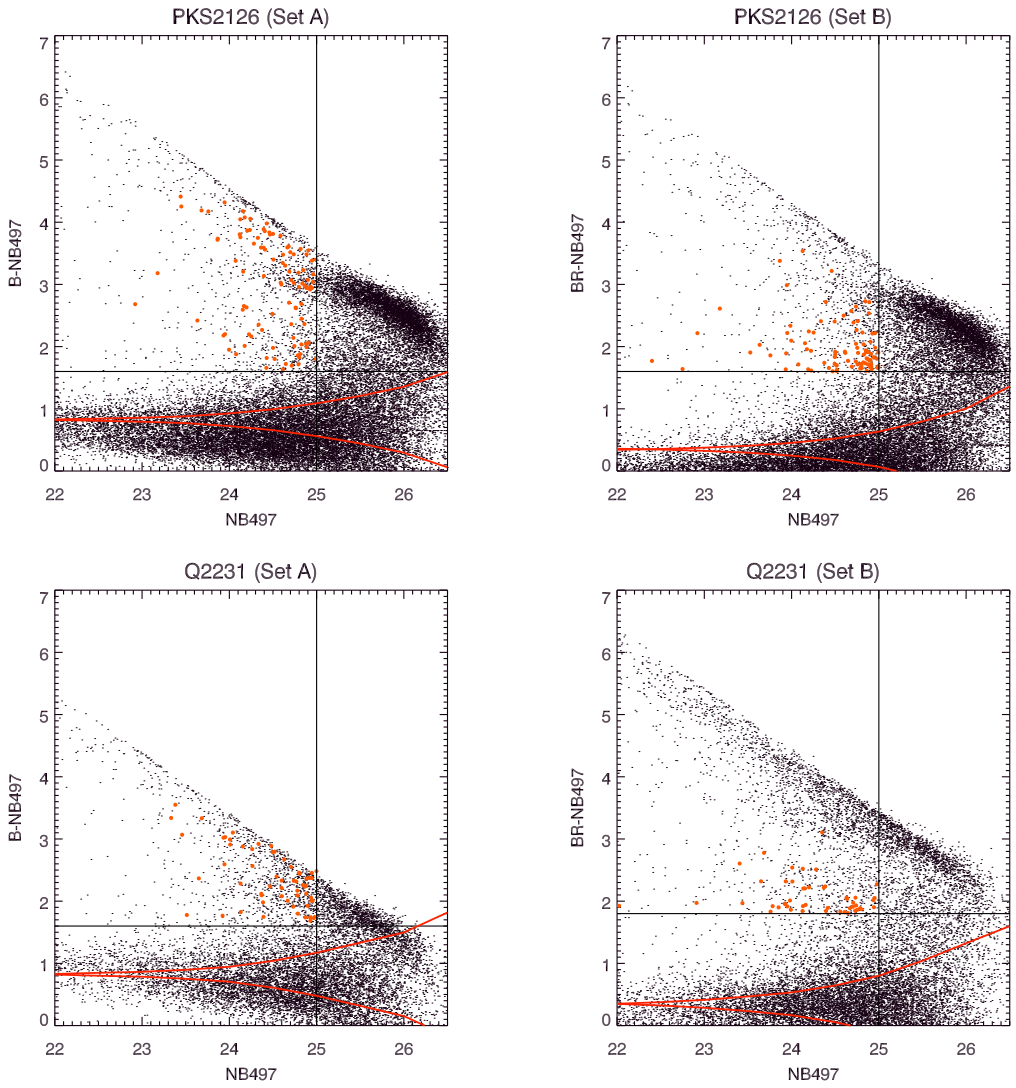

Figure 5.2: Colour magnitude diagrams of NB497 for PKS2126 and Q2231. The black dots are all the detected objects. Orange dots present the photometrically selected LAEs. At present, we have no LAE VIMOS observations for PKS2126 and Q2231. Red curves indicate the distributions of 3σ errors in measuring B-NB497 or BR - NB497 colour. LHS is Set A selection while RHS is Set B selection.

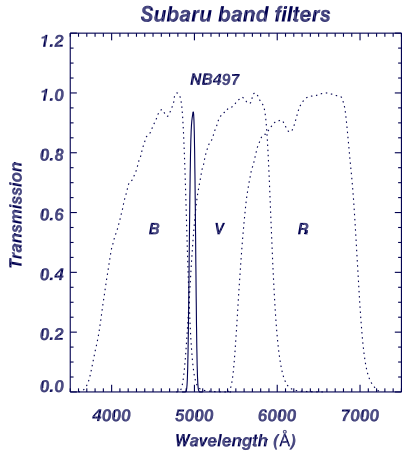

Figure 5.3: The transmission curve of the filters. The solid line indicates the narrow-band filter, NB497. The dot lines indicate broad-band filters, B, V, and R respectively.

$SetB$:

$$(B+R)/2 - NB497 > 1.3 \qquad (20 < NB497 < 25) \ : \ Q2359$$

$$(B+R)/2 - NB497 > 1.3 \qquad (20 < NB497 < 25) \ : \ Q0302$$

$$(B+V)/2 - NB497 > 1.7 \qquad (20 < NB497 < 25) \ : \ J0124$$

$$(B+R)/2 - NB497 > 1.6 \qquad (20 < NB497 < 25) \ : \ PKS2126$$

$$(B+R)/2 - NB497 > 1.8 \qquad (20 < NB497 < 25) \ : \ Q2231$$

Fig. 5.1 - 5.2 show colour-magnitude diagrams for Set A (left panel) and Set

Field	Set A	Set B
Q2359	98	118
Q0302	118	107
J0124	130	152
PKS2126	124	90
Q2231	80	55
Total	550	522

Table 5.5: Number of LAE Candidates from each selection.

B (right panel) selection. The black dots are all the detected objects. Orange dots present the photometrically selected LAEs. The observed VIMOS LAEs and the spectroscopically confirmed LAEs are represented by light blue circles and purple filled circles and are described in the next section. At present, we have no LAE VIMOS observations for PKS2126 and Q2231. The black horizontal lines indicate our equivalent width limit (EW_{rest}) of 44 Å (approximately 178 Å in the observers frame).

We aim to apply the same criteria to every field but in some fields their star locus lies above 0, we then need to adjust the criteria to have approximately the same cut (assuming they have their local distribution at zero). The difference in stellar locus for J0124 Set B is due to the use of (B+V)/2-NB in that field compared to (B+R)/2-NB elsewhere. We also rejected anything with NB/B/R band magnitudes fainter than the 1σ limits of each band.

After applying these criteria, we had to visually inspect each object. The reason for this is because there are many objects that look like artifact/cosmic rays even after we had applied the cosmic ray rejections in the reduction processes. Also there are lots of objects that lie in the gap between CCDs which need to be checked by eye. The image contains higher noise regions due to lower sampling and due to the gaps between ccds in the detector. These higher noise regions give spurious detections. We inspect thumbnail images of our selected objects on NB, B, and R or V images which helps us to clarify if they are free of artifacts or cosmic rays. The total number of objects that meet all the criteria are shown in Table 5.5. After getting the LAE confirmation from spectroscopy, we will use both LAE sample to compare with LBGs at the same redshift and in the same fields. Also shown in Fig. 5.4- 5.5 are the distribution of LAEs, LBGs and QSOs in the same area. No

Field	pointing centre		Seeing	total exposure time
	RA(J2000)	DEC	(arcsec)	(hr)
Q2359	00:02:11.457	+07:15:32.256	1.0	2.0
Q0302	03:03:10.208	-00:16:20.987	1.0	3.3
J0124	01:24:36.236	+00:51:07.19	1.0	4.3

Table 5.6: Details of VIMOS LAE observations.

LBGs were identified as LAE.

5.2 Spectroscopic Data - VIMOS observation

We have made LAE spectroscopic follow-up observation with the VIsible Multi-Object Spectrograph (VIMOS) (Le Fèvre et al., 2003) on the Very Large Telescope (VLT). The VIMOS focal plane is divided into 4 quadrants (4 slit masks) with size $7'$ x $8'$ each and its gap value $\sim 2'$. The field orientation is presented in Fig. 5.6. Each slit mask allowed us to observe $\sim$ 20-30 objects. VIMOS Mask Preparation was made by using VIMOS Mask Preparation Software (VMMPS)[2]. Fig. 5.7 , Fig. 5.8, and Fig. 5.9 show the slit masks in 4 quadrants for Q2359, Q0302, and J0124 observation respectively. We placed about 20 objects per each mask which included LAE candidates, LBGs, and QSOs, so that we have around 100 targets in total for each field. We used the high-resolution grism, HR-Blue, with the spectral coverage of 4150-6000 Å and resolution is $R \sim 2050$ for a $1''$ slit. The average dispersion is 0.51 Å/pixel. The observation was conducted at the end of August to the beginning of September, 2011 (part of the observing run ESO-ID 086.A-0520 B, P.I. H. Francke). Details of the observation of our 3 fields (Q2359, Q0302, and J0124) are given in Table 5.6.

The reduction was done by using Esorex from VIMOS pipeline[3]. The main procedure includes creating master calibration data, reducing science frames, and extracting objects. Following the pipeline manual, we firstly created a master-bias with the recipe *vmbias*. An output, master-bias, was then used in the reduction of the flat field, arc lamp, and scientific exposures. The next step was using the recipe

[2]http://www.eso.org/sci/observing/phase2/SMGuidelines/VMMPS.html
[3]http://www.eso.org/sci/software/cpl/esorex.html

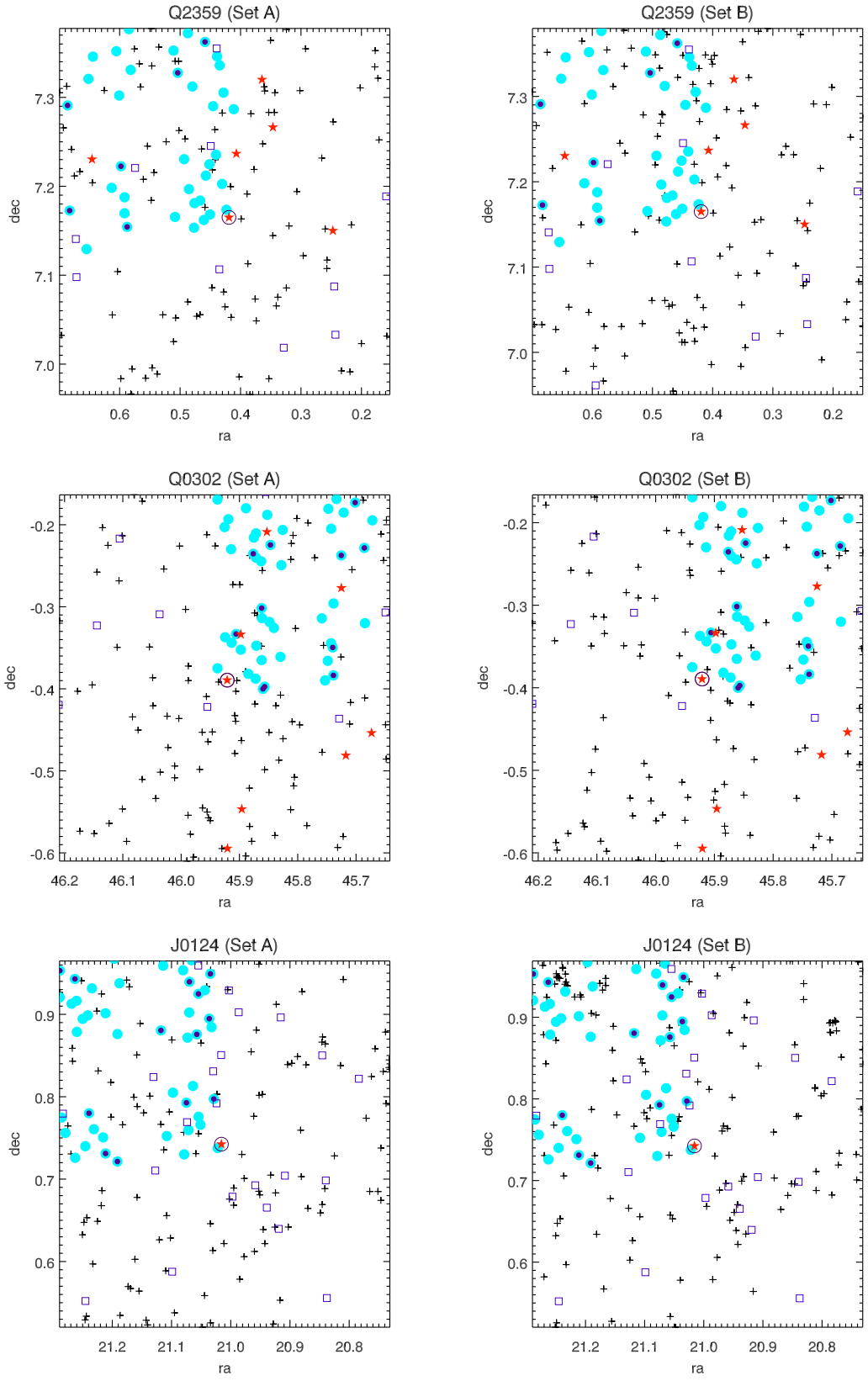

Figure 5.4: LAE distributions for Q2359, Q0302, and J0124. LHS show objects from Set A selection while RHS show Set B selection. Black plus signs are selected objects.The observed VIMOS LAES and the spectroscopically confirmed LAEs are presented with light blue circles and purple filled circles. Red stars are QSOs and navy squares are LBGs at the same redshift range.

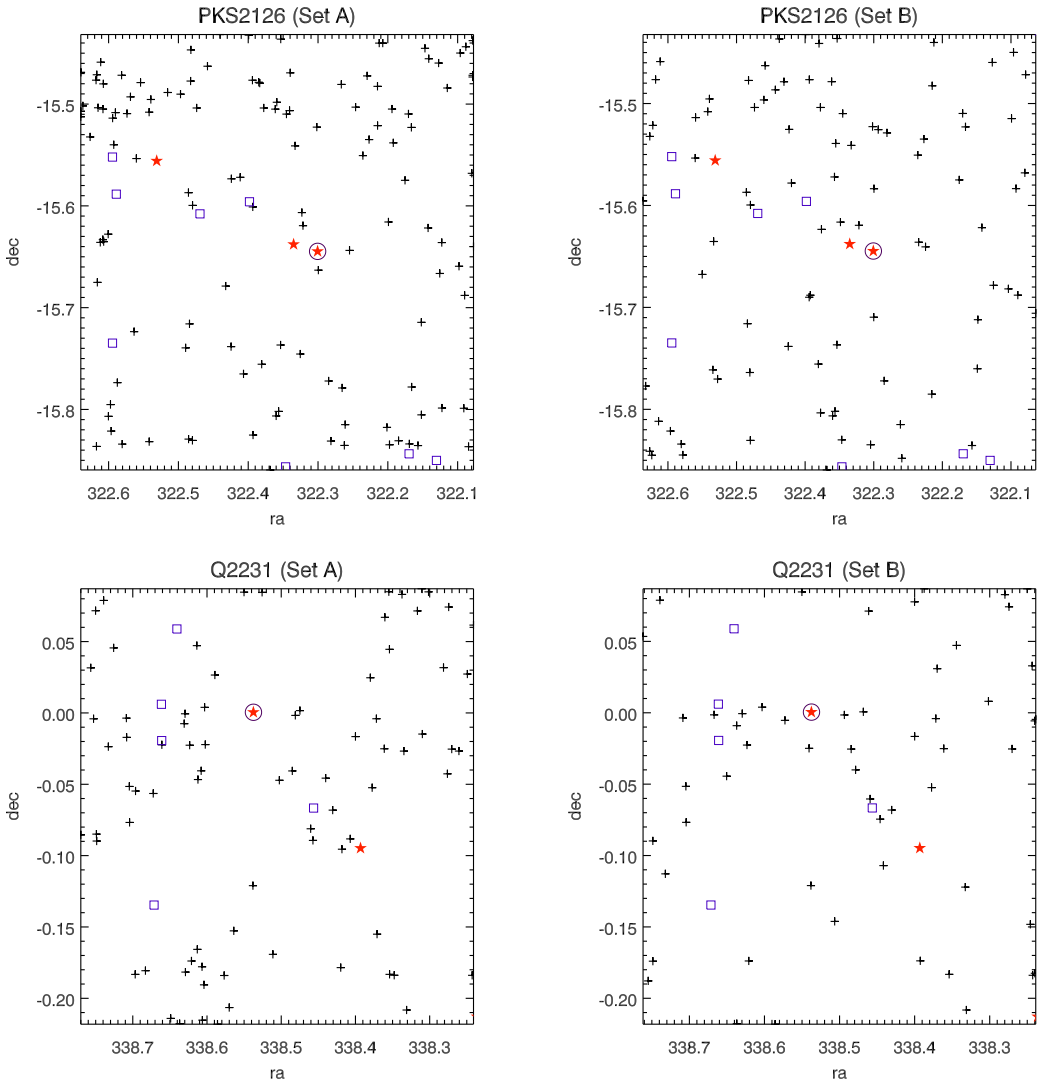

Figure 5.5: LAE distributions for PKS2126 and Q2231. Same as Fig. 5.3 but note that we do not have LAE VIMOS observations for these fields.

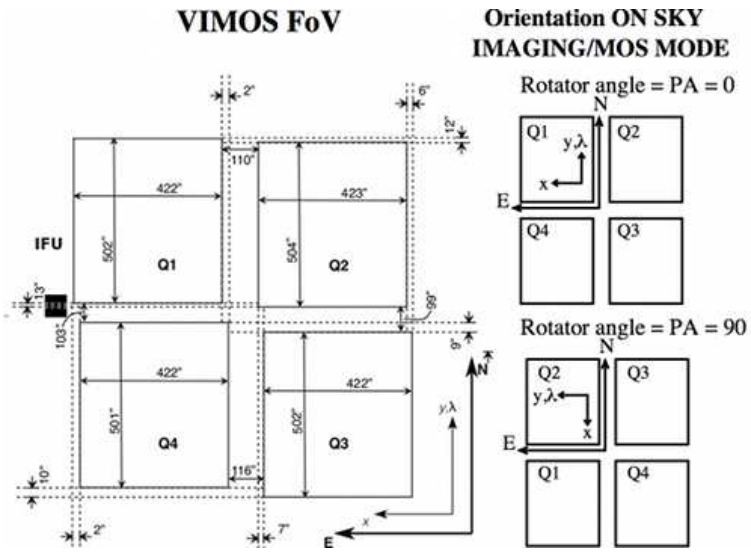

Figure 5.6: Layout of the VIMOS imaging field of view on sky for position angles 0° and 90°, in IMG and MOS mode. The field orientation consists of 4 quadrants (7′ x 8′ each) with the gap of 2′. The size of CCD is 2048 x 2440 and pixel size is 0″.205. (Retrieved from http://www.eso.org/sci/facilities/paranal/instruments/vimos/inst/imaging.html)

vmmoscalib to process flat field exposures and arc lamp exposures. This produces many necessary products for the scientific data reduction such as a normalised flat field, slit postition on the CCD, coefficients of the spatial curvature fitting polynimials, and coefficients of the wavelength calibration fitting polynimials. Finally, we used the recipe *vmmosscience* to process science frames with the cosmic ray rejection applied at this process. For each field, we combined all scientific frames from every night. The pipeline applied the reduction process to each frame and then all frames are aligned to the reference frame (the first one in the input file) and stacked before object extraction. The object extraction is processed by appling an optimal extraction algorithm (Horne, 1986). The wavelength calibration was performed using the input wavelength calibration and sky lines, and sky background subtracted. We found diagonal stray light interfered with the wavelength calibration and sky subtraction in quadrants 3 and 4. To fix this, we managed to isolate the brightest part of this light from the flat lamp, fitted the smooth pattern of the flat and subtracted it out (we used a python code provided by Harold Francke).

The number of LAE candidate and identified LAEs are in Table 5.10. We found that many objects in Q2359 were missed by the slit in 2 quadrants because the mask

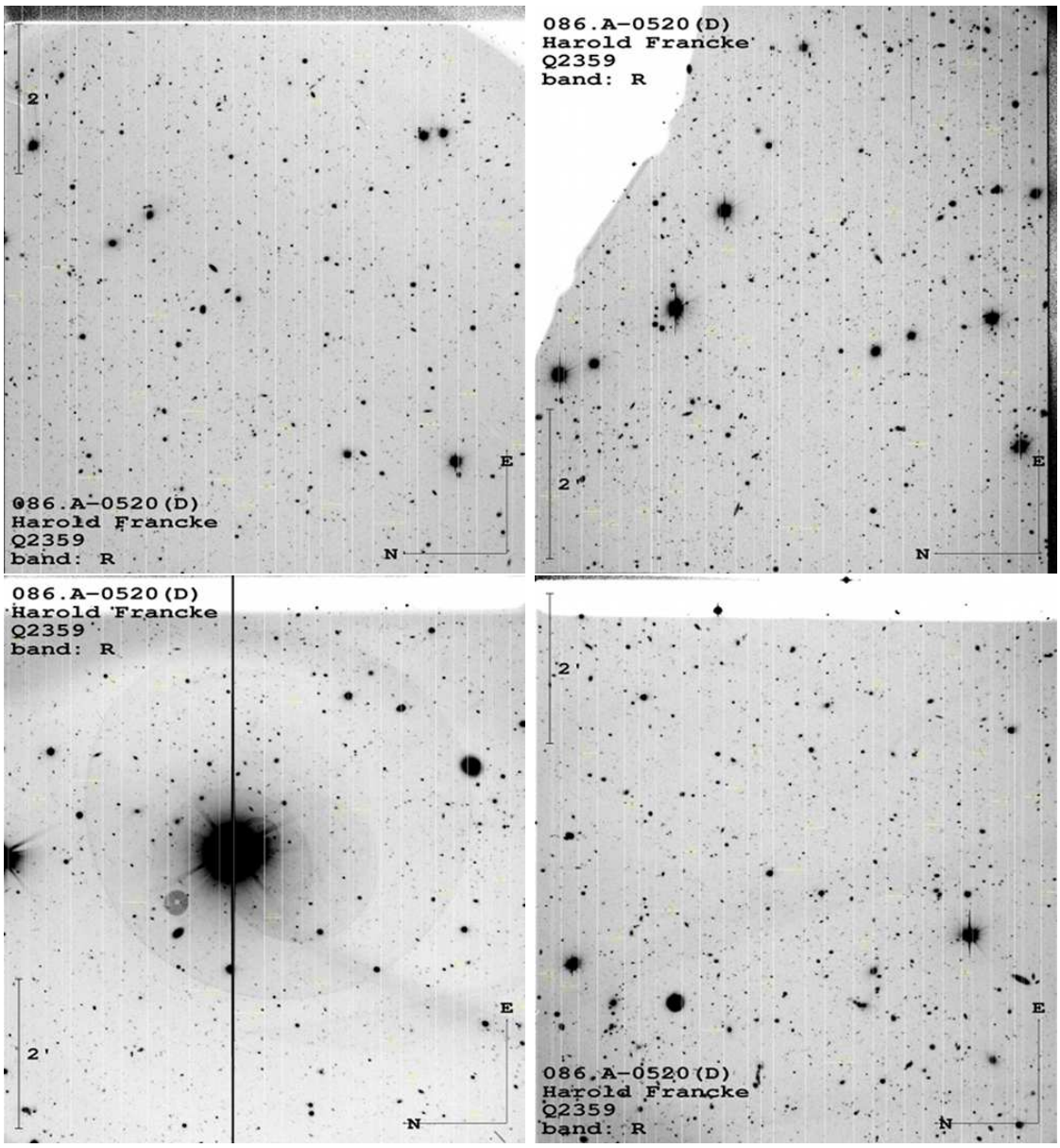

Figure 5.7: VIMOS slit masks in 4 quadrants for Q2359 area.

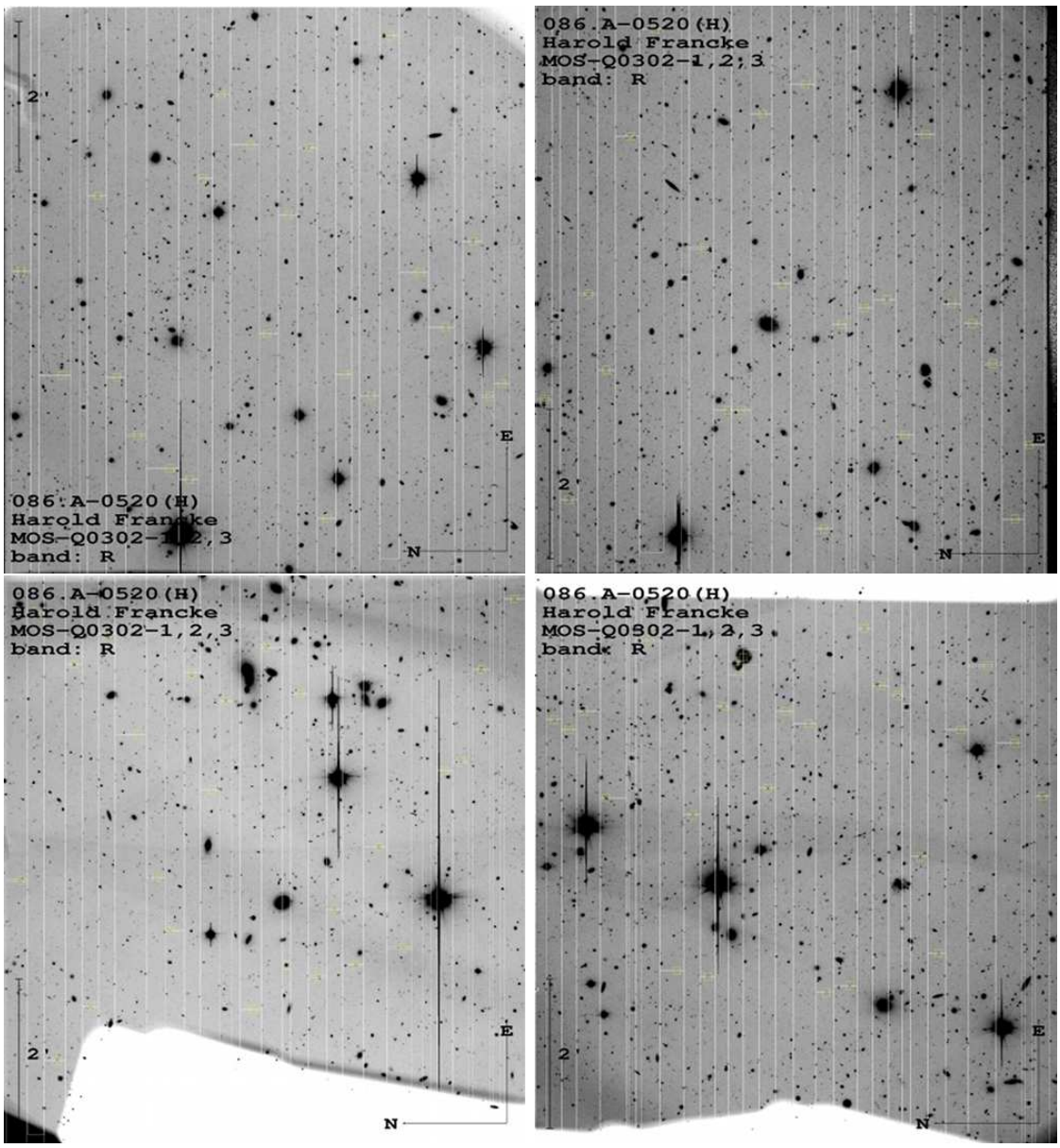

Figure 5.8: VIMOS slit masks in 4 quadrants for Q0302 area.

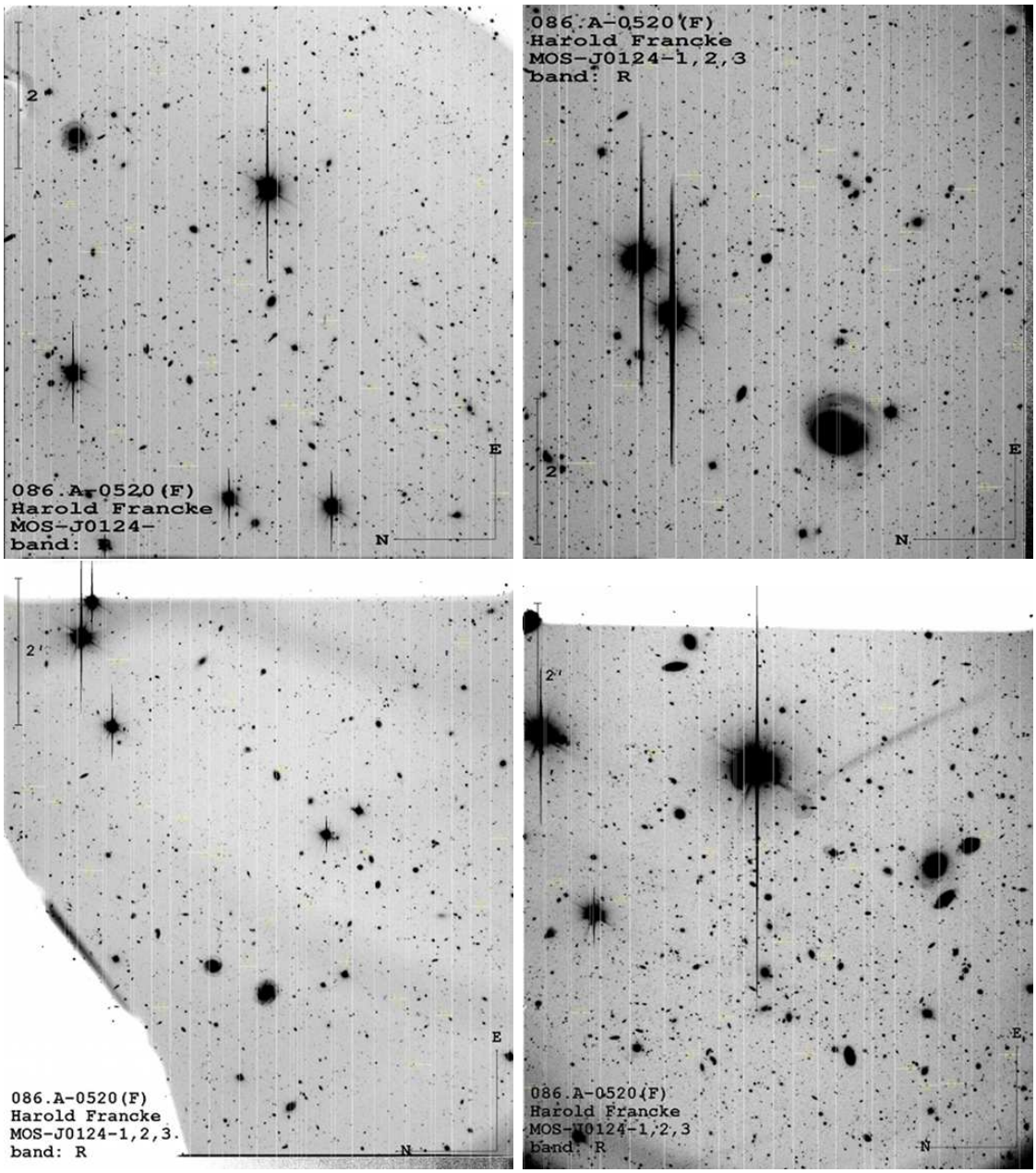

Figure 5.9: VIMOS slit masks in 4 quadrants for J0124 area.

was not inserted properly. As a result, the number of confirmed LAEs are less in field Q2539 compared to others. We show some spectra from VIMOS observation in Fig. 5.10 (Q2359), Fig. 5.11-5.12 (Q0302), and Fig. 5.13-5.14 (J0124). In each plot we show the 1-D spectrum with the position of Lyα shown by the red box which represents the wavelength range of the narrow band filter. Also shown in the plot is the 2-D spectrum in the small box at the top. Tables 5.7, 5.8, and 5.9 show details of identified LAEs for Q2329, Q0302, and J0124 respectively. We visually inspected every source targetted for spectroscopic observation both in 1D and 2D spectra. We determined sources where possible a redshift and classification such as $z \sim 3$ LAE, LBG or QSO. For every identified LAE, we assigned quality parameter, Found = 1 or Found = 9. A quality of Found = 1 indicates high confidence spectroscopic confirmed with high-SNR Lyα emission features at $\lambda \approx 4977 \pm 30\mathring{A}$. While, Found = 9 are the low confidence sources with some weak Lyα emission. LBGs are determined by the presence of Lyα emission/absorption line at 1216 Å and QSOs are determined by the presence of broad emission features. We also checked the possibility of O[II] emitters. Our spectral resolution allows identification of the [OII] line, the observation resolution is $\sim$ 2.5 Å while the [OII] doublet is about 2.7 Å. For the Found = 1 objects where the S/N was sufficient, we did not see any double peaked lines in our data although the S/N was poor in a few cases. Therefore there is no evidence for a significant contamination from OII emitters.

Fig. 5.15-5.16, 5.17-5.18, 5.19-5.20 show snapshots of our spectroscopically-confirmed LAEs from VIMOS observation. In each panel, we plot each object in NB497, R, and B (or V for J0124) images repectively. Objects appear in the middle of each box labelled by a red circle. The size of each box is $8''$x$8''$. Also labelled are the object IDs with object classification in parentheses.

5.3 Selection efficiency

Lyα emitter candidates can be selected through a variety of ways using colour selection. Many groups are using different selection criteria (ie. narrowband and combined broadband observations (eg, (B+R)/2), one narrowband filter and one

Table 5.7: Q2359 LAEs with spectroscopic redshifts.

ID	FOUND	RA(J2000) (deg)	DEC (deg)	z	NB (ap)	NB (au)	B (ap)	R (ap)
136738	1	0.5979306	7.2225003	3.09	24.01	23.38	26.74	25.33
132571	9	0.5918391	7.1876390	3.09	25.85	25.35	28.83	27.29
130971	1	0.6827382	7.1726434	3.11	24.94	24.72	29.07	27.51
128709	1	0.5876359	7.1543390	3.12	25.17	24.41	28.57	26.92
155011	9	0.5848160	7.3766903	3.13	25.41	25.16	28.42	27.65
151026	9	0.6442116	7.3458090	3.15	25.53	25.40	28.20	26.53
144615	1	0.6861331	7.2909262	3.08	24.99	24.71	28.92	26.40
153089	1	0.4588220	7.3623221	3.11	25.76	25.71	28.42	27.48
150892	9	0.4388538	7.3460512	3.10	25.53	25.41	27.80	27.65
148779	1	0.5039249	7.3275960	3.09	25.73	25.58	28.09	26.35
146941	9	0.4796325	7.3122059	3.14	25.69	25.23	27.02	26.28
134208	9	0.4304954	7.2026147	3.10	25.50	25.49	28.42	27.12
200086	9	0.4667795	7.1839175	3.07	26.43	26.23	30.60	27.08
200084	9	0.4761510	7.1810269	3.08	25.51	25.25	26.16	27.35
200082	9	0.4232990	7.1735804	3.14	25.72	25.68	26.67	25.93
200077	9	0.4505101	7.1682789	3.09	25.73	25.75	26.31	26.61
200073	9	0.5084172	7.1655586	3.13	25.45	25.40	26.39	26.18
129524	9	0.4607764	7.1620695	3.13	25.77	25.51	27.42	26.24
128529	9	0.4769844	7.1533928	3.10	25.03	24.30	27.54	27.65
200061	*	0.6547637	7.1293630	-	26.19	26.09	26.61	25.92
200141	*	0.6055044	7.3518811	-	25.86	25.76	26.11	26.31
200132	*	0.5818205	7.3308390	-	25.54	25.18	26.03	26.13
200126	*	0.6516562	7.3207827	-	25.78	25.84	26.14	25.61
200123	*	0.6007606	7.3020891	-	25.40	25.23	25.72	25.38
200144	*	0.5109679	7.3525577	-	26.11	26.09	25.63	26.17
200126	*	0.6516562	7.3207827	-	25.78	25.84	26.14	25.61
200135	*	0.4345563	7.3359807	-	25.96	25.46	26.27	25.73
200124	*	0.4282237	7.3052672	-	25.68	25.84	25.78	25.80
200105	*	0.4934078	7.2304861	-	25.62	25.18	26.26	25.75
200104	*	0.4515611	7.2247267	-	26.07	26.12	26.45	25.96
200118	*	0.4453679	7.2900357	-	25.45	25.41	27.44	25.50
200117	*	0.4112160	7.2867023	-	25.64	25.53	28.16	26.09
200108	*	0.4405602	7.2354502	-	25.44	25.37	26.07	25.33
200095	-	0.6131840	7.1982057	-	25.95	25.98	25.83	26.50
200079	-	0.5918720	7.1696291	-	25.05	25.01	26.19	25.85
135297	-	0.4574425	7.2119313	-	25.49	25.27	26.10	25.22
200094	-	0.4853260	7.1967991	-	25.83	25.63	25.64	26.14

* denotes the objects that were missed by the slit.

Table 5.8: Q0302 LAEs with spectroscopic redshifts.

ID	FOUND	RA(J2000) (deg)	DEC (deg)	z	NB (ap)	NB (au)	B (ap)	R (ap)
200048	1	45.8618569	-0.3016210	3.09	25.96	25.72	28.74	27.69
200034	1	45.9058535	-0.3331629	3.13	25.96	25.80	27.32	28.20
135084	9	45.8710897	-0.3474696	3.10	25.94	25.64	27.11	26.86
200024	9	45.8296409	-0.3610569	3.06	26.05	25.93	28.74	27.79
200022	9	45.8619395	-0.3650117	3.11	25.88	25.22	27.72	26.90
129186	1	45.8568102	-0.3973698	3.08	25.89	25.15	29.37	28.25
129064	1	45.8596435	-0.4000595	3.05	25.24	24.72	27.56	26.86
200080	9	45.8887853	-0.1798982	3.07	24.69	24.62	29.02	27.79
151860	9	45.8716091	-0.2105246	3.14	25.78	25.26	29.88	29.32
200059	1	45.8468168	-0.2246546	3.09	24.96	24.17	28.74	27.67
200056	1	45.8763139	-0.2354017	3.07	25.96	25.29	26.91	26.62
200053	9	45.8717925	-0.2400481	3.08	25.87	25.44	26.41	26.19
200051	9	45.8628189	-0.2445371	3.05	25.27	24.85	29.75	27.79
200081	9	45.7334860	-0.1686581	3.09	25.67	24.55	26.91	26.87
200078	1	45.7015111	-0.1729908	3.09	25.92	25.40	28.74	27.90
153835	9	45.6720010	-0.1946206	3.10	26.09	25.17	27.72	27.79
149742	1	45.6857287	-0.2282736	3.07	25.22	24.06	26.84	26.29
200054	1	45.7253371	-0.2373938	3.08	25.19	23.96	29.18	26.21
200049	9	45.7385901	-0.2959809	3.15	25.95	25.25	26.44	28.25
200037	1	45.6846825	-0.3199708	3.12	25.25	24.42	27.0	26.40
134818	1	45.7400458	-0.3495975	3.09	25.18	24.73	29.01	26.20
200010	1	45.7387753	-0.3836100	3.09	25.72	25.26	28.14	27.66
200042	-	45.8615316	-0.3139986	-	25.51	25.44	25.81	28.39
200039	-	45.8485514	-0.3186245	-	24.35	24.32	25.31	27.50
200035	-	45.8410366	-0.3259274	-	25.25	25.24	25.78	28.39
200033	-	45.9246314	-0.3372512	-	25.36	25.35	25.89	27.69
200032	-	45.9135162	-0.3439103	-	25.46	25.51	25.77	28.16
200025	-	45.8977845	-0.3523593	-	23.86	24.39	25.70	27.48
200017	-	45.9378002	-0.3751044	-	25.22	25.19	25.57	26.77
200013	-	45.8849155	-0.3818844	-	24.74	24.85	25.19	27.87
200008	-	45.8725575	-0.3877240	-	24.74	24.94	25.19	26.78
157346	-	45.9377785	-0.1692430	-	24.49	24.86	26.07	27.84
200070	-	45.9190518	-0.1932825	-	24.60	24.57	25.65	26.65
200061	-	45.8754786	-0.2157702	-	25.44	25.60	25.87	27.11
200072	-	45.7212709	-0.1852447	-	25.16	25.23	25.90	27.45
152485	-	45.7426946	-0.2050101	-	24.67	25.02	26.04	26.90
138887	-	45.7588554	-0.3143150	-	25.30	25.32	26.77	27.47
200030	-	45.7429894	-0.3447024	-	24.86	24.94	26.04	26.90
200019	-	45.7487272	-0.3660515	-	25.30	25.47	25.92	28.32
200003	-	45.7533152	-0.3899518	-	25.26	25.15	25.52	26.49
200071	-	45.8523954	-0.1880691	-	25.13	25.11	25.53	28.67
200068	-	45.9255966	-0.2029346	-	25.06	25.05	25.29	26.06
152379	-	45.8259247	-0.2064361	-	25.23	25.31	25.94	27.20
200058	-	45.9143845	-0.2298955	-	25.55	25.48	25.95	27.35
155649	-	45.7474915	-0.1806719	-	25.08	25.45	26.00	27.33

Table 5.9: J0124 LAEs with spectroscopic redshifts.

ID	FOUND	RA(J2000) (deg)	DEC (deg)	z	NB (ap)	NB (au)	B (ap)	V (ap)
200043	1	21.2393609	0.7799650	3.10	25.09	24.03	26.95	27.27
200021	1	21.2154450	0.7506720	3.05	25.34	24.73	28.06	27.96
200012	1	21.2113367	0.7311057	3.08	24.98	24.91	28.44	26.02
200005	1	21.1913110	0.7213967	3.07	25.28	24.88	28.45	27.88
200091	1	21.2884534	0.9530500	3.12	25.27	24.97	27.02	26.9
200087	1	21.2630301	0.9429632	3.11	23.82	23.63	26.23	25.98
200080	9	21.2886938	0.9206413	3.07	25.56	25.16	26.52	27.36
200078	9	21.2603419	0.9163973	3.07	26.03	25.66	27.47	27.08
200077	9	21.2686955	0.9128859	3.09	25.75	25.54	28.57	28.07
200060	9	21.1912251	0.8760458	3.10	24.67	24.51	25.57	25.26
200094	9	21.0657840	0.9656986	3.11	26.03	26.02	27.51	27.33
149863	1	21.0344201	0.9491617	3.07	24.54	24.38	27.57	27.84
200086	1	21.0697655	0.9395095	3.06	25.55	24.91	28.45	26.99
200081	1	21.0545545	0.9248621	3.07	25.81	25.79	26.31	26.71
143801	1	21.0362659	0.8947614	3.09	25.18	24.83	27.04	28.31
142267	1	21.1178735	0.8804999	3.07	24.37	24.01	28.31	26.25
200059	1	21.0573207	0.8757147	3.12	25.81	25.79	26.31	26.29
200047	1	21.0286622	0.7972924	3.08	24.57	24.53	26.94	26.64
132672	1	21.0748206	0.7927110	3.07	24.71	24.23	27.19	27.81
200031	9	21.0510826	0.7659462	3.08	25.99	26.06	27.68	26.31
200023	9	21.1078545	0.7523031	3.06	26.11	26.13	26.81	26.84
200037	-	21.2854303	0.774719	-	25.93	25.94	27.00	26.76
200027	-	21.2310484	0.7605423	-	26.34	26.23	28.08	27.20
200024	-	21.2780551	0.7556725	-	26.04	26.01	26.57	27.10
200017	-	21.2454878	0.7399309	-	25.69	25.53	26.65	27.16
200008	-	21.2626698	0.7258626	-	23.99	23.92	25.66	25.83
200095	-	21.1966679	0.967427	-	25.66	25.70	26.24	26.67
200085	-	21.1877893	0.9377005	-	25.70	25.72	26.75	26.30
200084	-	21.2342921	0.9315584	-	25.93	25.49	26.95	27.49
200073	-	21.2113427	0.901309	-	26.59	26.41	28.03	26.53
200070	-	21.2413183	0.8987411	-	25.81	25.47	26.14	26.98
143891	-	21.2499102	0.8944817	-	25.57	25.48	28.50	26.90
200063	-	21.2597495	0.8786979	-	25.81	25.21	26.08	26.07
200092	-	21.1141126	0.9590584	-	25.22	24.54	26.55	25.60
200090	-	21.0804503	0.9535012	-	24.39	24.31	25.66	25.60
200082	-	21.0436826	0.9292383	-	26.25	26.32	27.00	27.42
200075	-	21.0700794	0.9022646	-	25.21	24.54	26.69	26.51
200067	-	21.0324348	0.8844075	-	25.15	25.01	26.74	26.51
200056	-	21.072931	0.8717157	-	26.03	25.99	26.34	26.58
200048	-	21.0975542	0.80497	-	26.00	26.02	26.47	25.82
200038	-	21.054275	0.7757187	-	26.17	26.11	27.78	27.31
200026	-	21.0713368	0.7595479	-	25.98	25.96	28.38	27.55
200051	-	21.0637685	0.8130678	-	25.91	25.85	27.63	26.83
200015	-	21.0219188	0.7376403	-	25.93	25.81	28.06	26.46
200010	-	21.0785900	0.7300109	-	24.51	24.51	26.84	27.33

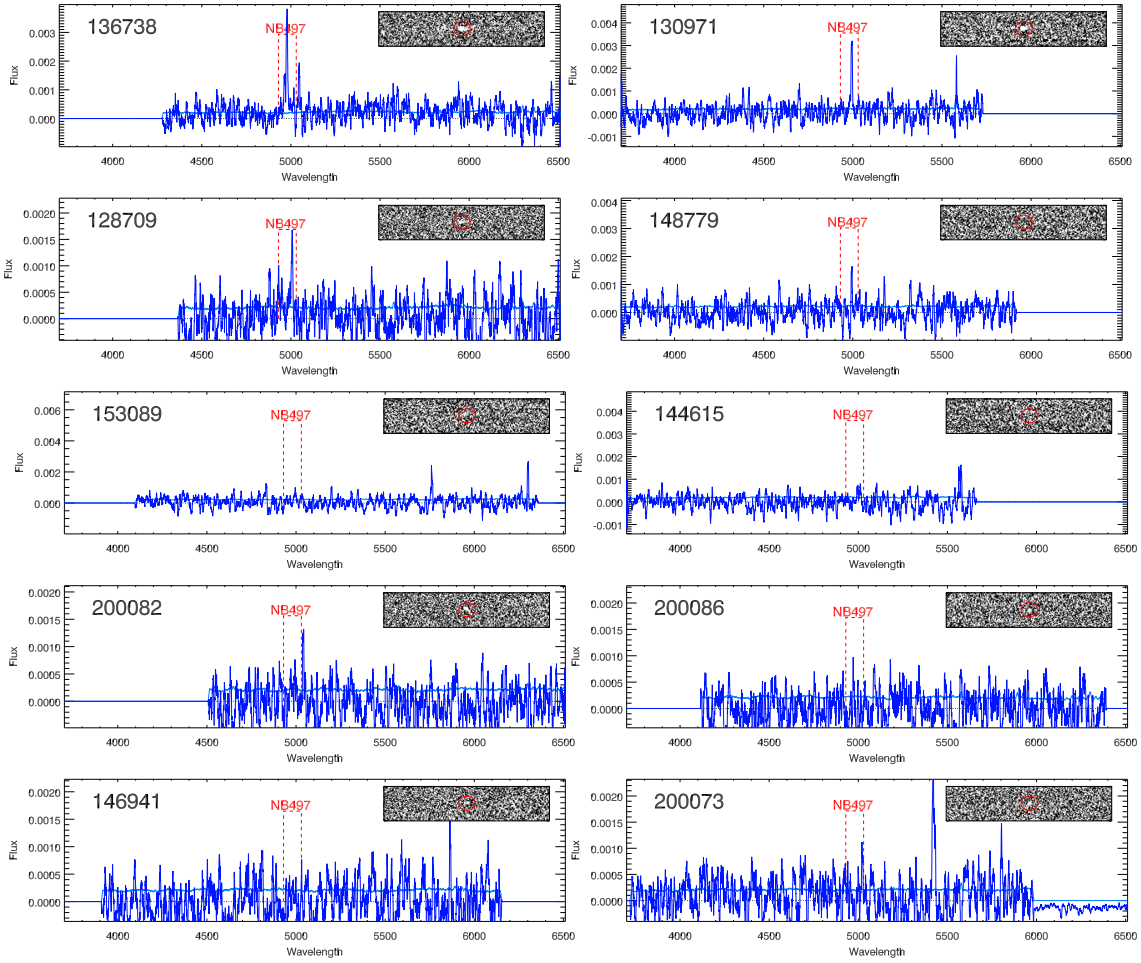

Figure 5.10: Q2359 VIMOS spectra. In each plot show the 1-d spectrum with the position of Lyα by the red box which represent the wavelength range of the narrow band filter. Also shown is the 2-d spectrum in the small box at the top. The top 3 rows are objects with Found = 1 while the rest are examples of objects with Found = 9.

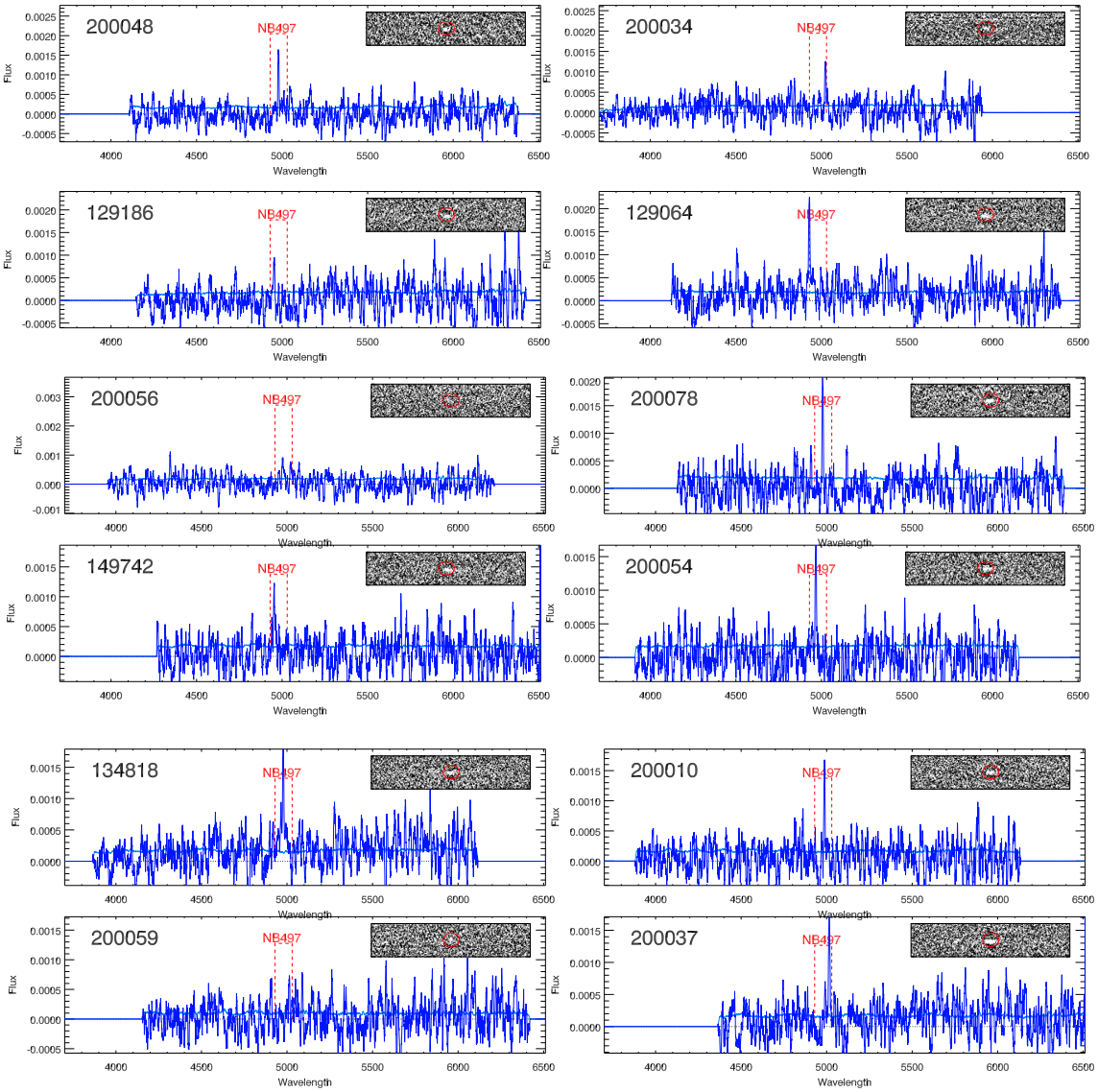

Figure 5.11: Q0302 VIMOS spectra for objects with Found = 1. In each plot show the 1-d spectrum with the position of Lyα by the red box which represent the wavelength range of the narrow band filter. Also shown is the 2-d spectrum in the small box at the top.

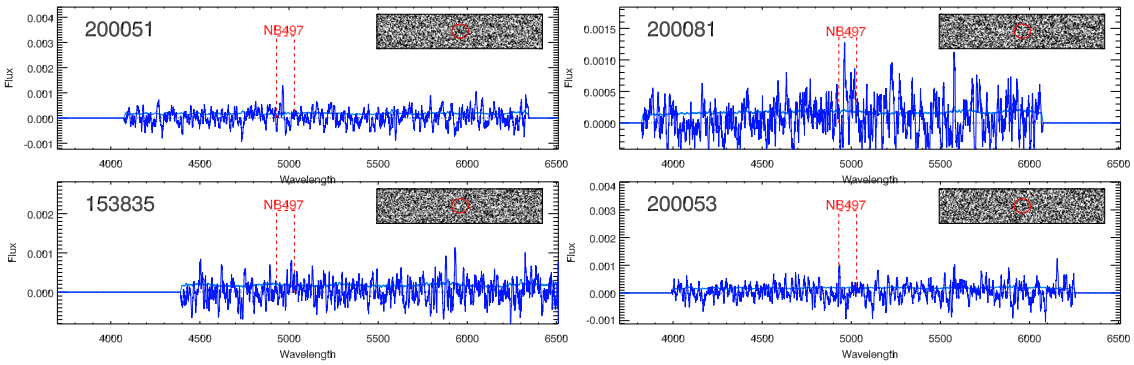

Figure 5.12: Same as Fig. 5.11. Examples of Q0302 VIMOS spectra for objects with Found = 9.

broadband filter) to search for LAE candidates photometrically. This motivated us to make two selection sets to find the best selection criteria. They can be compared by checking at their success rate from spectroscopic confirmation. At the same redshift ($z \sim 3.1$), our Set A selection is a two-colour approach which applied R-NB colour and B-NB colour, similarly to those in Fynbo et al. 2003; Nilsson et al. 2007; Ouchi et al. 2008. Our Set B, narrow-band/broad-band combinations, has previously been used by Hayashino et al. 2004; Gronwall et al. 2007.

As mentioned in previous section, we took spectra for our 128 LAE candidates which show a narrowband excess. We identified line emitters with the success rate of 0.62 ± 0.14 (Set A) and 0.57 ± 0.13 (Set B) of our all observed targets. The success rate is calculated from the ratio of the number of identified LAEs (Found =1) to the number of all observed LAEs in the selecion criteria. Table. 5.10 presents the number of observed LAEs and identified emission-line objects. Note that some of the undetected candidates may still have an emission line undetected at the S/N of our VIMOS spectra. We discuss later the difference it makes to counts and clustering if we assume that all the undetected targets are contaminating objects and not z $\sim$ 3.1 LAE.

Fig. 5.21 shows the colour magnitude diagrams of VIMOS LAE observations from the three fields observed with VIMOS (Q2359, Q0302, and J0124). The observed VIMOS LAE and the spectroscopically confirmed LAE are presented with light blue circles and purple filled circles respectively. The lines shows the selection criteria from Set A (left panel) and Set B (right panel). In the selection area, it shows that

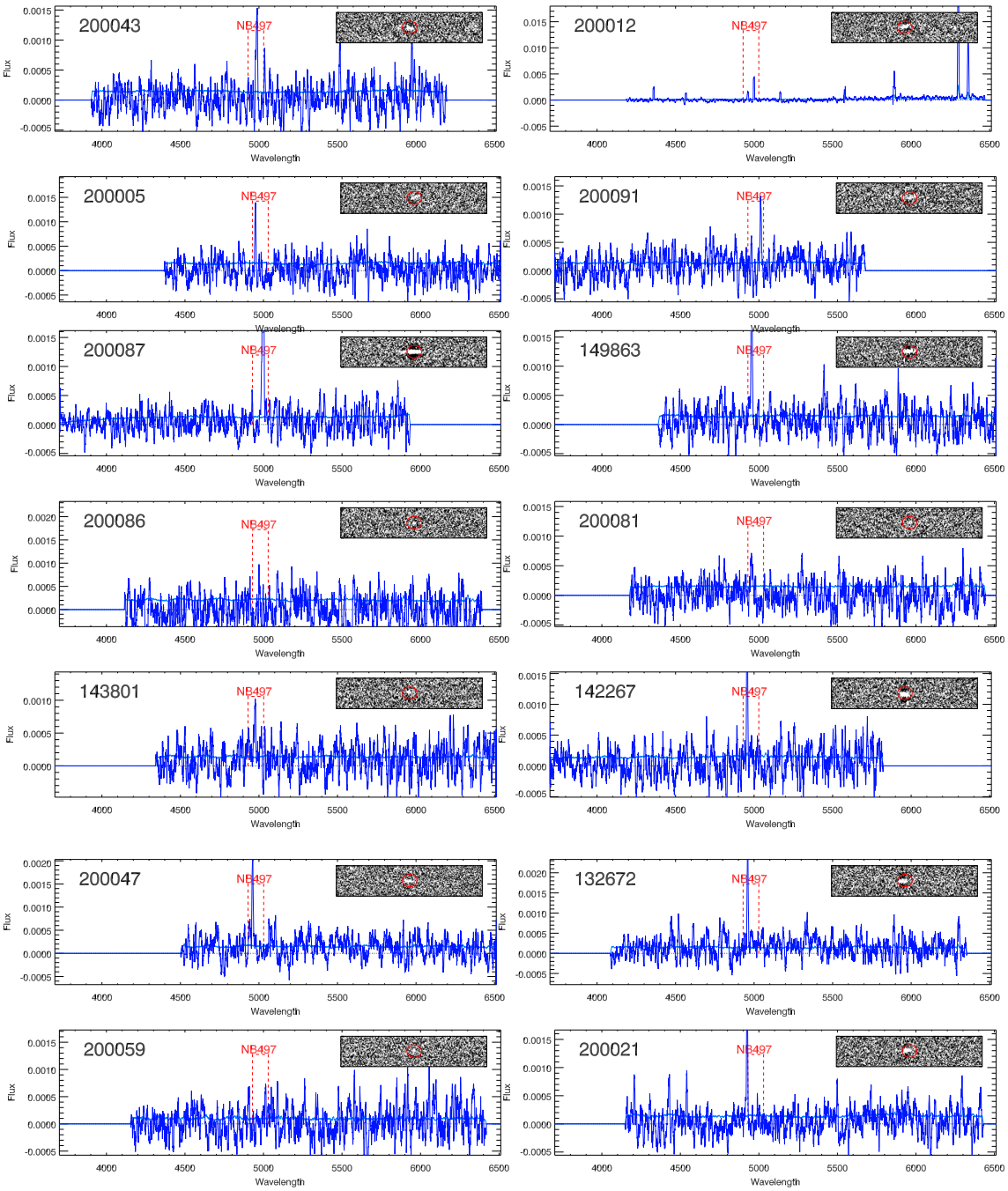

Figure 5.13: J0124 VIMOS spectra for objects with Found = 1. In each plot show the 1-d spectrum with the position of Lyα by the red box which represent the wavelength range of the narrow band filter. Also shown is the 2-d spectrum in the small box at the top.

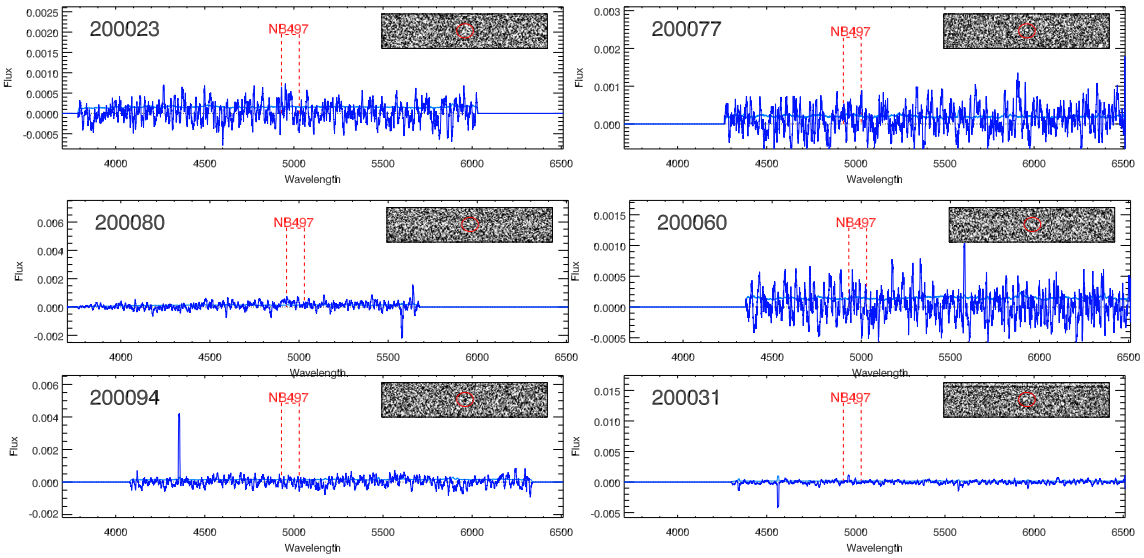

Figure 5.14: Same as Fig. 5.13. Examples of J0124 VIMOS spectra for objects with Found = 9.

Field	observed LAEs	Set A			Set B		
		N_{in}	f1	f9	N_{in}	f1	f9
Q2359	37	6	4/6	1/6	6	4/6	1/6
Q0302	46	12	5/12	3/12	13	5/13	3/13
J0124	45	14	11/14	1/14	16	11/16	1/16
Total	128	32	20/32	5/32	35	20/35	5/35

N_{in} : The number of observed LAEs in the selecion criteria.
f1 : The ratio of identified LAEs (Found =1) to observed LAEs in the selecion criteria.
f9 : The ratio of identified LAEs (Found =9) to observed LAEs in the selecion criteria.

Table 5.10: The number of VIMOS spectroscopically confirmed LAEs.

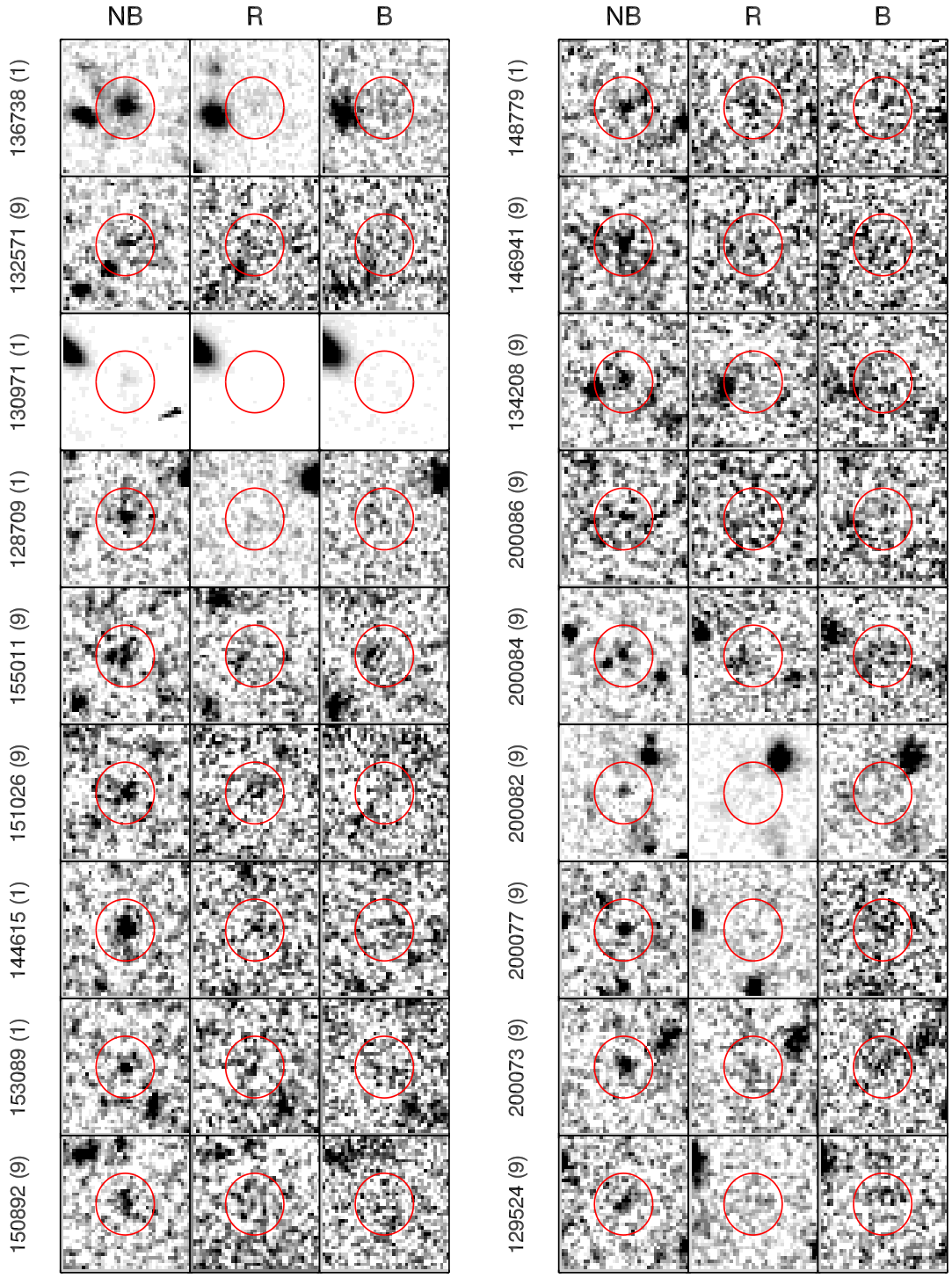

Figure 5.15: Snapshopts of our spectroscopically-confirmed LAEs in Q2359. Each object is shown in NB497, R, and B images repectively. Snapshotsize is a 8″x8″. ID of object is on the left of each panel with object classification in parentheses. Full details of objects are in Table 5.7.

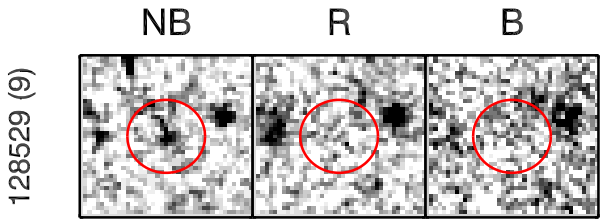

Figure 5.16: Snapshopts of our spectroscopically-confirmed LAEs in Q2359 (cont).

the success rate of Set A and Set B is similar (about 2/3). Compared to the success rate in other's work, Ouchi et al. 2008 have identified line emitters from 60% of their targets at this redshift. Fynbo et al. (2001, 2003) reported the spectroscopic follow-up success rate of 75 - 90% for z $\sim$ 3 surveys.

5.4 Narrowband counts

We estimated the sky densities of galaxies as a function of narrowband magnitude as shown in Fig. 5.22 (The top panel shows Set A LAEs while the bottom panel shows Set B LAEs). The different symbols show the surface densities in five different fields as labelled in the Figure. We show the average density of Set A and Set B LAEs by a blue solid line in each plot. If we apply a contamination correction, these averages will be reduced by a factor of $\approx 2/3$ (as described in Sec. 5.3). Our error bars were calculated by the field-to-field errors method. We compared our LAE densities with the z $\sim$ 3.1 LAE data of Ouchi et al. (2008) (green solid line) from Subaru/XMM Newton Deep Survey (SXDS) Field. The selection criteria of their LAE samples are based on a two-colour approach which applied V-NB503 >1.2 colour and B-V >0.5. They measured the surface densities of objects detected in the NB503 data over $\simeq$ 1 deg^2 survey field while ours were observed in $\simeq$ 5 x 0.25 deg^2 survey fields. Ouchi et al (2008) have 356 photometric LAEs in $\simeq$ 1 deg^2 area while we have 550 LAEs (Set A) and 522 (Set B) from our 5 x 0.25 deg^2 area. Considering our LAE NB counts from each field, J0124 (crosses) shows higher number of LAE candidates in Set B at $22.5 < NB497 < 24$. We did visual checks to discount cosmic ray contamination and noisy pixels for both sets. In J0124, the counts seem elevated in Set B but

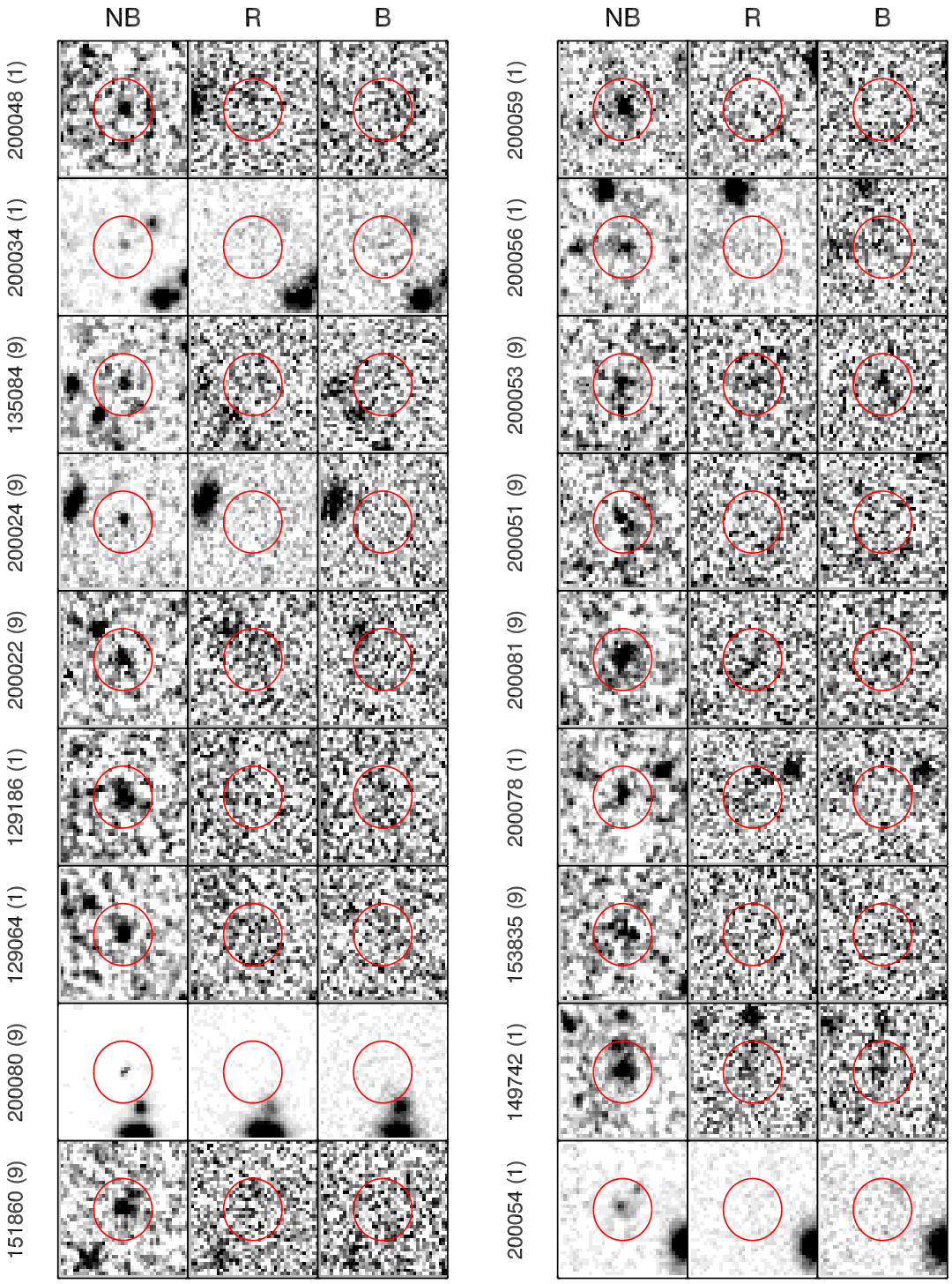

Figure 5.17: Same as Fig. 5.15 but for Q0302. Full details of objects are in Table 5.8.

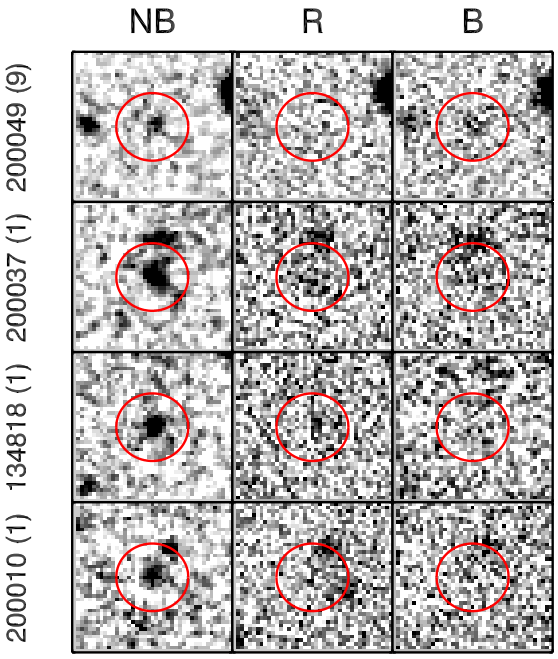

Figure 5.18: Snapshopts of our spectroscopically-confirmed LAEs in Q0302 (cont).

not in Set A. This is because many objects in Set A were cut out during the eye-selection process as they looked unlikely to be LAE candidates. The other fields are consistent with each other at the 1σ level across the wavelength range considered.

Also plotted is the luminosity functions for the Lyα galaxies at z = 3.1 found by Gronwall et al. (2007) (red line). They conducted a 0.28 deg^2 survey at $z \sim 3.1$ in the Extended Chandra Deep Field South using the MOSAIC camera on the CTIO 4-m telescope. Gronwall et al. (2007) made a selection based on a narrow-band frame compared to a combined broad-band B+V image. This method is comparable to our selection method for Set B. Their LAE candidates were identified using a scaled version of the B+V continuum image from the narrowband frame, ie, $NB5000 - (B + V) < 1.03$ with the narrow-band magnitude limit of 25.4. They identified a statistically complete sample of 162 galaxies. They calculated the density of their LAEs with rest-frame equivalent widths greater than 20 Å (approximately 80 Å in the observer's frame). A direct comparison of Gronwall et al. (2007) and (Ouchi et al., 2008) luminosity functions of z $\sim$ 3.1 LAEs is shown by Ciardullo et al. 2012. Ciardullo et al. 2012 extended the study of Gronwall et al. (2007) by

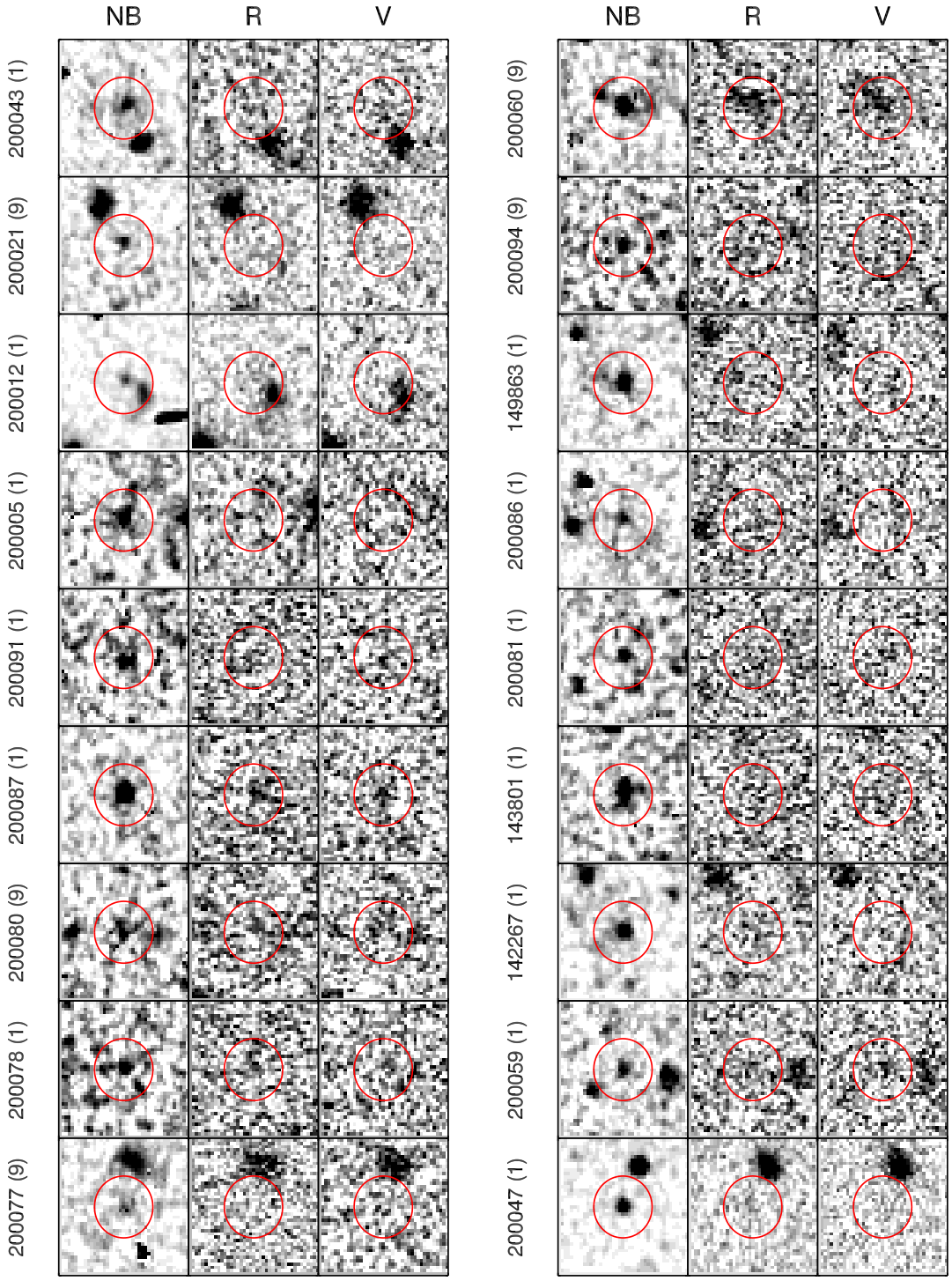

Figure 5.19: Snapshopts of our spectroscopically-confirmed LAEs in J0124. Each object is shown in NB497, R, and V images repectively. Snapshotsize is a 8″x8″. ID of object is on the left of each panel with object classification in parentheses. Full details of objects are in Table 5.9.

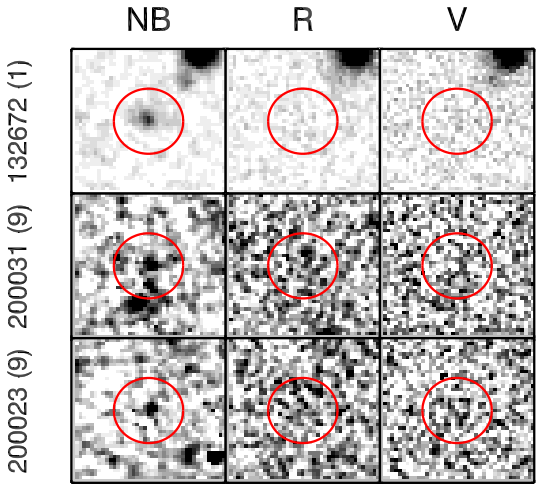

Figure 5.20: Snapshopts of our spectroscopically-confirmed LAEs in J0124 (cont).

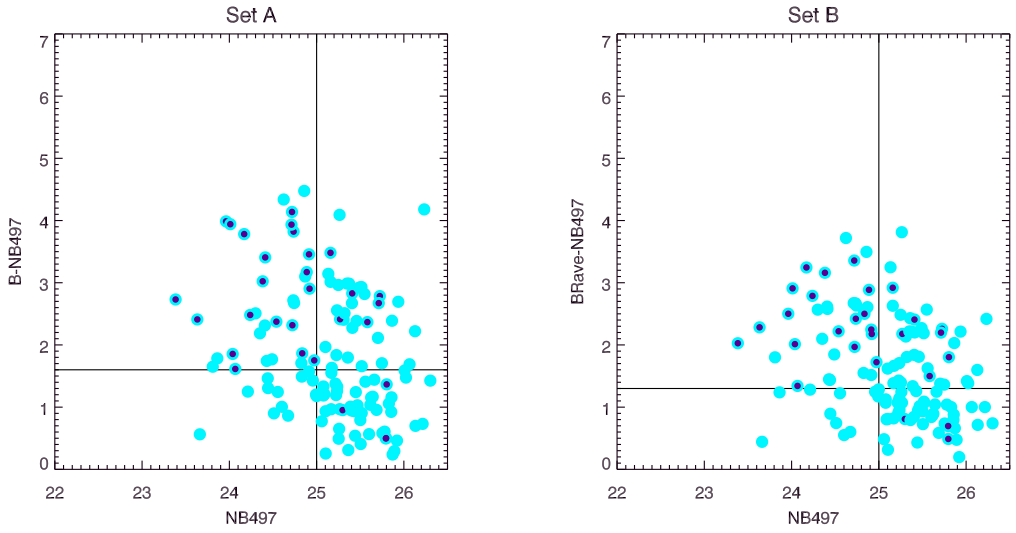

Figure 5.21: Colour magnitude diagrams of VIMOS LAE observation.The observed VIMOS LAE and the spectroscopically confirmed LAE (Found = 1) are presented with light blue circles and purple filled circles respectively. Black lines indicate the selection criteria (LHS for Set A, RHS for Set B).

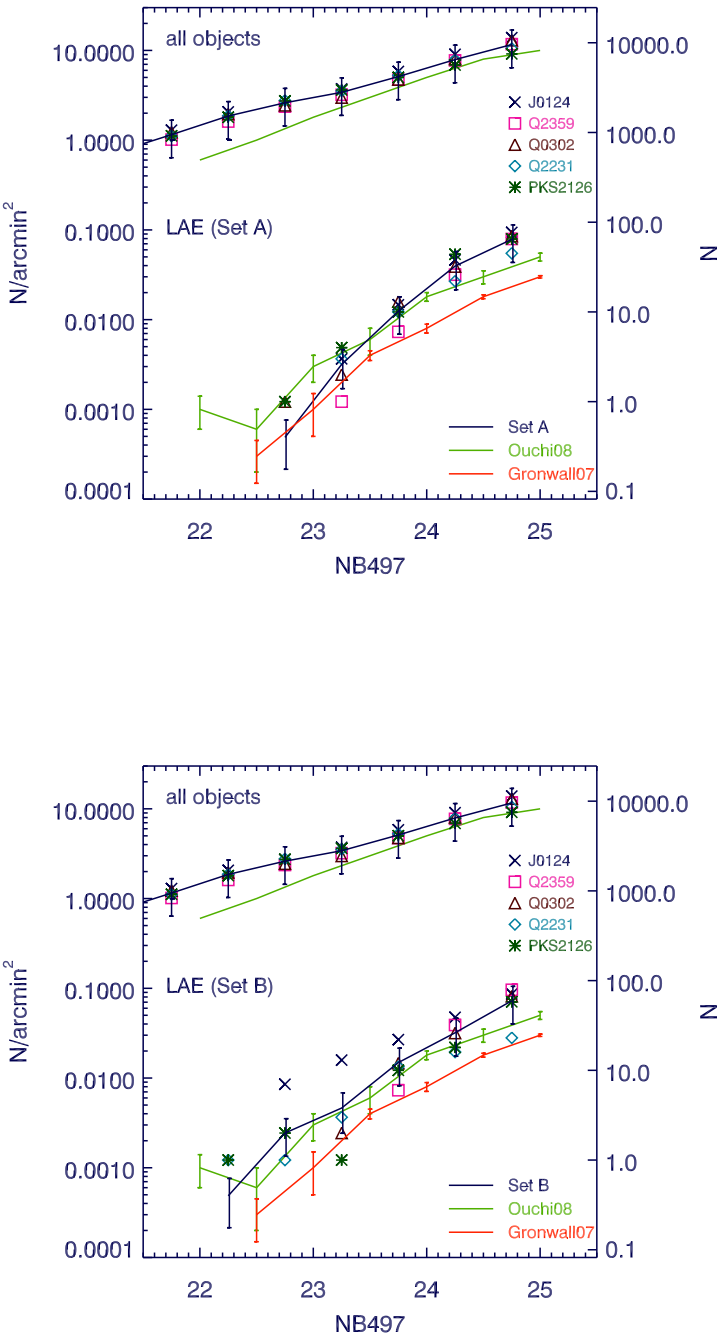

Figure 5.22: Surface densities of objects detected in the NB497 data. Objects from each field are shown in different symbols labelled in the plot. Y-axis on the left indicates the surface density while the right axis indicates the number of objects (per 0.25 deg^2 survey area). The upper points show the surface densities from all objects from the narrowband image while the lower points present the surface densities of our LAE candidates. Also shown are the average surface densities of our LAEs (blue solid line). We compared our LAE densities with Ouchi et al.(2008) (green solid line) and Gronwall et al. (2007) (red line). Top plot represents Set A LAEs while bottom plot represents Set B LAEs.

re-imaging the ECDF-S with a 57 Å FWHM nearly top-hat filter centered near 5010 Å. They found a total number of likely z $\sim$ 3.1 LAE to 360, some of which are overlapped with the sample from Gronwall et al. (2007). They then reproduced the luminosity function and concluded that their result is statistically identical to values in Gronwall et al. (2007) and Ouchi et al. (2008). The normalisations of the functions are also consistent to $\sim$ 25%.

Our NB LAE average counts reasonably agree with Ouchi et al. 2008 and are higher than for Gronwall et al. 2007. In Set A ($EW_{rest} \approx 20$ Å), our result is lower than Ouchi et al. ($EW_{rest} \approx 45$ Å) at NB497 < 23.5. As mentioned earlier, many bright objects in Set A were cut out by eye-selection as they looked unlikely to be LAE candidates thus the density is low at brighter magnitudes. Set B LAEs ($EW_{rest} \approx 44$ Å) shows an excellent agreement, both in shape and in normalisation, with Ouchi et al. (2008)($EW_{rest} \approx 45$ Å). However, the result of Gronwall et al. (2007) is lower than in Ouchi et al. (2008) and ours. The suggestion from Ciardullo et al. 2012 is that the luminosity function curve for Ouchi et al. (2008) is based on a rest-frame equivalent width limit of 45 Å, while the the sample of Gronwall et al. (2007) has the EW_{rest} of 20 Å. Thus for consistency with their (Gronwall et al., 2007; Ciardullo et al., 2012) selection criteria, their curve should be increased by $\geq$ 10%. When comparing our results to others based on the equivalent width limits, we found that our Set B result shows better agreement with those of Ouchi et al, probably due to their similar EW limit. However, this does not apply with our Set A where we have similar EW limit with Gronwall et al. We expect to see similar result with their result but our Set A result is higher than that of Gronwall et al. The suggestion is that these discrepancies may be due to other systematic effects.

5.5 Redshift distributions

The redshift distribution, $n(z)$, for VIMOS LAEs (histogram) is shown in Fig. 5.23. The $n(z)$ is in agreement with what might be expected given the throughput of the NB497 filter (blue line). Note that our VIMOS LAE redshift distribution is a combination of class Found = 1 (spectroscopically confirmed) and Found = 9 (more

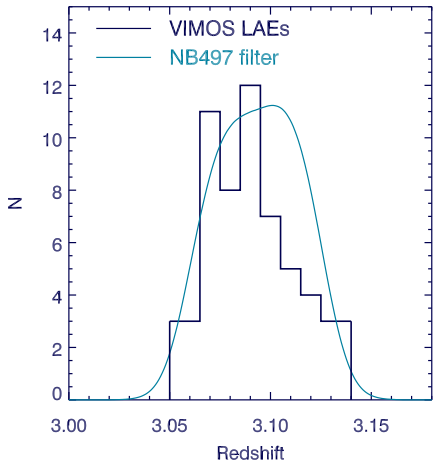

Figure 5.23: Redshift distribution for LAE spectroscopic identification from VIMOS (histogram) and the NB497 filter with wavelength converted to redshift (light blue solid line). The NB497 filter is normalised by the number of identified LAEs.

tentative detections are attributed) which gives a total number of 62 LAE redshifts. As our VIMOS LAE redshift distribution is in good agreement with the NB497 filter distribution, we will use these two distributions for our luminosity function and clustering analysis.

We calculated the survey volumes by using 3 redshift distributions: VIMOS LAE spectroscopic confirmation $n(z)$, redshift distribution deduced from NB497 filter, and a top-hat redshift distribution. We calculated the volume of our 0.25 deg^2 survey area by calculating the fraction of the volume from each 0.01 redshift bin and summing up all the volume in the distribution. The effective survey volumes are given as 51,963 Mpc^3 (VIMOS LAE $n(z)$), 61,715 Mpc^3 (NB497 filter), and 100,678 Mpc^3 (top-hat $n(z)$) from redshift range $3.05 \leq z \leq 3.14$.

5.6 Continuum luminosity function

We then estimated the R-band continuum luminosity functions of our sample of LAEs/LBGs and compared with other observations. We divided our number counts by the volume (discussed in Sec. 5.5) to obtain the luminosity functions. Our R-

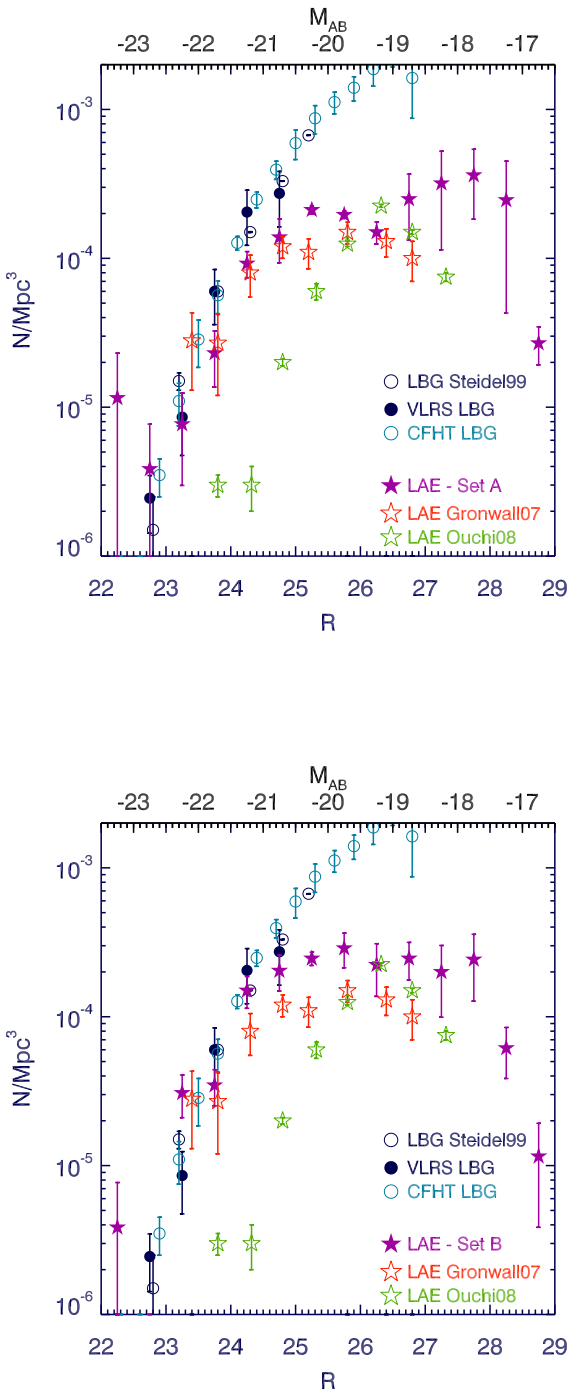

Figure 5.24: Luminosity function of our LAEs with (pink filled stars) compared to z = 3.1 LAEs of Gronwall et al 2007 (red stars) and Ouchi et al. 2008 (green stars). Also shown is the rest-frame 1700 Å luminosity function of z = 3.04 LBGs from Steidel et al (1999) (circles), while our VLRS LBGS are represent by filled circles. The UV luminosity function of z $\sim$ 3-5 LBGs from the CFHT fields of van der Burg et al. (2010) is also shown by light blue circles. Top plot represents Set A LAEs while bottom plot represents Set B LAEs.

band continuum luminosity functions are shown in Fig. 5.24 (The top plot shows Set A LAEs while the bottom plot shows Set B LAEs). We compared our results (pink filled stars) to Gronwall et al. 2007 (red stars) and Ouchi et al. 2008 (green stars). Our high LAE luminosity function (LF) may be due to high contamination. When we applied a contamination correction, we found that our 1700 Å continuum magnitude (auto) LAE luminosity function appears similar to that of Gronwall et al with a relatively high number density of LAE being detected at bright magnitudes. We note that there are only one LAE (Set B) or two LAEs (Set A) in the first magnitude bin. Those objects are from PKS2126 or Q2231 field which we have no spectroscopic data. Our results also lie close to the LF of Gronwall at $M_\star$ magnitudes and fainter. Our results and Gronwall et al's result appear in contradiction with the result of Ouchi et al. (2008) who found relatively lower LAE number densities at brighter magnitudes. The discrepancy between our results and Ouchi et al. at brighter magnitudes ($R < 23$) may be due to high contamination as we have no VIMOS LAE showing up at the bright end. In Set A where we have similar EW limit with Gronwall et al, we see a good agreement with their result. However, in Set B where the EW limit is higher than in Set A, one might expect to see the lower continuum LF. This is still difficult to explain by the EW limit. Note that our results shown here are the average R-band continuum luminosity functions from our 5 fields which gives more than 500 objects in 5 x 0.25 deg^2 survey area.

We also compared our VLRS LBG luminosity function (filled circles) with the rest-frame 1700 Å luminosity function of z $\sim$ 3.04 LBGs from Steidel et al. 1999 (navy circles) and with the UV luminosity function of z $\sim$ 3-5 LBGs from the CFHT Legacy Survey Deep fields (van der Burg et al., 2010) (light blue circles). van der Burg et al. estimated the rest-frame 1600 Å luminosity function of z $\sim$ 3-5 LBGs, from four independent fields spread across the sky, covering 4 square degrees. Our VLRS LBG LF is consistent with their results within the error bars. The turnover in the VLRS counts at R $\geq$ 24.5 is due to the magnitude limit of the redshift survey.

As usual for LAE detected by NB, our selection is basically limited by emission line equivalent width. This means that even LBGs with strong emission line strengths are unlikely to be selected because their strong continua reduce their

equivalent widths. Therefore we expect our NB counts not to include many LBGs at bright magnitudes. We have checked that when we relax the LAE selection at brighter magnitudes, emission line LBGs start to be included in the LAE sample.

Our continuum LAE LF lies well below the LBG LF at magnitudes fainter than $M_\star$. This result could be interpreted as indicating that the fraction of LBGs showing Lyman-alpha emission may decrease with fainter LBG magnitudes. This is also consisted with the idea that most of LAE lie at the faint end of the usual LBG luminosity function. However this would be at odds with the results of Stark et al. 2010 who found evidence in LBG samples that the fraction showing Lyα emission actually increased with decreasing galaxy continuum luminosity. Our LAE continuum LF appears similar to that of Gronwall et al with a relatively high number density of LAE being detected at bright magnitudes with the LAE number density dropping relative to the LBG number density at fainter magnitudes. These two results appear in contradiction with the result of Ouchi et al who found relatively lower LAE number densities at brighter magnitudes. If the result of Stark et al was correct we should have found that the LAE fraction should have increased at fainter luminosities due to less dust obscuration in fainter galaxies.

Unfortunately it may not be possible to rule out the Ouchi et al or the Stark et al results because of the possibility of magnitude dependent contamination in the LAE sample. For example, we find that in our sample of VIMOS confirmed LAE, the brightest LAE has R(auto)=24.9 and all other 31 confirmed LAE are fainter.

Orsi et al. (2012) compared their model predictions of the UV (λ $\sim$1500 Å) luminosity function of $z \sim 3$ LAEs to the observational data from Ouchi et al. (2008); Gronwall et al. (2007). They concluded that their models of the UV luminosity function of LAE and the fraction of LAE in LBG samples at high redshift are in partial agreement with observations. Their results seems to underpredict the observational results, however, they are in a reasonable agreement at the bright end of the LF measured by Ouchi et al. (2008) and inconsistent with the faint end result from Gronwall et al. (2007). Orsi et al. (2012) also predicted that Lyα emitters are a subset of the galaxy population with lower metallicities, lower instantaneous star formation rates and larger sizes than the overall population at the same UV

luminosity.

Most LAEs are known as star-forming galaxies at $z \approx$ 2-7 with a faint-ultraviolet (UV) continuum but a prominent Lyα emission line (Ouchi et al., 2008). A typical star formation rate found in Lyα emitters are $\sim$ 1-10 $M_\odot$ yr^{-1} (e.g. Cowie & Hu 1998; Hu et al. 1998; Gronwall et al. 2007; Nilsson et al. 2007). A number of authors (e.g. Ajiki et al. 2003; Taniguchi et al. 2005; Gronwall et al. 2007) have reported a discrepancy between the SFR estimated from Lyα luminosity and SFR estimated from UV luminosity. They found larger SFR derived from UV luminosity than those estimated from Lyα luminosity. However, Nilsson et al. (2007) found SFRs $\sim$ 0.5-6 $M_\odot$ yr^{-1} with no discrepancy between continuum and emission line derived SFRs. Gronwall et al. (2007) found the most likely value for the LAE SFR density of the $z \sim 3.1$ universe is 8.6×10^{-3} $h_{70} M_\odot$ yr^{-1} Mpc^{-3}. They suggested that the true SFR density is probably $\sim$ 3.5 times higher. For a comparison with LBG, the star formation rate density at $z \sim 3.1$ LBG is ~ 0.01 $h_{70} M_\odot$ yr^{-1} Mpc^{-3} before extinction (Madau et al., 1998; Steidel et al., 1999). Gronwall et al. 2007 estimated the dust-corrected SFR density for LAEs, ~ 0.03 $h_{70} M_\odot$ yr^{-1} Mpc^{-3} which is $\sim 75\%$ of the LBG value, however, this number is highly uncertain.

5.7 Clustering

To further evaluate the idea that LAEs are a subset of the LBG population, we now calculate the LAE clustering properties by using the angular two-point correlation function, $w(\theta)$.

5.7.1 Clustering Estimator and its error

We estimate the angular two-point correlation function, $w(\theta)$, using the Landy-Szalay estimator.

$$w(\theta) = \frac{\mathrm{DD}(\theta) - 2\mathrm{DR}(\theta) + \mathrm{RR}(\theta)}{\mathrm{RR}(\theta)} \tag{5.7.6}$$

where DD(θ), DR(θ), and RR(θ) is the number of galaxy-galaxy pairs, galaxy-

random pairs and random-random pairs as a function of θ. For each field, we generated the uniform random points with the same area as the Subaru Suprime-Cam observation. Our random catalogues have 40× of the number of LAE candidates in each field.

We use two error estimators here as mentioned in section 1.3.

1. We used Poisson error which is given by

$$\sigma_{\rm Poi}(\theta) = \frac{1 + w(\theta)}{\sqrt{DD(\theta)/2}} \tag{5.7.7}$$

2. The field-to-field error is also used. This is simply a standard error on the mean of the measurement in each field from the best estimate and is calculated using

$$\sigma_{\rm FtF}(\theta) = \sqrt{\frac{1}{N}\frac{1}{N-1}\sum_{i=1}^{N}[w_i(\theta) - \overline{w}(\theta)]^2} \tag{5.7.8}$$

where N is the number of fields, $N = 5$. $w_i(\theta)$ is a measurement from the ith field and $\overline{w}(\theta)$ is the mean value.

5.7.2 LAE random catalogues

A random catalogue is required when calculating the correlation function. We generated uniform random points with the same geometry as the Subaru Suprime-Cam observation, taking into account gaps caused by bright stars. We also masked out more gaps in some fields. In Q2231, the broad band imaging was performed using the INT Wide Field Camera and does not cover the top right region (North East) and also the observations were not performed with a large enough dithering to cover up the gaps between the chips, so we masked out both the chip gaps and the top right corner of the narrow band image. For J0124, we masked out objects that lie in the CCD gaps and also excluded the bottom-right corner as it was affected by a big halo from a bright star. We also excluded spurious objects or cosmic ray-like objects in the diagonal area in PKS2126 field. Our random catalogues have 40× of the number of LAEs candidates in each field.

Fig. 5.25 shows the distribution of LAE candidates (pink dots) and LAE randoms

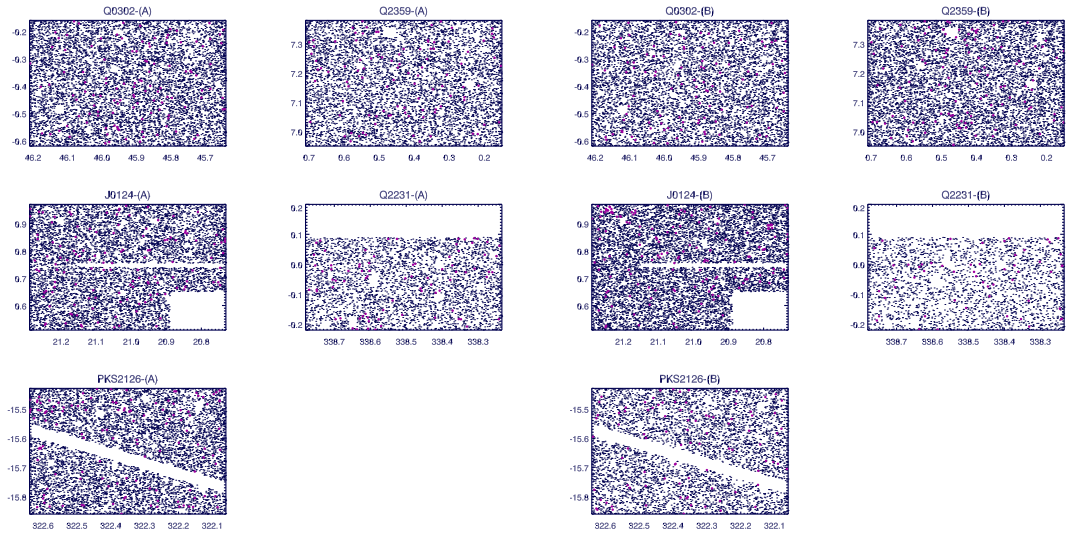

Figure 5.25: Randoms for Set A LAEs (LHS) and Set B LAEs (RHS). LAEs and randoms are presented by pink dots and blue dots. We masked out bad regions. There are more candidates in Set B thus the bigger number of ramdom points is made.

for Set A (LHS) and Set B (RHS). As shown, we masked out bad regions and bright stars. These randoms will be used to calculate the correlation function.

5.7.3 LAE-LAE clustering

We have measured the auto-correlation function for our $z \sim 3$ LAE samples as shown in Fig. 5.26. Poisson error bars are assumed at $\theta < 1'.0$ and Field-to-Field error at $\theta > 1'.0$. We used Field-to-Field error above $1'.0$ because this method is not good at the small separations where the number of LAE pairs is too small. Poisson statistics are more reliable at small separations but underpredict the error when the number of pairs becomes large at higher angular separations. Blue filled circles and pink filled circles present the result from LAE Set A and Set B respectively. The estimated integral constraints, as described in Sec 1.3.3, are $\mathcal{I} = 0.01$ and $\mathcal{I} = 0.02$ for Set A and Set B sample respectively.

We compared our results in Fig. 5.26 with several measurements from other authors. Ouchi et al. (2010) used 356 $z = 3.1$ LAEs from Ouchi et al. (2008) who carried out a wide-field narrowband survey in the wide-field (1 deg^2) Subaru/XMM-Newton Deep Survery (SXDS) to measure the correlation function. Their angular

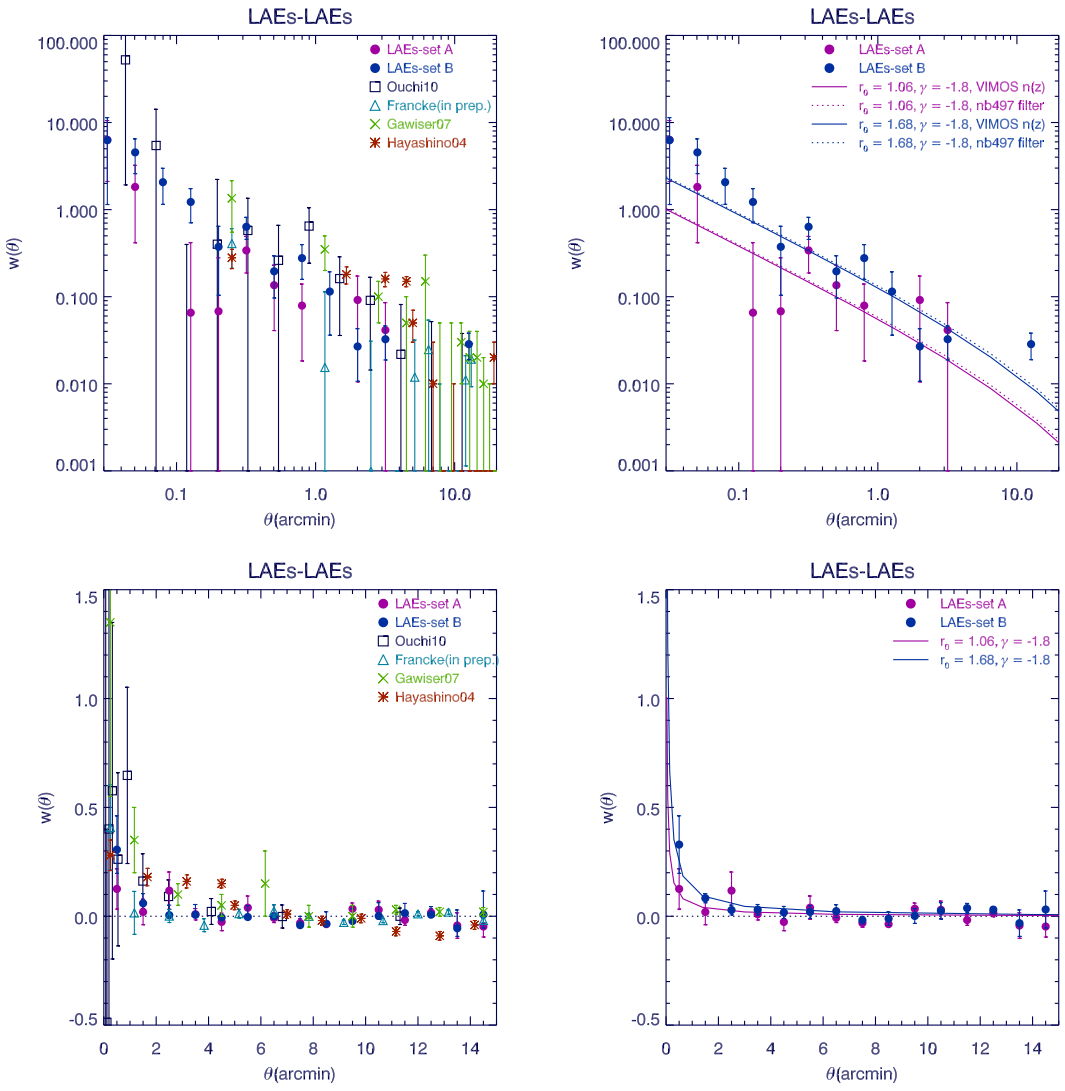

Figure 5.26: Angular correlation function of $z \sim 3$ LAEs. Result from Set A and Set B LAE are shown by pink filled circles and blue filled circles, repectively. We also compared our results with other measurements; Ouchi et al. (squares), Gawiser et al. (green crosses), Hayashino et al. (asterisks). Results from Francke et al. (in prep) are also presented by triangles (combined from sources in HE0940-1050 and Q0042-2627). On RHS plots, we show the correlation function, $\xi(r)$, from the projected $w(\theta)$, via the Limber's equation by pink line and blue line. In the Limber's approximation, we found $r_0 = 1.06$ h^{-1}Mpc. and $\gamma = 1.8$ (pink line) for Set A LAE, while we found $r_0 = 1.68$ h^{-1}Mpc. and $\gamma = 1.8$ (blue line) for Set B LAE. (Top panel show the result in log scale while bottom panel show the result in linear scale.)

correlation function of $z = 3.1$ LAEs with narrowband magnitude limits of 25.3 is represented by squares. We also compared our results with Gawiser et al. (2007) (represented by green crosses) who studied the clustering properties of 162 LAEs at $z = 3.1$ at a narrow-band completeness limit of 25.4 which were observed in the deep narrow-band MUSYC survey. Their EW_{rest} is about 20 Å. Asterisks show a result from Hayashino et al. (2004) which is obtained from 283 $z = 3.1$ LAE candidates with NB497 magnitude limit < 25.8 and EW_{rest} 38 Å observed in the SSA22a field using the Subaru Telescope. This was a further observation of SSA22a of Steidel et al. (2000) who found 72 LAEs. However, the observed area in Hayashino et al. (2004) is about 10 times larger than in Steidel et al. (2000). Both Steidel et al and Hayashino et al concluded that no significant clustering of $z = 3.1$ LAEs has been shown inside the SSA22a area. Results from Francke et al. (in prep) are also presented by triangles (combined from sources in HE0940-1050 and Q0042-2627). Francke et al. used Mosaic-II narrowband images from the Blanco telescope in CTIO and broadband images from CFHT in two fields, HE0940-1050 and Q0042-2627. Their narrowband magnitude limit is 25.5.

Results from Set B shows higher clustering than Set A but they are still statistically consistent at $\theta > 0.2$ arcmin. When we looked at the clustering result from individual fields in Set A, we found that some of our fields (Q0032 and J0124) have low/no clustering signal at separations < 1 arcmin. We have chosen to show the raw results here because frequently others did not apply the contamination correction at this stage. The contamination correction will be applied when we calculate the true r_0. Comparing our results with each measurement, we found that our results agree with Ouchi et al. (2010) within their error bars although their result show a high clustering at small scale $\theta < 0.1$ arcmin. At larger scale, Hayashino et al. (2004) and Gawiser et al. (2007) show slightly higher clustering amplitude than ours, but they are consistent within error bars. Francke et al. reported lower clustering than Gawiser et al. (2007) and Ouchi et al. (2008), and they did not get a clustering signal at separations below ~ 3 arcmin for the Q0042 field. However, their combined result is in agreement with our measurement. At the current state, it is still difficult to explain our discrepancies to other observations based on the equivalent width limits.

Our Set B result shows a better agreement with those of Ouchi et al. and Hayashino et al. due to similar EW limit. However, in Set A where we have similar EW limit with Gawiser et al., their clustering result is higher than ours.

$\xi(r)$ Power-law fits

By using Limber's equation (Limber, 1953), the spatial correlation function, $\xi(r)$ can be related to $w(\theta)$. The angular two-point correlation function $w(\theta)$ is basically a weighted projection of the spatial two-point correlation function $\xi(r)$. If the 3-D correlation function $\xi(r) \propto r^{-\gamma}$ then on small scales, the angular correlation function $w(\theta)$ shows the power-law behaviour but with a slope $1-\gamma$:

$$w(\theta) = (\theta/\theta_0)^{1-\gamma} \tag{5.7.9}$$

where θ_0 is the angular correlation scale-length and γ is the power-law slope of the spatial correlation function, $\xi(r)$.

Following Phillipps et al. (1978), the joint probability of finding galaxies in solid angles $\delta\Omega_1\delta\Omega_2$ separated by an angle θ that related with the angular correlation function is defined as

$$\delta P(\theta) = N^2[1 + w(\theta)]\delta\Omega_1\delta\Omega_2 \tag{5.7.10}$$

where N is mean number density of galaxies in the volume of interest.

Similar for the spatial correlation function, $\xi(r, z)$, the joint probability of finding galaxies in a volume $\delta V_1\delta V_2$ is

$$\delta P(r, z) = n^2(z)[1 + \xi(r, z)]\delta V_1\delta V_2 \tag{5.7.11}$$

The Limber's approximation is not appropriate for such a narrow redshift range. Therefore we did the full numerical transformation from $\xi(r)$ to $w(\theta)$ through the exact version of Limber's formula. With a narrow redshift distribution, $n(z)$, the power-law slope shows a different behaviour from $r^{-\gamma}$ to $\theta^{1-\gamma}$. By multiplying Eq. 5.7.11 by the sample selection function $\phi(z)$ and integrate over all the redshift z_1 and z_2, the spatial correlation function, $\xi(r)$ can be related to $w(\theta)$ by

$$w(\theta) = \frac{\int_0^\infty dz_1 f(z_1) \int_0^\infty dz_2 f(z_2) \xi(r)}{\left[\int_0^\infty dz f(z)\right]^2} \tag{5.7.12}$$

where $f(z)$ is the radial distribution of sources which is given by

$$f(z) \equiv \chi^2(z) \frac{d\chi(z)}{dz} n_c(z) \phi(z) \tag{5.7.13}$$

where $\phi(z)$ is the selection function of the sample, $n_c(z)$ is the comoving number density of the sources, χ is the radial comoving distance, and $r = r(\theta, z_1, z_2)$ is a comoving separation between two points at z_1 and z_2.

$$r \equiv \sqrt{\chi^2(z_1) + \chi^2(z_2) - 2\chi(z_1)\chi(z_2)\cos\theta} \tag{5.7.14}$$

We used the redshift distributions to determine the correlation function, $\xi(r)$, from their projected $w(\theta)$, via the Limber (1953) equation as described above. Firstly, we tested how well our model from the clustering given the uncertainty in the redshift distribution of our selection by using both the observed $n(z)$ and the filter curve as shown in Fig. 5.23. Both redshift distributions have similar $n(z)$ width, therefore they show no difference in the clustering slopes using Limber's equation (as the results shown by the dotted line (NB497 filter) and the solid line (VIMOS LAEs $n(z)$) in the top-right plot of Fig 5.26).

We fit a 3-D power law to our $w(\theta)$ clustering results by initially assuming a single power-law for $\xi(r)$ fixing $\gamma = 1.8$ and allowing r_0 to vary. We then calculated the χ^2 value for each r_0 from the version of Limber's formula (Eq. 5.7.12) and determined the 1σ error from the χ^2 distribution ,i.e., for 1 parameter/dof when χ^2 - min(χ^2) = 1.07. We used a polynomial to fit our χ^2 values and then find the minimum and the $\pm 1\sigma$ deviations. We found $r_0 = 1.06^{+0.23}_{-0.26}$ h^{-1}Mpc with a fixed $\gamma = 1.8$ (pink solid line) for Set A while $r_0 = 1.68^{+0.17}_{-0.19}$ h^{-1}Mpc with a fixed $\gamma = 1.8$ (blue solid line) for Set B as shown in Fig. 5.26.

We estimate the true (contamination-corrected) correlation length, r_0, by using,

$$A_{true} = \frac{A_{obs}}{(1 - f_c)^2} \tag{5.7.15}$$

where A_{true} and A_{obs} are the true correlation amplitude (where $A = r_0^{\gamma}$) and the observed correlation amplitude respetively. With the simplified correlation function form, the true correlation length is defined as

$$r_{0-true} = \frac{r_{0-obs}}{(1 - f_c)^{2/\gamma}} \tag{5.7.16}$$

We define the contamination fraction, f_c , with

$$f_c = 1 - \frac{N_{LAE}^{in}}{N_{LAE}^{all}} \tag{5.7.17}$$

where N_{LAE}^{in} and N_{LAE}^{all} are the numbers of spectroscopically identified LAEs and all spectroscopic LAEs, respectively.

In Sec. 5.3, we identified line emitters with two confidence levels, Found = 1 or Found = 9. However, we calculate the true r_0 for an extreme case with no unclear objects included (ie., only use objects with Found = 1). From Table 5.10, Set A has $N_{LAE}^{in} = 20$ and $N_{LAE}^{all} = 32$ thus $f_c = 12/32$, while Set B has $N_{LAE}^{in} = 20$ and N_{LAE}^{all} = 35 thus giving $f_c = 15/35$.

With $r_0 = 1.06^{+0.23}_{-0.26}$ h^{-1}Mpc , $\gamma = 1.8$, and $f_c = 12/32$, we obtain the contamination-corrected values of $r_{0-true} = 1.78^{+0.39}_{-0.44}$ h^{-1}Mpc for Set A LAE. For Set B, we found $r_0 = 1.68^{+0.17}_{-0.19}$ h^{-1}Mpc, $\gamma = 1.8$, and $f_c = 15/35$ thus $r_{0-true} = 3.13^{+0.31}_{-0.35}$ h^{-1}Mpc. Compared to other measurements, Ouchi et al. (2010) found a clustering length, $r_0 = 1.99^{+0.45}_{-0.55}$ h^{-1}Mpc while Gawiser et al. (2007) found $r_0 = 2.5^{+0.6}_{-0.7}$ h^{-1}Mpc. Similar to us, they assumed a power-law with $\gamma = 1.8$. We conclude that LAE may be less clustered than previously assumed with our results being more consistent with those of Gawiser et al. (2007) and Ouchi et al. (2010).

Compared to our LBG result, the best fit scale-length and slope for the observed Keck + VLRS LBG-LBG semi-projected $w_p(\sigma)$ for the data is $r_0 = 3.83 \pm 0.24$ h^{-1} Mpc with a slope of $\gamma = 1.60 \pm 0.09$ (Bielby et al., 2013). Therefore, LAE have a low clustering amplitude compared to LBGs. Even with the highest value of r_0 of LAE, it is significantly lower than those of LBGs, ie. beyond $\sim 4\sigma$ error.

Dark Matter Halo Mass

Following Bielby et al. (2013)b, we calculated the mean masses of dark matter halos within the galaxy samples by using the clustering results. We used the formalism developed by Mo et al. (1996) which provides a relationship between the halo-bias to the mean halo mass via (Sheth et al., 2001):

$$\mathrm{b}_h(M_{DM}, z) = 1 + \frac{1}{\sqrt{a}\delta_c}\left[a\nu^2\sqrt{a} + b\sqrt{a}(a\nu^2)^{1-c} - \frac{(a\nu^2)^c}{(a\nu^2)^c + b(1-c)(1-c/2)}\right] \tag{5.7.18}$$

Here, the critical overdensity, δ_c, is defined as $\delta_c = 0.15(12\pi)^{2/3}\Omega(z)^{0.005} \approx 1.686$ (Navarro et al., 1997). The constants a, b, c are obtained from Tinker et al. (2005) where $a = 0.707$, b =0.35, and $c = 0.8$. ν is defined as $\delta_c/\sigma(M_{DM}, z)$ where $\sigma(M_{DM}, z)$ is the rms fluctuation of the density field. $\sigma(M_{DM}, z)$ can be separated into dark matter halo mass and redshift dependancies via $\sigma(M_{DM}, z) = \sigma(M_{DM})D(z)$. $D(z)$ is the linear growth rate. The mass dependence of the rms fluctuation is given by:

$$\sigma(M_{DM})^2 = \frac{1}{2\pi^2}\int_0^\infty k^2 P(k) w(kr)^2 dk \tag{5.7.19}$$

$P(k)$ is the matter power-spectrum, which we calculate using CAMB (Lewis et al., 2000; Challinor & Lewis, 2011), which is based on CMBFAST (Seljak & Zaldarriaga, 1996; Zaldarriaga & Seljak, 2000). $w(kr)$ is the window function for a spherical top-hat function given by:

$$w(kr) = 3\frac{sin(kr) - krcos(kr)}{(kr)^3} \tag{5.7.20}$$

r is the top-hat radius and is related to the mass, M_{DM} by:

$$r = \left(\frac{3M_{DM}}{4\pi\rho_0}\right)^{1/3} \tag{5.7.21}$$

ρ_0, the present day mean density of the universe, is given by $\rho_0 = \Omega_m^0 \rho_{crit}^0 = 2.78 \times 10^{11} \Omega_m^0 h^2 M_\odot Mpc^{-3}$.

Therefore we estimated the dark matter halo mass from the clustering bias for each sample by combining equations 5.7.18, 5.7.19, 5.7.20, 5.7.21. Based on the LAE Set A clustering with the contamination correction where $r_{0-true} = 1.78$ h^{-1}Mpc, we have obtained $b = 1.39 \pm 0.29$ and halo mass $M_{halo} = 10^{9.72 \pm 0.76}$ $h^{-1}M_\odot$. For Set B where $r_{0-true} = 3.13$ h^{-1}Mpc, the values of bias and halo mass are $b = 2.31 \pm 0.22$ and $M_{halo} = 10^{11.19 \pm 0.22}$ $h^{-1}M_\odot$. Gawiser et al. (2007) found a bias factor of $b = 1.7 \pm 0.4$ which implies a median dark matter halo masses of $M_{halo} = 10^{10.9 \pm 0.9}$ $M_\odot$ while Ouchi et al. (2010) reported a bias value with the maximal contamination correction of $b = 1.7 \pm 0.8$ giving the halo mass $M_{halo} \approx 6.7^{+42.0}_{-6.7}x10^{10}$ $M_\odot$. Ouchi et al. (2010) concluded that the average dark halo mass of LAEs is roughly $\sim 10^{11 \pm 1}$ $M_\odot$ at z = 2-7 which is similar to our findings.

Comparing with LBGs, the mean halo mass of the VLRS spectroscopic $z \sim 3$ galaxy sample is $10^{11.57 \pm 0.15}$ $h^{-1}M_\odot$ with $b = 2.37 \pm 0.21$ (Bielby et al., 2013). A typical halo mass of LBG is estimated to be $10^{12 \pm 1}$ $M_\odot$, about one order of magnitude larger than that of LAEs (Hamana et al. 2004; Ouchi et al. 2004b, 2005; Lee et al. 2006, 2009; McLure et al. 2010; Hildebrandt et al. 2009). The bias values of LAEs are smaller than those of LBGs which indicates that LAEs may reside in less massive dark halos on average (Ouchi et al., 2010).

5.8 Discussion and Conclusions

In this chapter, we have presented LAE photometric observation for narrow band images obtained from the Subaru Suprime-Cam while we have obtained broadband (B,V,R) images with KPNO MOSAIC or CFHT MegaCAM. We then selected our LAE candidates by using two different sets of constraints. We have also made spectroscopic follow-up observation for our LAEs candidates with the Visible Multi-Object Spectrograph (VIMOS) on the Very Large Telescope (VLT) in 3 of our 5 fields. We use our observational data from 5 fields to perform the Lyman Alpha luminosity functions and two-point correlation functions of LAEs at $z = 3.1$.

The major findings of our study are summarised below.

1. We selected our LAE candidates based on narrow-band selection. We made two selection criteria comprising a two-colour approach which applied R-NB colour and B-NB (Set A) and a narrow-band vs broad-band combinations of B and R or B and V (Set B). Their success rates were estimated by our VIMOS LAE spectroscopic confirmations. We found that the success rate of Set A and Set B is similar (57-63 %) from which we can deduce that either sample can be used to base our analysis.

2. We visually inspected every source targetted for spectroscopic observation both in 1D and 2D spectra. For every identified LAE, we assigned a quality parameter, Found = 1 or Found = 9. A quality of Found = 1 indicates high confidence spectroscopic confirmed with high-SNR Lyα emission features at $\lambda \approx 4977 \pm 30\mathring{A}$. While, Found = 9 are the low confidence sources with some weak Lyα emission. Currently, we have 32 spectroscopically confirmed (Found = 1) and 30 high possibility to have spectroscopic confirmed (Found = 9) Lyα-emitters at redshift $z = 3.1$ from VIMOS observations from Q2359, Q0302, and J0124.

3. We first looked at the Lyα luminosity function. Our narrowband Lyα luminosity function is similar to previous observations (Ouchi et al., 2008; Gronwall et al., 2007). After correcting NB LAE average counts for contamination, we found that our Set A and Set B average surface-density magnitude relation is consistent to their measurements. Our results reasonably agree with Ouchi et al. 2008 and are slightly higher than for Gronwall et al. 2007. Our Set A result is lower than Ouchi et al. at at the bright end while our Set B is more consistent with their result at all magnitudes.

4. We estimated the R-band continuum luminosity functions of our sample of LAEs/LBGs and compared with other observations. We confirm that the LAE continuum lie at fainter end than the VLRS LBGs. Also the amplitude of the LAE LF is only ~ 30 % of the extrapolated LBG LF at faint magnitude. This is consistent with LAE being fainter counterparts to LBGs. Although our data (agreeing with Gronwall et al.) suggest that the LAE-LBG fraction may decrease with decreasing luminosity, other observations disagree on this point (eg, Stark et al. 2010; Ouchi et al. 2008). The possibility that our LAE continuum LF is contaminated by lower

redshift interlopers means that we cannot come to any firm conclusion on this point.

5. We have measured the angular correlation function for our $z \sim 3.1$ LAE sample in our 5 fields and found that our LAE clustering amplitudes are lower than LBGs. The correlation length from LAE measurement is lower than from LBG measurement. Even with the highest LAE r_0 value, it is significantly lower than those of LBGs, ie. beyond $\sim 4\sigma$ significant estimates. The lower correlation length from LAE measurement leads to lower halo masses. This result is also confirmed by our LAE continuum LF which showed lower densities for LAE than LBGs.

The confirmation of LAEs having low masses is in agreement with other findings that the average dark halo mass of LAEs is roughly $\sim 10^{11\pm1}$ $M_\odot$ at z $\sim$ 3 while a typical halo mass of LBG is estimated to be $10^{12\pm1}$ $M_\odot$, about one order of magnitude larger than that of LAEs. The bias values of LAEs are smaller than those of LBGs which indicates that LAEs reside in less massive dark halos on average.

Chapter 6

Conclusions

In this final chapter, we summarise our findings and potential avenues for further study.

6.1 Summary of main results

6.1.1 The interaction of galaxies and the IGM at $z \sim 3$ through LBG and Lyα

We presented a study of galaxies and gas at $z \sim 3$, combining the power of the VLRS at large spatial scales with the statistical power of the Keck sample of Adelberger et al. (2005) at smaller scales. Crighton et al. (2011) included the Keck data in the LBG-Lyα cross-correlation function by simply using an error weighted combination of the Keck and VLRS correlation functions. Our aim here was to combine the two surveys for 2-D, $\xi(\sigma, \pi)$ correlation function analyses at the deeper level of the Lyα fluxes and LBG positions. We therefore included 940 $2.67 \leq z \leq 3.25$ LBGs from the Steidel et al. (2003) Keck samples. We also re-reduced 6 high resolution spectra of the QSOs in these fields from the ESO or Keck archives. With ≈ 3000 galaxies the combined VLRS and Keck surveys covering the widest range of spatial scales for such a survey and are ideal to study the dynamical relationship between galaxies and the IGM at $z \approx 3$.

The other new feature of this work was our use of the GIMIC simulations to help

interpret the above correlation function results. The simulations are used to create synthetic Lyα spectra and galaxies. We studied both galaxy clustering and the relationship between gas and galaxies via the auto- and cross-correlation functions in both 1-D and 2-D.

In Chapter 2 we presented the observational data from a large VLT LBG Redshift Survey (VLRS) and Keck survey (Steidel et al., 2003). The details of publicly available QSO spectra and our own observations using the X-Shooter instrument on the VLT are also presented. We described the Galaxies-Intergalactic Medium Interaction Calculation (GIMIC) simulation in Chapter 3. The simulations are used to create synthetic Lyα spectra and galaxies. In Chapter 4 we presented the analysis of the interaction between IGM and galaxies at $z \sim 3$ with the data from VLRS and KECK. We also include interpretations from the GIMIC simulations.

We first compared the simulated galaxy-galaxy results in real- and redshift-space. The LBG-LBG $\xi(r)$ and $\xi(s)$ in real and redshift space are shown to be power laws at large scales. They show strong clustering at small separations. At small distances ($s < 1\ h^{-1}$ Mpc), the LBG-LBG $\xi(s)$ in redshift-space tends to have lower clustering than $\xi(r)$ in real space, while at larger scales the LBG-LBG $\xi(s)$ results appear to have higher clustering. Qualitatively this is as expected from 'finger-of-God' effects at sub 1 h^{-1}Mpc scales and dynamical infall at larger scales. Quantitatively, the large scale Kaiser boost for the galaxies is consistent with expectations. However, at smaller scales the peculiar velocity dispersion measured in the simulation overestimates the difference between real and z-space correlation functions. Similar results may have been found by Taruya et al. (2010) who found that at high redshift fitting finger-of-god damping terms, as we do here, tended to underestimate the peculiar velocity dispersion predicted by linear theory. Certainly, a 'local' velocity dispersion measured relative to galaxy pairs with separations $< 1\ h^{-1}$Mpc produces improved agreement. For the galaxy $\xi(\sigma, \pi)$ there appears again to be little difference between the real-and z-space correlation functions but the results are still noisy. Clearly none of the correlation function statistics will pick up the most obvious indication of peculiar velocity in these simulated data which is the bulk motion of ≈ 100 kms^{-1} across the simulated volume. We will see that these unexpectedly small effects of

peculiar velocity are also apparent as we move to study the gaseous component.

We then checked the LBG-Lyα transmissivity cross-correlation function as calculated directly from spectra and LBG positions of the Keck survey against the results of A03 and found good agreement, although we only had access to 6 out of their 8 QSO spectra. We checked the results for the combined surveys against the weighted combinations of Crighton et al. (2011) and again found good agreement. Our overall results for the combined LBG-Lyα $\xi(s)$ resemble more those of Adelberger et al. (2005) and Rakic et al. (2012) than those of A03 ie a continuous decrease in Lyα transmissivity around the LBG with no evidence for a spike in transmissivity due to feedback being seen. Crighton et al. (2011) noted that such a spike could still be present but smoothed away by the errors in the LBG velocities.

The inclusion of the gas component along with the galaxies makes possible the search for gaseous infall. Assuming the appropriate dynamical infall parameter for the simulated $M_\star \geq 10^8\ h^{-1}\mathrm{M}_\odot$ galaxies, the gas- galaxy cross-correlation model gave $\beta_{Ly\alpha} \approx 0.7$, lower than the expected range of $1 < \beta_{Ly_\alpha} < 1.6$ from McDonald (2003). This small effect of the peculiar velocities was confirmed in the analysis of galaxy-Lyα $\xi(\sigma, \pi)$ where again the circular contours of the real-real $\xi(\sigma, \pi)$ was almost matched by those from the z-space version. Again there seems consistency with our view of a broadly coherent motion between gas and galaxies.

From the Lyα auto-correlations $\xi(s)$ and $\xi(\sigma, \pi)$, we found similar results with again small differences between real- and redshift-space. At small scales, the velocity dispersion needed to fit the simulated $\xi(s)$ is less than measured directly in the simulation, although this may be partly explained by the intrinsic width of the Lyα lines contributing artificial autocorrelation below separations of $\leq 0.7\ h^{-1}$Mpc. At larger scales, the value of $\xi(s)/\xi(r)$ is more consistent with $\beta_{Ly\alpha} \approx 0.7 \pm 0.3$ rather than the range given by McDonald (2003), $\beta_{Ly\alpha} \approx 1 - 1.6$.

At larger scales, one possibility to explain the low gas infall rate may be due to the presence of feedback in the GIMIC simulations. Galaxy-wide winds powered with initial velocities of 600 km s^{-1} are invoked in the GIMIC simulations and this is a significant amount since this corresponds to 6 h^{-1}cMpc. These winds are modelled by each star particle that forms, imparting a randomly directed 600 km s^{-1} kick to 4

of its gas particle neighbours. It is possible that this outflow of the gas could cancel out some of the expected gravitational infall particularly in the neighbourhood of a galaxy. However, it remains to be seen whether enough gas particles are outflowing to explain the lack of infall in the gas cross- or auto-correlation functions. If the effects of gas outflow were detectable in the gas dynamics this could be a powerful probe, since there is not much evidence of feedback from any spike in transmission due to lower neutral gas density close to the galaxy.

Recent work by Rakic et al. (2012) and Rakic et al. (2013) have presented studies of the LBG - Lyα cross correlation at $z \sim 2.4$ with observations and simulations respectively. In both cases, the authors report a significant measurement of RSD, showing evidence for both small scale peculiar velocity effects and large scale bulk motion of gas in-falling onto observed and simulated galaxies. Rakic et al. (2013) find that in terms of the reported large scale 'flattening', the observations of Rakic et al. (2012) are consistent with the simulation results for galaxy samples selected with minimum halo masses of $\log M_{\rm min}/M_{\odot} \gtrsim 11.6$. This is slightly higher than the galaxy samples used here, whilst we are unable to probe this larger halo-mass constraint given the size limitations of GIMIC. However, we note that our results are consistent with the results of Rakic et al. (2013) at lower minimum halo masses, where very little sign of either peculiar velocity effects or Kaiser boost effects are seen in the Rakic et al. (2013) results. Unfortunately in terms of infall, higher mass, more highly clustered galaxies will have higher values of galaxy bias and lower values of the infall parameter β_{gal}. Hence we expect the combination $\beta_{gal} + \beta_{Ly_\alpha}$ to be slightly smaller for higher mass galaxies, although β_{Ly_α} is independent of galaxy mass. Thus although the Rakic et al. (2012, 2013) results appear consistent with the halo masses of their own galaxy sample estimated via the galaxy-galaxy auto-correlation function (Trainor & Steidel, 2012), there remains some tension between our results and those of Rakic et al. (2012) and Rakic et al. (2013) because of their claim that they are seeing stronger effects of infall in their higher mass sample.

6.1.2 Lyman Alpha Emitters

In Chapter 5 we presented LAE photometric+spectroscopic follow-up observations. We have made a photometric sample of $\sim$ 500 LAE candidates from 5 fields and a spectroscopic sample of $\sim$ 62 confirmed Lyα-emitters from high and low confidence objects in 3 of our 5 fields at redshift $z = 3.1$. Based on these samples, we have studied the Lyman Alpha and continuum luminosity functions and the two-point correlation functions of LAEs at $z = 3.1$.

We found that our narrowband Lyα luminosity function after contamination correction is in agreement with Ouchi et al. (2008) and is higher than for Gronwall et al. (2007). The suggestion from Ciardullo et al. 2012 is that the luminosity function curve for Ouchi et al. (2008) is based on a rest-frame equivalent width limit of 45 Å. Thus for consistency with Gronwall et al.'s selection criteria ($EW_{rest} \approx 20$ Å), their LF curve should be increased by $\geq 10\%$.

We then estimated the R-band continuum luminosity functions of our sample of LAEs. After the contamination correction, our 1700 Å continuum magnitude (auto) LAE luminosity function appears similar to that of Gronwall et al. (2007) with a relatively high number density of LAE being detected at bright magnitudes. Our high LAE LF at brighter magnitudes ($R < 23$) may be due to high contamination as we have no VIMOS LAE showing up at the bright end.

The comparison of LAE R-band continuum luminosity functions to the LBGs at this redshift show that LAEs in the magnitude range, R < 25.5, are $\sim$ 30 % the density of the LBGs at the same redshift and LAE luminosity functions extends much fainter (Gronwall et al., 2007). This is also consisted with the idea that most of LAE lie at the faint end of the usual LBG luminosity function.

Although our data (agreeing with Gronwall et al.) suggest that the LAE-LBG fraction may decrease with decreasing luminosity, other observations disagree on this point (eg, Stark et al. 2010; Ouchi et al. 2008). The possibility that our LAE continuum LF is contaminated by lower redshift interlopers means that we cannot come to any firm conclusion on this point.

A large data set is needed to reduce the statistical error bars. It was suggested that the LF should be based on only the spectroscopically confirmed LAEs to re-

duce the contamination from lower redshift interlopers. Spectroscopic follow-up will improve the statistic at the bright end of the LF. However the spectroscopic observation may be limited for the faint end obects because the fainter an object is, the harder it is to detect spectroscopically. Therefore, this might also lead to big error bars in the faint end due to incompleteness issues. Gronwall et al. (2007) also discussed that some LAEs may appear brighter or fainter than usual depending on how the photometric calibration has been done and where the filter is located in redshift space. These difficulties in determining a LAE LF explain the significantly different results from different authors.

Finally, we found that our LAE clustering amplitudes from the angular correlation function are lower than expected for LBGs, yielding the lower correlation length compared to the LBG measurement. Even the highest value of LAE r_0, is significantly lower than those of LBGs, ie. beyond $\sim 4\sigma$ error. The lower correlation length leads to lower halo masses. These results agree with our LAE continuum LF which is showed to fainter magnitudes for LAE than LBGs.

The galaxy clustering bias, b, can be simply quantified from the clustering results. This gives the relationship between the clustering of the tracer population, i.e. the selected galaxy samples and the underlying dark matter clustering. The more massive samples show stronger clustering. Based on the Mo et al. (1996) formalism, we have estimated mean dark matter halo masses from our LAE clustering measurements. We found the bias values of LAEs are smaller than those of LBGs which indicates that LAEs reside in less massive dark halos on average. This is in agreement with other findings that LAEs have lower mass than LBGs, about one order of magnitude smaller than that of LBGs references. A typical halo mass of LAE is estimated to be $10^{11\pm1}$ $M_\odot$ at $z \sim 3$.

6.2 Future Prospects

As presented in this thesis, the HI absorption close to LBGs (< 1 Mpc), which was interpreted as possibly being due to supernovae winds heating the IGM around the strongly star-forming LBGs, is still an issue. Currently we found little direct

evidence for feedback from both the Keck and VLRS results. Crighton et al. (2011) suggested that the precision of the LBG redshifts has a significant impact on the LBG-absorption line cross-correlation results at small scales (≈ 1 h^{-1}Mpc). Using rest frame UV features to measure LBG redshifts is problematic: absorption features arise in ISM gas outflowing in winds and are thus offset from the intrinsic LBG redshift, and Lyα emission is offset due to absorption of the blue Lyα wing by outflowing material. The intrinsic redshift can be inferred from the UV features, however the scatter in the outflow velocities combined with observational redshift errors gives an overall uncertainty of $\approx$ 300-400 kms^{-1}, ie $\approx$ 500 pkpc. This error dominates the peculiar velocity effect and leads to a smearing of the small-scale cross-correlation results. This problem can be overcome via intermediate resolution NIR spectroscopy in which the nebular emission lines originating in the star forming regions of galaxies are instead targeted.

Based on part of the UK-Durham KMOS guaranteed time, we shall make KMOS observations of VLRS LBGs, and LAEs from our complementary NB survey, to make a new attack on this problem. KMOS (K-band Multi-Object Spectrograph) (Sharples et al., 2013) is a near-infrared multi-object integral-field spectrometer at the European Southern Observatory's (ESO) Very Large Telescope (VLT). It is one of a suite of second-generation instruments for VLT, along with MUSE (Bacon et al., 2012) and SPHERE (Kasper et al., 2012). This spectrograph consists of 24 integral field units (IFUs) which can obtain spatially resolved spectra for up to 24 target objects selected from within an extended 7.2 arcminute diameter field of view (Sharples et al., 2010). We plan to observe 28 fields centred on z $\approx$ 3 QSOs with high S/N spectroscopy taken with the UVES, HiRES and X-SHOOTER echelle spectrographs. We will also observe $\approx$200, z $\sim$ 3, LAEs selected from a narrow-band survey in the same fields. KMOS observations in bright QSO fields produce unique advantages for studying the gaseous environment of galaxies during their formation process. The aims of this plan are: 1) to measure highly accurate 'nebular' redshifts for all galaxies near the QSO sightline and so significantly improve LBG/LAE-Lyα cross-correlation analyses; 2) to determine the kinematics of gas outflows within high-z galaxies by combining optical and NIR spectral features; and 3) to measure

the internal dynamics and hence the dark matter mass of z > 2 galaxies using the full 2-D IFU data for our strongest-lined targets.

In addition to these the observations, the high resolution OWLS/EAGLE simulations will be an option to help us interpret the dynamics of gas and galaxies in relation to the large scale structure. For instance, the OverWhelmingly Large Simulations (OWLS) (Schaye et al., 2010) is a suite of cosmological hydrodynamical simulations performed using a version of the Smoothed Particle Hydrodynamics (SPH) code GADGET (Springel, 2005). There are 7 different models , which varying the mass loading vs launch velocity of the winds as well as the scaling of those parameters with halo properties, in 25 comoving h^{-1}Mpc boxes with 512^3 particles at z ≈ 3. These choices might lead us to have a better model to compare with the observations.

As mentioned above, our future KMOS observations will provide us more LAEs. It will also allow a search for the Ly-α-nebular velocity offset in LAE (McLinden et al., 2011). We can determine the cross-correlation function between LAEs and LBGs, an thus to test whether LAEs trace large scale structure in the same way as LBGs. This dataset will be used to constrain the contamination rate due to low-redshift interlopers, which is critical for determining the true clustering strength of our candidates. In addition, we will also be able to search for Lyα "blobs" - extended regions of Lyα emission extending over tens of kpc that have been associated with LBGs in the smaller field analysed in Steidel et al. (2000). These peculiar objects have been found in highly clustered fields, but is not clear how common they are. Studies in blank fields such as these are necessary to test that.

Several techniques have been developed in theoretical work on LAE (eg., Furlanetto et al. 2006; McQuinn et al. 2007; Orsi et al. 2008; Zheng et al. 2010, 2011,Zheng et al. 2011b, Orsi2012). For instance, McQuinn et al. (2007) made theoretical predictions for the clustering based on radiative transfer simulations. They found that the observed clustering of very high redshift LAE may reveal the level of reionisation independently of the luminosity function and the line profile. Zheng et al. (2010, 2011) also made a model providing natural explanations to an array of observed properties of LAEs at $z \geq 4$, including morphology, size, Lyα spectra, Lyα and UV

luminosity functions, and Lyα equivalent width distribution. The model predicts new effects in galaxy clustering caused by radiative transfer selection, suppression of line-of-sight fluctuation and enhancement of transverse fluctuation in the spatial distribution of LAEs, which lead to anisotropic clustering. Orsi et al. (2008, 2012) used the galaxy formation model to predict the properties of LAEs at $0 < z < 7$. Orsi et al. (2012) compared their model predections of the UV ($\lambda \sim$1500 Å) luminosity function of $z \sim 3$ LAEs to the observational data from Ouchi et al. (2008); Gronwall et al. (2007). They concluded that their models of the UV luminosity function of LAE and the fraction of LAE in LBG samples at high redshift are in partial agreement with observations.

To make the LAE selection more accurate and gain insight in the physical properties of the selected galaxies, we shall employ GIMIC/OWLS/EAGLE to generate synthetic photometry in the narrow- and broadband filters used, following the physical properties of these galaxies and their most common low-redshift contaminants. Therefore, we can use that to compare to our LAE continuum, line luminosity functions and clustering results.

Bibliography

Adelberger K. L., Shapley A. E., Steidel C. C., Pettini M., Erb D. K., Reddy N. A., 2005, ApJ, 629, 636

Adelberger K. L., Steidel C. C., Pettini M., Shapley A. E., Reddy N. A., Erb D. K., 2005, ApJ, 619, 697

Adelberger K. L., Steidel C. C., Shapley A. E., Pettini M., 2003, ApJ, 584, 45

Aguirre A., Schaye J., Hernquist L., Kay S., Springel V., Theuns T., 2005, ApJ, 620, L13

Ajiki M., Taniguchi Y., Fujita S. S., Shioya Y., Nagao T., Murayama T., Yamada S., Umeda K., Komiyama Y., 2003, AJ, 126, 2091

Altay G., Theuns T., Schaye J., Crighton N. H. M., Dalla Vecchia C., 2011, ApJ, 737, L37

Bacon R., et al. 2012, The Messenger, 147, 4

Baugh C. M., Cole S., Frenk C. S., 1996, MNRAS, 283, 1361

Benson A. J., Cole S., Frenk C. S., Baugh C. M., Lacey C. G., 2000, MNRAS, 311, 793

Bertin E., Arnouts S., 1996, A&AS, 117, 393

Bielby R., Hill M. D., Shanks T., Crighton N. H. M., Infante L., Bornancini C. G., Francke H., Héraudeau P., Lambas D. G., Metcalfe N., Minniti D., Padilla N., Theuns T., Tummuangpak P., Weilbacher P., 2013, MNRAS, 430, 425

Bielby R. M., Gonzalez-Perez V., McCracken H. J., Ilbert O., Daddi E., Le Fèvre O., Hudelot P., Kneib J.-P., Mellier Y., Willott C., 2013, ArXiv e-prints

Bielby R. M., Shanks T., Weilbacher P. M., Infante L., Crighton N. H. M., Bornancini C., Bouché N., Héraudeau P., Lambas D. G., Lowenthal J., Minniti D., Padilla N., Petitjean P., Theuns T., 2011, MNRAS, 414, 2

Blanton M., Cen R., Ostriker J. P., Strauss M. A., Tegmark M., 2000, ApJ, 531, 1

Busca N. G., et al. 2013, A&A, 552, A96

Cen R., Ostriker J. P., 1999, ApJ, 519, L109

Cen R., Ostriker J. P., 2000, ApJ, 538, 83

Challinor A., Lewis A., 2011, Phys. Rev. D, 84, 043516

Ciardullo R., Gronwall C., Wolf C., McCathran E., Bond N. A., Gawiser E., Guaita L., Feldmeier J. J., Treister E., Padilla N., Francke H., Matković A., Altmann M., Herrera D., 2012, ApJ, 744, 110

Cole S., Fisher K. B., Weinberg D. H., 1994, MNRAS, 267, 785

Cowie L. L., Hu E. M., 1998, AJ, 115, 1319

Crain R. A., Theuns T., Dalla Vecchia C., Eke V. R., Frenk C. S., Jenkins A., Kay S. T., Peacock J. A., Pearce F. R., Schaye J., Springel V., Thomas P. A., White S. D. M., Wiersma R. P. C., 2009, MNRAS, 399, 1773

Crighton N. H. M., et al. 2011, MNRAS, 414, 28

Croft R. A. C., Gaztanaga E., 1998, ApJ, 495, 554

Croft R. A. C., Weinberg D. H., Pettini M., Hernquist L., Katz N., 1999, ApJ, 520, 1

da Ângela J., Outram P. J., Shanks T., Boyle B. J., Croom S. M., Loaring N. S., Miller L., Smith R. J., 2005, MNRAS, 360, 1040

da Ângela J., Shanks T., Croom S. M., Weilbacher P., Brunner R. J., Couch W. J., Miller L., Myers A. D., Nichol R. C., Pimbblet K. A., de Propris R., Richards G. T., Ross N. P., Schneider D. P., Wake D., 2008, MNRAS, 383, 565

Davis M., Efstathiou G., Frenk C. S., White S. D. M., 1985, ApJ, 292, 371

Davis M., Peebles P. J. E., 1983, ApJ, 267, 465

Dekel A., Birnboim Y., Engel G., Freundlich J., Goerdt T., Mumcuoglu M., Neistein E., Pichon C., Teyssier R., Zinger E., 2009, Nature, 457, 451

Dekker H., D'Odorico S., Kaufer A., Delabre B., Kotzlowski H., 2000, in Iye M., Moorwood A. F., eds, Optical and IR Telescope Instrumentation and Detectors Vol. 4008 of Society of Photo-Optical Instrumentation Engineers (SPIE) Conference Series, Design, construction, and performance of UVES, the echelle spectrograph for the UT2 Kueyen Telescope at the ESO Paranal Observatory. pp 534–545

Dicke R. H., Peebles P. J. E., Roll P. G., Wilkinson D. T., 1965, ApJ, 142, 414

Dolag K., Borgani S., Murante G., Springel V., 2009, MNRAS, 399, 497

Faucher-Giguère C.-A., Prochaska J. X., Lidz A., Hernquist L., Zaldarriaga M., 2008, ApJ, 681, 831

Finkelstein S. L., Rhoads J. E., Malhotra S., Grogin N., 2009, ApJ, 691, 465

Font A. S., McCarthy I. G., Crain R. A., Theuns T., Schaye J., Wiersma R. P. C., Dalla Vecchia C., 2011, MNRAS, 416, 2802

Frenk C. S., Evrard A. E., White S. D. M., Summers F. J., 1996, ApJ, 472, 460

Furlanetto S. R., Zaldarriaga M., Hernquist L., 2006, MNRAS, 365, 1012

Fynbo J. P. U., Ledoux C., Möller P., Thomsen B., Burud I., 2003, A&A, 407, 147

Fynbo J. U., Möller P., Thomsen B., 2001, A&A, 374, 443

Gawiser E., et al. 2007, ApJ, 671, 278

Giavalisco M., 2002, ARA&A, 40, 579

Gronwall C., Ciardullo R., Hickey T., Gawiser E., Feldmeier J. J., van Dokkum P. G., Urry C. M., Herrera D., Lehmer B. D., Infante L., Orsi A., Marchesini D., Blanc G. A., Francke H., Lira P., Treister E., 2007, ApJ, 667, 79

Groth E. J., Peebles P. J. E., 1977, ApJ, 217, 385

Guaita L., Acquaviva V., Padilla N., Gawiser E., Bond N. A., Ciardullo R., Treister E., Kurczynski P., Gronwall C., Lira P., Schawinski K., 2011, ApJ, 733, 114

Hamana T., Ouchi M., Shimasaku K., Kayo I., Suto Y., 2004, MNRAS, 347, 813

Hamilton A. J. S., 1992, ApJ, 385, L5

Harrison E. R., 1970, Phys. Rev. D, 1, 2726

Hawkins E., Maddox S., Cole S., Lahav O., Madgwick D. S., Norberg P., Peacock J. A., Baldry I. K., Baugh C. M., Bland-Hawthorn J., Bridges T., Cannon R., Colless M., Collins C., Couch W., 2003, MNRAS, 346, 78

Hayashino T., Matsuda Y., Tamura H., Yamauchi R., Yamada T., Ajiki M., Fujita S. S., Murayama T., Nagao T., Ohta K., Okamura S., Ouchi M., Shimasaku K., Shioya Y., Taniguchi Y., 2004, AJ, 128, 2073

Hayashino T., Tamura H., Matsuda Y., Shimasaku K., Okamura S., Ouchi M., Takami H., Komiyama Y., Ando M., 2003, Publications of the National Astronomical Observatory of Japan, 7, 33

Hildebrandt H., Pielorz J., Erben T., van Waerbeke L., Simon P., Capak P., 2009, A&A, 498, 725

Horne K., 1986, PASP, 98, 609

Hu E. M., Cowie L. L., McMahon R. G., 1998, ApJ, 502, L99

Hu E. M., McMahon R. G., 1996, Nature, 382, 231

Hubble E., 1929, Proceedings of the National Academy of Science, 15, 168

Kaiser N., 1987, MNRAS, 227, 1

Kasper M., et al. 2012, The Messenger, 149, 17

Lahav O., Lilje P. B., Primack J. R., Rees M. J., 1991, MNRAS, 251, 128

Landy S. D., Szalay A. S., 1993, ApJ, 412, 64

Landy S. D., Szalay A. S., 2002, ApJ, 579, 76

Le Fèvre O., Saisse M., Mancini D., Brau-Nogue S., Caputi O., Castinel L., D'Odorico S., Garilli B., Kissler-Patig M., Lucuix C., Mancini G., Pauget A., Sciarretta G., Scodeggio M., Tresse L., Vettolani G., 2003, in Iye M., Moorwood A. F. M., eds, Instrument Design and Performance for Optical/Infrared Ground-based Telescopes Vol. 4841 of Society of Photo-Optical Instrumentation Engineers (SPIE) Conference Series, Commissioning and performances of the VLT-VIMOS instrument. pp 1670–1681

Lee K.-S., Giavalisco M., Conroy C., Wechsler R. H., Ferguson H. C., Somerville R. S., Dickinson M. E., Urry C. M., 2009, ApJ, 695, 368

Lee K.-S., Giavalisco M., Gnedin O. Y., Somerville R. S., Ferguson H. C., Dickinson M., Ouchi M., 2006, ApJ, 642, 63

Lewis A., Challinor A., Lasenby A., 2000, ApJ, 538, 473

Liddle A. R., 2003, An introduction to modern cosmology

Limber D. N., 1953, ApJ, 117, 134

Liske J., Webb J. K., Williger G. M., Fernández-Soto A., Carswell R. F., 2000, MNRAS, 311, 657

Madau P., Pozzetti L., Dickinson M., 1998, ApJ, 498, 106

Matsuda Y., Yamada T., Hayashino T., Tamura H., Yamauchi R., Murayama T., Nagao T., Ohta K., Okamura S., Ouchi M., Shimasaku K., Shioya Y., Taniguchi Y., 2005, ApJ, 634, L125

McCarthy I. G., Font A. S., Crain R. A., Deason A. J., Schaye J., Theuns T., 2012, MNRAS, 420, 2245

McCarthy I. G., Schaye J., Font A. S., Theuns T., Frenk C. S., Crain R. A., Dalla Vecchia C., 2012, MNRAS, 427, 379

McDonald P., 2003, ApJ, 585, 34

McDonald P., Miralda-Escudé J., Rauch M., Sargent W. L. W., Barlow T. A., Cen R., Ostriker J. P., 2000, ApJ, 543, 1

McLinden E. M., Finkelstein S. L., Rhoads J. E., Malhotra S., Hibon P., Richardson M. L. A., Cresci G., Quirrenbach A., Pasquali A., Bian F., Fan X., Woodward C. E., 2011, ApJ, 730, 136

McLure R. J., Dunlop J. S., Cirasuolo M., Koekemoer A. M., Sabbi E., Stark D. P., Targett T. A., Ellis R. S., 2010, MNRAS, 403, 960

McQuinn M., Hernquist L., Zaldarriaga M., Dutta S., 2007, MNRAS, 381, 75

Miyazaki S., Komiyama Y., Sekiguchi M., Okamura S., Doi M., Furusawa H., Hamabe M., Imi K., Kimura M., Nakata F., Okada N., Ouchi M., Shimasaku K., Yagi M., Yasuda N., 2002, PASJ, 54, 833

Mo H. J., Jing Y. P., White S. D. M., 1996, MNRAS, 282, 1096

Mountrichas G., Sawangwit U., Shanks T., Croom S. M., Schneider D. P., Myers A. D., Pimbblet K., 2009, MNRAS, 394, 2050

Mountrichas G., Shanks T., 2007, ArXiv e-prints

Murphy M. T., Webb J. K., Flambaum V. V., 2003, MNRAS, 345, 609

Navarro J. F., Frenk C. S., White S. D. M., 1997, ApJ, 490, 493

Navarro J. F., Hayashi E., Power C., Jenkins A. R., Frenk C. S., White S. D. M., Springel V., Stadel J., Quinn T. R., 2004, MNRAS, 349, 1039

Nilsson K. K., Meisenheimer K., 2009, , 53, 37

Nilsson K. K., Møller P., Möller O., Fynbo J. P. U., Michałowski M. J., Watson D., Ledoux C., Rosati P., Pedersen K., Grove L. F., 2007, A&A, 471, 71

Oke J. B., 1990, AJ, 99, 1621

Oke J. B., Cohen J. G., Carr M., Cromer J., Dingizian A., Harris F. H., Labrecque S., Lucinio R., Schaal W., Epps H., Miller J., 1995, PASP, 107, 375

Oppenheimer B. D., Davé R., 2006, MNRAS, 373, 1265

Orsi A., Lacey C. G., Baugh C. M., 2012, MNRAS, 425, 87

Orsi A., Lacey C. G., Baugh C. M., Infante L., 2008, MNRAS, 391, 1589

Ouchi M., et al. 2003, ApJ, 582, 60

Ouchi M., Hamana T., Shimasaku K., Yamada T., Akiyama M., Kashikawa N., Yoshida M., Aoki K., Iye M., Saito T., Sasaki T., Simpson C., Yoshida M., 2005, ApJ

Ouchi M., Shimasaku K., Akiyama M., Simpson C., Saito T., Ueda Y., Furusawa H., Sekiguchi K., Yamada T., Kodama T., Kashikawa N., Okamura S., Iye M., Takata T., Yoshida M., Yoshida M., 2008, ApJS, 176, 301

Ouchi M., Shimasaku K., Furusawa H., Saito T., Yoshida M., Akiyama M., Ono Y., Yamada T., Ota K., Kashikawa N., Iye M., Kodama T., Okamura S., Simpson C., Yoshida M., 2010, ApJ, 723, 869

Ouchi M., Shimasaku K., Okamura S., Furusawa H., Kashikawa N., Ota K., Doi M., Hamabe M., Kimura M., Komiyama Y., Miyazaki M., Miyazaki S., Nakata F., Sekiguchi M., Yagi M., Yasuda N., 2004a, ApJ, 611, 660

Ouchi M., Shimasaku K., Okamura S., Furusawa H., Kashikawa N., Ota K., Doi M., Hamabe M., Kimura M., Komiyama Y., Miyazaki M., Miyazaki S., Nakata F., Sekiguchi M., Yagi M., Yasuda N., 2004b, ApJ

Peacock J. A., et al. 2001, Nature, 410, 169

Peebles P. J. E., 1980, The large-scale structure of the universe

Peebles P. J. E., Yu J. T., 1970, ApJ, 162, 815

Penzias A. A., Wilson R. W., 1965, ApJ, 142, 419

Pettini M., Shapley A. E., Steidel C. C., Cuby J.-G., Dickinson M., Moorwood A. F. M., Adelberger K. L., Giavalisco M., 2001, ApJ, 554, 981

Phillipps S., Fong R., Fall R. S. E. S. M., MacGillivray H. T., 1978, MNRAS, 182, 673

Phleps S., Peacock J. A., Meisenheimer K., Wolf C., 2006, A&A, 457, 145

Pirzkal N., Malhotra S., Rhoads J. E., Xu C., 2007, ApJ, 667, 49

Planck Collaboration Ade P. A. R., Aghanim N., Armitage-Caplan C., Arnaud M., Ashdown M., Atrio-Barandela F., Aumont J., Baccigalupi C., Banday A. J., et al. 2013, ArXiv e-prints

Power C., Navarro J. F., Jenkins A., Frenk C. S., White S. D. M., Springel V., Stadel J., Quinn T., 2003, MNRAS, 338, 14

Rakic O., Schaye J., Steidel C. C., Booth C. M., Dalla Vecchia C., Rudie G. C., 2013, MNRAS, 433, 3103

Rakic O., Schaye J., Steidel C. C., Rudie G. C., 2012, ApJ, 751, 94

Ratcliffe A., Shanks T., Broadbent A., Parker Q. A., Watson F. G., Oates A. P., Fong R., Collins C. A., 1996, MNRAS, 281, L47

Rauch M., 1998, ARA&A, 36, 267

Roche N., Shanks T., Metcalfe N., Fong R., 1993, MNRAS, 263, 360

Ross N. P., et al. 2007, MNRAS, 381, 573

Rudie G. C., Steidel C. C., Trainor R. F., Rakic O., Bogosavljević M., Pettini M., Reddy N., Shapley A. E., Erb D. K., Law D. R., 2012, ApJ, 750, 67

Scannapieco C., et al. 2012, MNRAS, 423, 1726

Schaye J., Dalla Vecchia C., Booth C. M., Wiersma R. P. C., Theuns T., Haas M. R., Bertone S., Duffy A. R., McCarthy I. G., van de Voort F., 2010, MNRAS, 402, 1536

Schneider P., 2006, Extragalactic Astronomy and Cosmology

Scranton R., et al. 2002, ApJ, 579, 48

Seljak U., Zaldarriaga M., 1996, ApJ, 469, 437

Shapley A. E., Steidel C. C., Erb D. K., Reddy N. A., Adelberger K. L., Pettini M., Barmby P., Huang J., 2005, ApJ, 626, 698

Shapley A. E., Steidel C. C., Pettini M., Adelberger K. L., 2003, ApJ, 588, 65

Sharples R., et al. 2010, The Messenger, 139, 24

Sharples R., et al. 2013, The Messenger, 151, 21

Sheth R. K., Mo H. J., Tormen G., 2001, MNRAS, 323, 1

Silva A. I., Viegas S. M., 2002, MNRAS, 329, 135

Slosar A., et al. 2011, JCAP, 9, 1

Somerville R. S., Lemson G., Sigad Y., Dekel A., Kauffmann G., White S. D. M., 2001, MNRAS, 320, 289

Springel V., 2005, MNRAS, 364, 1105

Springel V., Hernquist L., 2003, MNRAS, 339, 289

Springel V., White S. D. M., Jenkins A., Frenk C. S., Yoshida N., Gao L., Navarro J., Thacker R., Croton D., Helly J., Peacock J. A., Cole S., Thomas P., Couchman H., Evrard A., Colberg J., Pearce F., 2005, Nature, 435, 629

Springel V., White S. D. M., Tormen G., Kauffmann G., 2001, MNRAS, 328, 726

Stark D. P., Ellis R. S., Chiu K., Ouchi M., Bunker A., 2010, MNRAS, 408, 1628

Steidel C. C., Adelberger K. L., Giavalisco M., Dickinson M., Pettini M., 1999, ApJ, 519, 1

Steidel C. C., Adelberger K. L., Shapley A. E., Pettini M., Dickinson M., Giavalisco M., 2000, ApJ, 532, 170

Steidel C. C., Adelberger K. L., Shapley A. E., Pettini M., Dickinson M., Giavalisco M., 2003, ApJ, 592, 728

Steidel C. C., Erb D. K., Shapley A. E., Pettini M., Reddy N., Bogosavljević M., Rudie G. C., Rakic O., 2010, ApJ, 717, 289

Steidel C. C., Giavalisco M., Dickinson M., Adelberger K. L., 1996, AJ, 112, 352

Steidel C. C., Hamilton D., 1992, AJ, 104, 941

Suzuki N., Tytler D., Kirkman D., O'Meara J. M., Lubin D., 2003, PASP, 115, 1050

Taniguchi Y., et al. 2005, PASJ, 57, 165

Taruya A., Nishimichi T., Saito S., 2010, Phys. Rev. D, 82, 063522

Theuns T., Leonard A., Efstathiou G., Pearce F. R., Thomas P. A., 1998, MNRAS, 301, 478

Theuns T., Viel M., Kay S., Schaye J., Carswell R. F., Tzanavaris P., 2002, ApJ, 578, L5

Tinker J. L., Weinberg D. H., Zheng Z., Zehavi I., 2005, ApJ, 631, 41

Trainor R. F., Steidel C. C., 2012, ApJ, 752, 39

van der Burg R. F. J., Hildebrandt H., Erben T., 2010, A&A, 523, A74

Venemans B. P., Röttgering H. J. A., Miley G. K., van Breugel W. J. M., de Breuck C., Kurk J. D., Pentericci L., Stanford S. A., Overzier R. A., Croft S., Ford H., 2007, A&A, 461, 823

Vernet J., Dekker H., D'Odorico S., Kaper L., Kjaergaard P., Hammer F., Randich S., Zerbi F., Groot P. J., Hjorth J., Guinouard I., Navarro R., Adolfse T., Albers P. W., Amans J.-P. a., 2011, A&A, 536, A105

Vogt S. S., Allen S. L., Bigelow B. C., Bresee L., Brown B., Cantrall T., Conrad A., Couture M., Delaney C., Epps H. W., Hilyard D. a., 1994, in Crawford D. L., Craine E. R., eds, Instrumentation in Astronomy VIII Vol. 2198 of Society of Photo-Optical Instrumentation Engineers (SPIE) Conference Series, HIRES: the high-resolution echelle spectrometer on the Keck 10-m Telescope. p. 362

Weil M. L., Eke V. R., Efstathiou G., 1998, MNRAS, 300, 773

White S. D. M., Frenk C. S., 1991, ApJ, 379, 52

White S. D. M., Rees M. J., 1978, MNRAS, 183, 341

Worseck G., Wisotzki L., Selman F., 2008, A&A, 487, 539

Yagi M., Kashikawa N., Sekiguchi M., Doi M., Yasuda N., Shimasaku K., Okamura S., 2002, AJ, 123, 66

Zaldarriaga M., Seljak U., 2000, ApJS, 129, 431

Zehavi I., et al. 2005, ApJ, 621, 22

Zel'dovich Y. B., 1970, A&A, 5, 84

Zheng Z., Cen R., Trac H., Miralda-Escudé J., 2010, ApJ, 716, 574

Zheng Z., Cen R., Trac H., Miralda-Escudé J., 2011, ApJ, 726, 38

Zheng Z., Cen R., Weinberg D., Trac H., Miralda-Escudé J., 2011, ApJ, 739, 62